DISS. ETH NO. 21316

HYDROTHERMAL GASIFICATION OF FERMENTATION RESIDUES FOR SNG-PRODUCTION

A dissertation submitted to

ETH Zurich

for the degree of

Doctor of Sciences
(Dr. sc. ETH Zurich)

presented by

Hemma Zöhrer

Dipl.-Ing. TU Berlin

born 10.12.1983
citizen of Germany

accepted on the recommendation of

Prof. Dr. A. Wokaun, examiner
Prof. Dr. J. van Bokhoven, co-examiner
Prof. Dr. F. Vogel, co-examiner

2013

Danksagung:

An erster Stelle möchte ich meinem Doktorvater, Prof. A. Wokaun für die Möglichkeit danken, diese Arbeit am Paul-Scherrer Institut durchzuführen, sowie für die zahlreichen wertvollen Diskussionen. Prof. J. van Bokhoven danke ich für die Übernahme des Koreferats.

Mein herzlicher Dank gilt Prof. F. Vogel als dem direkten Betreuer meiner Arbeit, vor allem für die Möglichkeit, eine Doktorarbeit auf einem für mich sehr neuen Gebiet durchzuführen, für die vielen anregenden Gespräche und die Betreuung durch drei spannende Jahre.

Ein ganz besonderer Dank gilt E. De Boni, dessen Ideen und unermüdlicher Einsatz ein unverzichtbares Fundament unserer Gruppe bilden.

Meinen ehemaligen Kollegen Dr. M. Schubert und Dr. J. Müller danke ich insbesondere für die Unterstützung bei der Einarbeitung und die schöne gemeinsame Zeit, aus der eine bleibende Freundschaft entstanden ist.

Meinen Doktoranden- und Gruppenkollegen danke ich für die Zusammenarbeit. Besonders hervorheben möchte ich J. Reimer, dem ich für viele bereichernde Gespräche und natürlich für das Bekochen während meiner Schreibphase danke. Meinem Bürokollegen C. Bährle danke ich ebenfalls für spannende Gespräche die angenehme und oftmals lustige gemeinsame Zeit.

T. Wölfl und insbesondere F. Mayr danke ich herzlich für den Beitrag, den sie im Rahmen ihrer Abschlussarbeiten zu dieser Arbeit geleistet haben.

Für experimentelle Unterstützung und Gespräche danke ich herzlich T.-B. Truong (IC und XRD), A. Schuler für (ICP-OES), A. Frei (XRD), J. Schneebeli (GC-SCD), M. Elsener (Kugelmühle und experimentellen Rat), S. Viereck (Aspen), P. Hottinger (LabView), M. Hottiger (technische Unterstützung) und E. DeBoni (SEM).

Den Partnern vom EtaMax Projekt danke ich für die Zusammenarbeit. Besonders danke ich Dr. N. Boukis und E. Hauer vom KIT für zahlreiche wertvolle

Diskussionen, der Projektleiterin Dr. U. Schliessmann sowie A. Laug und S. Görner vom Fraunhofer IGB für die Belieferung mit Gärresten. Schliesslich gilt dem deutschen Bundesministerium für Bildung und Forschung (BMBF) grosser Dank für die finanzielle Förderung des Projekts.

Der Firma Norpro Saint Gobain, besonders Dr. M. Pabel danke ich für die Trägerproben und für die freundliche Zusammenarbeit.

Für ihre stille und immer spürbare Unterstützung durch alle Jahre hindurch möchte ich meinen Eltern danken; meinen Brüdern und meinen Freunden für die stets aufmunternden Worte, und natürlich ganz besonders Max Mehring – dem wichtigsten von allem, was ich von meiner Zeit am PSI mitnehmen durfte.

1 Abstract

Biogas plants, increasing in number, produce a stream of fermentation residue with high organic content, providing an energy source which is by now mostly unused. In this work the fermentation residue was tested as a potential feedstock for catalytic gasification in supercritical water (T ≥ 374°C, p ≥ 22 MPa) for methane production following PSI's hydrothermal gasification process. The process includes hydrothermal liquefaction in near-critical water, supercritical salt-separation and finally low-temperature catalytic gasification by a ruthenium catalyst.

The assessment was done by an experimental approach, firstly in a batch reactor system and secondly in a continuous lab test rig (Konti-2). The coke formation tendency during the non-catalytic heat-up phase was evaluated as well as the cleavage of biomass-bound sulfur with respect to its removal from the process as a salt.

In batch experiments the biomass was efficiently liquefied during heating up to a temperature of 410°C at 30-35 MPa. Sulfur was not sufficiently released from the biomass. More than 50% of the sulfur was still bound to the biomass. Addition of alkali improved the liquefaction of fermentation residues with a low content of minerals, probably by buffering the pH.

In continuous experiments a partial liquefaction was observed; some particles underwent carbonization. Tars were formed to a large extent. Around 50% of the feed carbon remained in the system as tars. Furthermore, a homogeneous coke was formed, presumably originating from condensed tars. The insufficient sulfur mineralization was confirmed by the continuous experiments.

Desalination was observed at a salt separator set point temperature of 450°C and 28 MPa; however, many salts could not be withdrawn as a concentrated brine. At 430°C no salt separation took place. For a particular pressure, generally high temperatures are favorable for salt separation; in this work, high temperatures were found to promote tar- and coke formation. It was therefore concluded that the process requirements for an efficient biomass liquefaction and salt separation are conflicting.

With respect to the catalytic gasification a deactivation of the carbon-supported ruthenium catalyst was observed in batch experiments, which was attributed to sulfur poisoning and fouling. For experiments with high catalyst loadings a temperature of 400°C was found to maximize the methane yield. A residence time dependent biomass to catalyst ratio of 0.45 $g_{(biomass)}\ g_{(catalyst)}^{-1}\ h^{-1}$ was found to result in nearly full conversion with the Ru/C catalyst. A Ru/ZrO_2 catalyst, tested under similar conditions, showed less conversion. In a continuous experiment the Ru/C catalyst was rapidly deactivated, which was attributed to incomplete sulfur separation in the preceding steps, i.e. liquefaction and salt separation.

In the second part, in-situ sulfur poisoning of two carbon and titania supported ruthenium catalysts was investigated. In this context, different regeneration methods were compared: flushing with subcritical water and an oxidative treatment with diluted H_2O_2 solution at 125°C. For the carbon supported ruthenium catalyst, only the oxidative treatment led to a reactivation. However, the catalyst system was severely damaged by the treatment. The titania supported ruthenium catalyst could be partially regenerated by subcritical flushing. Furthermore, the titania supported catalyst showed a higher resistance towards the oxidative environment.

In a third part of this work eleven commercial stabilized and unstabilized zirconia and titania samples have been tested for stability as potential catalyst supports for supercritical water gasification of glycerol solutions at 400°C and 28.5 MPa. Samples based on monoclinic zirconia and rutile and one sample based on stabilized tetragonal zirconia showed good physical stability. Most samples showed a loss of surface area during the first 20 hours of hydrothermal treatment, leveling out at longer exposure times. In a continuous fixed-bed reactor setup, a performance and stability test of the samples loaded with 2 wt% ruthenium gave good results for three samples, of which the sample based on stabilized tetragonal zirconia showed the best performance. A loss in surface area could be prevented by hydrothermal aging of the support prior to impregnation with ruthenium. Additionally, a 5 wt% ruthenium loading was tested, which led to a higher performance. A bimetallic ruthenium/rhenium catalyst showed neither improved performance nor improved sulfur tolerance as suggested in the literature.

2 Zusammenfassung

Durch die wachsende Anzahl an Biogasanlagen werden Gärreste gebildet, welche mit ihrem hohen Organikanteil ein bislang weitgehend ungenütztes Energiepotential darstellen. In dieser Arbeit wurde dieser Gärrest als möglicher Feed für die katalytische Vergasung in überkritischem Wasser (T ≥ 374°C, p ≥ 22 MPa) zur Methanerzeugung nach dem hydrothermalen Vergasungsprozess des PSI untersucht. Der Prozess umfasst eine hydrothermale Verflüssigung in nahekritischem Wasser, überkritische Salzabscheidung und schliesslich eine katalytische Vergasung durch einen Rutheniumkatalysator

Die Beurteilung geschah über eine experimentelle Herangehensweise, zunächst in einem Batch-Reactorsystem und anschliessend in einer kontinuierlichen Laboranlage (Konti-2). Bewertet wurden die Verkokungstendenz während des unkatalytischen Aufheizvorgangs sowie die Abspaltung von gebundenem Schwefel im Hinblick auf dessen Abscheidung als Salz.

In Batchexperimenten wurde die Biomasse in der Aufheizphase bis 410°C bei 30-35 MPa wirksam verflüssigt. Schwefel wurde nicht in ausreichendem Masse von der Biomasse abgespalten. Über 50% des Schwefels verblieb gebunden. Die Zugabe von Laugen verbesserte die Verflüssigung von Gärresten mit geringem mineralischem Gehalt, vermutlich durch ein Abpuffern des pH Wertes.

In kontinuierlichen Experimenten wurde eine teilweise Verflüssigung beobachtet. Einige Partikel wurden carbonisiert. Teere wurden in grossem Masse gebildet. Rund 50% des Feed-Kohlenstoffs verblieb als Teer in der Anlage. Die ungenügende Schwefelmineralisierung wurde durch die kontinuierlichen Experimente bestätigt.

Bei einer Salzabscheidertemperatur von 450°C und 28 MPa wurde eine Entsalzung beobachtet. Jedoch konnten einige Salze nicht in flüssiger Form abgetrennt werden. Bei 430°C fand keine Salzabscheidung statt. Bei einem bestimmten Druck sind generell hohe Temperaturen für die Salzabscheidung vorteilhalft. In dieser Arbeit stellte sich heraus, dass hohe Temperaturen Teer und Koksbildung fördern. Daraus wurde gefolgert, dass die Bedürfnisse für eine effiziente Biomasseverflüssigung und die Salzabscheidung schwer in Einklang zu bringen sind.

Hinsichtlich der katalytischen Vergasung wurde in Batchversuchen eine Desaktivierung des kohlenstoffgeträgerten Rutheniumkatalysators beobachtet. Dies

wurde auf Schwefelvergiftung und auf Fouling zurückgeführt. Bei hohen Katalysatorbeladungen zeigte sich, dass bei einer Temperatur von 400°C die Methanausbeute am höchsten ist. Ein verweilzeitabhängiges Biomasse zu Katalysator Verhältnis von 0.45 $g_{(Biomasse)}$ $g_{(Katalysator)}^{-1}$ h^{-1} wurde ermittelt, bei welchem eine nahezu vollständige Umsetzung durch den Ru/C Katalysator erfolgte. Ein Ru/ZrO_2, welcher unter ähnlichen Bedingungen getestet wurde, zeigte eine geringere geringere Umsetzung. In einem kontinuierlichen Versuch desaktivierte der Ru/C rasch, was auf die ungenügende Schwefelabtrennung in den vorherigen Schritten, der Verflüssigung und der Salzabscheidung, zurückgeführt wurde.

In einem zweiten Teil wurde die in-situ Vergiftung von einem kohlenstoff und einem titanoxidgeträgerten Rutheniumkatalysator untersucht. In diesem Zusammenhang wurden verschiedene Regenerierungsmethoden miteinander verglichen: Waschen mit heissem Hochdruckwasser und eine oxidative Behandlung mit verdünntem H_2O_2 bei 125°C. Bei den kohlenstoffgeträgerten Katalysatoren führte ausschliesslich die oxidative Behandlung zu einer Regenerierung. Jedoch wurde das Katalysatorsystem durch die Behandlung stark beschädigt. Der titanoxidgeträgerte Katalysator zeigte eine höhere Widerstandsfähigkeit gegenüber oxidativen Bedingungen.

In einem dritten Teil dieser Arbeit wurden elf kommerziell erhältliche stabilisierte und nicht stabilisierte Zirkonoxid- und Titanoxidproben als mögliche Katalysatorträger für die Vergasung von Glycerinlysungen in überkritischem Wasser bei 400°C und 28.5 MPa untersucht. Die Proben aus monoklinem Zirkonoxid und Rutile sowie eine Probe aus stabilisiertem tetragonalem Zirkonoxid zeigten eine gute physikalische Stabilität. Die meisten Proben wiesen eine Verringerung der Oberfläche während der ersten 20 Stunden im überkritischen Wasser auf; anschliessend nahm sie kaum weiter ab. Mit den mit 2% Ruthenium beladenen Trägern wurde in einem kontinuierlich betriebenen Festbettreaktor die Leistung und Stabilität getestet, welcher gute Resultate für 3 der Proben lieferte, von welchen die eine aus stabilisiertem tetragonalem Zirkonoxid die besten Leistung zeigte. Eine Abnahme der Oberfläche konnte durch hydrothermale Alterung des Trägers vor der Imprägnierung mit Ruthenium verhindert werden. Desweiteren wurde eine 5%ige

Beladung getestet. Dies bewirkte eine höhere Leistung. Ein bimetallischer Ruthenium/Rheniumkatalysator zeigte weder eine gesteigerte Leistung noch eine verbesserte Schwefeltoleranz, wie sie in der Literatur beschrieben wurde.

3 Introduction

3.1 Background

Due to the finiteness of fossil energy carriers that comes in parallel with a worldwide ongoing increase in the energy demand, renewable resources have gained widespread attention and have therefore been in the focus of energy research activities in the past decades.

Biomass has attained special interest as a renewable resource because of its nature providing a chemically fixed energy form that can be converted to other chemically fixed energy forms which are relatively similar to the energy carriers our infrastructure is built and optimized for, i.e. petroleum products and natural gas. Ethanol, oils from agricultural sources and bio-gas produced by microbial digestion of energy crops and other organic material are such examples. In many countries, the agricultural production of energy crops has been subsidized by their governments in order to promote energy independence from fossil fuels. However, these efforts have often been assigned as a main factor contributing to the high food price volatility over the last decades [1].

For the energetic utilization of waste biomass streams, a competition between food production and fuel and power generation is unlikely. Yet, these biomass resources are often poorly suitable for combustion or pyrolysis processes because of high moisture contents and a large variability of the composition. Solely, anaerobic biological digestion to methane has already become a widely applied method for recovering energy from sewage sludge and manure; however, biological processes generally suffer from slow rates of conversion as well as from the incomplete conversion of various components.

3.2 Concept of the EtaMax project

Methane (natural gas) is a generally favored energy carrier since it can be distributed over an existing grid. Besides the anaerobic biological digestion, gasification in supercritical water is a promising method to convert wet biomass efficiently and with a high rate to synthetic natural gas. However, it requires the feedstock to be a pumpable fluid, which is not the case for many wet organic waste streams. Therefore, a combination of biological digestion with hydrothermal gasification offers advantages for both processes. In this case, biological digestion can be regarded as a pretreatment step for the biomass, during which easily digestible components such as starch and proteins are degraded. This reduces the solid content of the biomass and increases the pumpability, while the external energy input to anaerobic digestion is low. The residual digested sludge contains mainly biologically persistent components such as lignin and cellulose and inorganic salts. Several groups have already successfully gasified cellulose and lignin in a hydrothermal environment [2-5].
Catalytic gasification in low temperature supercritical water with a combined salt recovery, proposed by Vogel et al. as PSI`s hydrothermal gasification process [6], might be a potential strategy to convert the residuals from anaerobically digested biomass to synthetic natural gas. By recovering nutrient salts from both processes, anaerobic digestion and hydrothermal catalytic gasification, a recycling of essential substances can be obtained by redirecting them to the natural cycle of nutrients.

In order to evaluate the potential of the high-performance anaerobic digestion and PSI`s hydrothermal gasification process to convert residuals from biomass digestion, the EtaMax project was set up. EtaMax was a joint project funded by the German educational department (BMBF) and initiated by Fraunhofer IGB (Stuttgart, Germany). This project intended to maximize the methane output of grocery market wastes by combining a two stage high-performance anaerobic digestion process with PSI`s hydrothermal gasification process. Different project partners from research and industry were involved in the anaerobic digestion part of the project including the upstream (milling) and downstream (gas purification) processes as well as a microalgae production in the nutrients recovered from the fermentation process. In the hydrothermal gasification part, KIT (Karlsruhe, Germany) and PSI (Villigen,

Switzerland) were involved. A scheme of the EtaMax concept is depicted in Figure 3-1.

This thesis addresses the gasification of the fermentation residue via PSI`s hydrothermal gasification process. By an experimental approach, liquefaction and gasification of the fermentation residue were studied in a batch reactor setup and in a continuous lab test rig implementing PSI`s hydrothermal gasification process.

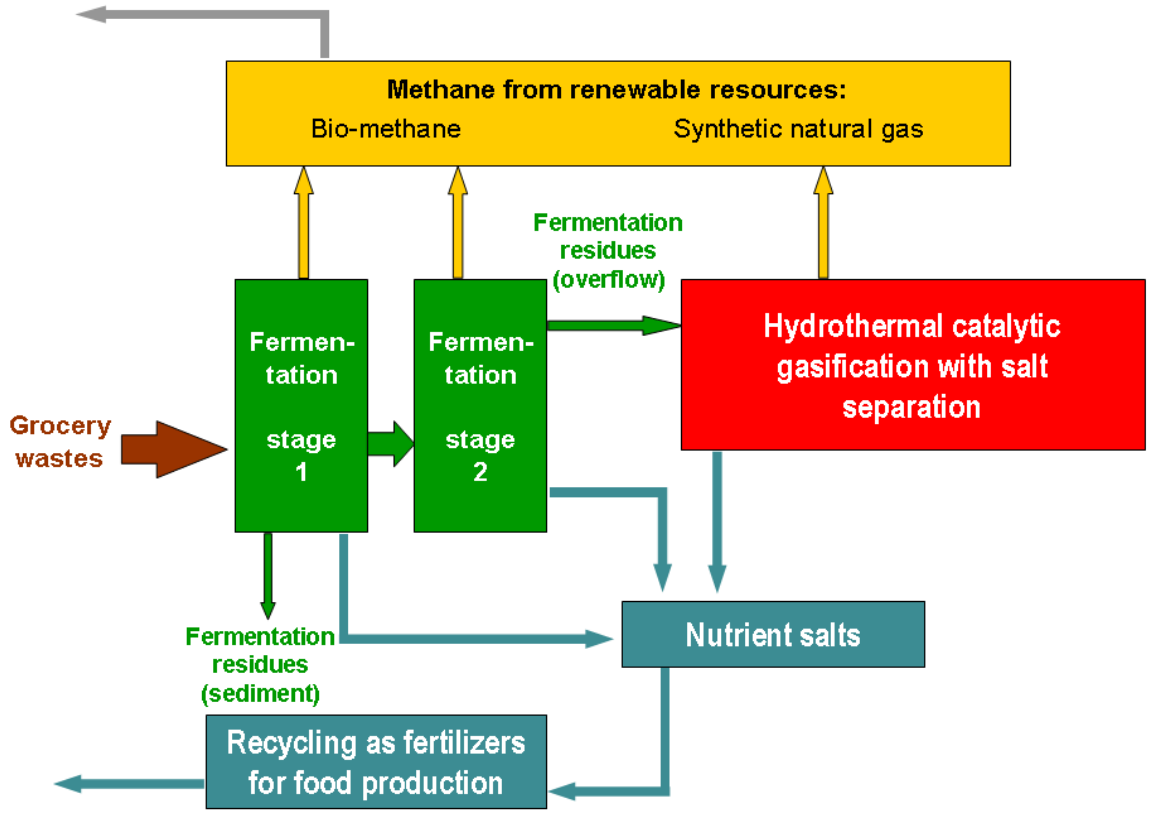

Figure 3-1: EtaMax concept. Scheme of the combined processes of anaerobic digestion and hydrothermal catalytic gasification for a maximum production of methane from grocery wastes.

3.3 Fermentation residue: Origin, Availability, Utilization and Composition

More than 12'000 biogas plants are located in Europe. The number has strongly increased over the past two decades. From the distribution of biogas plants in selected European countries, shown in Figure 3-2, it becomes obvious that especially in Germany an enormous number of plants was built.

In Germany, where a vigorous subsidy policy has brought forth an especially high density of biogas plants, around 8'000 plants have been installed by now with an installed electric capacity of more than 3 GW. The development over the past decade is shown in Figure 3-3.

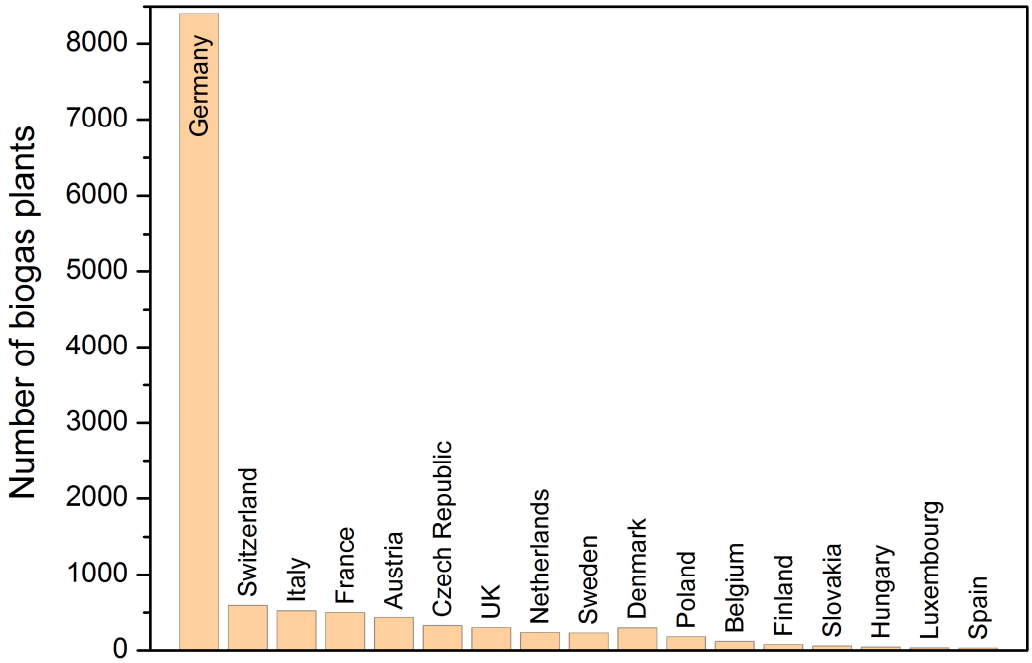

Figure 3-2: Number of biogas plants of selected European countries, year 2011 [7].

These plants are converting various sources of organic feedstocks to bio-methane and a fermentation residue. The methane is used for the production of electric energy on the site. The fermentation residue is typically returned to the farmland as organic fertilizer. The fermentation residues still contain a considerable amount of organic matter that has not been converted to methane by microbial digestion. Utilization of the fermentation residues for energy generation has not been reported. Any attempts to do this were relinquished sooner or later, because of legal issues on the one hand and even more importantly because of the high content of water and minerals on the other hand, that are detrimental for conventional combustion processes [8].

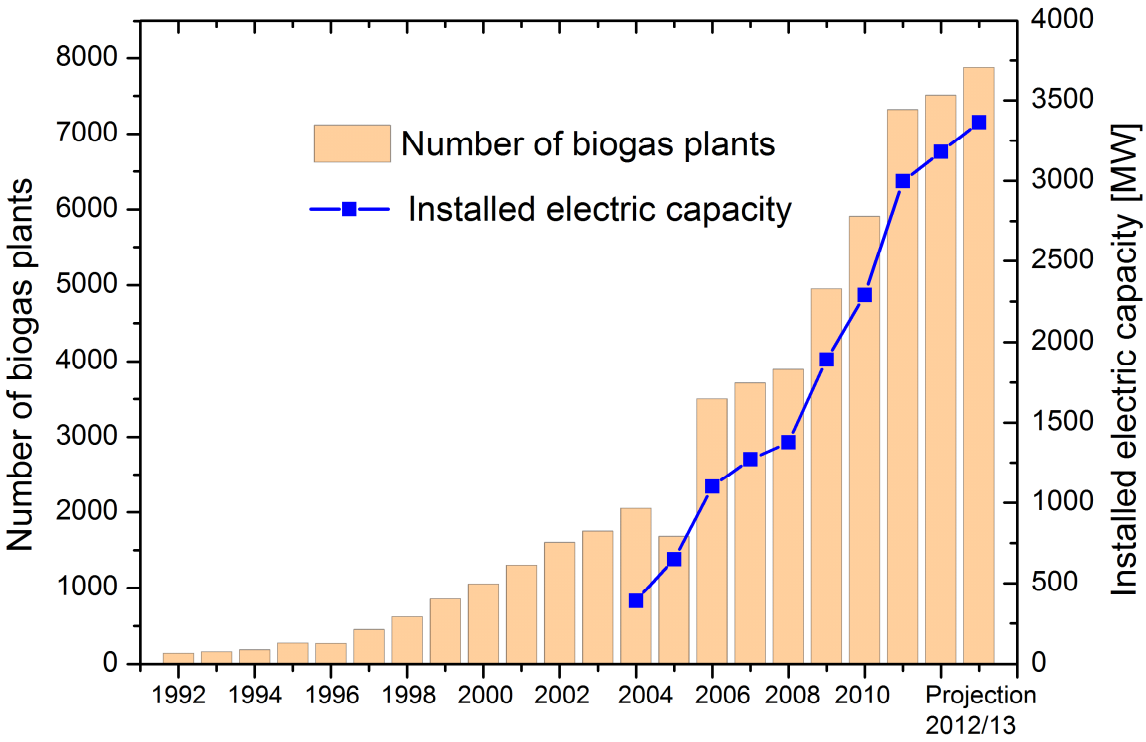

Figure 3-3: Development of biogas plants and the installed electric capacity in Germany over the last two decades [9].

From information supplied by the German Biogas Association, around 60 million tons of fermentation residues (wet) are annually produced in Germany, while 10 million tons stem from those plants that have been built in 2012. With this large increment, fermentation residues can be considered a promising energy source [8].
The fermentation residues consist mainly of water and ligno-cellulose rich organic material. The content of minerals is relatively high but strongly dependent on the feedstock. Phosphorus, nitrogen and sulfur as well as alkali and earth alkali compounds make up a considerable amount of these and are considered as nutrient salts [10].

In the European Union and other countries including Switzerland, fermentation residues stemming from the digestion of food wastes are legally obliged or at least recommended to be sanitized before disposal, e.g. on the farmland [11, 12]. The sanitization procedure includes pasteurization (70°C, 1 h for a particle size < 12 mm). For certain high-risk materials high-pressure steam sterilization is required (133°C, 0.3 MPa for a particle size of 50 mm). A thermophilic fermentation can redundantize

the pasteurization in the case a temperature of 55°C could be maintained over 29 days. Nevertheless, 4-5 million tons of the fermentation residues that are annually produced in Germany require a sanitization treatment [8]. The sanitization consumes energy which is lost in the energetic utilization of the feedstock.
For easier handling and storage, some operators of biogas plants dry the fermentation residue. This procedure is an additional loss in the energy balance of the whole conversion process.
Therefore, an energetic utilization of the fermentation residue provides a potential to increase the energetic output of the organic feedstock or at least compensate for the energy input that is required for sanitization in case of food wastes used as feedstock.

3.4 Hydrothermal processes for energy generation

3.4.1 Properties of sub- and supercritical water

For organic feedstocks with a high water content hydrothermal processes have the general advantage of a reduced process energy demand, since an energy-consuming drying process becomes obsolete. Water is retained in the system and acts both as solvent and reactant. Furthermore, in hydrothermal gasification, including processes operated both in sub- and in supercritical water, the properties of water are advantageous for degrading large biomass molecules to smaller ones [13]. The properties of hot compressed water can briefly be described as follows:

- In subcritical water (T< 374°C), the rate of hydrolysis is greatly enhanced due to the increased ion product of water [14].
- At supercritical conditions, the good solubility for organic molecules and gases reduces mass transport limitations.
- The poor solubility for salts at supercritical conditions can be utilized for separating salts from the biomass.

3.4.1.1 Phase behavior of pure water

During heat-up of water between the triple point (0.01°C, $611 \cdot 10^{-6}$ MPa) and the critical point (374°C, 22.1 MPa), it can exist in the liquid or in the gaseous phase. By isochoric heat-up, a co-existence of both phases is possible over a wide pressure

range. In Figure 3-4 a simplified phase diagram of water and a density-temperature diagram are depicted. The saturation line represents the pressures and corresponding temperatures at which both phases co-exist. The saturation line is thus representing the vapor pressure at a certain temperature.

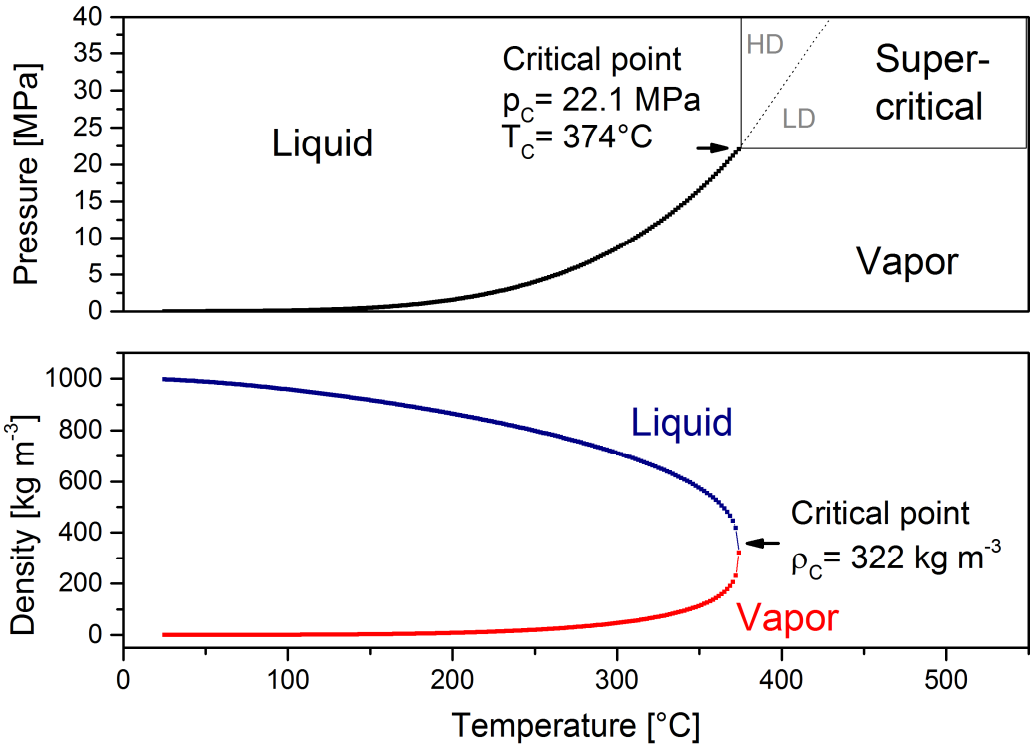

Figure 3-4: Simplified phase diagram for pure water (top) and density of the liquid and the vapor phase during heat-up at isochoric conditions [15]. HD: high density area ("pseudo-subcritical"), LD: low density ("true-supercritical") area.

Towards higher temperatures, the density of the liquid phase continuously decreases while the vapor phase becomes denser. For a closed system this results in a pressure increase along the saturation line. At a critical pressure of 22.1 MPa and temperature of 374°C the densities of both phases become identical, resulting in a mixing of both phases. No more phase boundary is visible for water above the critical point. The supercritical region can be divided into a high-density ("pseudo-subcritical") and a low-density ("true-supercritical") region indicated by the dotted line in prolongation of the saturation line, where the so-called pseudo-critical points are positioned. For a particular pressure, these can be defined as the temperature of the maximum specific enthalpy change or the maximum isobaric heat capacity. In the pseudo-subcritical area the properties of water are more similar to those of subcritical water than in the

true-subcritical area. This difference in the properties of water in both areas is expected to influence reactions.

3.4.1.2 Specific enthalpy and isobaric heat capacity

The phase change from liquid to vapor during heat-up of pure water at ambient pressures is associated with an abrupt and relatively high increase of the specific enthalpy (Figure 3-5, top). In comparison, the phase transition to supercritical shows a smooth s-shaped curve, which is associated with a lower increase of the specific enthalpy. In the temperature range relevant for hydrothermal processes (200-600°C) the specific enthalpy of pressurized water is generally lower than that of superheated steam. For the operation under supercritical water conditions this has the advantage of a considerable reduction in the process energy demand in comparison to superheated steam.

During heat-up at subcritical conditions the isobaric heat capacity shows a distinct peak as the water passes a phase transition (Figure 3-5, bottom). Beyond the critical point, the peak is progressively flattening out. The maximum can be assigned to the temperature of the pseudo-critical phase transition. Towards higher pressures, the peak of the isobaric heat capacity is shifted to higher temperatures and becomes less distinct.

Near the critical point, temperature and pressure changes thus have a great influence on the physical properties of the supercritical fluid. This allows a tuning of these properties according to the requirements. For higher temperatures and pressures the influence of changes in both parameters becomes less significant.

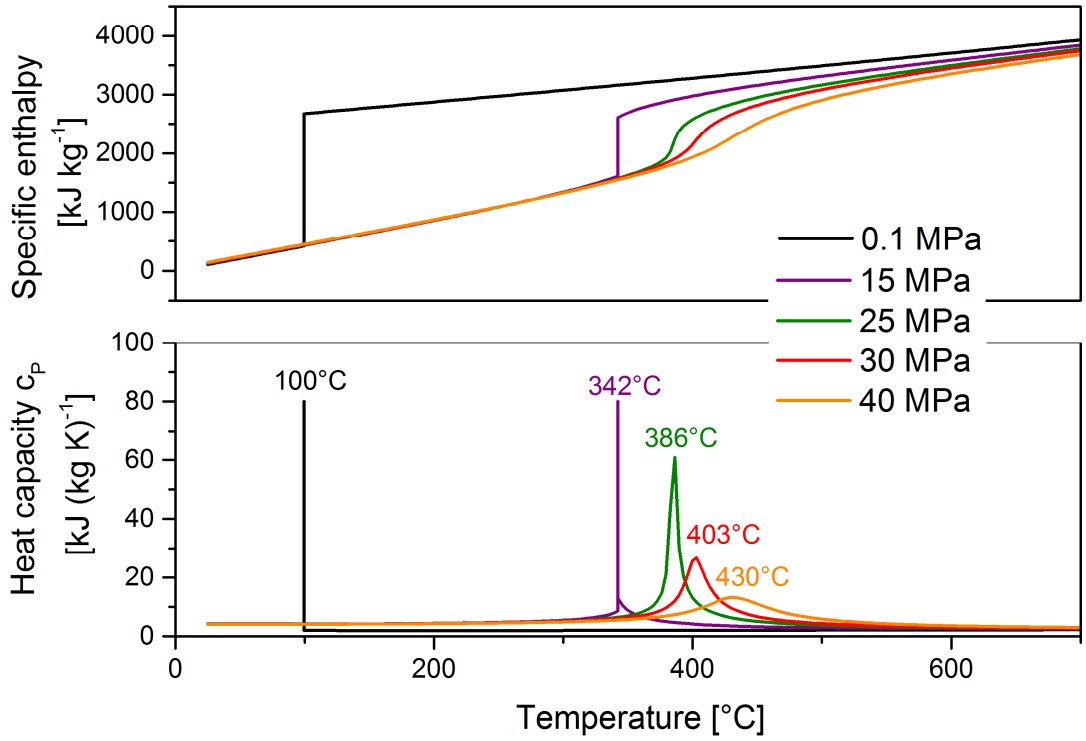

Figure 3-5: Specific enthalpy (top) and isobaric heat capacity (bottom) of pure water during isobaric heat-up at different pressures [15].

3.4.1.3 Density and dielectric constant

As a further parameter describing the physical conditions of water, the density is strongly connected with the strength of inter-molecular interactions. Upon isobaric heat-up of pure water, the density of the liquid phase is continuously decreasing, showing the highest gradient at the temperature of a phase transition (Figure 3-6, bottom). Similar to the specific enthalpy and isobaric heat capacity, the density change for the transition from the liquid to the vapor phase is more distinct than for the transition to the supercritical phase.

The solvent properties of water at different pressures and temperatures are determined by its dielectric properties, described by the static relative permittivity or dielectric constant ε. The dielectric constant is a measure for the polarity of a solvent and thus for the strength of electrostatic interactions between ionic solutes and solvent. Its value is closely connected with the density of the fluid. For polar solvents, it is additionally influenced by a negative temperature dependence, which is due to the breaking of the dipole correlations [16]. Like the density, the dielectric constant

sharply decreases as water passes the phase transition from liquid to vapor and smoothly decreases for pressures at which a phase transition to supercritical occurs (Figure 3-6, top).

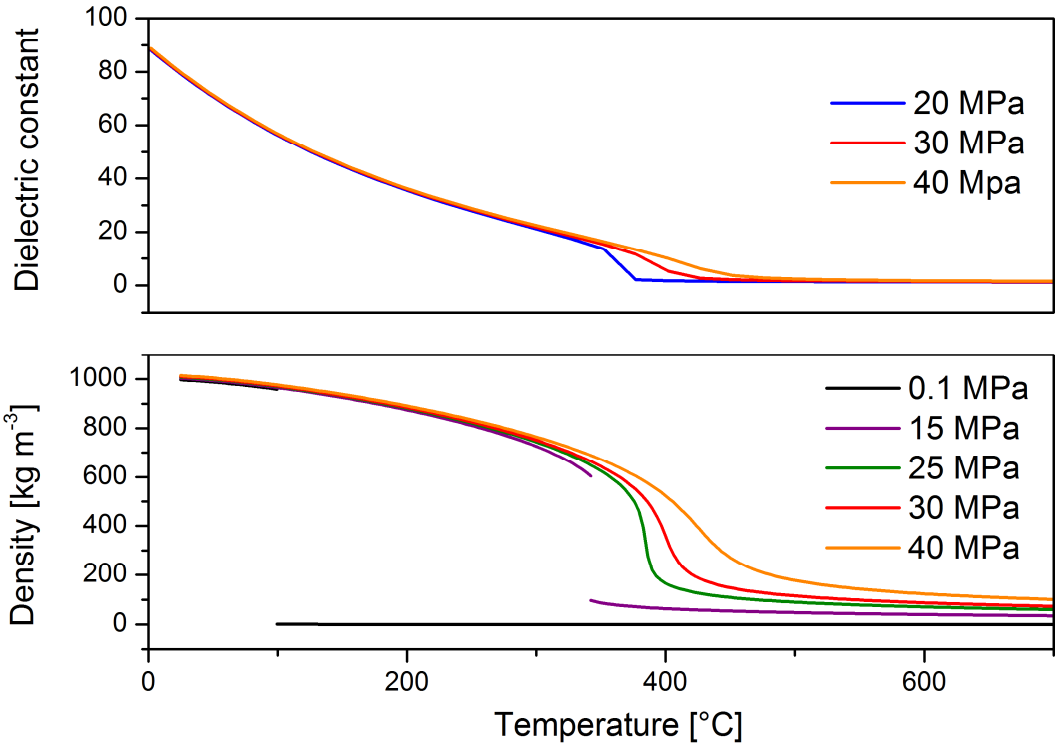

Figure 3-6: Dielectric constant (top) and density (bottom) during isobaric heat-up of water at different pressures [15, 16].

While water behaves like a very polar solvent at ambient conditions the solvent properties change with increasing temperature. The dielectric constant of near critical water is in the order of magnitude of polar organic solvents at ambient conditions (methanol: $\varepsilon = 33$, acetone: $\varepsilon = 21$). Beyond the phase transition the dielectric constant drops to values comparable to non-polar solvents at ambient conditions (hexane: $\varepsilon = 1.89$, benzene: $\varepsilon = 2.3$) [17]. This results in an improved solubility of organic molecules in subcritical water and a greatly improved solubility of non-polar molecules in supercritical water which furthermore results in an increased contact frequency between water and organic molecules facilitating reactions among them. A rapid hydration of degradation intermediates also diminishes the chance for condensation reaction and thus coke formation [18, 19]. Furthermore, a low dielectric constant increases the solubility of many gases in supercritical water [20, 21]. The resulting absence of phase boundaries strongly decreases limitations by mass transport effects. As a consequence of this, homogeneous reactions among

gases and liquid molecules are facilitated [22]. The reduced polarity of water at supercritical condition also leads to a reduced solubility of salts (Figure 3-7) [23, 24]. This characteristic allows the separation of salts from aqueous solutions [25-27].

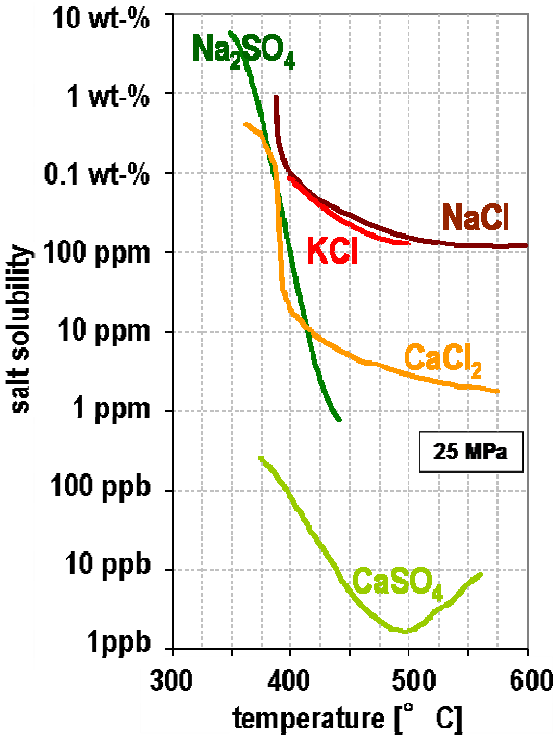

Figure 3-7: Solubility of salts in supercritical water. Graphic adapted from [23, 28].

3.4.1.4 Mass transport

Convective and diffusive mass transport in a fluid is basically determined by the viscosity. The kinematic viscosity v is in turn depending on the temperature and density of a fluid and influences convective and diffusive mass transport. The diffusivity is expressed by the diffusion coefficient D. In supercritical water an increased mass transport is observed resulting from a reduced viscosity and an increased diffusivity of the medium [20, 29].

The self-diffusion coefficient of supercritical water was reported to range from 4.71 10^{-7} m^2 s^{-1} (700°C, 39.7 MPa) to 4.74 10^{-8} m^2 s^{-1} (400°C, 105.6 MPa) [29], which is by more than one order of magnitude higher than liquid water at ambient conditions 2.2 10^{-9} m^2 s^{-1} [30].

Only few experimental data for molecular diffusion coefficients of different molecules in sub- and supercritical water are available. Molecular diffusion

coefficients of iodide ions at temperatures up to 375°C have been determined by Flarsheim et al. [31] and are depicted in Figure 3-8 . Goemans et al. [32] found diffusion values for alkali and earth alkali nitrates that were in good agreement with those for iodide ions reported by Flarsheim et al.

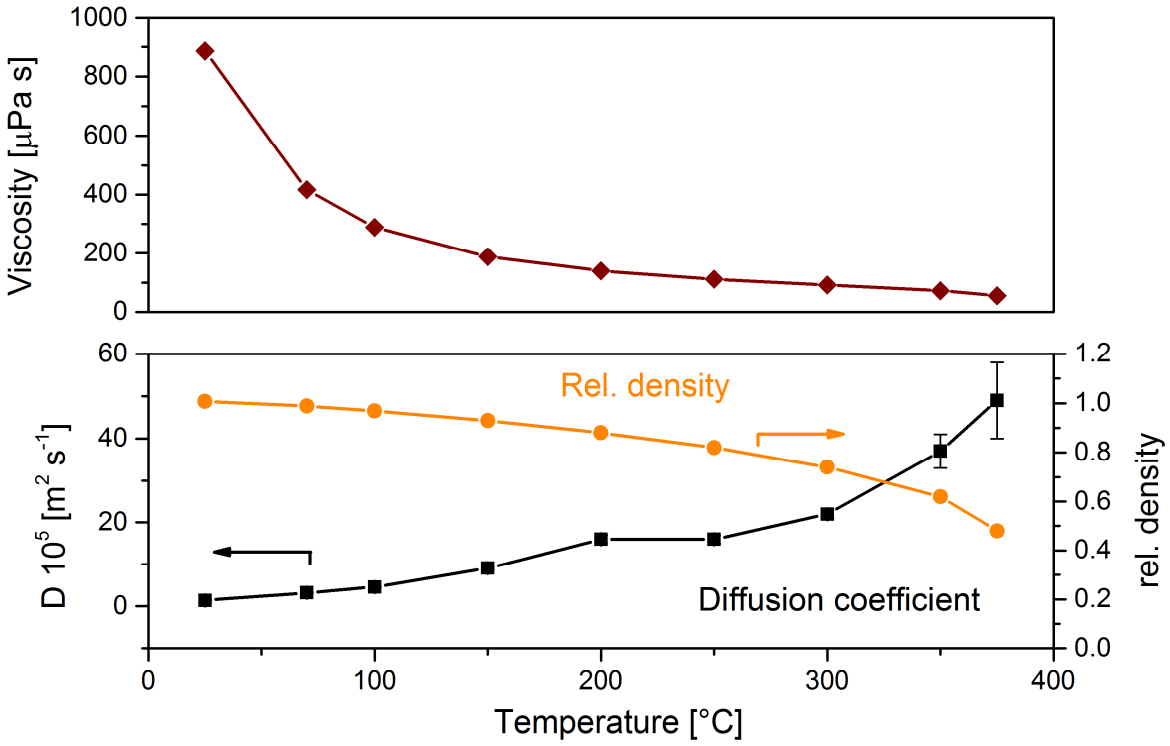

Figure 3-8: Viscosity of water and molecular diffusion coefficients for iodide ions in water in vs. temperature for the particular water densities (relative to 25℃, 0.1 MPa) plotted in this graph [15, 31].

From these and various other data Goeman et al. summarized that diffusion in near- and supercritical water is 15 to 35 times faster compared to ambient conditions. On the other hand, the diffusion values were more close to the values of liquid fluids than to those of gases [32]. Diffusion rates are in general expected to be inversely proportional to the fluid viscosity [33]. From this point of view, the observed constants are reasonable. Butenhoff et al., however, reported a phenomenon for concentrated aqueous $NaNO_3$ solutions, where the diffusion coefficient drastically dropped in the vicinity of the critical temperature of the solution [34]. Towards higher pressures, the diffusion coefficient was increasing again until a plateau was reached at some point. This phenomenon has previously been described in literature and is referred to as the critical slowing-down [34]. This observation may not be in contradiction to the data obtained by Flarsheim et al., who found an increased

diffusivity at the critical temperature of pure water: the critical temperature will be higher than 374°C in the presence of electrolytes, as will be discussed in section 3.4.1.6.

3.4.1.5 Ionization constant

The ionization constant of water K_W is defined as the product of the activities of H^+ and OH^- ions resulting from self-dissociation:

$$H_2O \leftrightarrows H^+ + OH^- \quad (3\text{-}1)$$

The temperature and pressure dependence of the ionization constant is shown in Figure 3-9. During heat-up of liquid water, the ionization constant continuously increases. Between 200 and 350°C a maximum is reached with values several orders of magnitude higher than at ambient conditions. Upon the phase change to supercritical, the ionization constant decreases again. Here, the pressure has a strong influence. At pressures near the (pseudo-) critical pressure the ionization constant decreases to a level which is by some orders of magnitude below the values at ambient conditions. This drop can be explained by the decreased solvation and stabilization power caused by the lower density and dielectric constant [22]. At elevated pressures, the decrease is less pronounced.

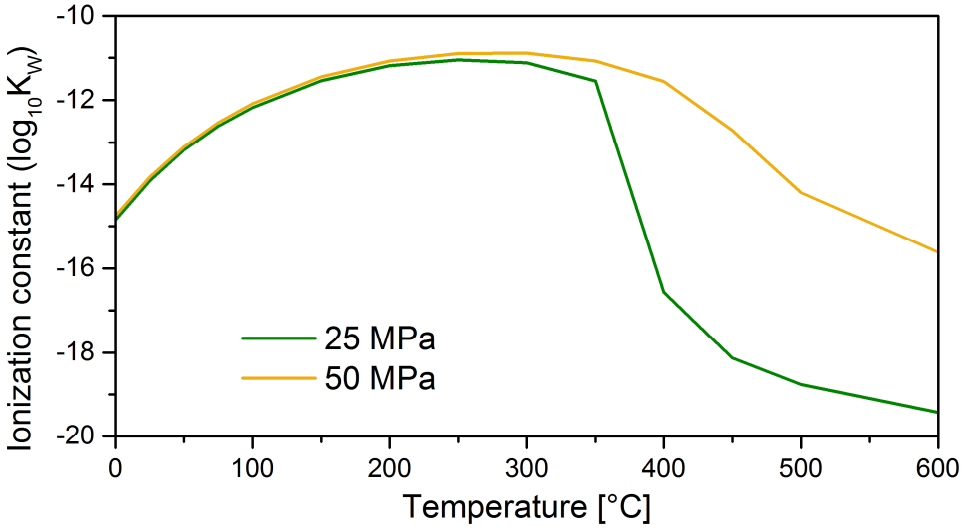

Figure 3-9: Ionization constant of water vs. temperature at different pressures [35].

A high ionization constant as it can be found in near-critical and high-pressure supercritical water promotes the rate of acid and base catalyzed reactions, which has been reported for different reactions, see [36] and literature cited therein.

3.4.1.6 Mixtures of water and other substances

The phase behavior of water changes in the presence of a solute. The critical point is shifted, resulting in a critical line depending on the concentration of the additional component. In the case of small quantities of small non-polar gases, the change of the critical temperature of water is only changed to a minor extent [20].
The influence of salts on the critical temperature of aqueous solutions has been investigated by Marshall and Jones [37]. In summary, an increase of the critical temperature was found, particularly for alkali halides. The presence of salts also greatly influences the phase behavior of water-gas mixtures [20]. Also organic molecules are expected to influence the critical temperature as a result of solvation phenomena. However, no experimental data are available since the measurements of the critical temperature are affected by degradation reactions.
In a multi-component mixture of gases, electrolytes and organic matter, the theoretical prediction of the phase behavior of water and thus a tuning of solvent properties is therefore fairly complex, requiring extensive experimental efforts.

3.4.2 Salts and supercritical water

3.4.2.1 Phase behavior of water-salt mixtures

The behavior of water-salt mixtures at elevated pressures and temperatures is determined by a complex set of immiscibility and phase equilibrium phenomena. For the proper description of a binary water-salt system a three-dimensional p-T-x-plot would be necessary. Usually, two-dimensional p-T-projections are found in literature. Here, the critical curve of the two components (water and salt) and the three-phase curve (S-L-V) are of particular interest. The critical curve connects the critical points of both pure components and describes all critical points of the two phase (V-L) equilibrium of the mixture. The three-phase curve describes the phase equilibrium between a saturated salt solution and the vapor phase and can thus be described by its vapor pressure curve [20].
Various different types of binary water-salt mixtures exist. Valyashko reduced the large number of known behavior types to two basic categories, referred to as type 1 and type 2 phase behavior [38].

The characteristic of the type 1 phase behavior is that the (V-L) critical curve is not intersected by the solubility curve (V-L-S_s) (see Figure 3-10). The solubility of salts with type 1 behavior increases continuously with increasing temperatures also at temperatures above the critical temperature of pure water. At certain salt concentrations liquid-liquid immiscibilities of a salt-rich water phase and a salt-depleted "supercritical-water" phase occur. In contrast, the type 2 phase behavior is characterized by an interruption of the critical curve between two critical endpoints by an intersection with the solubility curve. In this case the solubility drastically decreases with increasing temperature near the critical temperature of water. The region between the two critical endpoints is characterized by critical phenomena, i.e. the concentration of salt in the vapor and liquid phase are identical, and that is close to zero. A homogeneous supercritical fluid phase is in equilibrium with a solid salt phase [19, 20, 28, 38-40].

A very simplified p-T projection of type 1 and type 2 behavior can be found in Figure 3-10. Here, liquid-liquid immiscibility phenomena are not considered. Three-dimensional p-T-x plots can be found in [41].

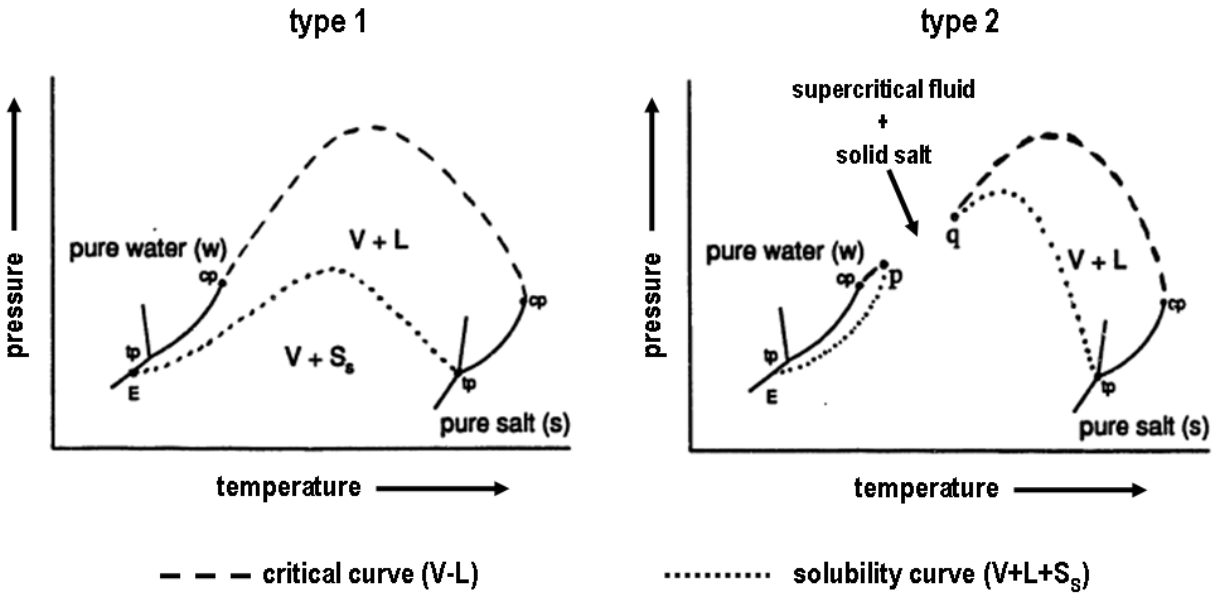

Figure 3-10: p-T phase diagrams for binary type 1 and 2 salt-water mixtures. cp: critical point of the pure components, tp: triple point of the pure components, p: lower critical endpoint, q: upper critical endpoint, E: eutectic point, V: vapor, L: liquid, S_S: solid salt phase. Modified version adapted from [19]; original source: [39].

The positive temperature coefficient of solubility of type 1 salts is seemingly in contradiction to the earlier mentioned decrease of the dielectric constant of water in

the supercritical region, which typically leads to a decrease in the salt solubility. Valyashko explained this by a non-aqueous solubilization mechanism which is characterized by a high level of ion-ion interaction, leading to a salt-rich aqueous phase comparable to the conditions of a hydrated melt [41].

3.4.2.2 Experimental studies on the behavior of binary and ternary salt mixtures in near- and supercritical water

The phase behavior of binary salt solutions (one salt plus water) and ternary salt solutions (two salts plus water) has been investigated by different groups. An excellent overview of the recent work on this field as well as technical salt separation approaches can be found in [19]. By their temperature coefficient of solubility near the critical point common salts were classified into type 1 and type 2. A list of some common salts divided into type 1 and 2 phase behavior after Valyashko can be found in Table 3-1. The order of temperature coefficients of solubility indicates an increasing level of type 1 behavior with increasing ion radius and decreasing hydration [41].

Table 3-1: Classification of binary salt-water systems according to Valyashko, sorted by the sign of the temperature coefficient of solubility in water [41]. Note that some salts are listed twice, because different ion combinations for a particular cation or a particular anion are listed in a row. Table taken from [19].

Type 2 salts	Type 1 salts
LiF, NaF	KF, RbF, CsF
LiF	LiCl, LiBr, LiI
NaF	NaCl, NaBr, NaI
Li_2CO_3, Na_2CO_3	K_2CO_3, Rb_2CO_3
Li_2SO_4, Na_2SO_4, K_2SO_4	Rb_2SO_4
Na_2SO_4	Na_2SeO_4
Li_2SiO_3, Na_2SiO_3	K_2SiO_3
Li_3PO_4, Na_3PO_4	K_3PO_4
CaF_2	$CaCl_2$, $CaBr_2$, CaI_2
SrF_2	$SrCl_2$, $SrBr_2$
BaF_2	$BaCl_2$, $BaBr_2$

Schubert and Müller investigated the separation of binary and ternary water-salt mixtures in a continuously operated salt separator that will be described later in

section 3.5.2 [19, 28]. Schubert tested the separation of different binary mixtures between 430°C and 500°C at 30 MPa and found increased separation efficiencies towards higher temperatures with a maximum efficiency of 80-92%. Type 1 salts could be recovered as a concentrated brine by continuous withdrawal from the lowest point of the salt separator, while type 2 salts formed a solid phase and thus stayed in the system. The tested ammonium salts were not separated because they formed ammonia which is completely miscible with supercritical water. Nitrates underwent reactions and decomposed. NaCl could not be recovered though it is classified as type 1 salt. The formation of a solid phase at the experimental conditions was suggested by a phase diagram [28]. Müller showed that the pressure negatively influences the separation efficiency. A high density leads to more fluid-like conditions and thus a better salt solubility of the supercritical water.

Concerning the behavior of ternary water-salt mixtures, the main conclusions of numerous studies by Schubert et al. are shortly summarized [25-27]. The behavior of a ternary mixture of two type 1 salts ($NaNO_3$ and K_2CO_3) was found to be similar to the single components in binary mixtures. For ternary mixtures of two type 2 salts (K_2SO_4 and Na_2CO_3) type 1 behavior was observed. This was explained by the formation of a type 1 salt by rearrangement of the ions (K_2CO_3) [26, 27]. For ternary mixtures of a type 1 and a type 2 salt the special phenomenon was described that type 2 salts solubilize in this liquid type 1 salt phase and subsequently show type 1 behavior [38, 41]. In the case of ternary type 2 salt mixtures where a rearrangement of ions led to type 2 salts only (Na_3PO_4-Na_2SO_4), as expected no liquid recovery was observed, indicating the formation of a solid phase. However, the mixture Na_2SO_4-K_2SO_4 formed a fluid phase, which was explained by the formation of mixed salts $Na_xK_ySO_4$ [28].

3.4.3 Biomass degradation reactions

3.4.3.1 General aspects on biomass reactions in sub- and supercritical water

The general reaction scheme in water at elevated temperatures and pressures is strongly dependent on the solvent properties represented by the dielectric constant and the ionization constant, and thus on the fluid density [42]. As mentioned earlier in section 3.4.1.5, the ionization constant of subcritical water is by orders of

magnitude higher compared to water at ambient conditions. In this region as well as in the high-density supercritical region ("pseudo-subcritical"), ionic reactions, e.g. hydrolysis, are thus favored.

As a consequence of the low ionization constant which is prevailing at supercritical water conditions in particular at low densities, free radical reactions are favored here [42]. Antal et al. observed a highly selective heterolytic dehydration of ethanol to ethylene in low-temperature high-density supercritical water (400°C, 34 MPa) which was enhanced in the presence of sulfuric acid [43]. This was attributed to the high degree of dissociation of the sulfuric acid as a consequence of the ionic properties of water, and to the high mobility of H^+ ions. At higher temperatures (500°C), an increase of homolysis products (CH_4, H_2, C_2H_6) was observed. The ionization constant at these conditions no more favors the dissociation of acid catalysts or the formation of carbonium ion intermediates [43].

Reaction rates are basically influenced by the temperature. Additionally, a change in the reaction regime has a strong effect on the rate constant. The change from predominantly ionic to predominantly free radical mechanisms which is connected with the transition from (pseudo-) subcritical to supercritical is certainly one of the most important effects that have been observed for reactions in hot compressed water [42]. In the vicinity of the critical point the influence of density on the fluid properties and thus on the reaction regime is particularly pronounced (see section 3.4.1). For this reason the choice of density can be regarded as a lever to manipulate reaction rates and selectivities. The effect of pressure and thus density on various reaction rate constants has been experimentally demonstrated for different reactions. A summary can be found in a review by Savage et al. [21].

Within a regime, reaction rates can be influenced by the polarity of the reaction media in the case of a polarity change between reactant, transition state and product. The relative dielectric constant is one aspect of the polarity of a solvent. If the dielectric constant is high, the activation energy is reduced if the transition state is of higher polarity than the reactant. Consequently, the reaction rate increases with increasing relative dielectric constant [21, 22].

Besides the polarity of water also the self-dissociation has an enhancing effect on the reaction rate of acid- and base catalyzed reactions. Since both dielectric constant and ion product increase with increasing pressure, a clear distinction of their effects on the reaction rate can hardly be made.

Kinetic studies on biomass degradation reaction in the literature often describe complex reaction networks. Elevated reaction rates in supercritical water have been reported frequently. In many cases the observed effect could as well be ascribed to the decreased phase boundaries and the increased mass transport rates in supercritical water. These data can therefore be regarded as macroscopic or observed conversion rates rather than actual kinetic effects. For this reason, care must be taken when observed conversion rates are interpreted as kinetic data.

3.4.3.2 Biomass liquefaction reactions in sub- and near-critical water

In hot compressed water below the critical point ionic reactions are dominating. Hydrolysis reactions are most important since water acts as solvent, reactant and precursor of a homogeneous catalyst (acid or base). The latter can be strongly enhanced by the addition of further acids or bases. Studies on hydrothermal degradation reactions have been reviewed by Bobleter [44].
For typical biomass with a high amount of ligno-cellulose composites, the degradation or liquefaction under sub- and near-critical water conditions can be roughly summarized by the following steps:

1. Break-down of polysaccharides. Polysaccharides are the main building blocks of organic matter (cellulose, hemicellulose, starch, pectin etc.). By hydrolysis of ether and ester bonds, those molecules are degraded to monosaccharides (glucose, fructose and other sugars). These reactions occur relatively fast [44]. Cellulose degradation is reported to be even faster at supercritical conditions, which was attributed to the solvent properties under these conditions causing a swelling of the outer layer of a particle. In this case, water attacks not only on the outer surface but on the whole region which has become accessible due to the swelling [45, 46].

2. Degradation of lignin. Besides polysaccharides, lignin is another predominant constituent of plant biomass. The composition of lignin - a high molecular-weight compound - is fairly random. As major components phenylpropane-derivatives have been identified: p-coumaryl alcohol, coniferyl alcohol and sinapyl alcohol [47]. A high percentage of all lignin bonds are ether bonds and are thus expected to be easily

hydrolyzed [48]. However, the high reactivity of lignin leads to condensation reactions [48, 49].

The degradation of isolated lignin as it was used for kinetic studies is usually harder to achieve than of lignin in real biomass. Bobleter assigns this to a more condensed structure of the extracted lignin [44]. Yoshida et al. found an enhanced conversion of isolated lignin in the presence of cellulose and xylan and attributed this to the polysaccharides acting as hydrogen donor [2].

Degradation products of lignin comprise a broad spectrum of aromatic compounds. Masselter et al. reported the detection of phenols with a great variety of substituents as well as different re-condensation products [50].

3. Further degradation of monosaccharides. The hydrolysis products of polysaccharides undergo further degradation reactions. The most prevalent monosaccharides in biomass are glucose and fructose, which can be converted into one another by isomerization reactions. Hydrothermal degradation reactions of both compounds have been studied for many decades. Excellent reviews can be found in [14, 19]. It can be summarized that monosaccharides undergo rapid degradation reactions [51]. The reactions include dehydration, retro-aldol, tautomerization, hydration, oxidation and rearrangements. Glucose is more prone to fragmentation reactions with glycoaldehyde, pyruvaldehyde, glyceraldehyde etc. as main products, whereas fructose primarily reacts to 5-hydroxy-methylfurfural (5-HMF) by dehydration [52, 53]. 5-HMF further reacts to small organic acids [54, 55]. Aromatic compounds can also be found as degradation product [56].

4. Degradation of fatty acids and glycerol. Lipids play a role in living organisms predominantly as energy storage. Triacylglycerides are the most prevalent form. They are easily degraded to fatty acids and glycerol by hydrolysis which has been made use of in the Colgate-Emmery process [57]. The further hydrothermal degradation of fatty acids has been investigated by Watanabe et al. [58]. They found them to be rather stable. The conversion was enhanced by the addition of alkali hydroxides or metal oxides, and mostly alkanes and alkenes formed. Holliday et al. tested the behavior of free fatty acids under near- and supercritical water conditions and found decomposition, pyrolysis, or polymerization to occur [59]. Glycerol has frequently been used as model compound for hydrothermal liquefaction and

gasification processes [19, 28, 60, 61]. The degradation of glycerol in sub- and supercritical water was studied by Müller and a proposed scheme can be found in [19].

5. Cleavage of biomass bound hetero-atoms (O, N, S, P, etc.). Oxygen makes up a considerable amount of biomass. Deoxygenation is important with respect to improving the heating value of a fuel. Deoxygenation can occur via dehydration or decarboxylation and decarbonlyation reactions. Further information can be found in [14] and the literature cited there. Nitrogen plays a role in protein-rich biomass (amino groups). Deamination reactions were studied by different groups. At subcritical conditions only insufficient levels of deamination could be observed [62, 63]. In the presence of carbonyls N-heterocyclic rings were found, which represent typical products of the Maillard-reactions [64]. Phosphorus is found as phosphates in nucleic acids. A mineralization by hydrolysis is very likely. High phosphate recoveries from biomass have been found in sub- and supercritical water [65, 66]. Sulfur is mostly found in protein-rich biomass as thiols and disulfides in the amino acids cysteine and methionine. These molecules can undergo desulfurization reactions similar to deamination reactions. H_2S is the main product. Sulfur removal from biomass will be discussed in more detail in section 3.7.

6. Condensation reactions; tar and coke formation. Reactive intermediates of biomass degradation reactions often tend to polymerize. It has been mentioned that degradation products of lignin are very reactive. Also 5-HMF and its degradation products can undergo condensation reactions and thus lead to the formation of aromatic and poly-aromatic compounds that are referred to as tars. At long residence times tars tend to further condensate leading to insoluble coke deposits [19]. At supercritical conditions coke formation is significantly reduced [18, 19]. Coke can generally be classified into primary and secondary coke [19, 67]. Secondary coke is the product of liquefied intermediates. This can result in well defined coke structures. Müller found a pattern of hollow spheres for coke from glycerol. Primary coke can be found by the carbonization of hard plant tissue. The organic structure is only partially destructed leaving a scaffold for further condensation reactions. The original structure of the tissue is thus preserved. A systematic investigation on coke and tar formation under sub- and supercritical conditions can be found in [19].

3.4.3.3 Gasification reactions in sub- and supercritical water

A further degradation of liquefaction products to gases can be accomplished in sub- and supercritical water environment. For low-temperature processes including near-critical and supercritical processes below 500°C, a catalyst is inevitable in order to achieve full conversion. In the absence of a catalyst, long residence times would be necessary offering the opportunity for high levels of tar and coke formation. Tars and particularly coke are less reactive towards gasification, thus reducing the gas yield.
The main gasification reactions can be summarized as follows [68, 69]:

$$CH_nO_m + (1\text{-}m)\ H_2O \rightarrow CO + (0.5\ n + 1\text{-}m)\ H_2 \text{ (steam reforming, endothermic)} \quad (3\text{-}2)$$

$$CO + H_2O \leftrightarrows CO_2 + H_2 \text{ (water-gas shift, } \Delta_rH_{298} = -41 \text{ kJ mol}^{-1}) \quad (3\text{-}3)$$

$$CO + 3\ H_2 \leftrightarrows CH_4 + H_2O \text{ (CO-methanation, } \Delta_rH_{298} = -211 \text{ kJ mol}^{-1}) \quad (3\text{-}4)$$

$$CO_2 + 4\ H_2 \rightarrow CH_4 + 2\ H_2O \text{ (CO_2-methanation, } \Delta_rH_{298} = -223 \text{ kJ mol}^{-1}) \quad (3\text{-}5)$$

The endothermic steam reforming reaction is the most crucial one for gasification. The water-gas shift reaction is more or less thermo-neutral and leads to an increased yield of hydrogen. In the presence of a catalyst the water-gas shift reaction is very fast. This becomes obvious by considering the fact that CO reacts to CO_2 solely by the effect of the reactor walls, whereas high CO yields are observed in the case inert materials are used [68, 70]. Homogeneous catalysts like alkali carbonates increase the rate of the water gas shift reaction. This effect was explained by the formation of a formic acid intermediate [36].

Both methanation reactions are exothermic. Hence, the equilibrium between hydrogen and methane is depending on the reaction temperature. Consequently, a low process temperature is required if methane is the desired product. In the absence of a catalyst, very low methanation rates are observed. This can be explained by the necessity of 3 and 4 molar equivalents of hydrogen for the reaction which is fairly unlikely to occur homogeneously.
Noteworthy is that results presented in this thesis (see section 5.2.3) and results of recent experiments by Dreher et al. [71] suggested that methane and CO_2 are

produced simultaneously on the catalyst, indicating that a differentiation into the above mentioned reactions (2-2 to 2-5) is probably not valid for catalyzed reactions.

3.5 Hydrothermal gasification of natural biomass feedstocks

3.5.1 Hydrothermal gasification processes

Hydrothermal gasification processes of natural biomass have been developed by different groups. The processes can generally be divided into high-temperature supercritical, low-temperature supercritical and subcritical water gasification.
The processes operated at high temperatures generally aim for a high hydrogen yield which is thermodynamically favored at high temperatures. No catalyst is needed, however the presence of activated carbon [72-75] and alkali carbonate supplements [76-78] were reported to reduce char formation and thus increase the gas yield.

Gasification in low temperature supercritical and subcritical water (< 500°C) has the advantage of a reduced process energy demand. Methane, which is the thermodynamically favored product at low temperatures, can be distributed over an already existing gas pipeline system. However, an efficient conversion of biomass at low temperatures requires the use of a catalyst. The group of Elliott et al. focuses on the catalytic conversion in near critical water, which is referred to as the TEES process (thermochemical environmental energy system) [79].

The advantage of working at temperatures above the critical point of water lays in the properties of water discussed in 3.4.1, that lead to a good solubility of organic molecules and a poor solubility of salts. Both characteristics of supercritical water are taken advantage of in PSI`s hydrothermal gasification process.

3.5.2 PSI`s hydrothermal gasification process

The PSI`s hydrothermal gasification process combines subcritical liquefaction in the preheater, supercritical salt separation in the superheater and salt separator and catalytic gasification at supercritical conditions in the reactor [6]. By a rational management of the process heat, the energy requirements can be drastically reduced. A scheme of the process is shown in Figure 3-11.

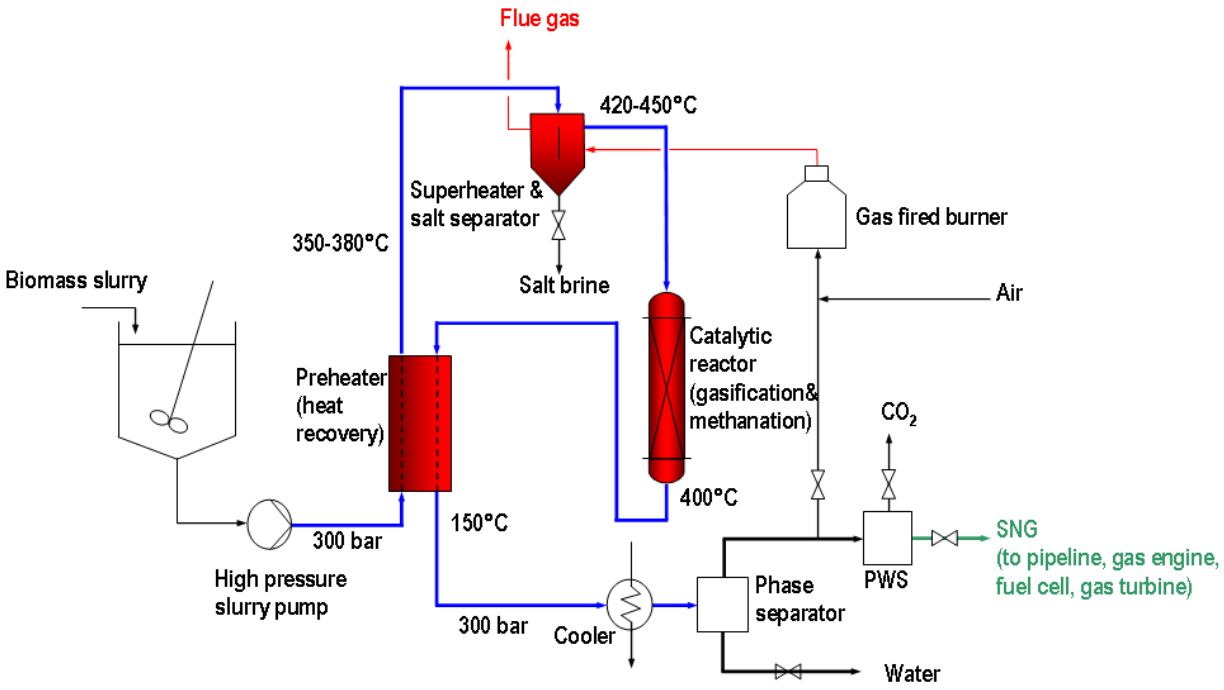

Figure 3-11: Flow-scheme of PSI`s hydrothermal gasification process, adapted from [28].

In this process, the biomass is first pressurized to the desired pressure of 28-30 MPa. In the preheater it is liquefied at near-critical conditions. Hydrolysis reactions are dominating in this region. The liquefaction is also supposed to include the cleavage and mineralization of biomass bound hetero-atoms such as nitrogen, phosphorus and sulfur. After liquefaction the fluid enters the supercritical region in the salt separator, where salts precipitate and can be withdrawn at the lowest part of the vessel. Goal of the desalination is on the one hand their recovery for the use as fertilizers and on the other hand to avoid deactivation of the catalyst by hetero-atoms such as sulfur or plugging by salt precibitates. The liquefied, desalinated biomass stays solubilized within the supercritical water and is further transported to the catalytic reactor, where gasification and methanation take place. The reactor is operated at relatively low temperatures around 400°C, because methane is the desired product. The reactor is filled with heterogeneous catalyst pellets to accomplish complete conversion of the biomass even at low temperatures. In the ideal case, the reactor effluent should only contain water, methane, CO_2 and small traces of hydrogen.

3.5.3 Experimental studies of natural biomass gasification

Waste water and other natural feedstocks containing a broad range of components similar to fermentation residues have been tested for hydrothermal gasification by several authors in a batch [80-82] and in a continuous system [74, 83-86]. Fermentation residues have been continuously gasified at a temperature of 600°C for hydrogen production [75]. The processes of Osada et al. [82] and Elliott et al. [83, 84] are of particular interest for this work since they are operated at low temperatures and therefore employ heterogeneous catalysts.

The TEES process of Elliott et al. is operated at 350°C and 20 MPa [79, 87]. For gasification of different industrial waste water samples over a nickel catalyst in a batch system they reported good conversion [88]. A good conversion of oxygenated compounds and a poor conversion of high-molecular weight aliphatic compounds was observed, which later was confirmed by continuous experiments [89]. Continuous experiments with industrial wastewater led to a high conversion during 219 h. Towards the end, a change in the gas composition pointed to a catalyst deactivation. The organic content of the wastewater was very low (COD below 12'000 ppm) [83]. Further continuous gasification tests with a Ru/C catalyst and significantly higher feed concentrations (COD: 33'000 to 126'000 ppm) were reported later [84]. They reported high conversion of manure and distillers' dried grain and solubles. The experiments were performed up to 14 h. Plugging of the reactor after 5 h was reported for feedstock with the highest organic content. For a scale-up test with lower organic content (COD up to 70'000 ppm), plugging and catalyst deactivation was observed after 8 h. Analysis of the solids revealed that it consisted mainly of inorganic matter, in particular hydroxyapatite ($Ca_5(PO_4)_3OH$) [84]. For experiments with lignin-rich residual material they reported the formation of viscous tarry material plugging a line. Sulfur and minerals were removed from the liquefied biomass by specially designed traps [85].

Osada et al. gasified lignin, cellulose and sugarcane bagasse in batch reactors at 400°C and varying density over 5% Ru/C and 2% Ru/TiO_2 catalysts. The gas yield of sugarcane bagasse was higher than for lignin but lower than for cellulose. Gasification of lignin and sugarcane bagasse yielded a high amount of THF-soluble products [82].

Schubert [28] and Müller [19] gasified crude glycerol over 2% Ru/C in the continuous lab test rig Konti-2, which is a simplified setup of PSI`s hydrothermal gasification process. The gasification included simultaneous salt separation. Crude glycerol is the by-product from the bio-diesel production and can thus be considered a natural feedstock. In contrast to fermentation residue, it consists exclusively of liquid or soluble compounds, mainly glycerol and fatty acids. Müller could improve the salt separation efficiency by optimized process parameters [19]. At the beginning, high gasification efficiencies were reached. After few hours a massive decrease took place. A decrease in the metal surface area of the used catalyst was observed [19, 28]. This was confirmed by RBS, ERDA and XPS measurements by Wambach et al. who attributed this to a deposition of thin carbonaceous layers [90].

3.6 Catalyst systems for supercritical water application

For biomass conversion reactions at low temperatures (< 500°C), catalysts are necessary. The conversion rates for the reactions 2-2 to 2-5 (section 3.4.3.3) are increased by various catalysts to a different extent. Usually methane is the desired product for processes carried out at low temperatures. In this case catalysts for steam reforming, water-gas shift and methanation reaction are needed. However, some processes are designed to maximize the hydrogen yield even at lower temperatures to save process energy. In this special case the requirements for a catalyst are high reforming and water-gas shift and likewise low methanation activities.

3.6.1 Catalytic Mechanism

The catalytic steam reforming reaction has been assumed to proceed following a Mars-van Krevelen redox mechanism [68]. Park and Thomiyasu proposed a mechanism for the gasification of naphtalene over RuO_2 involving Ru^{IV} and Ru^{II} [91]:

$$CH_2O + RuO_2 \rightarrow CO + RuO + H_2O \quad (3\text{-}6)$$

$$RuO + H_2O \rightarrow RuO_2 + H_2 \quad (3\text{-}7)$$

The detection of metallic ruthenium on used catalyst samples by XPS or XAS measurements, however, suggested that the oxidation state 0 of ruthenium plays a role in gasification reactions [92-94]. Newly gained evidence from in-situ XAS studies

confirmed that ruthenium is present in its metallic form at elevated temperatures also during gasification of at 400°C, 24.5 MPa [71, 95, 96].

The steam reforming reactions over a ruthenium catalyst is assumed to be structure sensitive and to occur only at low-coordinated ruthenium sites that can be found on one-dimensional edges [97].
For the methanation reaction an extreme structure sensitivity has been reported for ruthenium by Vendelbo et al. [98] and for nickel by Rostrup-Nielsen et al. [99]. They suggested that the methanation reaction takes place on under-coordinated ruthenium sites such as steps and kinks. A special arrangement of step-sites in ruthenium clusters, named B_5-site, is assumed to present the active site of ruthenium [100]. These sites were postulated by Hardeveld and Van Montfoort in 1966 [101].

3.6.2 Heterogeneous reforming and methanation catalysts

Systematic investigations on the activity of different metals have been made for methanation and reforming reactions. Vannice reported the following order of activity for gas phase CO methanation (275°C, 0.1 MPa) : Ru >> Fe > Ni > Co > Rh > Pd > Pt > Ir [102]. For the steam reforming reaction of ethane (500°C, 0.1 bar) a different order was reported Rh, Ru > Ni, Pd, Pt > Re > $Ni_{0.7}Cu_{1.7}$ > Co [103]. The activity of iron was located in the range of copper by Satterfield [104]. Also, for the gasification of phenolic compounds ruthenium and rhodium have been shown to be the most active metals [87, 105]. Skeletal nickel was found to be highly active as well, but it suffered from poor stability [87, 106]. Attempts were made to stabilize nickel by doping with other metals [107]. An overview of studies on different catalyst systems and development on new formulations can be found in [68].
With its high activity and stability, ruthenium finally became the metal of choice for many groups working with hydrothermal gasification processes and was used for subsequent studies [28, 107-109]. Notworthy is, however, that ruthenium is a very expensive metal.

3.6.3 Support materials

Ruthenium is a precious metal and therefore its amount in a supported catalyst must be optimized. Only few materials are suitable as supports, providing sufficient stability in a supercritical water environment. Activated carbon has shown good

stability in a reducing environment, dominating in SCWG. Many researchers have used it as support material for gasification of pure substances [92, 106, 110]. However, surface groups are exposed to the reactive media and may undergo reactions such as steam reforming. If oxidizing substances are present, a degradation of the support material by oxidation reactions is also supposable. Furthermore, the stability of the catalyst towards an oxidizing environment might also be important with regard to regeneration of the catalyst [60, 108].

Supports based on ceramic materials have been tested by several authors. Elliott et al. tested various catalysts and support materials in a batch reactor and found that only ZrO_2, α-Al_2O_3 and carbon were stable supports in near-critical water (350°C, 20 MPa). SiO_2, TiO_2 and all of the other tested forms of alumina were either unstable, hydrolyzable or lost their physical shape [87]. Elliott et al. also tested numerous catalyst systems in a continuous system gasifying 10% phenol in water. 3% Ru on rutile showed a good activity and stability; however, a mixture of anatase and rutile used as support was converted to rutile over time. They also tested 5% Ru on ZrO_2, which exhibited good activity and stability [107].

Boukis tested corrosion of ceramic materials at simulated supercritical water oxidation (SCWO) conditions and found only a few Al_2O_3- and ZrO_2-based materials to be stable [111].

Byrd et al. tested various catalyst systems for hydrogen production at 600°C and 25 MPa including ZrO_2 and TiO_2 support samples and found a significant surface area loss for all support samples tested, which was attributed to sintering [112].

Osada et al. tested 2% Ru/TiO_2 (anatase), 5% Ru/γ-Al_2O_3 and 5% Ru/C for gasification of lignin in supercritical water using a batch reactor. Ru/TiO_2 showed the highest initial activity. The stability was tested by reusing the spent catalyst for two more times. This resulted in a decrease of activity in the order Ru/TiO_2 < Ru/C < Ru/γ-Al_2O_3. [109]. Yamaguchi et al. also found carbon and TiO_2 to show the highest stability for lignin gasification in batch experiments at 673 K and 723 K, using 5% metal loading [113].

Yamaguchi et al. found that carbon and TiO_2 were more active when impregnated with $Ru(NO)(NO_3)_3$ rather than with $RuCl_3$. This was attributed to a smaller ruthenium particle size found on the catalysts prepared with $Ru(NO)(NO_3)_3$ [93]. Ketchie investigated the particle growth of ruthenium for various support materials in hot compressed water (473 K) via X-ray absorption spectroscopy using a

continuous reactor setup and found TiO_2, besides carbon, to be most stable [92]. ZrO_2 was used as support material for Ni in continuous H_2 production from polyethylene glycol at 663 K, showing a good stability [86]. May et al. stated that 1% Ru/ZrO_2 showed limited activity for gasification of glycerol in supercritical water (SCW) at 510–550°C [114].

Gasification of model compounds and real feedstocks (see section 3.5.3) over Ru/TiO_2 was tested by different researchers in a batch reactor [70, 106, 115].

3.6.4 Bimetallic catalysts

The catalytic activity and selectivity of metal surfaces can be altered by the addition of a second metal. In some cases this leads to great improvements of the catalytic performance [116]. A change in the properties of a catalyst can be explained by "ensemble" or "ligand" effects. An ensemble effect may occur if an assembly of contiguous surface atoms is required for the adsorbate to bind. The number of active sites may thus be changed in the presence of a second metal. Ligand effects are caused by electronic interactions between the two metals [116-118].

The electronic perturbation caused by the metal-metal bonding can influence the binding energy between metal and adsorbate. On the other hand, it can influence the binding strength of catalyst poisons. Rodriguez and Hrbek reviewed effects of altered catalyst-sulfur interactions caused by the presence of other metals [119]. In this context both, changes in the metal-sulfur interaction by the presence of a second metal as well as changes in the physical and chemical properties of bimetallic systems by sulfur binding are relevant. This points to a high complexity of the nature of interactions between metals, reactant and poison, thus making predictions difficult.

In practice, improved sulfur tolerance of ruthenium catalysts by the presence of rhenium has been reported by Braden et al. [120]. In the presence of 0.5 M sulfuric acid, the conversion of formic acid and levulinic acid to γ-valerolactone over a Ru-Re bimetallic catalyst was hardly affected, whereas a massive decrease was observed for the pure ruthenium catalyst (150°C, 3.5 MPa). Also for other surface metal alloys improved sulfur tolerance was reported [121, 122].

3.6.5 Homogeneous catalysts

Homogeneous supplements such as alkali hydroxides or alkali carbonates are reported in literature to be catalytically active for the water-gas shift reaction, resulting in an elevated hydrogen yield [76, 123]. The effect was ascribed to the formation of a formate intermediate which has been proposed for subcritical [124] and supercritical conditions [125]:

$$K_2CO_3 + H_2O + CO \rightarrow KHCO_3 + HCO_2K \quad (2\text{-}8)$$

$$HCO_2K + H_2O \rightarrow KHCO_3 + H_2 \quad (2\text{-}9)$$

$$2\ KHCO_3 \rightarrow 2\ K_2CO_3 + 2\ H_2O + 2\ CO_2 \quad (2\text{-}10)$$

Gadhe et al reported an adverse effect of KOH on the methanation reaction. However, they conceded that this observation may also be due to a coverage of the catalyzing reactor wall by precipitates [126].

Alkali compounds were furthermore reported to enhance degradation reactions and reduce coke formation [64, 125, 127]. This can either be explained by hydrogenation resulting from the high hydrogen yield, decreasing the level of condensation reactions [64, 128] or by an enhancement of the acid- and base catalysis effect caused by an increased dissociation of the additive, similar to what was described by Antal et al. [43]. Kruse and Gawlik mentioned an increased C-C scission in supercritical water [54].

The reduction of coke and tar formation by alkaline additives can also simply be explained by suppressing acid catalyzed side reactions such as dehydration. Acidic conditions have been reported to promote coke and tar formation [19, 129, 130]. In this case, the additive is misleadingly termed a homogeneous catalyst.

Other effects of alkali supplements have been reported that may be useful in biomass conversion processes. Capturing of heteroatoms by $Ca(OH)_2$ was reported [66, 131]. KOH and NaOH were effective supplements for desulfurization processes [132, 133].

3.7 Sulfur in supercritical water: reactions, catalyst deactivation, regeneration

3.7.1 Sulfur compounds in natural biomass

Sulfur is one of the prevalent hetero-element in natural biomass. As a component of two amino acids, i.e. cysteine and methionine, which are the building blocks of all proteins, sulfur is found in all biomass types with a considerable content of proteins. Bound in the biomass framework, sulfur is predominantly present as thiols, sulfides and disulfides, thus in the reduced form [134, 135].

In general, conversion processes of sulfur compounds by various organisms can be described by a simple scheme which is depicted in Figure 3-12.

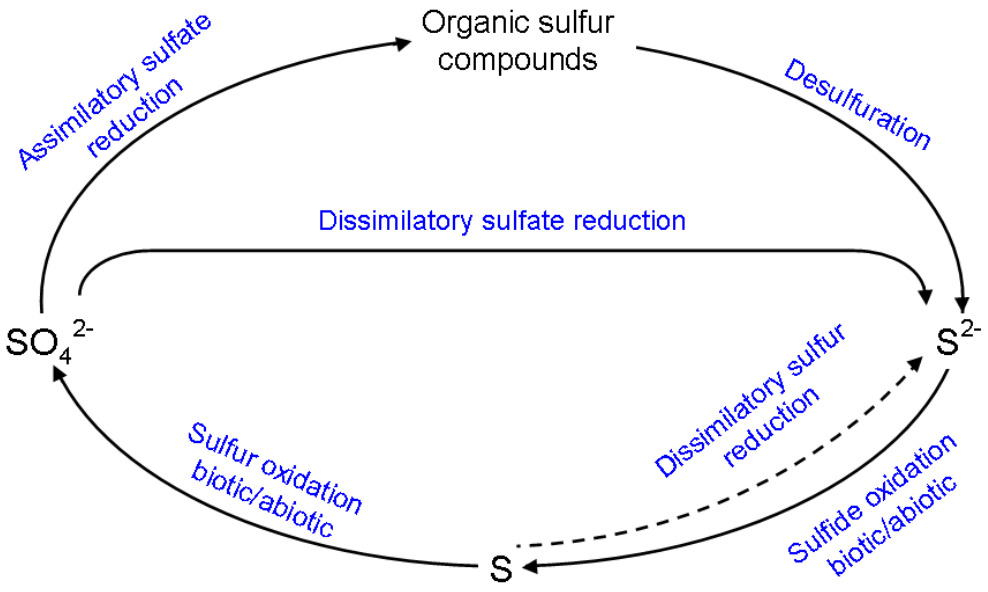

Figure 3-12: Biological cycle of sulfur after [134].

In the digestion process, a part of the biomass-bound sulfur is released by dissimilatory processes, i.e. desulfuration. This leads to the formation of H_2S which is found as a contaminant in the bio-methane. On the other hand, sulfur is integrated into the microbial structure by assimilatory sulfur reduction. Other biotic conversion processes of sulfur compounds are the oxidation to elemental sulfur or sulfate under aerobic conditions. Since the fermentation residues are exposed to air, the formation of sulfate is likely. Under anaerobic conditions, only phototrophic bacteria can oxidize sulfide to sulfur or sulfate.

The network of microbial conversion processes in a biogas plant is by far not fully understood. Based on the given information, sulfur is expected to prevail in the fermentation residue mainly as sulfide, thiol and the most stable form, sulfate.

Since sulfur is known to be a poison to many catalysts, the cleavage of the biomass-bound sulfur species in the preheater and their separation in the salt separator before the entrance to the catalytic reactor are of highest importance. For this, a proper understanding of the reactions in supercritical water leading to the mineralization of sulfur is crucial. However, the innumerable components and intermediates that play a role in these reactions make a prediction difficult.

3.7.2 Reactions of sulfur compounds under hydrothermal conditions

Reactions of elemental sulfur and inorganic sulfur compounds in hydrothermal media have been studied in the mid of the 20th century in the context of hot springs, predominantly in Japan. The originator for many of these studies was the occurrence of surprisingly high amounts of sulfate in hot spring water, which was believed not to stem solely from the oxidation of H_2S with air. A dissproportionation reaction of sulfurous acid to sulfuric acid and elemental sulfur has been proposed by Iwasaki and Osaza in 1960 [136]:

$$3\ H_2SO_3 \leftrightarrows 2\ H_2SO_4 + S + H_2O \qquad (2\text{-}11)$$

Since this would still not explain the origin of all sulfate Oana and Ishikawa did more detailed studies on the reactions of SO_2 and sulfur under hydrothermal conditions using ^{34}S isotope labeled SO_2. They postulated a sulfur hydrolysis around 200°C, producing hydrogen sulfide and sulfuric acid [137].

$$4\ S + 4\ H_2O \leftrightarrows 3\ H_2S + H_2SO_4 \qquad (2\text{-}12)$$

Ellis and Giggenbach later supplied quantitative data for sulfur hydrolysis reactions for temperatures up to 350°C [138].

Giggenbach tested the solubility of elemental sulfur in near-neutral aqueous sulfide solutions and found polysulfide ions that became dissociated to radicals and disproportionated to sulfide and thiosulfate above 150°C. A higher pH led to a decreased stability of the polysulfide ions. Sulfate was not formed under these conditions.

These studies give valuable information on the characteristic behavior of sulfur and inorganic sulfur compounds at hydrothermal conditions. In the presence of organic molecules, however, reactions become more complex. For the reactions in the preheater, primarily reactions involving the cleavage of the organically bound sulfur from the organic backbone and the mineralization of sulfur are of interest. In literature, a relatively small number of publications can be found dealing with the cleavage of C-S bonds in hot compressed water. However, very little has been reported about the transformation of sulfur in natural biomass samples into inorganic salts under hydrothermal conditions.

Katritzky et al. reviewed reactions of model compounds in high-temperature aqueous media where they dedicated one chapter to compounds with sulfur-containing functional groups [139].

Sulfur loss of alkylthiols was found to occur predominantly in a water environment at temperatures of 300°C. Here the extent of sulfur loss was enhanced compared to the corresponding experiments that were performed in cyclohexane. This was attributed to an ionic contribution. For organic sulfides and disulfides they reported a higher reactivity under thermolysis conditions than under aquathermolysis conditions. Dominating reactions were homolytic C-S bond cleavage and further reactions of the radicals that were generated.

Yang et al. suggest a free radical reaction for the thermal decomposition of alkanethiols to H_2S [140]. Since free radical mechanisms are also favored in supercritical water at low fluid densities, this reaction may also be relevant for decomposition in supercritical water conditions.

Kamimura et al. found an increased sulfur removal for bitumen at hydrothermal conditions compared to thermal cracking without water [133]. They found an increased sulfur removal towards higher temperatures (until 430°C), longer residence times and higher water loadings up to 40%. However, a residual amount of sulfur could not be removed for any of the tested conditions. GC-AED measurements revealed that alkyl benzothiophenes and dibenzothiophenes had formed at higher residence times. Experiments on the hydrothermal decomposition of benzothiophene and dibenzthiophene by the same group showed that benzothiophene decomposed well at near-critical and dibenzothiophene at supercritical conditions. They

interpreted this as a detrimental influence of the presence of oils on the hydrothermal decomposition of this class of molecules. The fact that the experiments with model substances had been performed in the presence of 5 M NaOH and 5 M KOH, respectively, while only 1 M KOH was present in the experiments with real bitumen as feedstock, was not commented. It was furthermore not mentioned where the removed sulfur ended up; it was only mentioned that no H_2S was detected in the product gas in the case of alkali solutions. It is therefore presumable that a mineralization of sulfur had taken place, but no evidence is provided [133].
Kishita et al. emphasized the pressure sensitivity of benzothiophene and dibenzothiophene degradation in sub- and supercritical water in the presence of alkali. They found good results at 430°C, 42 MPa (40% water) in the presence of 5 M KOH. High pressures were reported to improve the degradation [141].
Desulfurization of coal by pyrolysis and subsequent washing with water at 60°C was investigated by Liu et al. They found an increased sulfur removal by the addition of 10% NaOH or KOH and suggested that KOH catalyzes organic sulfur decomposition. Sulfur was reported to be captured as K_2S [132].

Desulfurization of high molecular weight crude-oil components as H_2S in supercritical water has been studied by different groups. Ogunsola et al. studied the behavior of heterocyclic sulfur in supercritical water and under pyrolysis conditions. They found increased rates for sulfur removal as H_2S under hydrothermal conditions. For benzothiophene they observed a rupture of the C-S bond only in the presence of Fe_2O_3 [142].
Vogelaar tested desulfurization of gasoil in supercritical water and found a marginal effect particularly for aromatic sulfur compounds. Only in the presence of conventional presulfided hydrodesulfurization catalysts (CoMo on γ-Al_2O_3) desulfurization was observed [143].

From the presented studies it can be concluded that aromatic sulfur compounds are stable under hydrothermal conditions. In the presence of some catalysts, cracking of these compounds has been successful. Sulfur is released as H_2S in this case. Alkaline supplements also improve the desulfurization of aromatic sulfur compounds; this effect is very sensitive to the process conditions, i.e. pressure, temperature and the

presence of other substances. All these parameters influence the phase behavior of water (see section 3.4.1). In the presence of alkali, sulfur is not released as H_2S.

3.7.3 Catalyst deactivation by sulfur poisoning

Sulfur is well known to be a poison to many catalysts. For hydrothermal reactions catalyzed by ruthenium, a poisoning effect of sulfur was shown by a decreased conversion of an organic feedstock in the presence of sulfate and sulfite by Waldner et al. [106] and by a decreased conversion of an organic feedstock after treatment with sulfur by Osada et al. [144, 145]. In both cases, sulfur species were found on the catalyst by XPS measurements, giving proof to the assumption of sulfur being responsible for the decreased conversion. For natural feedstocks, a decreased activity of the catalyst was attributed to the sulfur content of the biomass [84, 146]. By SEM imaging, Elliott et al. found sulfur in the catalyst pellets to be highly associated with ruthenium. Also XPS measurements pointed to the presence of sulfates on the catalyst [84].

The sulfur species responsible for the deactivation of the catalyst were studied by Osada et al. [145]. They tested gasification of lignin in batch reactors over supported metal catalysts including ruthenium in the presence of various organic and inorganic sulfur compounds as well as elemental sulfur. They found all species to have an inhibiting effect on the catalytic conversion. By XPS measurements of a ruthenium catalyst poisoned with sulfur in the absence of biomass they found sulfur in the form S^{2-}, SO_3^{2-} and SO_4^{2-} and postulated the formation of RuS_2, $Ru(SO_3)_2$, and $Ru(SO_4)_2$. In the presence of lignin they identified S^{2-} and SO_4^{2-}.
Waldner [106] and Elliott [84] found only sulfate on the poisoned catalyst by XPS. Since XPS measurements were done ex-situ, reaction with air-oxygen cannot be excluded for those findings.
In systematic in-situ poisoning experiments, Waldner found a poisoning effect of sulfate on the ruthenium catalyst only in presence of biomass and above a temperature of 320°C. This was attributed to an irreversible binding of sulfate to Ru(III), which was thought to be an intermediate of the assumed redox cycle involving Ru(IV) and Ru(II) and thus leading to an interruption of this redox cycle. Alternatively, the sulfate was assumed to be reduced to sulfide by the biomass, binding to Ru(II) with the same effect [108].

Dreher et al. could finally elucidate S^{2-} being the poisoning sulfur species by in-situ EXAFS measurements of a Ru/C catalyst under operating conditions combined with information gained from ex-situ measurements of the sulfur K-edge XANES [71]. They also found traces of SO_4^{2-} on the catalyst, which they, however, attributed to a contact with traces of air during the sample preparation in a glove box. Furthermore, small amounts of S^0 were found.

Regarding the reactions influenced by poisoning of the catalyst, Osada et al. compared the conversion of model substances by fresh and ex-situ poisoned Ru/TiO_2 catalysts and in the absence of catalysts. They found a significant decrease in the gasification of 4-propylphenol when using a poisoned catalyst, which was close to the conversion in the absence of a catalyst. For formaldehyde, they found the gasification still to be strongly enhanced compared to the conversion without a catalyst. The gas composition pointed to non-equilibrium conditions regarding the methanation reaction. They postulated a poisoning of the active sites for C-C bond breaking and the methanation reaction. The catalytic gasification of formaldehyde and the water-gas shift reaction was not influenced by sulfur poisoning.
Further insight into the methanation reaction on the surface of a fresh and a sulfur-poisoned ruthenium catalyst could be achieved by D-isotope water labeling measurements by Dreher et al. [71]. In the case of a poisoned catalyst, they found a decreased rate of hydrogen stripping from the hydrocarbon adsorbates. With the help of DFT calculations of the free energies of CH_X adsorbates on ruthenium surfaces and on sulfur-poisoned ruthenium surfaces this observation as well as the reduced overall activity for the methanation reaction could be explained.

3.7.4 Regeneration of sulfur-poisoned ruthenium catalysts

Waldner regenerated an in-situ sulfur-poisoned Ru/C catalyst by oxidative treatment with a 1 wt% H_2O_2 solution at a temperature of 50-90°C and found a reactivation of the catalyst followed by a re-deactivation after some time during gasification of sulfur-free biomass [108]. This was attributed to an incomplete removal of sulfur. HAADF-STEM imaging showed only minor particle growth for ruthenium that could not even solely be ascribed to the oxidative treatment since the catalyst was used for several experiments. No sign of ruthenium leaching was found.

Osada et al. proposed a regeneration method for an ex-situ sulfur poisoned Ru/TiO_2 catalyst consisting in flushing with subcritical water at 300°C and 25 MPa [147]. Via XPS they found three fourth of the sulfur being removed from the catalyst. This method suggests that sulfur is reversibly bound to ruthenium under subcritical conditions. Noteworthy is that the catalyst was poisoned by soaking in aqueous sulfuric acid solution and dried by evaporation. The catalyst was then flushed under subcritical water conditions in continuous mode. Finally, the gasification test run was done in a batch reactor setup with lignin as model biomass. With this experimental setup, the treatment with sulfuric acid does not represent poisoning conditions that may occur under operating conditions. As previously mentioned, Waldner showed deactivation to take place only above a certain temperature. In this context, it cannot be excluded that the SO_4^{2-} was never really attached to the ruthenium and could thus be flushed off easily.

Schubert et al. did a systematic test of regeneration methods [60]. They tested regeneration of an in-situ poisoned Ru/C catalyst firstly by subcritical water flushing as Osada et al. had proposed for the Ru/TiO_2 catalyst. This method was, however, not successful for the in-situ poisoned Ru/C catalyst. No evidence was given whether this had to do with the catalyst system or with the poisoning procedure.
Secondly, a reductive regeneration by formic acid, decomposing to H_2 and CO_2, was tested. Here, an ionic binding of ruthenium and sulfide was assumed (RuS or RuS_2). H_2 was thus supposed to reduce ruthenium. Sulfide would then be released as H_2S. The reductive treatment showed no reactivation of the poisoned catalyst.
Finally, the oxidative treatment as previously tested by Waldner was repeated. This method was based on the assumption of sulfide or elemental sulfur being adsorbed to the catalyst. By the oxidative treatment, these species would be oxidized to sulfate, which redissolves in water under subcritical conditions. Since Waldner's regeneration protocol had only led to an insufficient regeneration of the initial conversion, Schubert et al. used a 2 wt% H_2O_2 solution for regeneration. Also the regeneration temperature was higher (up to 200°C). This regeneration protocol led to a full recovery of the initial performance with no sign for a re-deactivation. However, turbidities occurring after random time intervals were reported, which was not the case for the fresh catalyst. This was interpreted as a still incomplete regeneration. A severe decrease of the catalyst's metal surface area was found, but could not be

distinctly ascribed to the oxidative treatment, because the same catalyst loading was used for all regeneration tests. However, the fact that this method was principally successful was understood as a verification of the assumption that the deactivating sulfur is in the oxidation state (0) or (-II). The possibility of adsorbed sulfate poisoning the catalyst was thus dismissed.

The results of Waldner and Schubert were later supplemented via XAS experiments by Dreher et al. [71, 148]. They could verify that sulfur poisoning of a Ru/C catalyst is irreversible [71]. Furthermore, they also tested the oxidative regeneration of the Ru/C catalyst, similar to Schubert and Waldner. By this treatment ruthenium was found to be fully oxidized to RuO_2 by a temperature of 100°C [148]. The incomplete regeneration observed by Waldner and Schubert during the short lifetime of the reactivated catalyst, however, could not be explained by the XAS measurements.

3.8 Reactions of high molecular-weight substances (tars, heavy oils, bitumen)

The production of sticky tars has often been reported to be a problem during conversion of biomass in hot compressed water. For processes in near-critical water, Elliott et al. [84] reported plugging of lines as a consequence of tar production when lignin-rich feedstocks were used. Osada et al. [82] found water-insoluble and THF-soluble products at low-temperature supercritical conditions even in the presence of a catalyst (see section 3.5.3). Also at temperatures >600°C, tar formation is an issue [149]. Müller defined tars as aromatic and polyaromatic compounds with different functional groups. Furthermore, Müller suggested that tars are coke precursors that were formed by dehydration of aromatic intermediates and were subsequently converted to coke by further condensation [19]. Osada et al. emphasized the importance of a high degradation of reactive intermediates to avoid condensation. A higher decomposition rate of tar-precursors was found with increasing water densities [128].

For a better understanding of the reactions of already formed tars and bitumen-like substances in hot compressed water environment, valuable information can be adopted from the field of oil refining. Various studies on the upgrading of heavy oils

such as bitumen (asphalt) to maltene can be found in literature. Heavy oils comprise the group of viscous, low-boiling fractions of crude oil and comparable fossil deposits such as oils sands.

Sato et al. tested the upgrading of asphalt in supercritical water (340-400°C) and found an increased maltene yield towards higher temperatures and higher water densities (0-500 kg m^{-3}). They attributed this observation to a "capping" of free radicals by hydrogen provided by the water [150].
Kamimura et al. reported a reduced viscosity after treatment of bitumen at 427°C and 31 MPa at a water loading of 20% in the presence of 0.1-1 M KOH [133].
Watanabe et al. tested the hydrothermal upgrading of oil sand bitumen at 450°C and water densities of 100 and 200 kg m^{-3} and found a higher coke formation rate for the higher water density while the maltene yield was barely affected. The proposed explanation was an extraction of the lighter oil fractions by supercritical water resulting in a condensation of the heavy oil fractions. A more homogeneous shape of the coke formed at the high water density is mentioned to support the formation of a condensed "core-asphaltene" phase [151]. The extraction behavior of water at densities higher than 200 kg m^{-3} was not tested; therefore no comparison with the results gained by Sato et al. [150] and Kamimura et al. [133] can be made.
Morimoto et al. found a minor chemical influence of water on oil-sand bitumen for temperatures between 420 and 450°C and pressures between 20 and 30 MPa. They found the hydrogen supply by water to be negligible. The formation of lower molecular-weight substances by hydrothermal treatment was assigned to physical dispersion effects leading to dehydrogenation reactions [152].

Conclusively, it can be stated from the presented literature that heavy oils are degraded to lower molecular weight products (maltene) under hydrothermal conditions [133, 150, 152]. At relatively low densities, coke formation is promoted by the addition of water, presumably by forming a two-phase system of heavy and light component, which leads to condensation reactions within the more packed heavy fraction [151].

3.9 Conclusions from previous studies and open questions

Valuable knowledge about biomass conversion processes in sub- and supercritical water has been collected over the past, as summarized in the previous chapters. However, many open questions are remaining. Especially the for implementation of a continuous process for gasifying natural feedstocks many steps require better understanding and improvement:

- The heat-up of the biomass requires the passing of the sub-critical area. In this region, coke and tar formation are promoted. These processes are by far not understood. However, for certain biomass constituents (lignin, carbonyls etc.) it is known that they strongly contribute to such reactions. With a detailed knowledge of the biomass composition, coke and tar formation tendency could be better understood and possibly even be predicted.

- Little is known about the mineralization of biomass bound sulfur under sub- and supercritical water conditions. With respect to the salt separation, this is a crucial step. A removal of sulfur before the entrance of the catalytic reactor is very important to avoid catalyst poisoning. Therefore, this step requires further investigation.

- Even in the case of a well functioning salt separation, small traces are assumed to be transported to the reactor. A regeneration could increase the lifetime of the catalyst. An oxidative regeneration showed promising results in experiments by Schubert et al. [60] and Waldner [108], however, the regenerated catalyst showed a decreased performance. This method requires further investigation and improvement.

- Various catalyst systems have been tested for hydrothermal processes. Different Ru/C systems were identified as the most active ones. However, the system also has drawbacks, e.g. a low stability in an oxidizing environment. Furthermore, a higher sulfur tolerance of a Ru/ZrO_2 system was suggested by Brandenberger and Schubert [153, 154]. Unfortunately, this system was not stable on the long term [60]. Since ruthenium catalysts based on ceramic support materials could provide valuable characteristics such as an increased sulfur tolerance, a higher

stability, and possibly an improved accessibility of meso- and makropores by large biomass molecules, further screenings of stable compounds need to be done.

3.10 Scope of the thesis

Gasification of fermentation residues, representing a complex natural feedstock containing solids, via PSI`s hydrothermal gasification process was the scope of this thesis. By an experimental approach the suitability of the fermentation residue as feedstock for the catalytic gasification in supercritical water should be validated. The validation comprised the following aspects:

- Compositional analysis of the feedstock for understanding and eventually confirming potential reaction schemes that have been proposed earlier for isolated components.
- Liquefaction of ligno-cellulose rich solids of the fermentation residue in the heat-up section in PSI`s hydrothermal gasification process.
- Mineralization of biomass-bound sulfur.
- Continuous salt separation.
- Catalytic gasification of the liquefied fermentation residue.

As a first step, potential challenges in the process were intended to be identified via batch and continuous liquefaction and gasification experiments. The experimental approach comprised an elaborate extraction of the reaction products, analytical tools including TOC, TS, GC, IC, ICP-OES analyses as well as catalyst characterization methods including gas sorption measurements, SEM and TPO.

Based on the results of the liquefaction and gasification experiments, more detailed investigations on the identified challenges and their optimization was intended.

In addition to the above mentioned aspects, a further intention of the thesis was the synthesis and screening of alternative ruthenium catalyst systems. This intention was based on the assumption that the microporous support material of the commonly used Ru/C catalyst might not be optimal for a high contact rate between active sites

and the macro-molecules biomass feedstock. The screening included performance and stability tests in the continuous setup Konti-1, and additional to the above mentioned catalyst characterization methods XRD and gas sorption measurements.

4 Materials and Methods

4.1 Compositional analysis of the fermentation residue

4.1.1 Determination of dry matter and loss on ignition

The fermentation residue samples that were used in this work originated from a two-stage laboratory fermentation plant of Fraunhofer IGB (Stuttgart, Germany). The plant was fed with vegetable grocery wastes that have been disrupted by a colloid mill and a macerator. The first stage is operated under mesophilic conditions (37°C). In the second stage which is unheated, the biomass is further concentrated by a filtration unit. The space velocity of the fermentation process was 7 $g_{(org.DM)}$ $(l \cdot d)^{-1}$. A simplified scheme of the plant can be found in Figure 3-1.

The fermentation residue samples originating from the second stage were continuously withdrawn as an overflow. In this work they are designated with an O. In the first stage a sediment accumulated which was periodically removed; those samples are designated with an S. The samples were numbered chronologically, however O and S samples were delivered independently and do thus not necessarily originate from the same batch.

The samples (O1-O5, S1-S2) were analyzed for dry matter content (DM) and loss on ignition (LOI) following standardized procedures [155, 156]. The residue on ignition is also reported as "minerals" and is defined by equation 4-1.

$$\text{ROI [wt\%]} = 100 - \text{LOI [wt\%]} \qquad (4\text{-}1)$$

4.1.2 Determination of elemental composition

For elemental composition analysis, different methods were applied according to the applicability of the respective method for a group of elements.

Elements bound in the organic structure such as phosphorus, sulfur, metals and other trace elements were determined by acid digestion and ICP-OES measurement. For this purpose 0.5 - 0.6 g of the fermentation residue as received were digested with 4 ml of concentrated *aqua regia* (3 ml HCl, 1 ml HNO_3) in a 100 ml PTFE vessel

using a microwave oven (Multiwave 4000, Anton Paar; program: 15 min at 800 W, 90 min at 400 W). The solution was then diluted to 50 ml with water for analysis with ICP-OES (Cirros, Spectro). For determination of the elemental composition regarding the organic stoichometry, the dry matter (DM) was analyzed using an elemental-analyzer (CHONS analyzer, LECO) by an external service at the ETH Zürich (Mikrolabor, Labor für organische chemie). Sulfur and carbon were additionally analyzed by a TOC analyzer and a CNS analyzer (Elementar).
Anions such as chloride, sulfate, phosphate and nitrate were determined by IC (Dionex Summit). Since the aqua-regia digestate could not be used for determination of nitrate and chloride, an aqueous Soxhlet extract of the fermentation residue (a.r.) was used for ion chromatography (Extraction duration: 3 h). Nitrate and chloride were assumed to be completely extracted by water.

4.1.3 Determination of macromolecules

For the analysis of macromolecules, a method adapted from fodder analysis was applied in a slightly altered way [157]. The method comprises a stepwise extraction and gravimetric determination of the following components: substances soluble in a neutral detergent solution, substances soluble in an acid detergent solution (hemicelluloses), substances soluble in acid (cellulose), acid-insoluble substances (lignin and acid insoluble ash).
The procedure as it was used here is a combination of the conventional method described by Goering et al. [157], in which solids and the solublized components are separated by vacuum filtration after reflux boiling in the respective solution, and an automated method by Ankom using sealed filter bags [158-160]. The combined method includes the use of filter bags which were immersed into the extraction solution using a conventional reflux system. This combination allows the parallel analysis of more than one sample and can be easily performed with standard laboratory equipment. The procedure was as follows:
The first extraction step was performed with a neutral detergent solution containing sodium dodecyl sulfate, sodium borate, ethylenediamine tetraacetate and triethyleneglycol. Non-fiber material like fatty acids, sugars, (water-soluble) starch, salts and proteins are solublized in this step leaving hemicellulose, cellulose and lignin in the matrix. These remaining components are referred to as neutral detergent

fibers (NDF). The amount of NDF can be determined gravimetrically. The non-fiber fraction can be calculated from the difference of NDF and the raw material.
In the second step, an acid detergent solution was used to solublize hemicellulose. The detergent solution consists of cetyl-trimethylammoniumbromide in 1 N sulfuric acid. The remaining material is cellulose and lignin (acid detergent fiber, ADF).
In a third step, 72 wt% sulfuric acid (specific gravity: 1634 g l^{-1} at 20°C) was used to digest cellulose and hence separate it from lignin which remains undigested (acid detergent lignin, ADL). Ashing of the lignin following the standardized procedure for LOI determination (see section 4.1.1) gave the corrected amount of organic material.
All extraction steps were performed in specific filter bags *F57 for Fiber* with a pore diameter of 25 µm, purchased together with the extraction solutions from Ankom Technology, USA. Prior to extraction the fermentation residue was wet sieved over a 250 µm sieve and after that dried. These steps were done in order to assure all particles of small size are removed, which would otherwise pass the pores of the filter bag and thus lead to an overestimation of soluble substances. It has to be mentioned that consequently only a small fraction of particles (7-10 wt% of the DM) is considered with this method. The particle size distribution was determined as a slurry with a particle size analyzer based on laser diffraction (CILAS 1190 wet, detection range 0.04 µm - 2500 µm) (Figure 4-1).

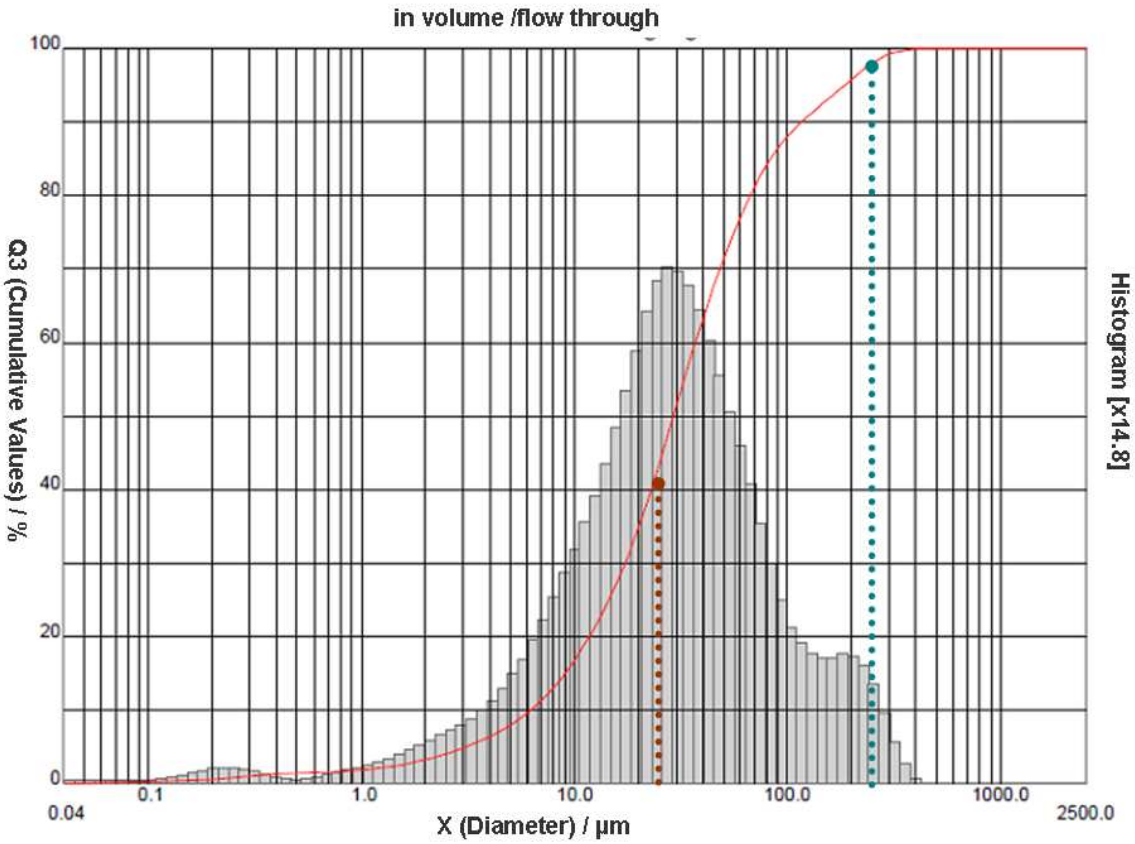

Figure 4-1: Particle size measurement of fermentation residue O1, CILAS 1190 wet, measured range: 0.04 µm - 2500.00 µm / 100 classes. Red dotted line: Pore size of filter bags, blue dotted line: minimum particle size of fermentation residue sample after sieving.

4.2 Catalysts and supports

A list of all catalysts and the designations used in this work can be found in Table Appendix A. More detailed information on the different catalyst systems is given in the following sub-sections.

4.2.1 Ruthenium on activated carbon support

2 wt% ruthenium on granular activated carbon from pyrolyzed coconut shell, purchased from BASF, was used as catalyst for the majority of the experiments. This catalyst will be referred to as 2% Ru/C. The catalyst was used as received for the batch experiments. For the continuous experiments, it was dried in a vacuum oven (50°C, overnight) before it was filled in the reactor. Fine particles were removed by flushing with pure water.

4.2.2 Ruthenium on supports based on refractory oxides

4.2.2.1 Ruthenium catalysts

Various catalysts supported on refractory oxide pellets were prepared in house. Support samples were provided by Norpro Saint Gobain and are listed in Table 4-1 with the respective sample numbers as referred to in the following. Samples that were used as ruthenium catalyst systems for the continuous experiments discussed in section 5.7 are marked with an asterisk. The in house prepared catalysts are referred to as A% Ru/B with A being the ruthenium loading in wt% and B the respective support material.

Table 4-1: Support samples provided by Norpro Saint Gobain. SA: surface area. *Samples used as ruthenium catalysts for continuous experiments.

Sample No.	Manufacturer`s Product designation	Composition (given by manufacturer)	Diameter of pellets [mm]	BET SA [m^2/g]
1	SZ 61152	t-ZrO_2 94%, HfO_2 2.4%, SiO_2 3%	1.5	156
2*	SZ 61156	t- ZrO_2 88.2%, HfO_2 1.77%, La_2O_3 9.7%	3	114
3	SZ 61157	t- ZrO_2 90.44%, HfO_2 1.85%, SiO_2 0.11, Y_2O_3 7.34%, Al_2O_3 0.17%	3	114
4	SZ 61191	t- ZrO_2 78.75%, HfO_2 1.56%, SiO_2 0.6, CeO_2 18.83%, Al_2O_3 0.72%	3	101
5*	SZ 31140	ZrO_2 56.7%, TiO_2 41.3%, $HfO_2$1.1%, SiO_2 0.4%	3	78
6	ST 61120	TiO_2 anatase	3	151
7*	SZ 31163	ZrO_2 monoclinic	3	54
8*	ST 51122	TiO_2 rutile	3	3.9
9	SZ 61143	t- ZrO_2 82.4%, HfO_2 1.49%, Al_2O_3 0.17%, WO_3 15.94%	3	115
10	SZ 31107	ZrO_2 monoclinic	3	90
11*	SZ 31262	ZrO_2 monoclinic	1.5	26

The support samples were aged in a supercritical water environment at 415°C for 20 hours prior to impregnation. This was done in order to achieve a hydrothermally

stable structure. Aging was performed in a stainless steel reactor as described in section 2.3.1, whereby 40 g of support material was treated at once. 16 g of water was added in order to reach a pressure between 30 and 35 MPa.
Impregnation was performed in a rotary evaporator with a 1.5 wt/vol% rutheniumnitrosylnitrate solution (Alfa Aesar) at a low agitation rate, ambient pressure and room temperature. After 3 h, the solvent was removed by evaporation at 70°C water bath temperature and water-jet pump vacuum. The sample was dried for 80 min at 105°C and calcined at 560°C for 240 min, both at ambient pressure and in flowing air atmosphere.

For the batch experiments and for the mixing experiments in a mini batch reactor (section 5.2.2), a 2% Ru/ZrO_2 catalyst was used, which was prepared following the same procedure except no aging of the support was done before. The support material pellets were used as received (Daiichi Kigenso Kagaku Kogyo Co., Japan). The particle size was between 1.25 and 2 mm as determined by sieving. The catalyst is referred to as 2% Ru/ZrO_2 (DKKK).

4.2.2.2 Bimetallic ruthenium-rhenium catalyst

With respect to the bimetallic catalyst 7.5% Ru-Re/t-ZrO_2 (2), the impregnation procedure was performed twice, first with 75-80% perrhenic acid (Alfa Aesar) and later with rutheniumnitrosylnitrate. Then the catalyst was calcined. The amount of precursor was chosen in order to get the same total molar metal loading as the 5% Ru/t-ZrO_2 (2) catalyst, with a Ru/Re molar ratio of 1. This resulted in a 7.5 wt% metal loading because of the higher molar weight of rhenium.

4.2.2.3 Impregnation mass balance

The effective ruthenium and rhenium content of the catalyst was determined by a mass balance of the fresh rutheniumnitrosylnitrate-solution and the resolved residue in the flask used for impregnation. The ruthenium and rhenium content of both solutions was determined by ICP-OES (Liberty 110, Varian). In Table 4-2 the effective ruthenium and rhenium concentrations of the respective catalyst samples are listed. For the ICP-OES measurements an error of ± 12% for a confidence level of 95% was estimated.

Table 4-2: Effective amount of ruthenium and rhenium loading determined by a metal balance of the impregnation solution. *The additional uncertainty results from the concentration range in the impregnation solution. n.a.: not analyzed.

Sample	2% Ru/2	2% Ru/5	2% Ru/7	2% Ru/8	2% Ru/11
Ru wt%	2.1 ± 0.3	2.2 ± 0.3	1.9 ± 0.2	2.2 ± 0.3	2.2 ± 0.3

Sample	5% Ru/(2)	5% Ru/(8)	7.5% Ru-Re/(2)	2% Ru/ZrO_2 (DKKK)
Ru wt%	5.5 ± 0.7	5.3 ± 0.7	2.6 ± 0.3	n.a.
Re wt%			(3.1 - 4.7)* ± 0.6	

4.3 Liquefaction and gasification experiments in a batch reactor setup

Parametric liquefaction and gasification experiments with fermentation residue samples were performed in a batch reactor system. The influence of several process parameters was tested independently. The set of experiments can be subdivided into two groups, liquefaction and the gasification experiments. The conditions in the liquefaction experiments were chosen to simulate the preheating section of the continuous process, i.e. slow heating rate, subcritical temperatures and no catalyst present. The conditions in the gasification experiments were chosen corresponding to the conditions prevailing in the catalytic reactor, i.e. fast heating rate, rapid transition to supercritical region, presence of a catalyst.

4.3.1 Experimental setup and procedure

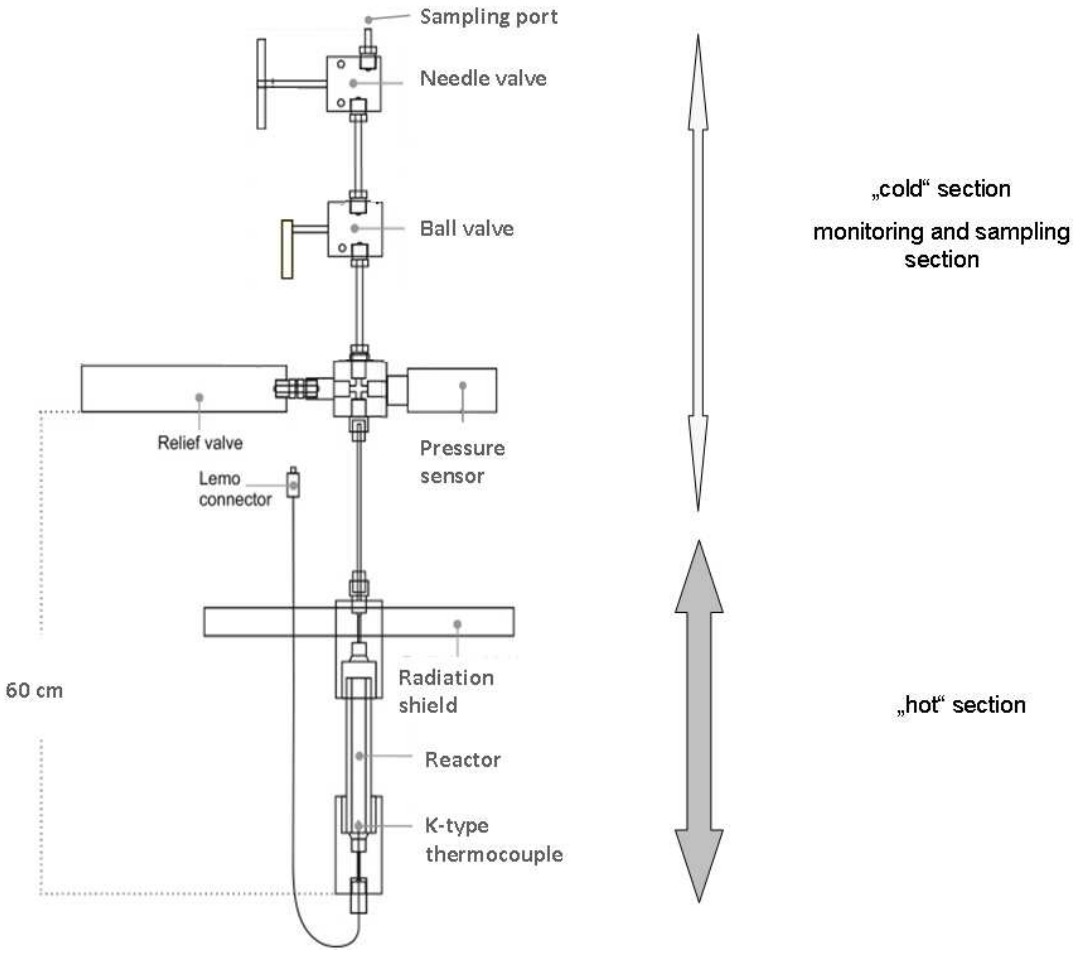

Figure 4-2: Scheme of the batch reactor setup as used for the liquefaction and gasification experiments described in section 2.3. Modified from [106].

Liquefaction and gasification experiments were conducted in a 316 stainless steel reactor (HIP, USA) with an inner volume of 52.5 ml (tube dimensions: 9/16'' ID, 12'' length). A thermocouple in contact with the reactor media was used to monitor the effective reaction temperature. A stainless steel capillary was attached to the reactor, connecting the reaction chamber with the monitoring section containing a pressure sensor and a valve for withdrawal of gaseous reaction products after the experiment. The reactor was heated in a preheated fluidized sand bath (Techne, SBL-2D). The temperature increase inside the reactor leveled out at a temperature which was usually 5-15°C below the setpoint temperature of the sandbath, depending on fluidization. The monitoring section with a total volume of ca. 2 ml was not heated. The reaction was quenched by immersing the hot reactor in a cold-water (ambient temperature) bath. The term "reaction time" always refers to the entire time span from immersing the reactor into the sand bath until quenching of the reaction. The

time required to heat the reactor up to a temperature of 300˚C - the temperature approximately at which the gasification reactions were assumed to start - was ca. 5 min. The time span at a temperature higher than 300°C was referred to as "residence time".

The reactor was flushed with argon before every experiment. For the first part of the gasification and liquefaction experiments, the reactor was pressurized to 4 MPa with argon in order to reduce the evaporation of water during the heat-up phase. However, the second part of the experiments was performed without argon since it was found in a comparison that the presence of argon had no significant influence on the product composition. Instead of adding argon, the reactor was evacuated at the beginning for this second part of experiments. By this measure, a higher reactor loading could be achieved, reducing the errors due to the influence of cold zones and small sample amounts

The fermentation residue was used as received and was not previously dried in order to avoid a loss of volatile compounds. For maintaining a stable quality of the fresh fermentation residue, it was stored in a refrigerator. Only for the heat-up experiments (H10 and H11, Table Appendix B), the feed was previously dried and milled to a particle size of <1 mm by a cutting mill.

The final pressure of an experiment was tuned by adjusting biomass, water and catalyst loading. Since the final pressure could not be predicted with high accuracy, variations within a set of experiments could not be avoided.

After an experiment, gaseous reaction products were withdrawn from the sampling port. Before this step, the sampling line was evacuated up to the ball valve (Figure 4-2). With the needle valve the flow of gas phase could be adjusted gently. The gas phase was collected in a gas sampling bag purchased from SKC Inc., USA. For those experiments with no argon added prior to the experiment, the reactor was pressurized to 4 MPa with argon prior to withdrawal. This step was done to dilute the otherwise very small gas volume. The gas composition was analyzed by gas chromatography. Liquid and solid reaction products were extracted as described in section 4.6.2.

A list of all experimental conditions for liquefaction and gasification experiments in a batch reactor is given in Table Appendix B.

4.3.2 Liquefaction experiments

The liquefaction of biomass in the absence of a catalyst was studied in a series of experiments with slow heating rate. For this purpose, the sand bath was preheated to a temperature of 200°C. As soon as the reactor was immersed into the sand bath, the bath temperature was set to 420°C. The heat-up rate could not be kept totally identical for all liquefaction experiments, because it was strongly influenced by the air flow through the sand bath. Only a coarse regulation of this air flow was possible. The reaction time was therefore slightly different for each experiment in order to get similar retention times.

In this set of experiments, alkali compounds were added to the biomass. They were added undissolved to the biomass in the reactor. After closing the reactor, it was shaken carefully by hand for mixing.

4.3.3 Gasification experiments

In a series of gasification experiments the conditions in a continuous reactor were simulated, i.e. fast heating rate and the presence of a catalyst. The fast heating rate was accomplished by preheating the sand bath to 10 K above the desired temperature. The catalyst usually sank to the bottom of the reactor because of its high density. In some experiments, the catalyst was fixed in the middle of the reactor by a stainless steel wire mesh with a pore size of 0.45 mm in order to bring it in contact with the gas phase, which may not be completely miscible with the supercritical water phase. This will be indicated when the respective results are discussed.

The temperature, reaction time and residence time, ratio of biomass to catalyst (also denoted by molar ratio of sulfur to ruthenium, n(S)/n(Ru)) and additives were varied in the different sets of experiments. The constant parameters (e.g. pressure) had to be adjusted accordingly, e.g. by varying the total loading.

4.3.4 Assessment of mixing quality in mini-batch reactors

A test series on the influence of agitation in the batch system on the conversion rate of solids containing biomass was done in a 316 stainless steel reactor (HIP, USA) with an inner volume of 5 ml (tube dimensions: 5/16'' ID, 4'' length), referred to as mini-batch reactor. The small size of the mini-batch reactors made it possible to position them horizontally within the sand bath. A thermocouple was attached on the side of

the mini-batch reactor. The monitoring unit which was used for the large batch reactor was not used for these experiments, because the ratio of hot and cold volume was in a range where we would expect major influences by the cold zone.

The experiments were performed with 2% Ru/C catalyst and dry fermentation residue O1 (ratio 0.5 g $g_{biomass}^{-1}$) with extra water added, as well as with 2% Ru/ZrO_2 and fermentation residue O3 (as received, ratio 0.3 g $g_{biomass}^{-1}$, corresponding to a ratio of 5 g $g_{biomass}^{-1}$ on a dry basis). The loading for the 2% Ru/ZrO_2 catalyst was chosen 10 fold higher because it was found to show a lower activity than 2% Ru/C. Experiments were performed pairwise with one reactor in vertical and one in horizontal position (see Figure 4-3). Each pair of experiments was done simultaneously to compare the influence of mixing. The reactor in horizontal position was tilted back and forth by hand in order to mix the contents during the whole reaction time. A short reaction time was chosen to avoid full conversion, which would prevent the observation of any kinetic or mass transfer effect. The sand bath temperature was set to 400°C. A temperature of around 380°C was reached inside the reactor.

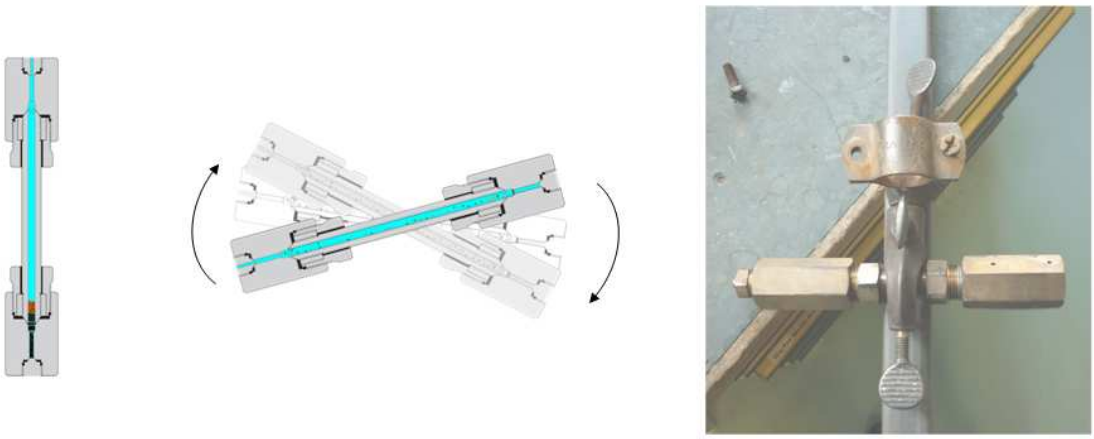

Figure 4-3: Scheme and picture of the mini-batch reactors.

The reaction time was between 5 and 15 minutes for the experiments with the 2% Ru/C. The reaction time was identical for a pair of experiments.

For the experiments with the 2% Ru/ZrO_2 catalyst, the reaction time was also in the range of 5 to 15 minutes; however, in these experiments the residence time (t for T ≥ 300°C) was identical for a pair of experiments. The reaction time was slightly longer for the vertical reactors, since the heat-up was slower (see Figure 4-4). The pair-

experiments are designated as A1-A8; V stands for vertical and H for horizontal. The experimental conditions can be found in Table Appendix B.

Only the liquid and solid reaction products could be recovered. The gas phase escaped when opening the reactor. Liquid and solid products were extracted following the procedure described in section 4.6.2.

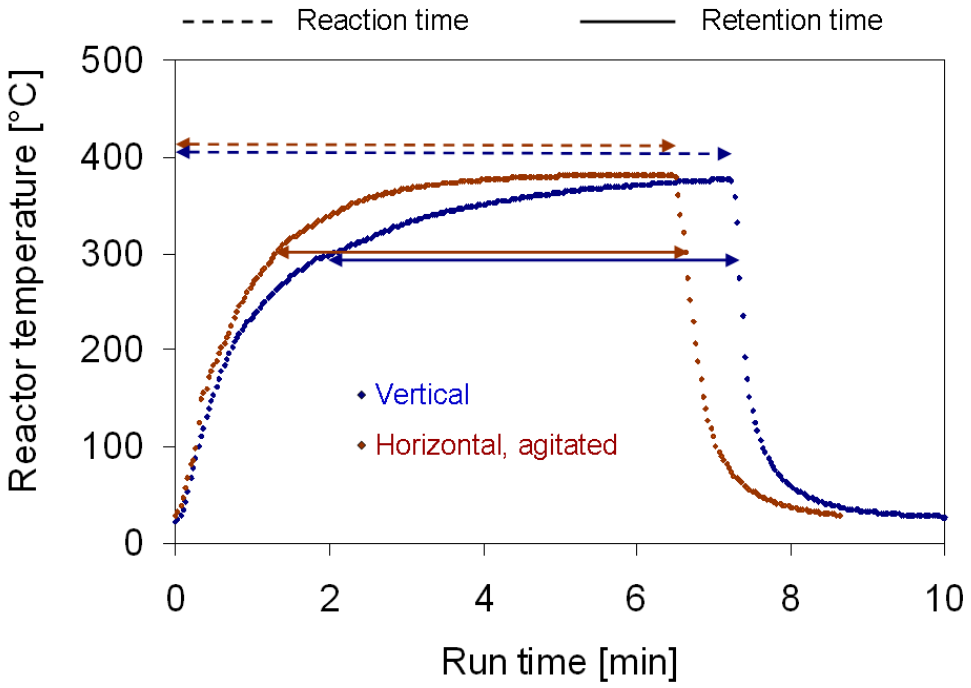

Figure 4-4: Temperature as measured inside the horizontal and vertical reactor during heat-up. Solid arrows indicate the residence time which was identical for a pair of experiments.

4.3.5 Experiments with gaseous feed

A few tests with gaseous feed were done for qualitative testing of the behavior of the gas phase in an unstirred two-phase system and the influence of the cold zone. For this purpose, the reactor containing only water and catalyst was pressurized with a gas mixture via the sampling port. After the reaction, the product gas mixture was withdrawn as described in section 4.3.1. Liquid and solid products were not formed. The composition of the gas mixture and experimental conditions can be found in Table Appendix B. The experiments are designated as G1-G7.

4.4 Gasification experiments in the continuous reactor setup Konti-1

4.4.1 Experimental setup

The continuous gasification was performed in a continuous reactor setup named Konti-1 which has previously been described by Waldner et al. [108]. Few modifications were applied. The modified sampling port allows the collection of a sample whilst the gas phase is directed back into the phase separator. The dimensions of the stainless steel catalytic reactor were as follows: L: 450 mm, ID 12 mm, OD: 18 mm. A picture of the Konti-1 is shown in Figure 4-5. A flow scheme of the setup can be found in Appendix G.

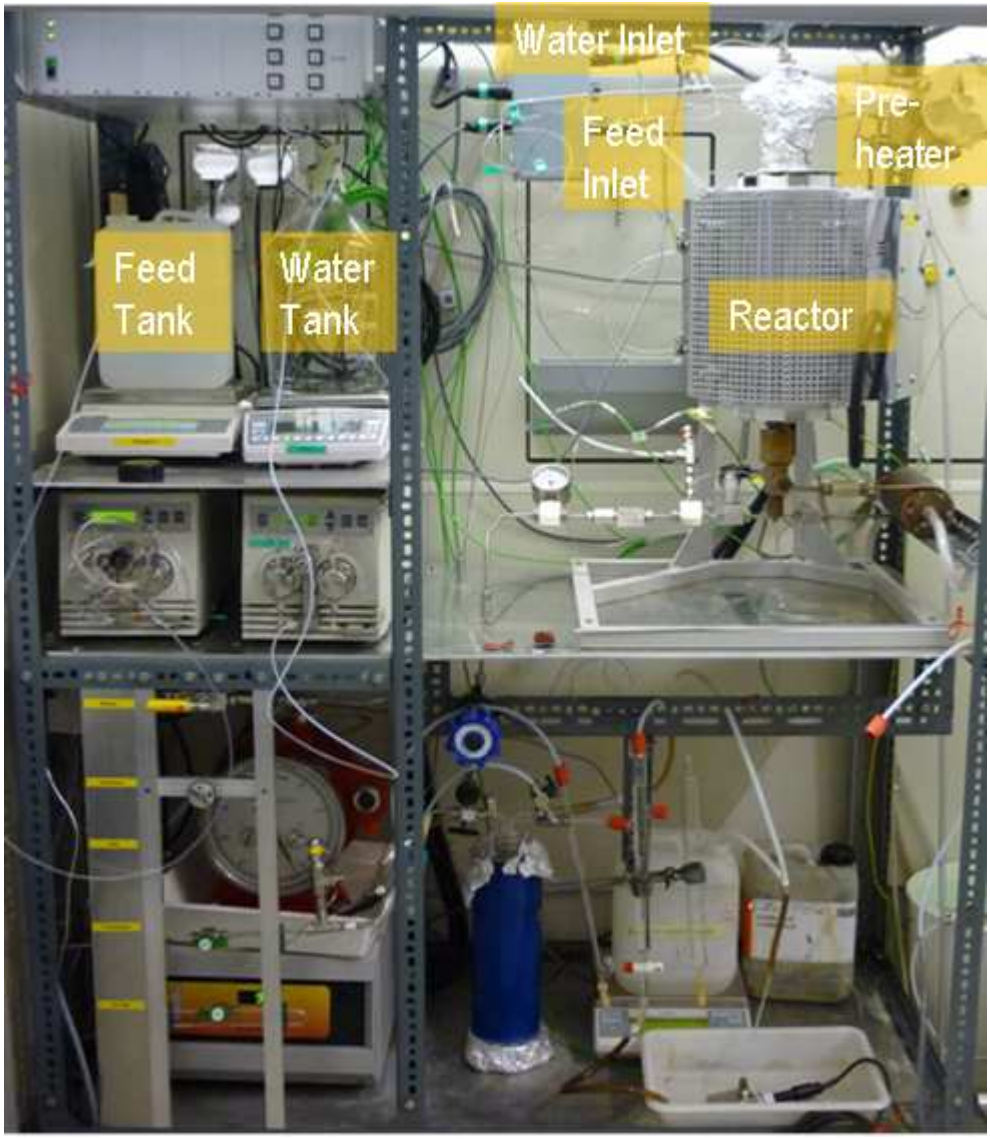

Figure 4-5: Picture of the Konti-1.

The reactor and the corresponding connections (316L stainless steel) were purchased from SITEC-Sieber Engineering AG (Switzerland). Up- and downstream of the heated zone, Swagelok connections were used. A steel tube closed on one end (ID: 1/32'', OD: 1/16'') was located inside of the reactor vertically over the whole length, through which a movable thermocouple could be inserted in order to measure the axial temperature profile of the reactor. Water and organic solution were pumped separately by two Waters 515 HPLC pumps. The unheated organic solution was directly injected into the preheated water stream just before entering the reactor. This had the advantage of avoiding unwanted reactions and coke formation caused by a slow heat-up rate of the carbonaceous feed. The effluent leaving the reactor was cooled down to ambient temperature by a heat exchanger with tap water. A 5 µm filter (SITEC) was placed upstream of the manually operated pressure regulator (Tescom, model 54-2000, valve seat made of PEEK) to avoid entrance of fine particles. Downstream of the pressure regulator, liquid and gaseous effluent phases were separated in a phase separator. In contrast to the setup described by Waldner et al., the total gas phase was dried in a cryogenic trap (isopropanol cooled with liquid nitrogen). The accumulated volume of the dry gas was determined by a wet gas meter.

The gas composition was analyzed by GC. For this purpose, a stream was continuously withdrawn from the product gas stream by a gas pump (KNF Laboport, model 1393-86) downstream of the cold trap and upstream of the gas meter. The flow rate of this stream was determined by a bubble meter periodically in order to correct the amount of the product gas stream by this subtracted stream. It was in the range of 12-20 ml/min. From this partial stream, samples were taken with an injection loop. In case of poor gas production, the total gas stream was often not sufficient to provide enough flux for the GC measurement. In this case, a defined stream of argon was directed into the phase separator in order to dilute the product gas. From the liquid product phase, samples were taken at certain time intervals. TOC, TS and ion content of the effluent were measured off line.

For some experiments, a conductivity sensor (Schott, handylab pH/LF/12SET) was placed in the outlet stream of the phase separator.

A temperature profile over the length of the reactor was measured before an experimental run and in certain time intervals during gasification.

A LabView control program was used to control the temperatures and to monitor the remaining process parameters such as pressure and flow rates (see Figure 4-6). The latter had to be controlled manually. The reading of the wet gas meter was recorded manually.

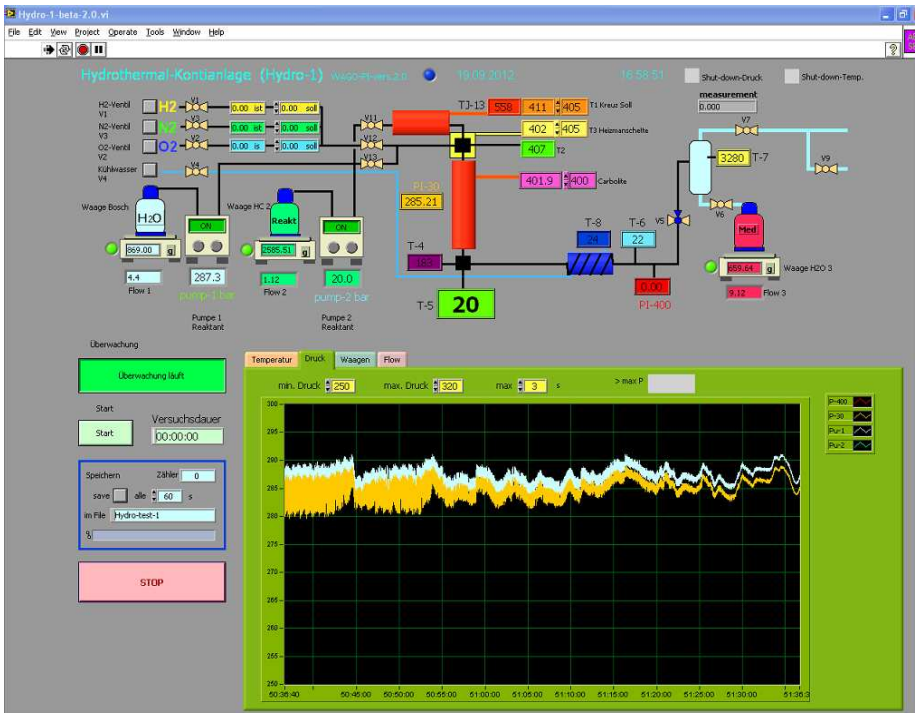

Figure 4-6: Screen shot of the LabView control program for the gasification test rig Konti-1.

4.4.2 Experimental procedure

The catalyst pellets were filled into the reactor tube. A layer of the neat support material was placed below and above the catalyst. For the experiments with 2% Ru/C, ZrO_2 pellets were used instead of the neat carbon support. The total mass of catalyst was 10 g for the Ru/C and 30 g for the Ru/ZrO_2 and Ru/TiO_2 experiments. This adjustment was needed because the high difference in bulk density (see Table Appendix A) between activated carbon and the refractory oxides would have led to a much shorter catalyst bed for 10 g of the refractory oxide catalyst system. The length of the catalytic bed was in the range of 20 cm and varied according to the bulk density of the respective sample. The flow rates of water and the organic solution were 4 and 1 ml min^{-1}, respectively. The flow rates were kept constant in order to maintain a constant temperature at the reactor inlet resulting from the mixing ratio of the preheated water and the cold feed. The organic concentration in the top inlet of

the reactor was adjusted by the organic concentration in the stock solution. For each catalyst sample gasification experiments were run at fixed feed concentrations. The weight hourly space velocity (g_{feed} ($g_{catalyst}$ h)$^{-1}$, WHSV) depended on the feed concentration because of the constant flow rate and on the mass of the catalyst bed.
The reactor bed was flushed with water at ambient pressure and temperature prior to heating in order to remove fine particles that would otherwise get stuck in the filter and cause a pressure drop between reactor and valve. For this purpose, the line was opened upstream of the filter. Afterwards, the heating of the preheater and the reactor as well as the heat tracing were set to the desired temperatures at a pressure of 28.5 MPa still flushing the system with water. When a stable temperature profile was reached, the feed solution was changed from water to a model biomass solution.

During gasification, samples were taken at certain time intervals. The reading of the balances and the gas meter were recorded regularly for the determination of the flow rates. The carbon gasification efficiency and the gas composition were monitored regularly in order to notice a change in performance during the time on stream. The shape of the temperature profile in the reactor was used as an additional indication for possible shifts of the reaction zone.
After the experiment, the catalyst was flushed with pure water at reaction conditions for several hours, with ethanol at 50°C and 28.5 MPa for half an hour, and was then dried at 50°C in a vacuum oven prior to characterization. The catalyst bed was split into three equal sections according to the distance from the top inlet. The characterization was applied to catalyst pellets randomly picked out of the first section.

4.4.3 Catalyst screening

For the catalyst screening (section 5.7), the performance and the stability of the conversion of different catalyst systems was tested for gasification of glycerol as model compound. The performance test was done at full conversion to avoid fouling as a consequence of the formation of intermediates.
The aim of this test was to determine the highest space velocity at which full gasification could be maintained over 24 h without a significant change in gas composition. The feed concentration was increased stepwise resulting in the following concentrations of the feed mixture: 6 wt%, 11 wt%, 16 wt% and 19 wt%. A

concentration higher than 85 wt% glycerol for the pure organic stream (19 wt% for the mixture) could not be pumped because of the high viscosity.
Since the flow rates and the mass of the catalyst bed were kept constant for all experiments, the WHSV changed only depending on the feed concentration: 0.6 h^{-1}, 1.1 h^{-1}, 1.6 h^{-1} and 2 h^{-1}.

4.4.4 Poisoning and regeneration tests

The Ru/C catalyst was poisoned on pourpose by sulfate. Following the considerations of Schubert et al. [60], potassium sulfate was chosen as poisoning agent because of the relatively high solubility in supercritical water. Precipitation of the salt in the reactor was not intended, because this may lead to physical blocking of the active sites by salt particles. Therefore the concentration was chosen to be below saturation at the experimental conditions. The choice of the concentration was based on solubility data from literature [161-163] and led to a 0.002 M K_2SO_4 solution. Experiments with a pure salt solution were performed as well as experiments in which the salt was added to the organic feed. In both cases the salt was added to the total feed stream over the organic feed line at a corresponding concentration of 0.01 M.

For poisoning experiments, two characteristic times, t_1 and t_2, were calculated. t_1 was defined as the time after which the molar amount of sulfur fed into the reactor corresponded to the molar amount of ruthenium exposed on the surface of the fresh catalyst as determined by chemisorption (see section 4.7.8.2). t_2 was defined as the time after which the molar amount of sulfur corresponded to the total molar amount of ruthenium in the reactor. The actual time, after which a dramatic decrease in gasification efficiency and methane production was observed, is referred to as t_3.

$$t_1 = \frac{n_{Ru(s)}}{\dot{n}_S} \qquad \textbf{(4-2)}$$

$$t_2 = \frac{n_{Ru(tot)}}{\dot{n}_S} \qquad \textbf{(4-3)}$$

(t = time [min]; n = molar amount [mol]; $\dot{n}$ = molar flow rate [mol/min]; index (s) = surface, index (tot) = total).

Regeneration was performed with H_2O_2, which was added over the organic feed line at a concentration of 10-15 wt%, resulting in a concentration of 2 and 3 wt%, respectively, in the reactor. The regeneration procedure was performed at temperatures between 100 and 150°C and at a pressure of 28 MPa. The regeneration time varied between the experiments and is given in the respective sections.

4.5 Liquefaction and gasification experiments in the continuous reactor setup Konti-2

4.5.1 Experimental setup

The continuous test rig Konti-2 was used for gasification experiments with fermentation residue. The assembly has been described in detail earlier [19, 28]. However, various modifications were applied since then. Therefore it will be described as a whole again in this thesis. The Konti-2 is depicted in Figure 4-7.

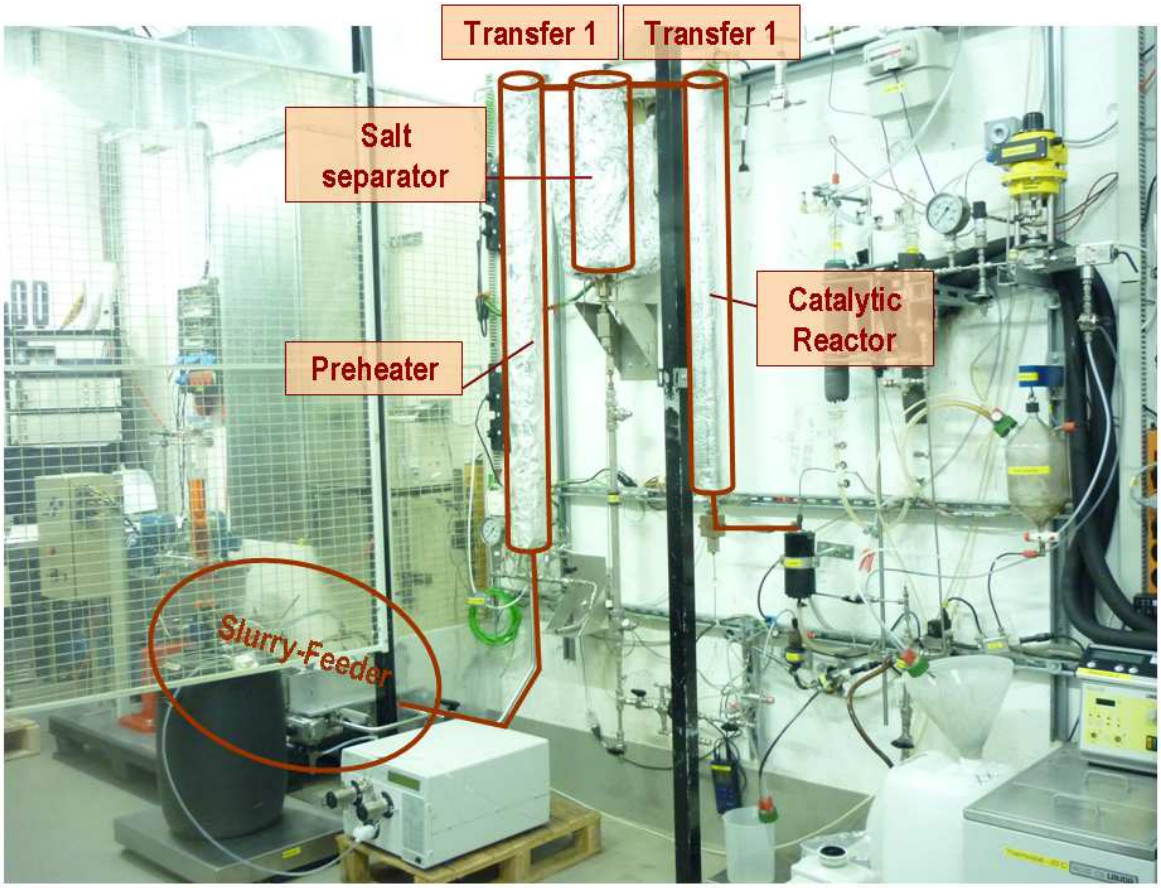

Figure 4-7: Photograph of the continuous test rig Konti-2.

The setup is based on the process scheme of PSI`s hydrothermal process (see section 3.5.2), however, being a lab test rig, it is simplified in many respects as for example in regarding heat recovery, which is not implemented. The maximum capacity is 1 kg h^{-1}.

Basically, it consists of a pump compressing the feed to the desired pressure before entering the heated zone. The heated zone is devided in three sections, preheater, salt separator and reactor. At the end the fluid is cooled and depressurized to ambient conditions.

Pumping was accomplished by a preparative HPLC pump (Varian, PrepStar, Solvent Delivery Module SD-1) for flushing with pure water and by a custom made piston pump, referred to as Slurry-Feeder (see 4.5.2), for biomass containing solids.

First, the biomass enters the preheater (SITEC, stainless steel 1.4435, length 1.70 m, 12 mm ID, 18 mm OD), in which the biomass is electrically heated to near-critical temperatures and thereby liquefied. From there, the liquefied biomass enters the salt separator via a heated transfer tube (stainless steel 1.4435, length 0.335 m, 2.4 mm ID, 6.35 mm OD). The salt separator can be described as the superheater; it was custom made by SITEC (titanium grade 5, length 694 mm, 12 mm ID, 50 mm OD), including six ports for SITEC fittings. Biomass enters the salt separator from the top via a dip tube (stainless steel 1.4301, length 0.23 m, ID 2 mm, OD 4 mm). The setup of the salt separator is shown in Figure 4-8. A detailed description can be found in [19].

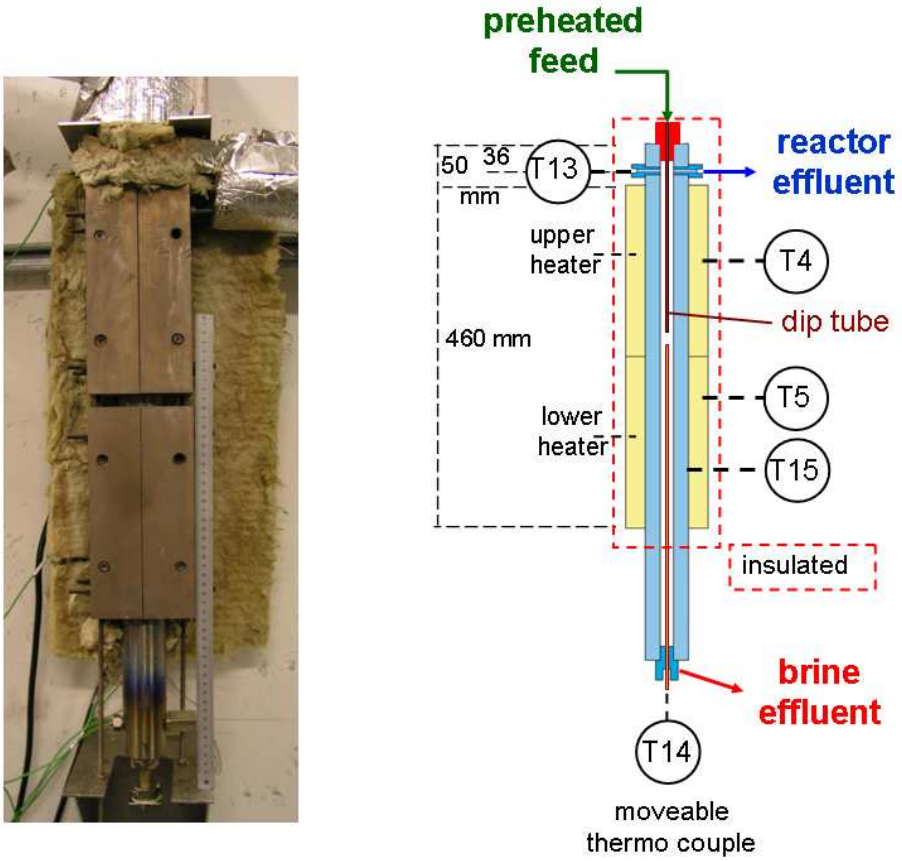

Figure 4-8: Photograph (left) and scheme (right) of the salt separator in the heating blocks. Graphic taken from [19].

In the supercritical water environment prevailing in this part of the process, the biomass is further degraded, promoted by the good solubility for organic molecules. Precipitated salts and other particles with high density are withdrawn at the lowest point of the salt separator and subsequently cooled by a tube-in-tube cooler. Particles are collected in a particle trap while the brine containing the redissolved salts is depressurized by a relief valve (Swagelok) after passing a filter (stainless steel, pore size 25 µm, Internormen). The stream is controlled by a mass flow controller (Bronkhorst, Liquiflow) which is located on the high pressure side of the relief valve. The desalinated biomass leaves the salt separator at the top exit and is transferred to the reactor (SITEC, stainless steel 1.4435, length 1.40 m, 12 mm ID, 18 mm OD) via a heated transfer tube (stainless steel 1.4435, length 0.145 m, 2.4 mm ID, 6.35 mm OD). The reactor is held at a temperature of 400°C, low enough to shift the thermodynamic equilibrium of the exothermic methanation reactions to the product side, but still supercritical to maintain a good miscibility of the different phases. For the gasification experiment, the reactor was filled with 40 g of 2% Ru/C catalyst from the top to half of the reactor length. The remaining part was filled with 2 mm ZrO_2

extrudates. For the liquefaction experiments, the reactor was replaced by an unheated steel tube (SITEC, stainless steel 1.4435, length 1.40 m, 12 mm ID, 18 mm OD) for the reduction of the dead volume.

The fluid leaving the reactor was cooled by a heat exchanger with water at a temperature of 40°C (stainless steel 1.4435, coiled tube, length 3.8 m, 2.4 mm ID, 6.35 mm OD, manufactured at PSI). Particles are removed by a particle trap and further downstream by a stainless steel filter (pore size 15 µm), which is present in double, having a parallel arrangement such that it can easily be switched from one to the other by a three way valve in case of plugging.

The fluid is depressurized to atmospheric pressure by a manually adjustable spring loaded relief valve (SITEC). A control valve (Kämmer) combined with a pressure controller (Flowserve) located upstream of the relief valve, regulates the pressure in a range of around 5 MPa. The depressurized fluid is directed to a phase separator (borosilicate glass, 2000 ml) where the gas- and liquid phases are separated. In the case of poor gas production, a defined argon stream was fed into the phase separator in order to dilute the product gas.

The gas phase passes a cooling trap (-20°C) for drying and a gas meter (Wohlgroth 0402464) and is directed to a gas burner. A gas stream is withdrawn for GC analysis as it is described for Konti-1 (4.4.1).

Flow rates are measured gravimetrically by monitoring the weight change of feed, salt separator effluent and reactor effluent over time. For the Slurry Feeder the feed mass flow could only be determined for an integral time period. The electrical conductivities of the two product streams are measured on-line by conductivity meters (WTW Cond 340i) in flow-through cells. The axial temperature profiles of the preheater, salt-separator and reactor can be measured manually with moveable thermocouples (diameter 1 mm). Several thermocouples are installed to monitor the temperature at various parts of the test rig. Pressure transmitters record the pressure up- and downstream of each section, facilitating the localization of any potential plugging. Samples of the effluents were taken manually after certain time intervals.

A LabView control program written in house was used to monitor an experiment. The control for the Slurry Feeder is included as well. Figure 4-9 shows a screenshot visualizing the setup of the test rig and control unit.

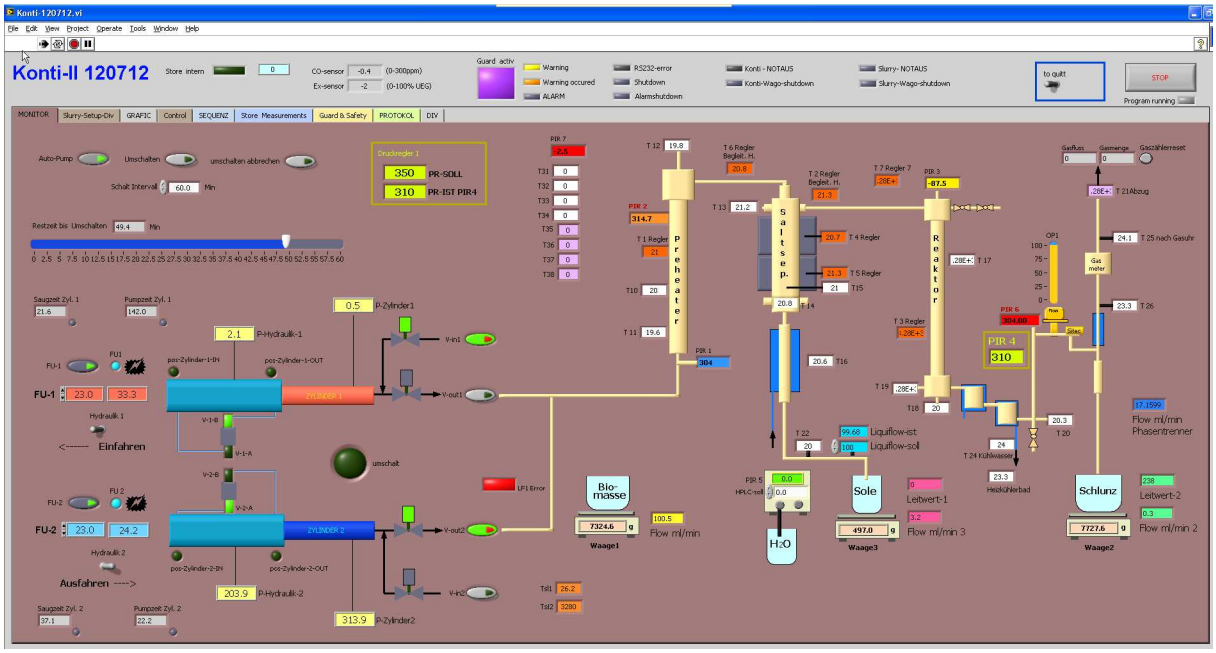

Figure 4-9: Screen shot of the LabView control panel for the gasification test rig Konti-2 and the Slurry Feeder.

4.5.2 Setup of the slurry feeder

For the processing of heterogeneous feedstocks, i.e. feedstocks containing solids, a custom made piston pump, in the following refered to as *Slurry Feeder*, was used. The Slurry Feeder was designed by Erich DeBoni (PSI) and constructed by the PSI engineering department (AMI). It consisted of two 316 LN stainless steel cylinders (*Schenker*, Switzerland) with a working volume of 2.6 l each that were operated by a hydraulic drive (Bosch Rexroth). Inlet and outlet port of the Slurry feeder could be opend and closed by pneumatically operated ball valves (*AFS*, 16 mm, purchased from *Swagelok*). The hydraulic pump could be operated at a frequency of 0-50 Hz. The pumping rate at a given frequency depended on the back pressure of the system and slightly differed for both of the two pistons because of the individual oil slip. At operating conditions, i.e. 28 MPa, a frequency of around 20.5 and 21 Hz was necessary to operate the respective piston at a rate of 1 kg h^{-1}.

Two *Baluff* inductive sensors were located on the cylinders' rear and front end, indicating the stop positions of the piston.

The components of the Slurry Feeder were controlled by a measurement and control unit purchased from *WAGO* (Germany). It could be directly operated by the same control panel as used for Konti-2 (Figure 4-9). The pistons could be operated manually or in an automated mode. In the automated mode, switching between the two pistons was initiated after a pre-selected time interval. In this procedure, the

second piston was started with all valves closed until the pressure inside reached the system pressure. Only then the valves of both pistons switched, avoiding a reflux of hot fluid in the case of a failure of the check valve, located upstream of the preheater. The duration of the switching process therefore depended on the pumping frequency and on the system pressure and had to be added to the given switching interval.

The position of the respective piston could be identified by a specially designed indication system based on displacement of air in the dead volume of the cylinder behind the piston that in turn displaces a fluid from a reservoir tank into a graduated flask. A schematic of the Konti-2 can be found in Appendix F.

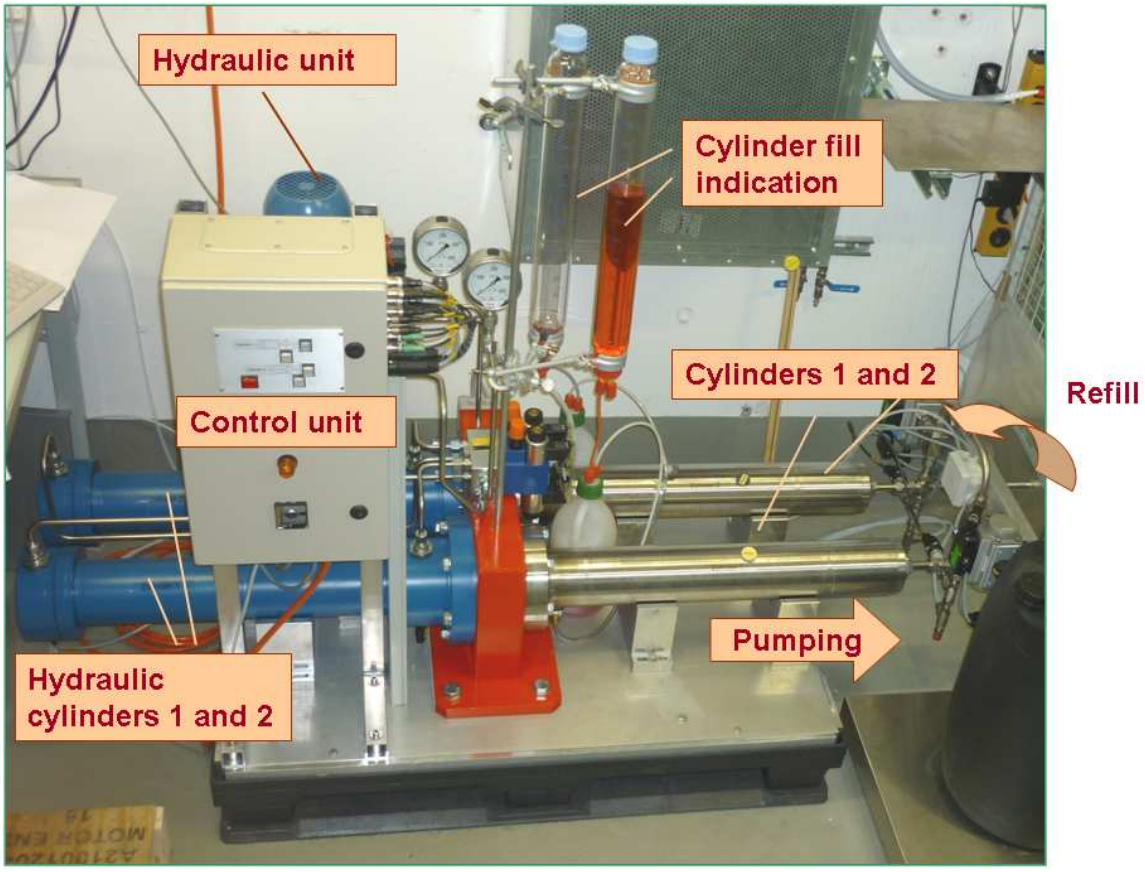

Figure 4-10: Picture of the Slurry Feeder.

4.5.3 Experimental procedure

Before any experiment, the whole test rig was flushed with deionized water for several hours at ambient conditions to remove fine particles from the catalyst bed or corrosion dust. Afterwards, the system was pressurized and heated to experimental conditions; it was flushed at those conditions for another few hours. Temperature profiles were measured as reference for reaction-free conditions.

The fermentation residue was pretreated by dilution with water, sieving and addition of supplements such as alkali compounds or thickening agents, as described in the result sections (5.4 and 5.5).

The starting point of the experiment was defined as the time at which the feed was changed from water to the organic feed. During the experiment, samples were taken from the salt separator and reactor effluents. The extraction of the samples including the feed followed the procedure described in section 4.6.2. Temperature profiles were measured for some experiments. Heavy pressure fluctuations occurred occasionally especially when fermentation residues were gasified. In this case, the automated pressure control needed to be assisted by manual adjustment of the relief valve. As soon as the gas production started, the gas burner was ignited. The product gas was diluted with 25 ml min^{-1} of nitrogen to provide a gas flow sufficient for GC measurements.

After the experiment, the test rig was flushed with pure water under experimental conditions for several hours and later with ethanol at 80°C and elevated pressure.
The experimental settings are listed in Table 4-3.

Table 4-3: Settings for gasification (G) and liquefaction experiments withthe lab test rig Konti-2

Experiment	G1	L1	L2	L3
Total flow rate [g min^{-1}]	17	17	17	17
Flow rate salt separator effluent [g min^{-1}]	1.9, later 2.4	2.0	2.0	3.0
Temperature preheater [℃]	370	350	350	350
Temperature transfer 1 [℃]	370	350	350	350
Temperature salt separator upper block [℃]	450	430	470	430
Temperature salt separator lower block [℃]	450	430	470	430
Temperature transfer 2 [℃]	400	350	350	350
Temperature catalytic reactor [℃]	400	-	-	-
Pressure [MPa]	28	28	28	28

4.5.3.1 Gasification experiment

The gasification experiment was done with fermentation residue sample O4. As it was the first experiment, an extensive pretreatment was done removing particles larger than 1 mm in order to avoid plugging of the test rig especially at bottle neck positions such as the dip tube. Note that particles may grow under coke formation conditions. For this purpose, the fermentation residue was first mashed in a food mill with a pore size of 2.5 mm. Afterwards it was wet sieved over a stainless steel wire mesh with a pore size of 0.45 mm. During this procedure, water was added. The dry matter content as given for the respective experiments referred to the sample after the pretreatment procedure.
Five samples were taken during the experiment. Fermentation residue was fed for 2.5 hours. The WHSV was in the range of 0.3-0.5 $g_{biomass,DM}$ $g_{catalyst}$ h^{-1}. A characterization of the spent catalyst was not done, because the same filling was used for other experiments.

4.5.3.2 Liquefaction experiments

For all liquefaction experiments, fermentation residue sample O5 was used. The sieving procedure was simplified after the gasification experiment due to the fact that neither large particles were found in the filters nor had any blockage occurred. However, in contrast to the gasification experiment, a food thickening agent, xanthan, was added in order to avoid phase separation of the feed during the residence time in the Slurry Feeder. The amount added corresponded to 1.3 g kg^{-1} of the fermentation residue on a wet basis. K_2CO_3 (70 g kg^{-1} of the dry matter) was added to prevent coke formation.

The experimental procedure was similar to the gasification experiment with few variations: Only one sample was taken during an experiment, starting at the time of changing the feed to biomass and ending one hour after changing the feed back to water. The total period of feeding biomass was 2 hours. After the experiment, the content of the particle traps, dispersed in ethanol, was collected and characterized.

4.6 Sample preparation and analytics

4.6.1 Gas phase analytics

The composition of the gas phase was determined by gas chromatographic measurement. Ar, N_2, CO_2, CH_4, H_2, CO and higher hydrocarbons (C2-C4) could be detected and quantified by the applied method.

The content of H_2S, SO_2, CS_2 and mercaptans in the gas phase could not be determined by the GC method. These compounds were detected using test tubes (Dräger, 50/b for SO_2, 3/a for CS_2, 0.5/a for mercaptans and 100/a for H_2S).

The gas volume was determined by a gas-tight 1L Hamilton syringe for the batch-experiments and by a gas meter for the continuous experiments with the test rigs Konti-1 and Konti-2.

Carbon and sulfur recovery from the feed were calculated following Equations 4-4 and 4-5:

C-recovery:

$$w_{c,g} = \frac{\frac{V_{Gas}}{V_m} \cdot M_C \left(y_{CO_2} + y_{CH_4} + y_{CO} + 2y_{C_2H_6} + 3y_{C_3H_8} + 4y_{C_4H_{10}} \right)}{w_{C,F} \cdot m_F} \text{ [mg g}^{-1}\text{ (feed C)]} \qquad (4\text{-}4)$$

S-recovery:

$$w_{s,g} \geq \frac{\frac{V_{Gas}}{V_m} \cdot M_S \left(y_{SO_2} + 2y_{CS_2} + y_{H_2S} \right)}{w_{S,F} \cdot m_F} \text{ [mg g}^{-1}\text{ (feed S)]} \qquad (4\text{-}5)$$

(V_{Gas} = Gas volume in L, V_m = molar volume (22.4 L mol^{-1}), M_C and M_S = Molar mass of C and S, respectively, w_c and w_s = mass fraction of C and S, respectively, [mg g^{-1}] y_i = gas volume fraction, m = mass, F = feed, g = gaseous)

The temperature was not included in the calculation because of inhomogeneous local and temporal distributions. The error resulting from this simplification is discussed in section 4.7.12.

4.6.2 Work-up of liquid and solid reaction products

The liquid and solid reaction products were processed following the work-up scheme proposed by Müller [19], consisting of an extraction with a water/hexane

mixture and in a next step with methanol, and the separation of the insolubles by a successive vacuum filtration of the extract phases over a cellulose filter (Whatman Grade 1, 11 µm) in the order: 1st water, 2nd hexane, 3rd methanol.

The extracted phases represent the salts and very polar organics (water phase), aliphatic and other non polar organics (hexane phase), polar water-insoluble organic substances, e.g. tars (methanol phase), as well as insoluble solid matter, including precipitated salts and other minerals, and coke (solid phase). Catalyst grains were selectively removed from the solid phase. The total carbon content (TC) of each phase and the total inorganic carbon content (TIC) of the solid and water phases were determined using a TOC analyzer. The total sulfur content (TS) of the single phases was determined using a CNS analyzer (Elementar, Germany). TC, TOC, and TS of the feed were determined by analyzing the fermentation residue as received. Likewise, the feed was subjected to the same extraction procedure and analyses. The solvents used for the extraction (analytical grade) were purchased from Sigma Aldrich.

The content of anions (chloride, nitrate, sulfate, fluoride, phosphate) in the extracted water phase was determined via ion chromatography. The corresponding content of the feed was determined as described in section 0.

The recovery of carbon relative to the feed carbon was calculated for each phase using Equation 4-6:

$$\text{C-recovery}_{(P)} = \frac{w_{C,P} m_P}{w_{C,F} m_F} \cdot 1000 \qquad \text{[mg g}^{-1}\text{ (feed carbon)]} \qquad (4\text{-}6)$$

(w_c: carbon mass fraction [mg g^{-1}], m: mass of the sample [g], P: Phase and F: Feed).

An overall balance for carbon recovery was calculated by summing up the recovered carbon from the respective phases. The sulfur recovery and balance and the respective balances for other elements or ions were calculated accordingly.

4.7 Analytical tools

4.7.1 Gas Chromatography

Gas analysis was carried out using a Hewlett Packard (Agilent) HP-6890 gas chromatograph. Two identical setups were employed for the on-line measurements with the continuous setups and for the off-line measurements for the batch

experiments. For the on-line measurements samples were withdrawn from the product gas stream by an injection loop. For off-line measurements, sampling was performed with a SGE 250 µl gas tight syringe.

The GC instrument was equipped with a two column systems and two detectors. Hydrocarbons were dectected by a flame ionization detector (FID) (back position, operating at 250°C, H_2 flow 35 ml min^{-1}, air flow 350 ml min^{-1}). Separation was accomplished on an HP-1 Hydrocarbon column (30 m x 0.52 mm x 40 µm film thickness) with helium as carrier gas at a flow rate of 4.8 ml min^{-1}.

Ar, N_2, CO_2, CO, methane and H_2 were detected by a thermal conductivity detector (TCD) (front position, heated to 250°C) after separation over the second column system, which consisted of two columns connected by a switching system, where CO_2 was separated from the other gases (column HP-Plot Q 30 m x 0.53 mm x 40 µm) in the first step and thereafter a HP-Plot Molecular Sieve 5A column (30 m x 0.53 mm x 40 µm film thickness) separated the rest of the product gas. Helium was used as carrier gas at a flow rate of 4.5 ml min^{-1}.
A split ratio of 5:1 and 30:1 was used for the front line and the back line, respectively.

The temperature program differed for the on-line and for the off-line measurements. Therefore, retention times and the valve switching times were different for both GCs. The temperature program for the on-line and off-line measurement is listed in Table 4-4.

Table 4-4: Temperature program for GC analysis (on-line and off-line measurements)

On-line measurement		**Off-line measurement**	
time min]	**temperature program**	**time [min]**	**temperature program**
0	Isothermal at 50℃	0	Isothermal at 50℃
2.5	Ramp 50 K min^{-1} to 150℃	2.5	Ramp 25 K min^{-1} to 75℃
4.5	Hold at 150℃ for 0.5 min	3.5	Ramp 50 K min^{-1} to 125℃
5	Cool down: Ramp 100 K min^{-1} to 50℃	4.5	Hold at 125℃ for 1.5 min
6.5	End of run	6	Cool down: Ramp 100 K min^{-1} to 50℃
		6.75	End of run

The GC was calibrated using a set of gas mixtures purchased from Messer Schweiz AG (Switzerland), containing the relevant gas components CO_2, CH_4, C_2H_6 – C_4H_{10}, H_2, CO and Ar at various concentrations. The gas mixtures are listed in Table 4-5. The calibration was not changed within an experimental sequence. However, a daily factor was determined by measuring one calibration gas mixture before measurement of the gas phase samples. For a rough estimation of the nitrogen and oxygen content, which was used to check for leakages in the gas line or gas bag, a calibration with air was done.

Table 4-5: Gas mixtures used for calibration of the gas chromatographs.

	Concentration of gas components in vol%				
Component	Mixture 1	Mixture 2	Mixture 3	Mixture 4	Mixture 5
CH_4	45	29.96	2	50	10
H_2	-	15	2	-	10
CO	0.4	10.07	1	-	5
CO_2	45	15	-	-	10
C_2H_6	1	-	-	7	-
C_3H_8	0.5	-	-	4	-
C_4H_{10}	0.1	-	-	-	-
Ar	-	29.97	95	39	65

4.7.2 Gas chromatography with sulfur chemiluminescence detection (GC-SCD)

For qualitative determination of sulfur coumpounds a gas chromatograph (GC) with a Varian fused silica column (WCOT 30mX0.32mm ID, CP-SIL 5CB, 4.0 ¹m) with He as carrier gas with a sulfur chemiluminescence detector was used (SCD, Agilent 355), with a flame dual plasma burner using a mixture of hydrogen and oxygen was used. The measurements were done by Jörg Schneebeli.

4.7.3 Carbon analyzer

For carbon quantification a TOC analyzer (Vario TOC cube, Elementar, Germany) was used. The instrument can be used in two configurations, i.e. for liquid and for solid samples. For both configurations, the quantification is accomblished by conversion of carbon to CO_2 and transport to a non-dispersive IR detector by a 200 ml min^{-1} oxygen stream and the integration of the CO_2 signal.

For liquid samples, both TC and TIC determination is done automatically. For TC determination, the sample is injected into a combustion chamber at 850°C, containing a platinum catalyst. For TIC determination, the sample is injected into a 10% phosphoric acid solution. The outgassing CO_2 is then transported to the detector by the oxygen stream. The TOC value was calculated by subtraction of the TIC from the TC. The water phase of reaction products was determined using the TOC analyzer in the liquid mode.

For solid samples, TC and TOC determination were done separately. For TC analysis the samples were filled into 0.1 ml tin capsules and then transferred into a combustion chamber, where they were heated up to 950°C in order to oxidize the carbon totally.

The TOC was determined by acidifying the sample with 1M HCl and subsequent drying and degassing in a vacuum oven at 80°C. The TIC was determined by subtracting the TOC from the TC. The solid phase of reaction products was determined using the TOC analyzer in the solid mode. The hexane and methanol phases were determined after removing the solvent at 50°C and 10 kPa in a vacuum oven.

The instrument was calibrated using a 100 ppm and a 1000 ppm TOC standard and self-made TOC standards, all based on potassiumhydrogenphthalate. For the calibration of the TIC a self-made K_2CO_3 standard was used. The calibrated range was between 0.02 and 2.5 mg carbon per sample. The calibration was verified with a standard for each series of measurements.

4.7.4 Sulfur analyzer

Sulfur and nitrogen were quantified by a CNS-analyzer (Vario EL cube, Elementar, Germany). As the TOC analyzer, the instrument can be operated in a solid and liquid mode. For handling reasons, all samples were measured in the solid mode. For this

purpose, the samples were filled into 0.05 ml tin capsules. Hexane and methanol were removed by evaporation at 50°C and 10 kPa in a vacuum oven. Water was not removed. The tin capsules were closed under a helium atmosphere to avoid nitrogen from air. Since nitrogen measurements were not reproducible, they were not used in this thesis.

The sample was measured by combustion in a 1200°C chamber under helium (234 ml min^{-1}) and oxygen (35-38 ml min^{-1}) atmosphere over a WO_3 catalyst. The produced SO_2 was detected by an infrared detector. The instrument was calibrated using a sulfanilamide standard for the range of 0.005 to 0.03 mg sulfur per sample.

4.7.5 Ion chromatography

Ion chromatography was used for the quantification of the anions fluoride, chloride, nitrate, phosphate and sulfate. The instrument used was an HPLC Summit system (*Dionex*) equipped with a Metrosep A Supp 5 analytical anion separation column (*Metrohm*) and an ASRS 300 anion suppressor (*Dionex*). An ED 50 electrochemical detector was used in the conductivity mode. The mobile phase was a mixture of 1 mmol l^{-1} $NaHCO_3$ and 3.2 mmol l^{-1} Na_2CO_3. The flow rate of the mobile phase was 0.7 ml min^{-1} at a column backpressure of 12 MPa. A sample volume of 20 µl was injected per run. Each sample was injected three times. Samples were filtered over PTFE syringe filters (pore size 0.45 µm) prior to measurement. Calibration was done with standard solutions of the respective ions in a concentration range of 2-250 mg l^{-1}.

4.7.6 X-ray diffraction (XRD)

The X-ray diffraction patterns of catalyst and support material samples were measured by a powder diffractometer. Two different instruments were used, an Empyrean (*PANalytical*) and an X`Pert MPD/DY636 (*Philips*), both equipped with a Cu Kα radiation source (λ=1.54 Å). The samples were dried in a vacuum oven at 80°C and 10 kPa and finely milled by a mortar prior to measurement. The minimum crystal size that can be detected is 5 nm. The measurements on the *Philips* instrument were done by Alwin Frei (PSI) and on the *PANalytical* instrument by Thanh-Binh Truong (PSI).

4.7.7 Scanning Electron Microscopy (SEM) and Energy Dispersive X-ray spectroscopy (EDX)

The visual appearance and the elemental composition on the surface of catalyst samples were examined using a scanning electron microscope, Ultra 55 (*Zeiss*) with energy dispersive X-ray spectroscopy. The samples were dried in a vacuum oven at 80°C and 10 kPa prior to measurement. The measurements were carried out at an accelerating voltage of 7 to 20 kV. In some cases the conductivity of the samples was not sufficient; those samples were sputtered with a noble-metal layer (Au/Pd, 80/20% wt) by an EM SCD500 (*Leica*) instrument for ca. 60 s at 10^{-5} MPa and 47 mA. An In-lense detector for secondary electrons was used for the topographical characterization of the surface. For the visualization of heavy atoms such as ruthenium, rhenium and corrosion products, a back-scattering electron detector was used. The measurements were done by Erich De Boni (PSI).

4.7.8 Gas sorption methods

For the determination of the total surface area and the active metal surface area, gas sorption methods were applied. The total surface area was determined via nitrogen physisorption. Hydrogen chemisorption was used to determine the surface area of the active metal. Both measurements were done using a *Quantachrome* Autorsorb AS1 instrument.

4.7.8.1 Nitrogen physisorption

The mass of the sample for nitrogen physisorption was chosen in order to obtain an estimated sample surface area between 1 and 10 m^2. Before any measurement, the sample was outgassed at the outgasser port of the instrument at 300°C until the outgassing test was passed. The sample was then transferred to the measurement port. The adsorption measurement was carried out at a temperature of -196°C, the boiling point of liquid nitrogen at ambient pressure. For microporous samples such as 2% Ru/C, the adsorption and desorption points were measured for the range of $10^{-6} \leq p\ p_0^{-1} \leq 1$ with p being the equilibrium pressure in the sample cell at a certain gas dose and p_0 the corresponding vapor pressure of liquid nitrogen as measured in the reference cell. The range for mesoporous samples such as ceramic support materials was $5 \cdot 10^{-2} \leq p\ p_0^{-1} \leq 1$.

The specific surface area was calculated using the BET equation [164] and will be referred to as BET surface area (BET SA) in the following. For the calculation, only adsorption points within the linear region of the linearized isotherm were used, i.e. $0.01 \leq p\ p_0^{-1} \leq 0.03$ for microporous samples and $0.05 \leq p\ p_0^{-1} \leq 0.35$ for mesoporous samples.

4.7.8.2 Hydrogen chemisorption

The mass of the sample for hydrogen chemisorption was chosen in order to obtain an estimated metal surface area of approximately 1 m^2. The sample amount was however limited by the size of the flow-through cell. Before any measurement, the sample was pretreated in place. The pretreatment included evacuation for 30 min, heat-up at 20 K min^{-1} for drying and outgassing under helium at 120°C for 30 min, then heat-up at 5 K min^{-1} under hydrogen and hold at 350°C for 120 min for reduction of the metal. Afterwards, the cell was evacuated again for 120 min. The measurement was carried out at 40°C. The first isotherm is a combination of weakly and strongly adsorbed hydrogen. In order to obtain the isotherm of the strongly adsorbed species alone, a second isotherm was measured after evacuation of the cell, which was then subtracted from the first one. The second isotherm represents the weak adsorption.
Generally, the measurement of both isotherms was carried out at a pressure range of 10-800 mmHg. For each point, an equilibration time of 15 min was set.

The monolayer uptake of hydrogen $n_{H_2}^m$ was calculated by linear extrapolation of v(p) for the measured data points with the slope $v \cdot p^{-1}$ for $v_{H_2}^m(p=0)$ with

$$v(p) = V_{H_2} \cdot M_{sample} \qquad \textbf{(4-7)}$$

The extrapolation was applied to the pressure range of 240-560 mmHg, in which the slope was relatively linear.

The metal surface area was calculated following Equation 4-8 with X_m being the adsorption stoichiometry of hydrogen for which 2 was used. N_A is the Avogadro

number and A_{Ru} the surface area which is occupied by one ruthenium atom (8.17 Å^2, [165].

$$MSA = X_m \cdot n_{H_2}^m \cdot N_A \cdot A_{Ru} \qquad \textbf{(4-8)}$$

The stoichiometry for hydrogen chemisorption may diverge from the assumed value of 2 in the case of metal crystallites smaller than 2 nm [166]. In this case, the stoichiometry is reported to exceed this number. This means that the metal surface area of small crystallites might be overestimated. In the case of surface area loss due to particle growth, this would also result in an overestimation of the surface area loss. Since we are basically interested in the question, whether there is a significant loss in surface area or not, the qualitative or semi-quantitative results as gained from hydrogen chemisorption provide a satisfactory level of information.

The metal dispersion was calculated following Equation 4-9:

$$D = \frac{n_{Ru,s}}{n_{Ru}} = \frac{n_{H_2}^m \cdot X_m \cdot M_{sample}}{n_{Ru}} \quad \textbf{with} \quad n_{Ru} = \frac{x_{Ru} \cdot M_{Sample}}{M_{Ru}} \qquad \textbf{(4-9)}$$

$n_{Ru,s}$ is the number of exposed surface ruthenium atoms.

4.7.9 Thermogravimetry

A further method used for catalyst characterization was thermogravimetry coupled with infrared spectroscopy (TG-IR). Two methods were applied, for identification of coke deposits on catalyst grains on the one hand and for the determination of a material's acidity by ammonia desorption on the other hand.

4.7.9.1 Temperature programmed oxidization

For qualitative identification of coke deposits on catalyst samples based on ceramic support after gasification experiments, temperature programmed oxidation (TPO) was done using a *Netzsch* STA 449C Jupiter thermogravimeter with a *Bruker* TGA-IR Tensor 27 (FTIR). 80 mg of a sample were placed in a quartz crucible which was then placed on the micro balance. The heating program is listed in Table 4-6. The measurement was performed under a 10 ml min^{-1} argon flow which was changed to

a 10 ml min^{-1} oxygen flow shortly before the heating ramp R4. The measurements were done by Franziska Mayr (PSI).

Table 4-6: Temperature program of TPO measurements

Ramp	Temperature [℃]	Heating rate [K min^{-1}]	Hold time [min]
R1	105	10	10
R2	480	10	30
R3	750	10	120
R4	900	10	30

4.7.9.2 Ammonia desorption

The acidity of catalyst support materials was determined by ammonia desorption measurements performed on a redesigned TG-FTIR (TGA/DSC1, *Mettler Toledo*) instrument [167]. The measurement was done in a nitrogen stream at a flow rate of 100 ml min^{-1}. The temperature program is listed in Table 4-7. In a first heating ramp the sample was outgassed (R1). Then, 1000 ppm of ammonia were dosed at 100°C for 120 min (R2). After a flushing period of 80 min at 100°C, ammonia was desorbed in a further heating ramp at 10 K min^{-1} (R3). The measurement was done by Max Mehring (PSI).

Table 4-7: Temperature program for ammonia desorption measurements.

Ramp	Temperature [℃]	Heating rate [K min^{-1}]	Hold time [min]
	50	-	10
R1	550	10	120
R2	100	10	200
R3	550	10	30
R4	50	10	30

4.7.10 ICP-OES

ICP-OES was used for quantitative determination of elemental composition. For the elemental composition of fermentation residue, the digested and diluted samples

(see section 4.1.2) were measured using a Cirros ICP-OES device (Spectro). The samples were diluted by a factor of 100 in order to gain concentrations within the calibrated range. The instrument was calibrated by a commercial multielement standard, purchased from *Merck*.

The mass balance for the active materials ruthenium and rhenium (see section 4.2.2.3) was calculated based on ICP-OES measurements of the fresh impregnation solution and the redissolved residue from the flask. For this measurement a Liberty 110 ICP-OES spectrometer (Varian) with argon as carrier gas was used.

4.7.11 Equilibrium calculations

The thermodynamic equilibria of the reaction products were calculated with the software Aspen Plus, being the gas and water composition with the minimum free Gibbs energy. The calculations were performed by F. Vogel and S. Viereck.

4.7.12 Error estimation

For the estimation of the reproducibility of the batch experiments, two single experiments were performed twice, once for the experiments with catalyst and once for the heat-up experiments. The difference of the recovered carbon and sulfur for each phase has been calculated and is listed in Table 4-8.

Table 4-8: Distance between upper and lower value for carbon and sulfur recovery in product phases in a reproducibility test.

Carbon	Gasification [mg g^{-1}(Feed-C)]	Liquefaction [mg g^{-1}(Feed-C)]	Sulfur	Liquefaction [mg g^{-1}(Feed-S)]
Gas	25.4	39.8		
Water (TIC)	2.8	46.2		
Water (TOC)	8.2	11.7	Water	100.4
Methanol	2.3	21.8	Methanol	1.9
Hexane	0.3	10.5	Hexane	10.6
Solid	1.5	32.5	Solid	47.3

For the continuous gasification experiments in the test rig Konti-1, an error of ±10% for the quantification of gaseous products was estimated. The estimated error included the fact that the temperature of the product gas varied during an experiment, depending on the flow rate and the temperature of the cold trap. At different gas flow rates, the residence time in the cold trap varied.

For the continuous gasification experiments with fermentation residue in the test rig Konti-2, no error was estimated. The large dead volume of the rig compared with the relatively short run time of an experiment did not allow a proper quantification of products and the calculation of mass balances. Therefore, the results of the Konti-2 experiments are only semi-quantitative.

5 Results

5.1 Compositional analysis of the fermentation residue

(Parts of this chapter are published in [168])

The composition of the fermentation residue varies because of seasonal changes in the feed and depends on the point of withdrawal from the biogas plant (see section 4.1.1). In a two-stage fermentation plant, as it was used in our case, two generally different types of fermentation residues accumulate. In the first stage, particles with a high density settle at the bottom of the fermenter. In the second stage, a liquid "overflow" stream is continuously removed from the fermenter. Both types of fermentation residues were used for the experiments. We refer to the respective samples as "overflow type" and "sediment type". A picture of both types is shown in Figure 5-1.

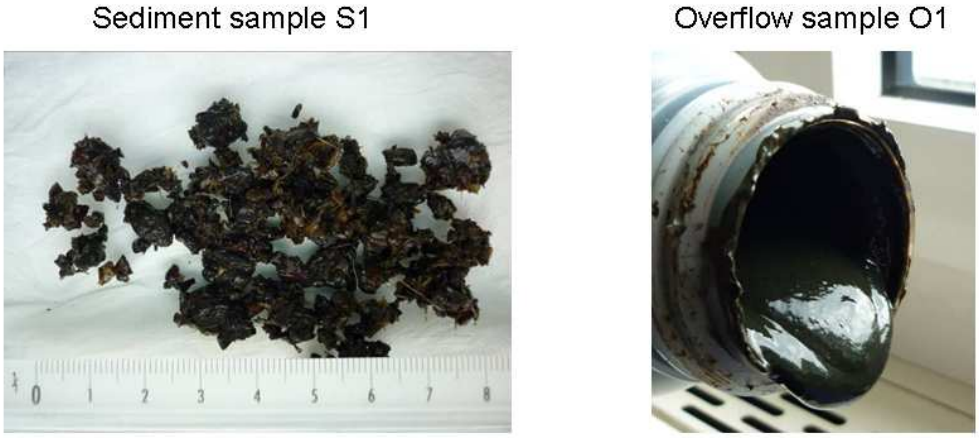

Figure 5-1: Picture of a typical sediment and overflow sample.

The content of minerals, determined as the residue on ignition, is high for the overflow type (up to 300 mg g^{-1} of the dry matter), compared to the sediment type (< 30 mg g^{-1}), as can be seen in Table 5-1. The water content of the overflow type is high (> 800 mg g^{-1}) and relatively low for the sediment type (ca. 500 mg g^{-1}).
Regarding the elemental composition, it can be seen that the heteroatoms N, P and S, which are expected to be mostly organically bound, occur preferentially in the overflow type while their amount in the sediment type is low. However, a high content of sulfur species will have a detrimental effect on the catalyst. On the other

hand, alkali salts have been reported to have a positive influence on biomass degradation (see section 3.6.5).

Table 5-1: Compositional analysis of fermentation residue samples. O = overflow type, S = sediment type, DM = dry matter, LOI = loss on ignition, n/a = not analyzed.
*** white precipitate after dilution of digested samples; values may be underestimated**
**** sample O5 was analyzed after pretreatment (dilution, sieving, supplementation)**

		O1	O2	O3	O4	O5**	O6	S1	S2
DM	mg g^{-1} a.r.	87	58	78	63	48	67	560	413
LOI	mg g^{-1} dry	687	732	741	740	724	724	976	976
C	mg g^{-1} dry	355	343	366	403	396	378	500	495
H	mg g^{-1} dry	50	45	50	50	53	54	61	61
O	mg g^{-1} dry	271	284	390	327	302	294	399	417
N	mg g^{-1} dry	45	49	50	45	42	38	4	2
S	mg g^{-1} dry	11	11	12	10	16	9	1	6
P	mg g^{-1} dry	24	12	17	10*	6*	7*	1	5
Cl	mg g^{-1} dry	50	41	n/a	n/a	n/a	n/a	11	12
Na	mg g^{-1} dry	1	30	0	4*	2*	0.4	n/a	n/a
Ca	mg g^{-1} dry	38	24	26	11*	18*	10*	n/a	n/a
K	mg g^{-1} dry	19	64	34	2*	8*	7*	n/a	n/a
B	mg g^{-1} dry	0	0	0	2*	2*	1*	n/a	n/a
Mg	mg g^{-1} dry	3	3	2	3*	4*	2*	n/a	n/a
Al	mg g^{-1} dry	11	3	5	2*	2*	0*	n/a	n/a
Fe	mg g^{-1} dry	12	10	11	7*	12*	7*	n/a	n/a
Si	mg g^{-1} dry	10	6	7	6*	5*	12*	n/a	n/a

In Figure 5-2, the composition regarding macromolecules of different fermentation residue samples is depicted. The sediment type consists mainly of cellulose (acid soluble), hemicellulose (acid detergent soluble) and lignin (acid insoluble), similar to wood. The overflow type contains a fraction of almost 300 mg g^{-1} of the dry matter consisting of substances soluble in a neutral detergent solution. This fraction corresponds mainly to minerals, plus small organic molecules such as sugars, amino

acids, soluble proteins and lipids. Note that organic molecules are not only degraded during fermentation, but also produced by assimilatory pathways of the bacterial culture. It is therefore not surprising to find molecules not belonging to the group of ligno-cellulose. Proteins are generally rich in nitrogen (amino groups) and sulfur (mercaptane). Amino acids can react with monosaccharides from cellulose decomposition to form Maillard products (see section 3.4.3.2). Thus, proteins can lead to a reduced gas production [81]. Amino groups can furthermore react by deamination to form ammonia. This may compensate a drop in pH resulting from organic acid intermediates (see section 3.4.3.2) and thus prevent coke formation. An acidic pH is reported to promote coke formation (see section 3.6.5). However, ammonioum salts can not be recovered by salt separation (see section 3.4.2.2).

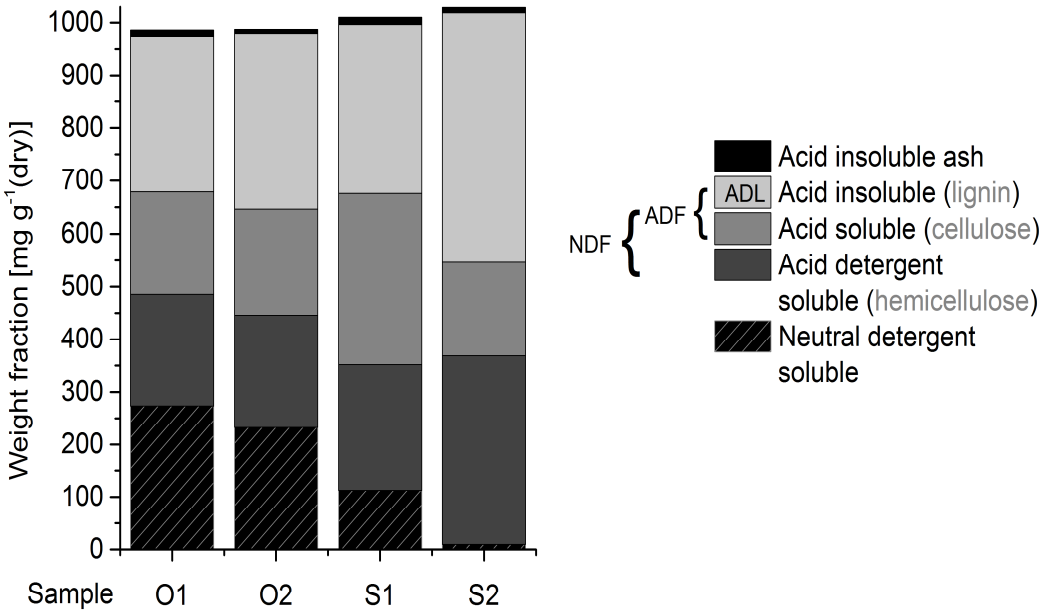

Figure 5-2: Composition of macromolecules of fermentation residue samples; O = overflow type, S = sediment type. For NDF, ADF, ADL see section 4.1.3)

For both types of fermentation residue the amount of lignin is considerable. Lignin-rich feedstocks have been gasified by other groups and have led to tar formation (see section 3.5.3). However, catalytic gasification of wood has successfully been performed in a batch reactor [169].

5.2 Some considerations and experiments on the validity of results gained from a batch system

(Parts of this chapter are published in [168])

5.2.1 Introduction

Even though the conditions in a batch system can never fully represent those of a continuous system for different reasons, we can gain useful information based on comparative studies. Generally, the potential limitations of our batch system include i) the lack of active mixing, which might be important when dealing with biomass containing insolubles, ii) the presence of a cold zone connecting the reactor and the monitoring section, and iii) the impossibility of keeping the system at isobaric conditions during heat-up. Additionally, the presence of a catalyst may affect the mass balance of products. In the following sections, these limitations will be shortly discussed and, if available, evaluated based on experimental data. A list of all batch experiments can be found in Table Appendix B.

5.2.2 Experiments on the influence of mixing

In contrast to a continuous system where a forced convection is accomplished by the biomass flow, only diffusion and free convection are driving forces for mass transport in an unstirred batch reactor. The influence of forced agitation was tested by a gasification experiment. Small reactors were used having the same geometry as the reactors used for the batch experiments but without a monitoring and gas collection section (see 4.3.4). Two reactors were immerged simultaneously into the sand bath, one in horizontal and the other in vertical position. The reactor in horizontal position was shaken manually during the reaction time. All other parameters were kept the same for both reactors. The amount of unconverted carbon within the reaction time interval was used as a relative indicator for the conversion rate. In Figure 5-3 the unconverted carbon in the product phases is shown for gasification experiments with 2% Ru/ZrO_2 (DKKK) where the residence time was identical for both reactors, with a slightly longer reaction time for the vertical reactor. No significant difference in conversion could be found for the agitated and the non-agitated system. Figure 5-4 shows the unconverted carbon for gasification over 2% Ru/C where the reaction time was identical for a pair with shorter residence times

for the vertical reactors. A higher level of conversion was found with the 2% Ru/C catalyst. In these experiments, a slightly higher conversion can be found for the agitated reactor. This may result from higher heat-up rate for the horizontal reactor. The difference is not striking, however.

Generally, the reproducibility of the experiments was poor because some spill of reaction products could not be avoided while opening the pressurized reactor. Additionally, the impact of small losses or contaminations contributes strongly to the carbon balance of a small system.

The influence of the reaction time and residence time, respectively, can hardly be compared between different pairs of experiments, because the heat-up rate of the experiments differed according to the exact position in the sand bath and the flow rate of air, which was hardly reproducible. Within a pair of experiments this was better reproducible because both reactors were immerged together.

Since a significant impact of agitation on the conversion cannot be found, we conclude that the free convective motion during heat-up is sufficient to maintain a properly mixed system.

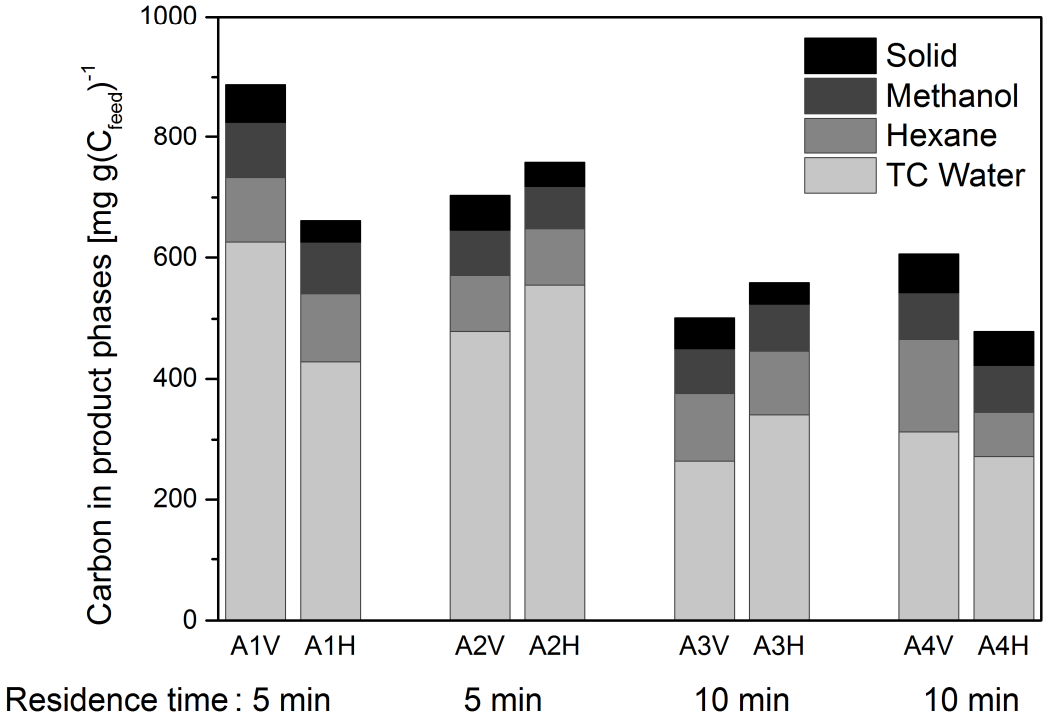

Figure 5-3: Distribution of feed carbon over the liquid and solid product phases after gasification of fermentation residue O3 a.r. over 2% Ru/ZrO_2 (DKKK) in a mini-batch reactor. Each pair was in the sand bath simultaneously. V = vertical and static, H = horizontal and agitated.

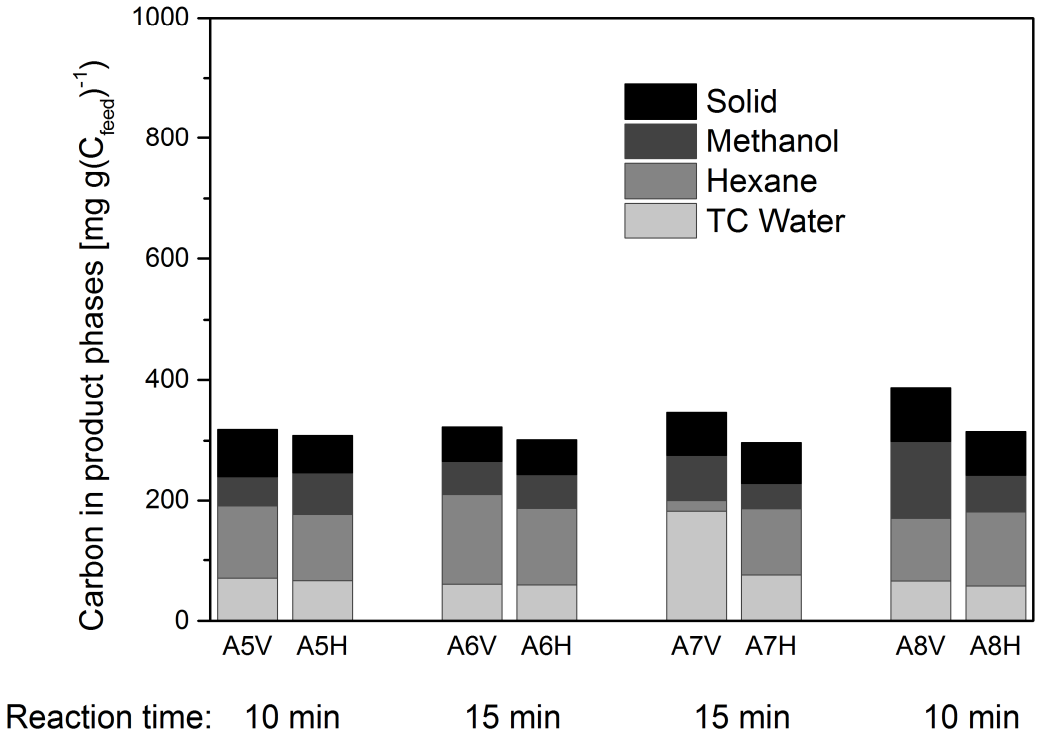

Figure 5-4: Distribution of feed carbon over the liquid and solid product phases after gasification of dry fermentation residue O1 with water added over 2% Ru/C in a mini-batch reactor. Each pair was in the sand bath simultaneously. V = vertical and static, H = horizontal and agitated.

5.2.3 Influence of the cold zone

The monitoring section of the batch reactor system is part of the reaction volume but is not heated. This zone is expected to have some influence on the reaction. The exact extent of this influence could not be determined because this test would require gasification experiments in the presence and absence of a cold zone under equal conditions, i.e. pressure, temperature, residence time etc. Since neither pressure nor gas composition could be determined with simple batch reactors lacking a monitoring section, a direct comparison was not possible. However, departure from the expected equilibrium gas composition and, to a lesser extent, incomplete conversion even at long reaction times have been observed in many experiments (see chapter 5.3) and can be attributed to the cold zone: Gases and possibly organic vapors "trapped" in the cold zone would hardly diffuse back into the hot reaction zone and thus undergo no further reaction.

This effect has been qualitatively tested and visualized in a set of experiments shown in the following. Gaseous compounds have been used as feed, because here the focus has been laid on the behavior of gases within a reaction chamber with a cold zone.

The gas mixture (for composition see G6 in Table Appendix B) was exposed to supercritical water conditions with varying reaction times in the presence of a 2% Ru/C catalyst. The gas composition was expected to approximate the calculated equilibrium gas composition for increasing reaction times. The result of this experiment was almost no change from the original composition even at a long reaction time of 90 min as shown in Figure 5-5.

The quasi absence of reaction among the gas components led to the assumption that no contact with the catalyst took place. Therefore, in the next experiment the catalyst was located in an elevated position by a "cage" made of a wire mesh. The results of the experiments with this new setup showed a clear shift of the gas composition towards the calculated equilibrium (see Figure 5-6). Still, after 60 min of reaction time the equilibrium was not reached. A leveling in the gas composition change is visible between 30 and 60 min. This observation supports our assumption of gases being trapped in the cold zone. The mass transport from the cold zone back into the reaction zone becomes the limiting factor in reaching the calculated equilibrium composition.

The results of this experiment provide even more information: A complete mixing of argon and the product gases with supercritical water is not given in this case. In literature complete miscibility of many gases with supercritical water has been reported [14, 20, 22]. Small quantities of gases may dissolve in the supercritical fluid. In the presence of large amounts of gases, as it was the case in this experiment, presumably a two phase system exists of which one is the gas phase and the other the supercritical water phase.

With the knowledge gained from these experiments, we would expect nearly no methane production for gasification of fermentation residue in a batch system, since the catalyst was never fixed in the superior part of the reactor for these experiments. The fact that we indeed observe the formation of methane (see chapter 5.3) is a hint that those reactions occur very rapidly within the denser water phase and on the catalyst surface, directly after the decomposition of the organic biomass constituents. Once a component has diffused into the gas phase, further reaction may become unlikely.

Biomass gasification was described by a set of reactions (see section 3.4.3.3), i.e. the production of CO and H_2 by the steam reforming reaction and the gasification reaction to produce CH_4 and H_2O from the gases. The presented experiments suggest

that these reactions occur in very rapid succession, since CO and H_2 would otherwise diffuse into the gas phase and not further react to CH_4. It is furthermore likely that only one reaction is taking place on the catalyst that includes both steps.

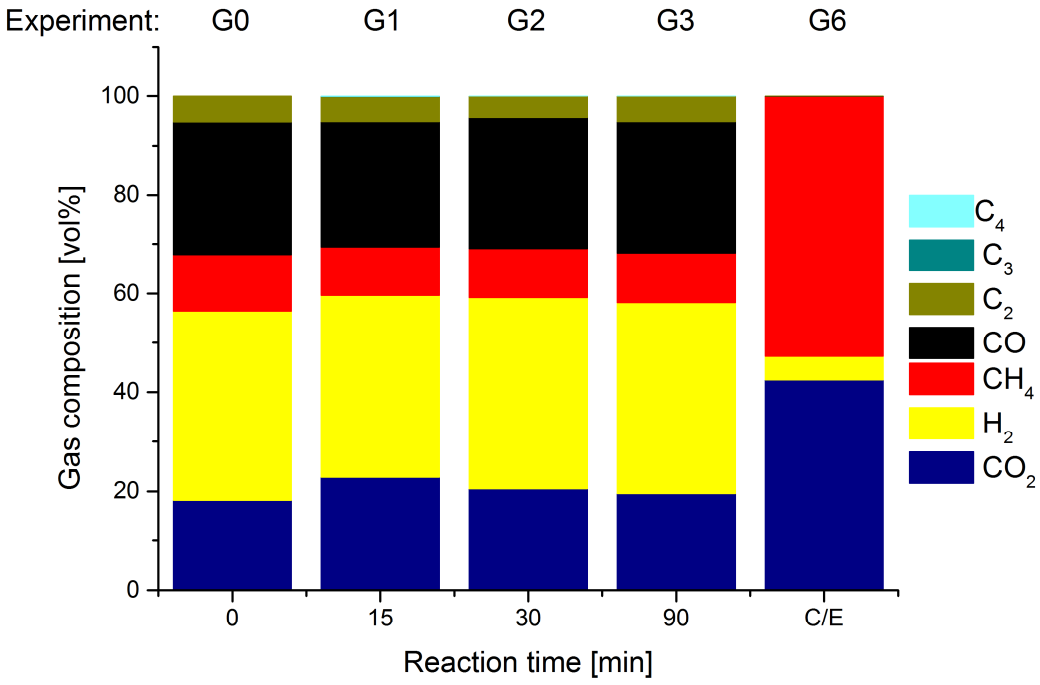

Figure 5-5: Change in gas composition after exposure to supercritical water conditions for various reaction times in the presence of a 2% Ru/C catalyst on the bottom of the reactor. C/E = calculated equilibrium for the respective gas composition.

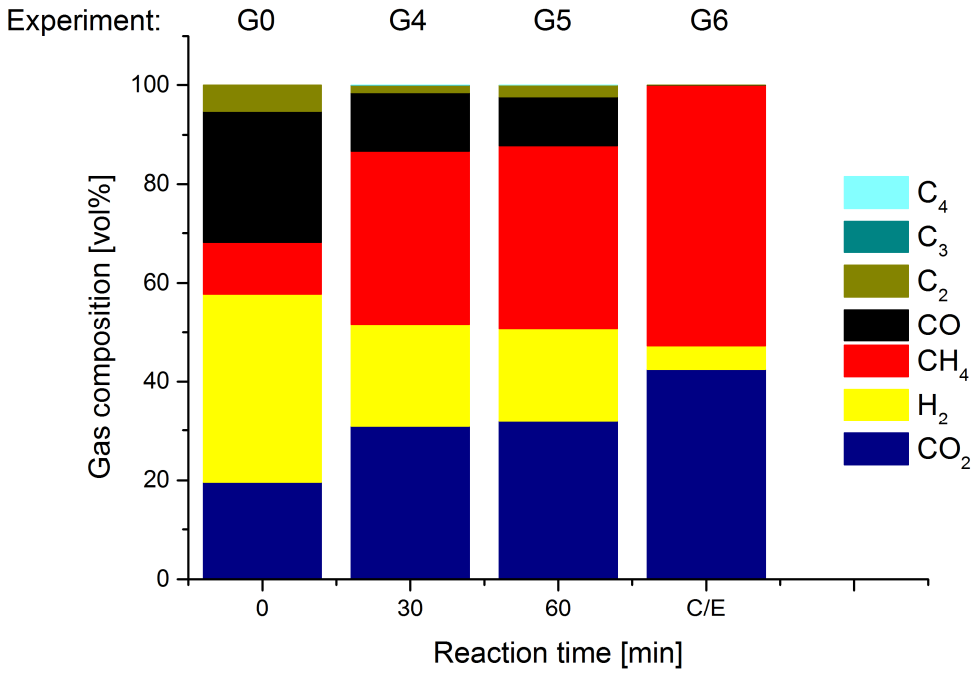

Figure 5-6: Change in gas composition after exposure to supercritical water conditions for various reaction times in the presence of a 2% Ru/C catalyst fixed in the middle of the reactor. C/E = calculated equilibrium for the respective gas composition.

5.2.4 Influence of non-isobaric conditions

The non-isobaric heat-up phase is a characteristic feature of most batch systems, which can only be avoided by a variable-volume reactor system. Increased coke formation may be a result of passing the vapor phase during heat-up.

Pre-pressurization of the reactor with argon has been an attempt to avoid the formation of a vapor phase. However, experiments have shown no significant differences in the product composition between experiments with and without argon (see Figure 5-7). In addition, the influence of a gas phase occupying a considerable part of the reactor volume cannot be predicted as already mentioned in the previous section. Solubility data of gases in supercritical water as well as vapor pressure data of water are available for mixtures of very few, clearly defined components; however, a multi-component mixture such as the fermentation residue may behave differently and thus the presence of a gas phase may influence the phase behavior of water. Therefore, an unknown influence either by passing the vapor phase or by the presence of large amounts of gases has to be considered in discussing the results of batch experiments.

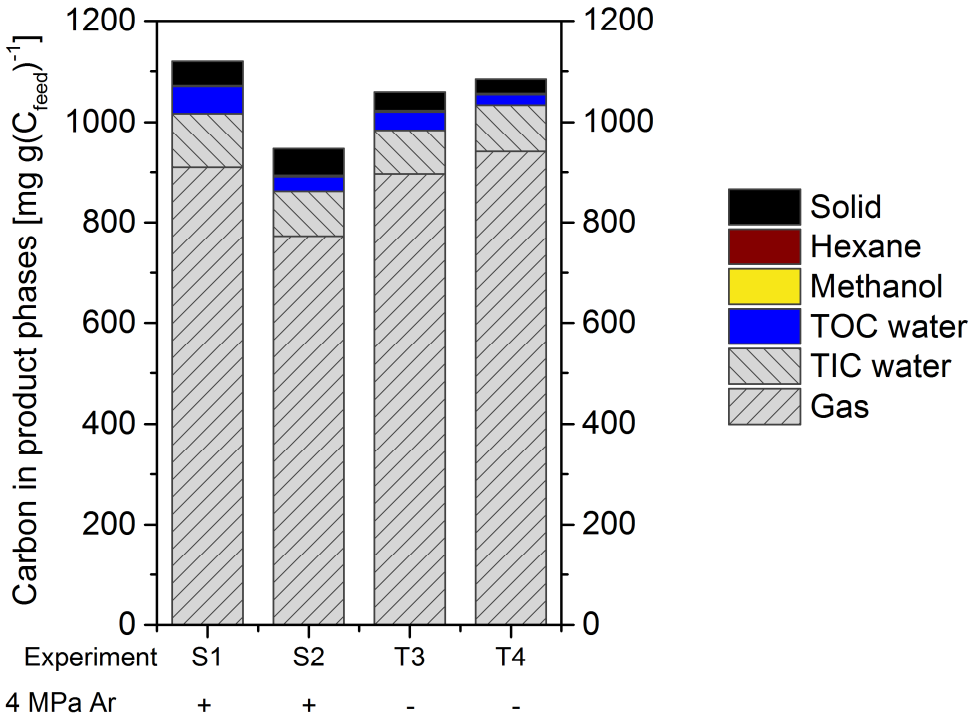

Figure 5-7: Comparison of experiments with and without pre-pressurization with argon. All other parameters were similar.

Despite of these limitations, the batch system is a useful tool to give a first assessment of the general suitability of this complex feedstock for hydrothermal gasification with a reasonable effort and to find optimum conditions that later need to be verified in a continuous system.

5.2.5 Influence of the carbon support on the carbon balance

In the experiments with carbon-supported catalyst, attrition, and self-gasification of the support may lead to an overestimation of carbon found in the product phases. We therefore tested the self-degradation of the catalyst in an experiment without biomass and found only CO_2 in the gas phase as well as fine carbon dust in the solid phase. The CO_2 is very likely a product of decarboxylation or decarbonylation of surface groups of the support or from desorption of adsorbed CO_2. No organic carbon was found in the water, hexane and methanol phase. The total amount of carbon found in the gas- and solid phase corresponded to 20 mg g^{-1} catalyst. For an experiment with an extremely low biomass : catalyst ratio, this corresponds to approximately 400 mg g^{-1} of the total feed carbon (experiment C3, discussed in section 5.3.5) and less than 100 mg g^{-1} for those with extremely high biomass : catalyst ratios (experiment S4, discussed in section 5.3.4). We can, however, not simply transfer the results found in a biomass free environment to the gasification experiments. In experiments with a low biomass : catalyst ratio, we found no more than 150 mg g^{-1} carbon-overestimation (experiment S1, discussed in section 5.3.4). In this case, as in all other cases with high gasification efficiency, we can exclude a significant extent of carbon deposits on the catalyst grains since only traces of tars were produced.

5.3 Liquefaction and gasification experiments of fermentation residues in a batch reactor setup

(Parts of this chapter are published in [168].)

5.3.1 Introduction

Parametric experiments were performed in a batch reactor system in order to screen for the optimum conditions with regard to a future test in a continuous gasification system. The influence of different parameters was tested independently. Some of the

experimental conditions were chosen to simulate the preheating section of the continuous process, i.e. by applying subcritical temperatures with no catalyst present. Other experiments corresponded to the conditions prevailing in the salt separator and the catalytic reactor, respectively. Regarding the preheater, the coke formation tendency of the feedstock and the influence of different alkali compounds on it were studied. Alkali additives have been reported to reduce coke formation (see section 3.6.5). Regarding the salt separator, we focused on the separation of biomass-bound sulfur. Sulfur is known to have a poisoning effect on the catalyst and therefore needs to be separated before the catalytic reactor in a continuous system (see section 3.7.3). For the reactor, two different supported ruthenium catalysts were tested, and the reaction temperature was varied. The influence of reaction time at supercritical conditions was also investigated. This parameter cannot be transferred directly to a continuous system because of the different hydrodynamic situation. By monitoring the time dependent pressure changes, the effective reaction time was determined. Using this effective reaction time, a proposal was made for correlating the reactivity in the batch system to the expected one in a continuous fixed-bed system. Ruthenium was used as catalyst because it has a good activity and selectivity towards methane production as well as a good stability in the hydrothermal environment (see section 3.6.2).

This series of batch experiments was designed to answer the following questions:

- Is a hydrothermal liquefaction of fermentation residue possible?
- Is organically bound sulfur mineralized during liquefaction?
- Do alkali salts improve the liquefaction and the mineralization of sulfur?
- How high is the catalyst deactivation potential?
- Which catalyst system shows the best conversion of fermentation residue to gases?
- Which is the minimum temperature to yield full conversion?
- How long is the minimum residence time for full conversion at a given catalyst loading?

A list of all batch experiments can be found in Table Appendix B.

5.3.2 Liquefaction: Effect of alkali compounds on coke formation

In any continuous system, the biomass experiences subcritical conditions during heat-up. Coke formation occurs preferentially under these conditions [19]. Assessing the coke formation tendency of the fermentation residue with the goal to avoid it is therefore an important issue. In a series of batch experiments, the heat-up phase in a continuous process was simulated in an exaggerated way by immersing the reactor into the sand bath preheated to 200°C and increasing the temperature up to 410°C with an average heating rate of 4 K min^{-1}. Corresponding to the conditions in the preheater, no catalyst was used in these experiments. Different alkali compounds were added to test for any possible effect on coke avoidance by buffering the pH value. An acidic environment has been reported to promote coke formation by enhancing the dehydration reaction [19, 129, 130].

Fermentation residues of the overflow type (O3 and O4) and the sediment type (S1) were used in these experiments. The distribution of carbon over the product phases for the untreated fermentation residue as received and after reaction is shown in Figure 5-8. H6, H9 and H12 represent the untreated fermentation residues of O3, O4 and S1, respectively.

The results show a strong transformation of carbon bound in the solid phase to soluble carbon compounds, even without additives. This effect is more pronounced for the samples of the overflow type (H1-H5, H7-H8) than for the sediment type (H10, H11). For the overflow type, the additives improved the conversion to liquid products only marginally. Neither was the gas production affected by the additives. We attribute this observation to the minerals (high in potassium and calcium) that are naturally present in the biomass. The amount of salts and the released ammonia were sufficient to buffer the produced organic acids, avoiding the usual drop in pH during the reaction. For the fermentation residue of the sediment type, however, we found a significant improvement of the carbon conversion and a strong reduction of coke formation in the presence of K_2CO_3 (60 mg g^{-1} of the dry matter), an amount that was chosen to yield a potassium concentration equivalent to the overflow type fermentation residue. This observation fits well with the content in minerals of the feedstock. The pH of the water-soluble product phase was 4 for the experiment without additive (H10) and 6 for the experiment with K_2CO_3 supplement (H11). In contrast, it was around 8 to 9 for the experiments with the overflow type (H1-H5, H7-H8). Therefore, even more K_2CO_3 would be necessary to avoid an acidic pH.

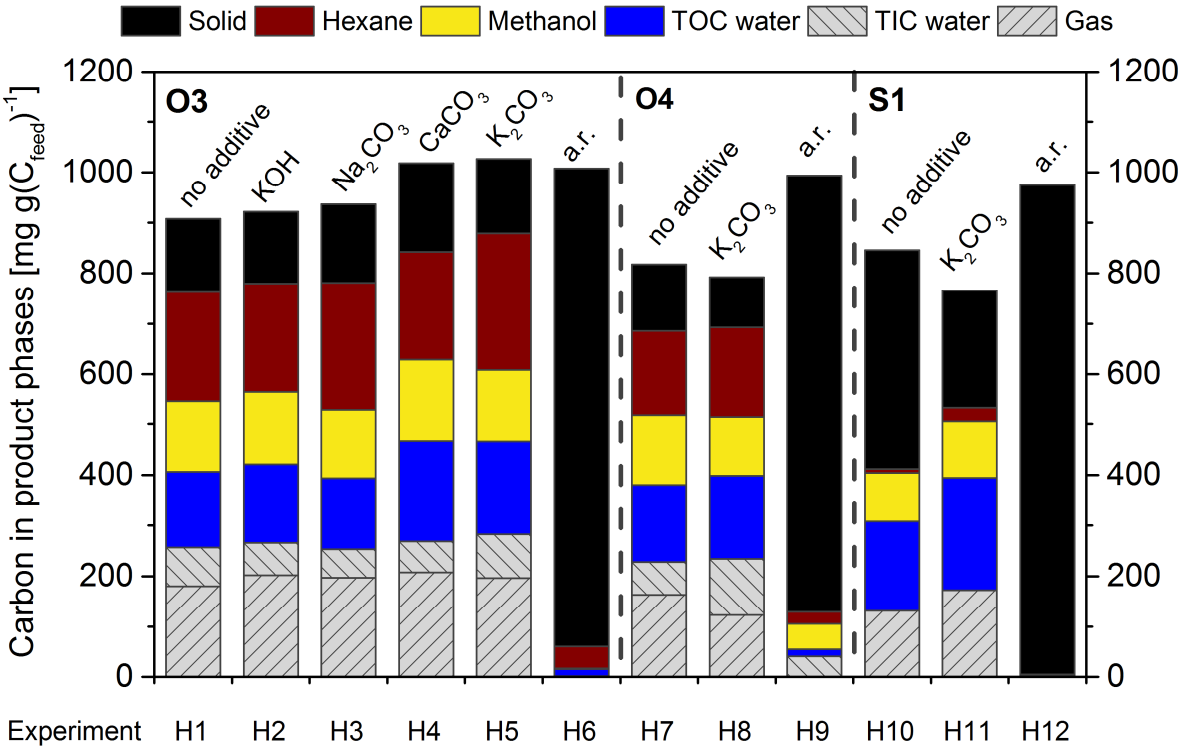

Figure 5-8: Carbon distribution for the extracted product phases of heat-up experiments (no catalyst present) with different samples of fermentation residue, overflow type (O3 and O4) and sediment type (S1). The reactant was supplemented with different alkali compounds. H6, H9 and H12 represent the untreated fermentation residues of O3, O4 and S1, respectively.

A growth of particles could not be observed for the overflow type of fermentation residue. As can be seen in Figure 5-9, the solid residue after liquefaction (H7) is homogeneous and fine-grained. For the sediment type (H10), coke particles of a size similar to the feed appeared. The coke from the experiment with K_2CO_3 supplement (H11) contained fewer grains.

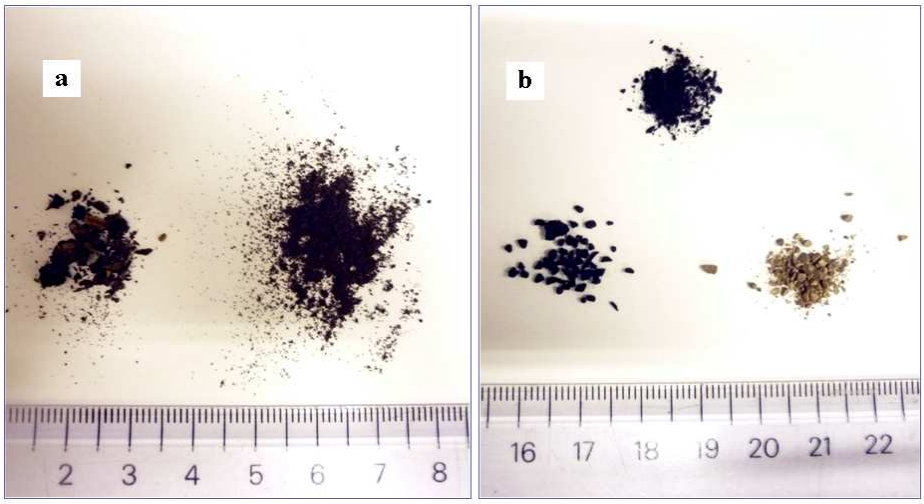

Figure 5-9: a) Dried fermentation residue O3 (left), solid product phase after heat-up experiment (right); b) dried fermentation residue, S1 (right), solid product phase after heat-up experiment without additives (left) and with supplement of K_2CO_3 (top).

5.3.3 Liquefaction: Distribution of sulfur in products

Maintaining high activity of the catalyst over a long period is of highest importance for a continuous process. However, many possibilities of catalyst deactivation by biomass components exist. The three most expected ones are:

- Poisoning of the active ruthenium surface by sulfur
- Fouling of the whole catalyst surface by precipitated salts and other minerals
- Coverage of the ruthenium surface by coke

The sulfur contained in the biomass feedstock presents the most serious cause for catalyst deactivation. With an amount of 10 mg g^{-1} of the dry matter of the overflow type fermentation residue, the impact on the catalyst activity is expected to be considerable.

In the PSI process, most salts and other minerals are removed from the liquefied biomass by a salt separator prior to entering the reactor. In plant biomass, however, a major fraction of sulfur is incorporated into the organic matter. It is predominantly present as thiols, sulfides and disulfides within proteins and peptides [135]. During anaerobic fermentation, a certain amount of organically bound sulfur may have been converted to H_2S by microbial dissimilative reduction or oxidized to sulfate.

However, the experimentally determined sulfate-sulfur to total sulfur molar ratio of 100 - 1000 µmol mol^{-1} for the overflow type fermentation residues indicates that sulfate-S is only a minor amount.

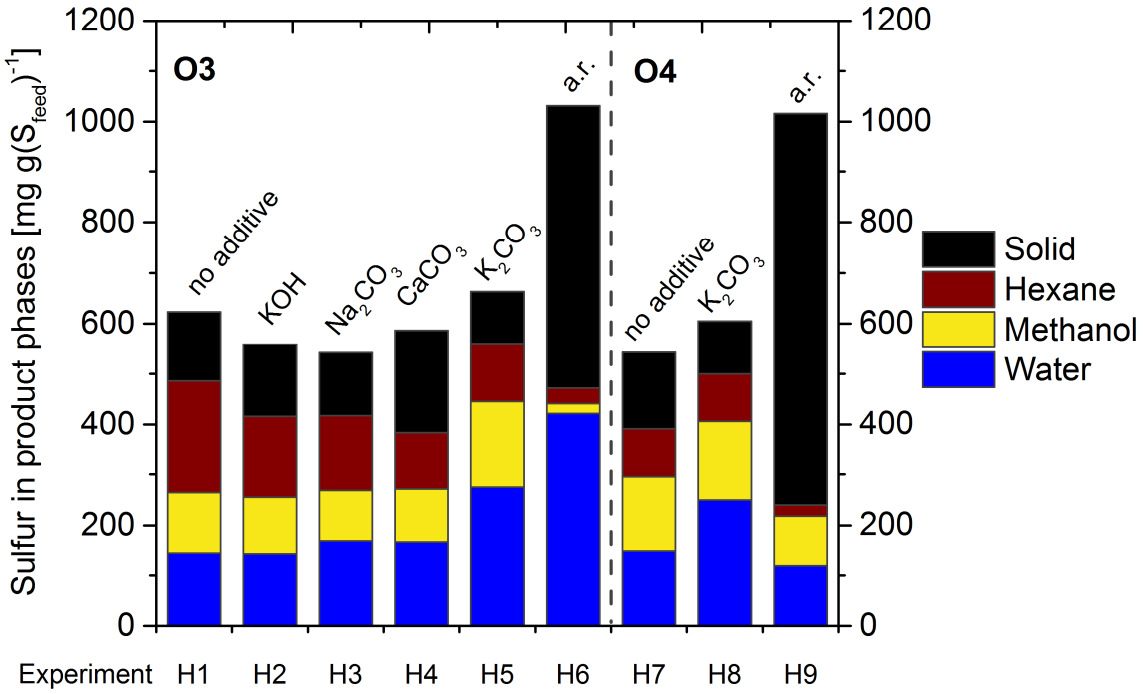

Figure 5-10: Sulfur distribution over product phases of heat-up experiments with different samples of fermentation residue, overflow type (O3 and O4). The gas phase was not analyzed. The reactant was supplemented with different alkali compounds.

The fate of sulfur in the biomass during heat-up was studied by analyzing the sulfur content in the different extract phases of the batch experiments simulating the heat-up phase. The influence of additives was also studied (H1-H5, H7-H8). Because of the very low sulfur content in fermentation residue of the sediment type, only the overflow type was considered in this experiment. Figure 5-10 shows the recovery of sulfur in the respective product phases after extraction of the untreated fermentation residue as received and after hydrothermal treatment. The sulfur content is given as weight fraction of the total amount in the feed. The recovery of nearly 1000 mg g^{-1} for the untreated feedstock demonstrates the viability of the procedure for quantifying sulfur in the different extract phases. For the hydrothermally treated samples, 350-400 mg g^{-1} of the sulfur in the feedstock could not be recovered in the liquid and solid phases. We attribute this difference to sulfur present as gaseous compounds.

Since our gas chromatographic method was not able to measure such sulfur compounds, we attempted to quantify them using test tubes.
We identified H_2S, whereas SO_2, CS_2 and mercaptans were not detected in the gas phase. The amount of gaseous sulfur compounds quantified with the test tubes corresponded to ca. 100 mg g^{-1} of the expected amount, or 40 mg g^{-1} of the feed (DM). The detection limit for SO_2 corresponded to 10 mg g^{-1} of the feed TS, for CS_2 to 4 mg g^{-1} and for mercaptans to ca. 1 mg g^{-1}. Due to the affinity of many sulfur-containing compounds towards metals and synthetic materials, a strong underestimation in our measurement would not be surprising but could not be quantified.

We conclude from these experiments that the major amount of sulfur bound in the solid structure of the biomass is transformed to soluble organic compounds by the hydrothermal treatment. However, a considerable amount of sulfur remains organically bound and therefore appears in the hexane and methanol phases. A transformation of sulfur compounds to inorganic salts, which would end up in the water phase, was not observed.
In fact, the content of water-soluble sulfur compounds is actually reduced by the hydrothermal treatment in the case of sample O3, which contains a considerable share of these compounds in the untreated sample. This observation may be explained by a degradation of water-soluble sulfur compounds, i.e. proteins, peptides, soluble inorganic salts, to water-insoluble and/or gaseous compounds.

In the literature, a few publications can be found dealing with the cleavage of the organically bound sulfur from the organic backbone in hot compressed water (see section 3.7.2). However, very little is known about the transformation of sulfur in real biomass samples into inorganic salts. In desulfurization processes under reducing conditions sulfur is released H_2S. Alkali additives have been reported to enhance desulfurization and capture sulfur, avoiding the formation of H_2S (see section 3.7.2). In the presented experiments no such effect is visible since no sulfur was enriched in the water phase.
Provided that the total amount of non-identified sulfur is present in the gas phase, 350-400 mg g^{-1} of the sulfur has been gasified. This share is higher than the share of gasified carbon (compare Figure 5-8). An explanation could be that thiol groups in

proteins in their position as side-chains are more accessible for hydrolysis as compared to the carbonaceous backbone, leading to an enhanced cleavage of sulfur. The absence of SO_2 in the gas phase is in disagreement with the findings of other authors at similar conditions. Bircan et al. found SO_2 and H_2S in similar concentrations gasifying animal manure [66]. Alif et al. detected SO, SO_2 and SO_3 gases by an online sampling method during gasification of L-cysteine. They attributed the occurrence of SO_2 (and SO_3) to an oxidation of SO by water. SO resulted from the oxidation of cysteine by water [131].

The residual sulfur in the solid product phase may be present either as water-insoluble salts or coke. The addition of K_2CO_3 leads to a slight enrichment of sulfur in the water phase, which is possibly due to formation of K_2SO_4, a type 2 salt which precipitates under hydrothermal conditions as a solid and redissolves again at ambient conditions. The experimentally determined amount of sulfate is by several orders of magnitude below the solubility of K_2SO_4 at ambient temperature (10^{-6} vs. 10^2 g L^{-1}), which supports this assumption. The sulfur content of the methanol phase is simultaneously reduced, indicating that the sulfur species that are enriched in the water phase may preferentially originate from tar precursors. After addition of $CaCO_3$, an increased amount of sulfur is found in the solid phase. Precipitation of $CaSO_4$ is, however, unlikely, because also in this case the detected amount of sulfate is lower than the solubility of $CaSO_4$. Interestingly, there is a slight decrease in the sulfur content of the hexane phase for the experiments with carbonates supplement in the case of sample O3. However, this trend is not seen for sample O4. A considerable depletion of sulfur in the organic phases by addition of K_2CO_3 is therefore not taking place.

5.3.4 Gasification: Ratio of biomass to catalyst

An assessment of the catalyst deactivating potential of the fermentation residues was done by the following series of batch experiments conducted with a varying ratio of biomass to catalyst (S1-S4). This ratio was defined as the molar ratio of the sulfur in the feedstock to the ruthenium in the catalyst, n(S)/n(Ru). The experiments were conducted at a sandbath temperature of 420°C over a period of 60 min with a final pressure of approximately 30 MPa.

For overflow type residue, a clear trend of decreasing gas production with lower catalyst loadings can be seen (S1-S2). The carbon distribution over the product phases is shown in Figure 5-11. The underestimation of recovered carbon for low catalyst loadings (S3-S4), i.e. high n(S)/n(Ru), is probably due to carbon deposits on the catalyst, insoluble in both methanol and hexane, which is in agreement with an observed mass gain of the catalyst grains.

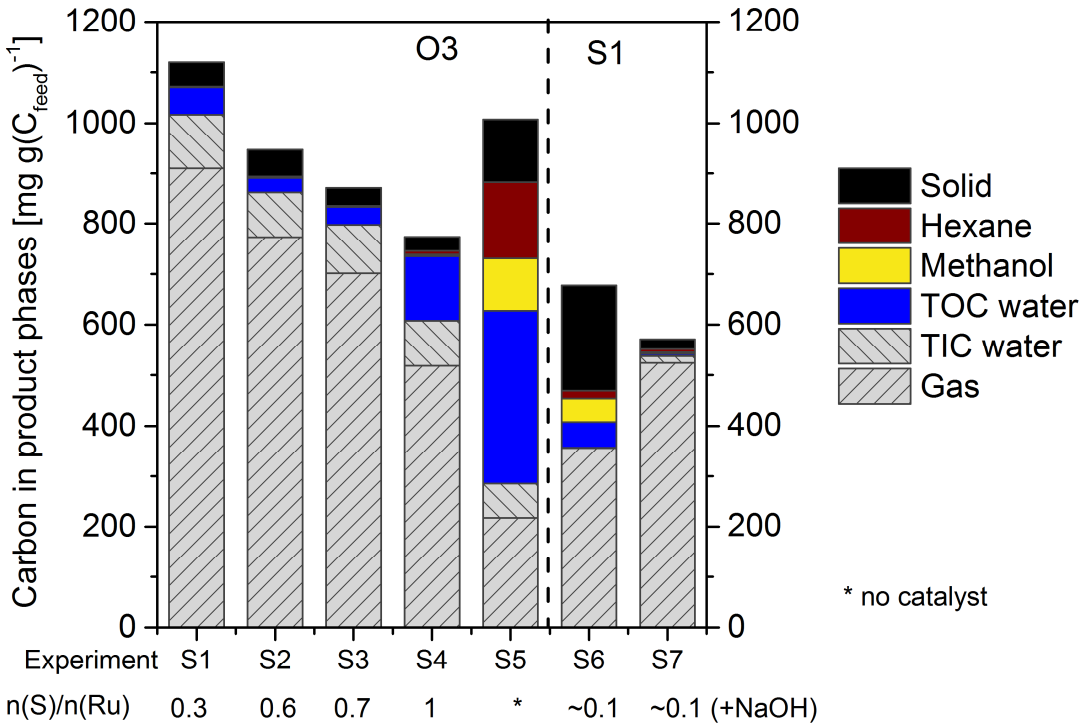

Figure 5-11: Carbon distribution over the product phases after gasification of overflow type residue for different n(S)/n(Ru) ratios. T = 410℃, p = 30 MPa, reaction time = 60 minutes (S1-S5). Carbon distribution over the product phases for sediment type residue with and without addition of NaOH. T = 410℃, p = 35 MPa, reaction t ime: 60 min (S6-S7).

For the fermentation residue of the sediment type, almost no conversion took place in the presence of a catalyst even at high catalyst loadings (S6-S7). Instead, a large amount of coke and tarry compounds was produced (S6). The carbon balance could not be closed well because the feed was strongly inhomogeneous and furthermore because coke grains could not be distinguished from catalyst particles. Since the concentration of sulfur is very low for the sediment type, we assume that the catalyst deactivation was mostly due to coke and tar formation and not to sulfur poisoning. This assumption is supported by the acidity of the reaction mixture and the observation that an acidic environment promotes coke formation. The pH of the water-soluble product phase was acidic (pH 4). As expected, the coke and tar

formation could be significantly reduced by supplementing the feed with a small amount of NaOH solution until a pH > 9 was reached (S7). This result is in agreement with the results from the heat-up experiments with the sediment type residue. We can therefore assume that extensive coke and tar formation during the heat-up phase has led to a more or less complete deactivation of the catalyst. Figure 5-11 shows the carbon distribution over the product phases of the sediment type residue after gasification with and without NaOH addition.

5.3.5 Gasification: Catalyst system

Gasification of biomass at temperatures < 500°C with the purpose of producing methane requires a catalyst. 2% Ru/C as well as 2% Ru/ZrO_2 (DKKK) showed good results in previous studies performed in our lab with batch reactors using glycerol as feedstock. In particular, 2% Ru/ZrO_2 showed good activity even in the presence of sulfate [154]. The product composition after experiments with two different catalysts at around 414˚C and a reaction time of 60 min is shown in Figure 5-12. The distribution of carbon over the product phases indicates that Ru/ZrO_2 (C2) increased the conversion of the fermentation residue to gaseous products significantly compared to an experiment without catalyst (C1); however, full conversion was not reached within the reaction time. This becomes visible by the significant amount of carbon in the methanol- and hexane phase. For Ru/C (C3), almost full conversion was reached. Note that the inorganic carbon (TIC) is also gasified carbon, dissolved in the water. Thus, more than 900 mg g^{-1} of the feed carbon was gasified with the Ru/C catalyst. The occurrence of small amounts of ungasified carbon for the experiment with Ru/C as for any other experiment is most probably a result of the influence of the cold zone (see section 5.2.3). The slight overestimation of total carbon may result from attrition or from decarboxylation or desorption of CO_2 from the catalyst support (see section 5.2.5). The underestimation of total recovered carbon for the reaction performed with Ru/ZrO_2 can be explained by coke formation (compare section 5.3.4), that has often been found at high levels of tar formation. This assumption was supported by temperature programmed oxidation (TPO) measurements of the spent catalyst, where CO_2 was detected. We also considered the visual appearance of the extract phases. While they were clear for Ru/C, they appeared with a strong yellow to brown color for Ru/ZrO_2.

We conclude from this comparison that Ru/C provides a higher performance than Ru/ZrO_2 regarding the conversion of fermentation residue to gaseous compounds. Nearly full conversion can be reached with this catalyst in a batch reactor system.

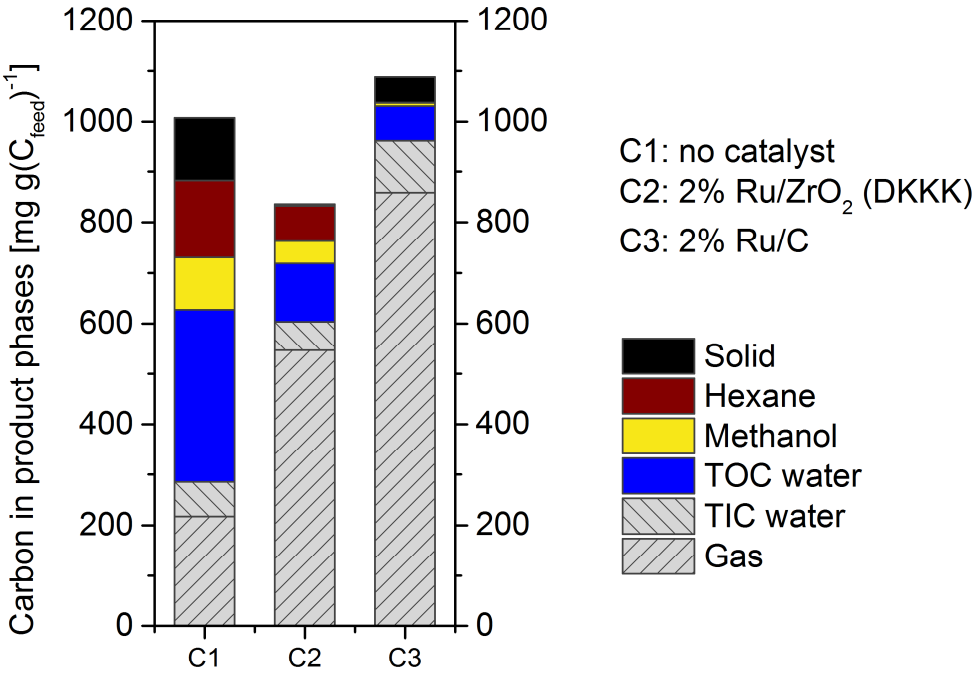

Figure 5-12: Carbon distribution over the product phases of the overflow type fermentation residue after gasification over different catalyst systems (2% Ru/C, 2% Ru/ZrO_2 and without catalyst).

5.3.6 Gasification: Influence of temperature on methane production

In this series of experiments, the influence of reactor temperature on the carbon conversion and gas composition was investigated (T1, T3-T5). The goal was to find out if low supercritical temperatures could lead to a full conversion of the fermentation residue in the presence of a catalyst within a reasonable reaction time. The experiments were performed at a shorter reaction time of 30 min, because no increase in pressure was measured after 20 min, indicating that the gas-producing reactions were finished. Fermentation residue of the overflow type was used for this test. A high loading of the 2% Ru/C catalyst was used to have an amount of active catalyst enough to see the effect of varying the temperature. In Figure 5-13 the relative amount of gases produced at different reactor temperatures is shown in comparison to the calculated maximum theoretical gas production at 400°C (T2). It

can be seen that after 30 min at subcritical conditions the biomass has by far not been fully converted to gases. The methane production per unit mass of feed reaches a maximum value at a temperature of 400˚C. For higher temperatures, no further increase in methane production occurs. A shift from methane to hydrogen is visible, though, which is in accordance with the thermodynamic predictions. From these results, we conclude that a reactor temperature of 400˚C is a good compromise between thermodynamic and kinetic aspects for maximizing methane production from fermentation residue. For a fine adjustment of the ideal reactor temperature and the reaction time, experiments in a continuous reactor system will be necessary.

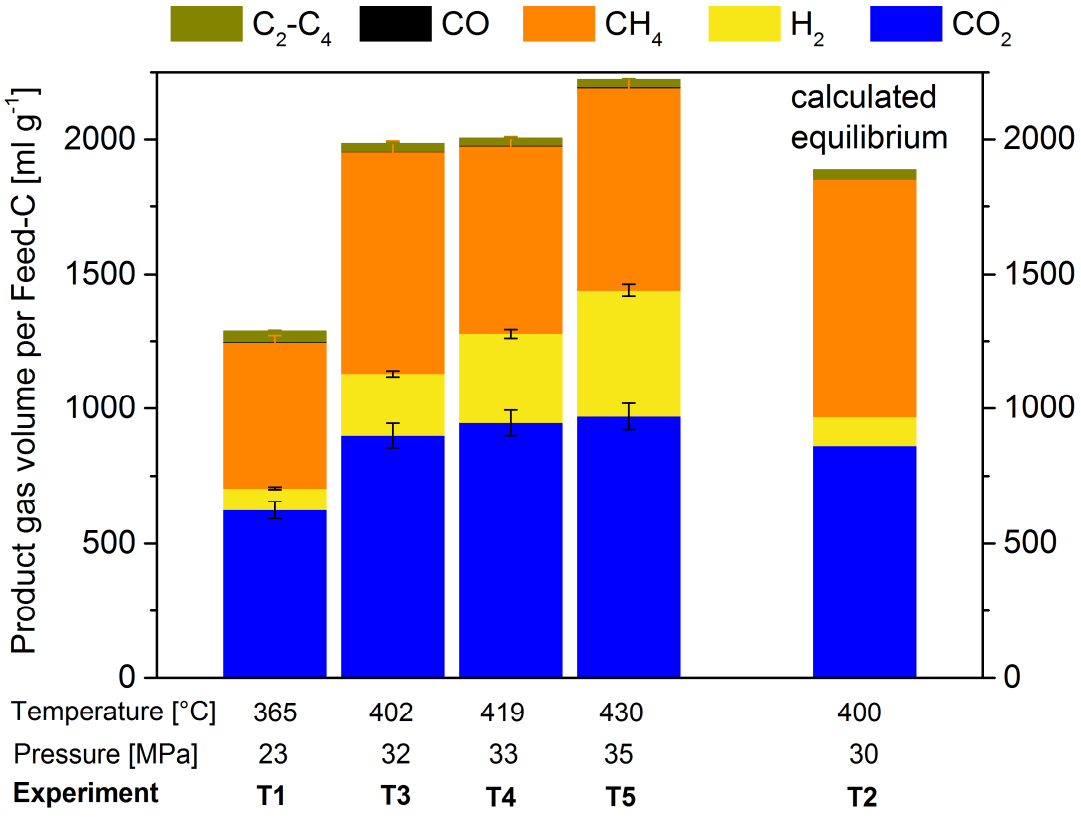

Figure 5-13: Relative amount of gases per gram of feed-carbon produced at different reactor-temperatures and pressures.

5.3.7 Gasification: Effect of reaction time on gas production

The required reaction time for a certain biomass feedstock in the reactor is an important parameter for the assessment of the gasification rate of this feedstock. The reaction time in a batch reactor necessary for full conversion provides useful information for comparing different feedstocks and reaction parameters. However, the reaction time in a batch reactor is not directly transferable to a continuous system. In continuous mode, a shorter reaction time in the reactor is expected because of the

thermolysis in the preheater and salt separator, leading to a liquefaction of the biomass already before entering the reactor. According to the results of gasification experiments with varying reaction time (R1-R4), as shown in Figure 5-14, after about 20-25 min the conversion of carbon to gaseous products is finished (R2, R3). As can be seen in Figure 5-15, the derivative of pressure vs. reaction time becomes zero after 20-25 min. Noteworthy is the strong influence of temperature changes on the pressure within the supercritical region. This plot therefore suggests that the actual reaction time for full conversion is on the order of 25 min or less. The experiments were performed at 410°C and 30 MPa with high catalyst loadings (n(S)/n(Ru) < 0.4).
Even though the conditions in a batch system are different from a continuous system, we propose a parameter that gives us an estimation of the corresponding minimum WHSV (weight hourly space velocity) that would be chosen for transferring the experimental conditions to a continuous plant. $\dot{\zeta}$ describes the mass ratio of biomass and catalyst at the respective residence time and is calculated according to equation 5-1:

$$\dot{\zeta} = \frac{m_{Feed\,(DM)}}{m_{Catalyst}\,\tau}\left[g\ g^{-1}h^{-1}\right] \qquad \textbf{(5-1)}$$

m = Mass [g], DM = Dry matter, τ = Residence time [h]
In our case, with fermentation residue O3, a temperature of 410°C, and n(S)/n(Ru) of < 0.4, nearly full conversion takes place at $\dot{\zeta}$ values of 0.45 g g^{-1} h^{-1} or lower.

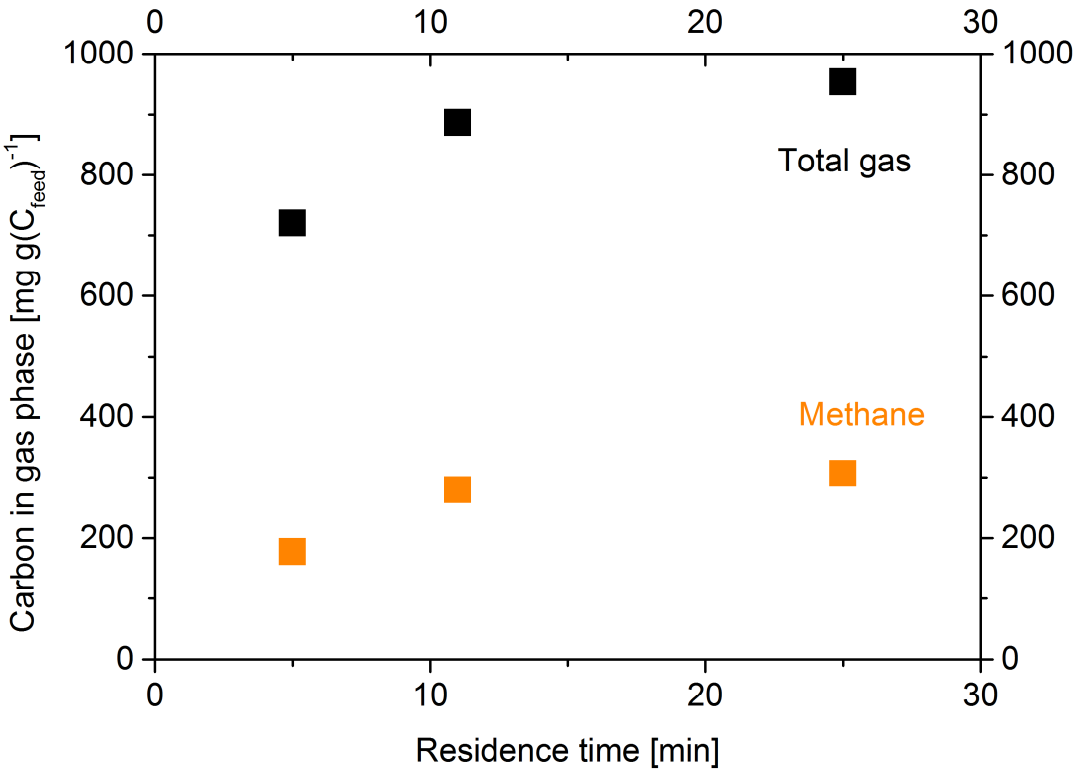

Figure 5-14: Carbon conversion to gaseous products and methane for various residence times. Experiments from left to right: R4 – R2.

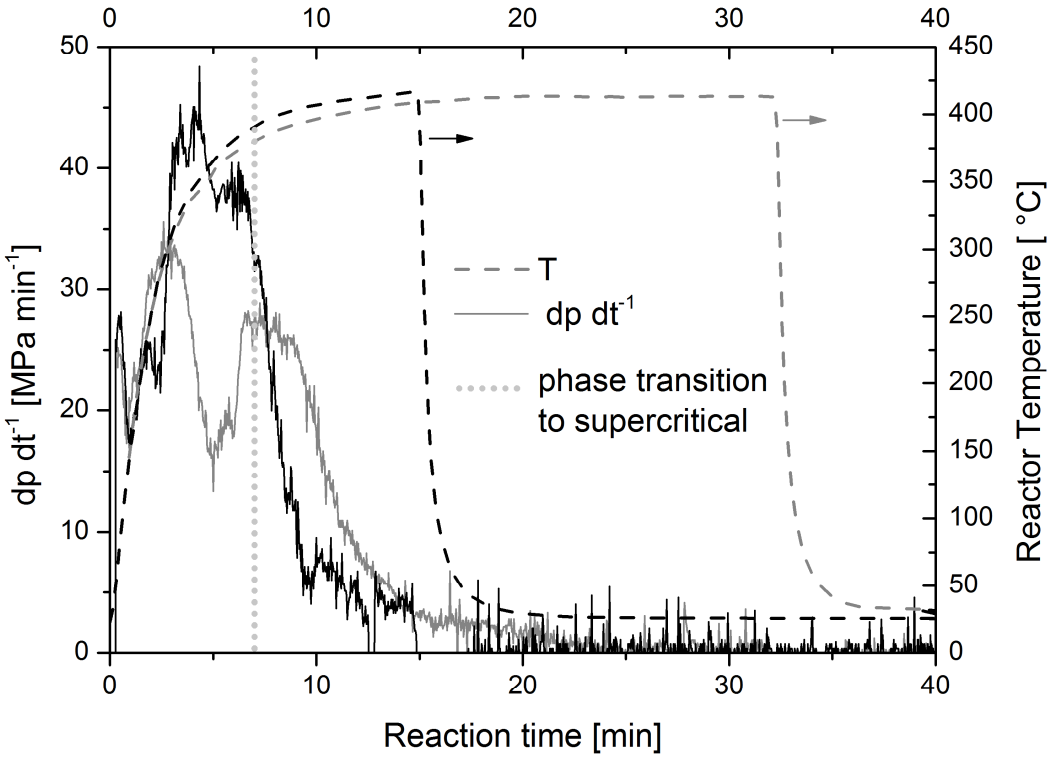

Figure 5-15: Plot of reactor temperature and the derivative of reactor pressure vs. reaction time for experiments R3 (black) and R2 (grey).

5.3.8 Conclusion

The content of minerals in fermentation residue of the overflow type and the releases ammonia buffered the pH during the liquefaction reaction and thus reduced coke formation. The addition of minerals to this residue did therefore not reduce the coke formation further. Fermentation residue of the sediment type has a low content of minerals and was therefore more prone to coke formation during the heat-up phase. Organically bound sulfur was not sufficiently mineralized and transformed to a salt during heat-up below 410°C. In a continuous process, the remaining sulfur would therefore not be separated from the reactant stream before entering the reactor, which will result in catalyst poisoning.

Low catalyst loadings in a batch reactor led to incomplete conversion for the overflow type fermentation residue, while high loadings yielded nearly complete conversion. For the sediment type, also at high catalyst loadings incomplete conversion was observed. We attribute the deactivating effect of the overflow type to sulfur poisoning and for the sediment type to fouling.

Ru/C yielded a higher conversion than Ru/ZrO_2 (DKKK). At a temperature of 400°C, nearly full conversion was reached, while the ratio of CH_4/H_2 was highest. At a reaction temperature of 410°C, the conversion was complete after a reaction time of approximately 25 min.

5.4 Gasification of fermentation residues in a continuous reactor setup (Konti-2)

5.4.1 Introduction

With the optimum process parameters gained from preliminary experiments in batch reactors (see chapter 5.3), a first continuous gasification experiment in the test rig Konti-2 was done with fermentation residue O4 (for composition see Table 5-1). It was basically a test for obtaining a first assessment of which process steps behaved as expected and which ones needed further study and testing. These steps included

- Slurry Feeder: Pumping of the fermentation residue
- Preheater: Liquefaction of the fermentation residue

- Preheater and salt separator: Separation of N, S, P from biomass and their conversion to inorganic salts
- Salt separator: Enrichment of salts in the brine effluent
- Salt separator: Depletion of salts in the biomass transferred to the reactor
- Catalytic reactor: Gasification, water-gas shift, methanation

The wet sieving required rinsing with water, resulting in a dry matter content of 4 wt%. The consistency of the fermentation residue in terms of viscosity was still pumpable at this concentration. A dilution by mixing with the residual water in the Slurry Feeder`s hose resulted in an actual feed concentration of maximum 3 wt%. The corresponding amount of organic material in the feed was therefore assumed to be 2.2 wt%.

The duration of the experiment, from the change to biomass feed to the change back to water, was 150 minutes. After this time the pressure drop over the filter downstream of the reactor started to become significant (>2 MPa). The filter was changed for several times after the experiment so the rig could be flushed. A steady state was not reached within this time interval, neither for the salt separation nor for the biomass conversion. This has to be kept in mind when interpreting the results. We can see trends, but we cannot make conclusive statements from the results of this test run.

5.4.2 Slurry Feeder: Pumping of the fermentation residue

The fermentation residue could be pumped by the Slurry Feeder without any problems such as clogging of the outlet, blocking of the valves or leakages caused by contamination of the seals by particles. A phase separation of the fermentation residue could, however, already be seen in the hose connecting the feed container to the Slurry Feeder. Therefore it was assumed that this phase separation proceeded within the cylinders, resulting in an instationary feeding. The amount of biomass that was actually fed into the plant had to be assumed much lower than expected, since the cylinders were not fully ejected leaving a condensed sediment inside. Note that the residence time of biomass in a cylinder can be up to 150 min for the injection of a full cylinder's content at a feeding rate of 1 kg h^{-1}. A mass balance could not be determined because of the instationarity.

The phase separation caused also difficulties when the feed was changed to water after the experiment. Large amounts of biomass deposits were still present in the cylinders and were kept feeding into the test rig, complicating the cleaning procedure. Therefore the Slurry Feeder was replaced by the HPLC pump for cleaning in subsequent experiments. For this first run it was not available, though.

5.4.3 Preheater: Liquefaction of the fermentation residue

The liquefaction of particulate matter in the preheater at a setpoint temperature of 370°C can be stated as successful. No blocking occurred in this section of the Konti-2, particularly at bottleneck-positions such as the connection to the salt separator and the dip tube. A growth of particles caused by coking was not observed; no large particles were found in the filters or particle traps. The interior of the preheater itself was, however, not inspected after the experiment, nor could particles which might have settled at the bottom of the preheater be recovered without the necessity to completely dismantle the respective section. It is therefore possible that coke deposits have remained in the preheater and would have caused problems after longer feeding durations.

The low level of coke formation during heat-up is in agreement with the observation from the batch experiments (see section 5.3.2), which was attributed to the high content of minerals, especially alkalis, and the formation of ammonia, preventing a drop in pH by the formation of acidic degradation intermediates.

The liquefaction of biomass would ideally lead to a cleavage of the biomass bound heteroatoms N, S and P from the carbonaceous framework. These heteroatoms would ideally become mineralized by the time they reach the salt separator, where they would be separated from the residual biomass by precipitation. The achievement of this mineralization and the salt separation efficiency will be discussed in the next section.

5.4.4 Salt separator

The salt separator was heated to 450°C by both heating blocks. The temperature profile in the salt separator was not measured for this particular experiment. A temperature of 435–440°C was assumed to prevail at the hottest spot based on measurements at pure water conditions. The salt separator effluent was withdrawn at a flow rate of 1.9 ml min^{-1} which was increased to 2.4 ml min^{-1} after a short time,

corresponding to 14.4 wt% of the total flow or 16.4 wt% of the stream directed to the reactor. This change was done because the salt separator effluent's conductivity increased weakly in comparison to the one of the reactor effluent (see Figure 5-17), which was due to the large dead volume in relation to the low flow rate. The negative side effect of a higher salt separator effluent flow rate is the removal of organic matter from the system. This could presently be seen in the dark stain of effluent stream (Figure 5-16).

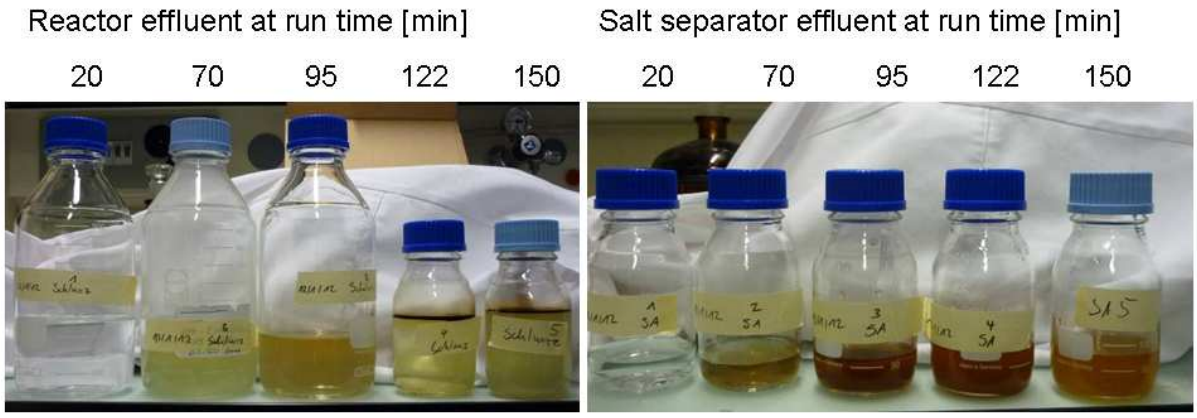

Figure 5-16: Photographs of the effluent samples of the gasification experiment in chronological order.

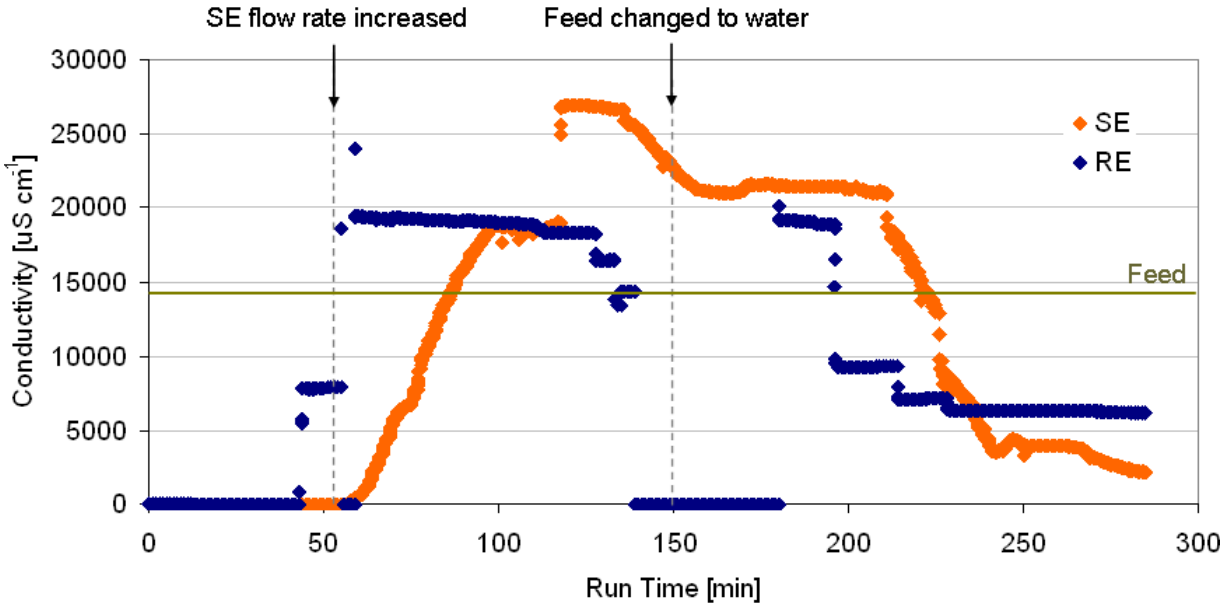

Figure 5-17: Conductivity of the salt separator effluent (SE) and the reactor effluent (RE) over run time. The conductivity of the feed is indicated by a green line.

From the development of the effluent`s conductivities it can be asserted that some salt separation occured. Noteworthy is that in the presence of biomass an increase of the conductivity can also be caused by organic acids. Ion chromatographic

measurements of the water phase of the collected effluent samples demonstrate the separation efficiency of single anions (Figure 5-18). We find a depletion of phosphate and chloride in the reactor effluent and an enrichment of phosphate and sulfate in the salt separator effluent. Sulfate, as it is not depleted in the reactor effluent, was apparently generated by oxidation of organic sulfur compounds. This is an indication for a partial mineralization of organic sulfur compounds.

Chloride, which is depleted in the reactor effluent, does not show the corresponding enrichment in the salt separator effluent. This suggests that chloride remained in the salt separator by forming a solid phase. NaCl is classified as a type 1 salt. However, it is solid at the conditions prevailing in the salt separator according to the phase diagram of NaCl (see section 3.4.2.2). Therefore it is not surprising that chloride was not recovered as a brine. In fact, chloride and also phosphate were found in the salt separator effluent in high quantities during the cool-down phase of the salt separator. Sulfate was also found there. The most common sulfate salts are type 2 salts. The fact that it was partially recovered in the salt separator effluent can be explained by a mixing with other type 1 salts. Such effects have been described earlier (see section 3.4.2).

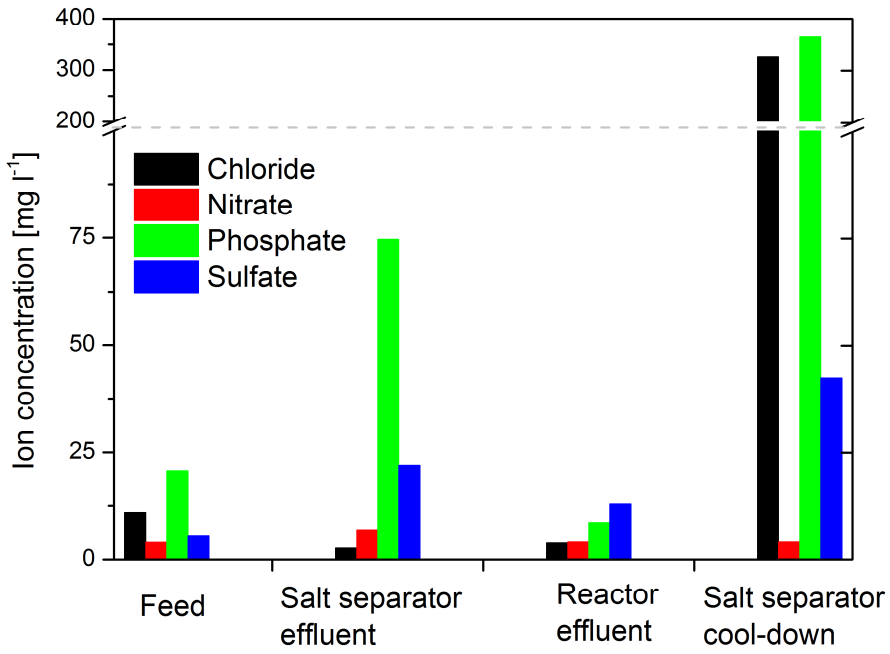

Figure 5-18: Ion concentrations in the water extract phase of the feed, reactor effluent, salt separator effluent and salt separator effluent during cool-down of the salt separator.

Of special interest regarding the separation efficiency is sulfur. The formation of sulfate in an overall reducing environment is both unexpected and beneficial from a process engineering point of view. Unlike sulfide and organic sulfur compounds, sulfate can be separated (see section 3.4.2). The fate of the total sulfur content of the fermentation residue has been analyzed in more detail. The extract phases of both effluent streams have been analyzed for their TS content, so that the sulfur containing compounds can be classified as polar and water soluble, polar and water insoluble as well as non-polar. For comparing the actual separation of sulfur and biomass, also the TC of the phases has been measured. The results are shown in Figure 5-19. The total amount of sulfur and carbon in the effluent streams is depicted in Figure 5-20. The distribution of the feed carbon and sulfur over the extract phases can be found in Figure 5-8 and Figure 5-10, respectively (experiment H9).

The salt separator effluent contained mainly water- and methanol-soluble carbon compounds. Ungasified carbon left the reactor as hexane-soluble compounds. Likewise, the sulfur leaving the salt separator was found in the water and methanol phase. However, a considerable amount of sulfur is transported to the reactor in the form of hexane- and water soluble compounds.

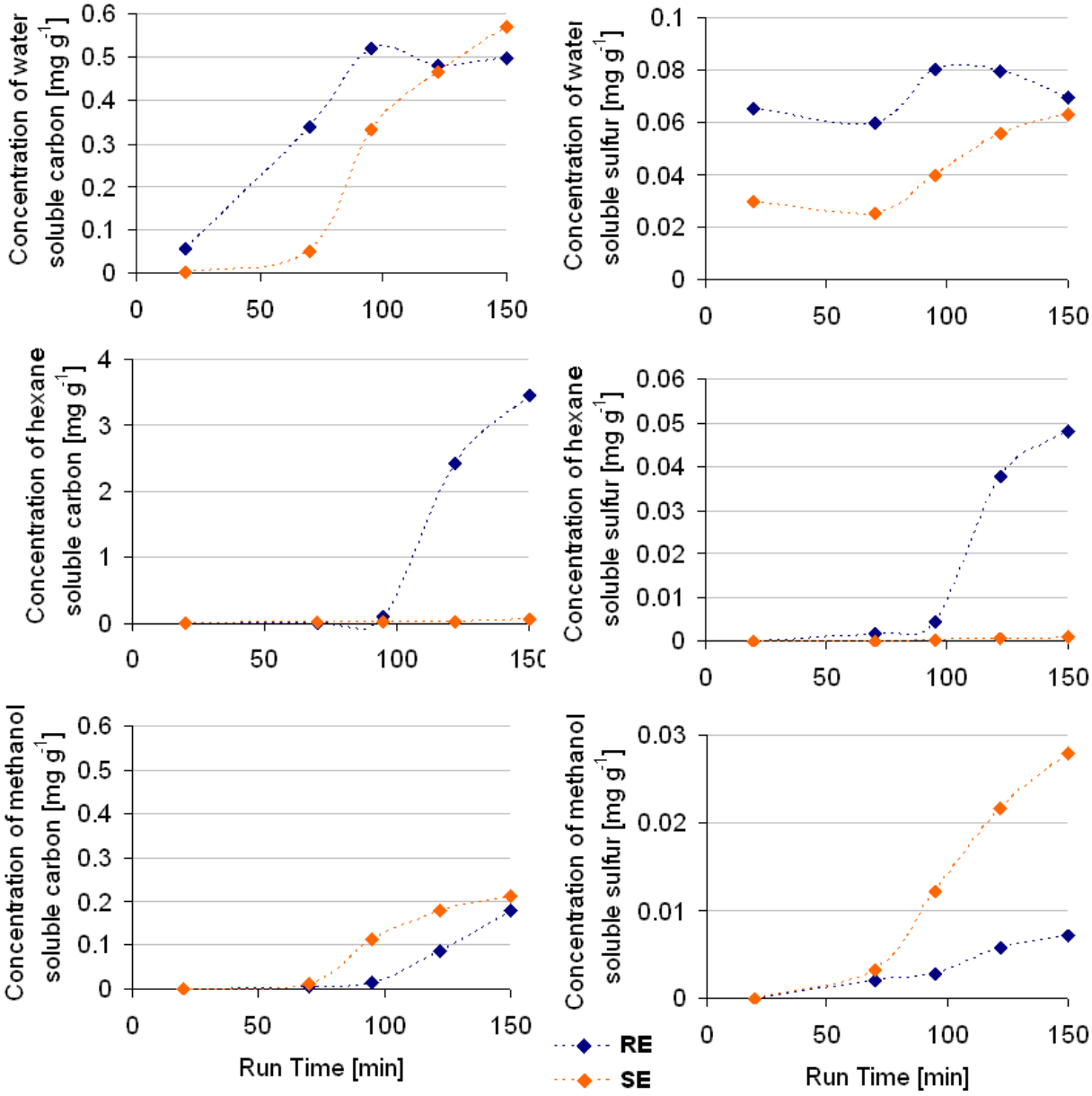

Figure 5-19: Carbon and sulfur concentrations in the reactor effluent (RE) and salt separator effluent (SE) over the run time, itemized by the extract phases.

Regarding the total concentrations of sulfur and carbon in the effluent streams (Figure 5-20), we find an enrichment of both carbon and sulfur in the reactor effluent. The enrichment factor for carbon is, however, ten times higher than for sulfur.

The difficulty in interpreting the results was the lack of steady state conditions. Furthermore, gasified carbon and sulfur could not be quantified. Therefore the total amount of carbon and sulfur that had entered the reactor is unknown. Nor are the carbon and sulfur compounds considered that have been irreversibly adsorbed on the catalyst or that have formed solid deposits. Thus we have no information about the actual separation of carbon and sulfur in the salt separator. At steady state conditions, the concentration of carbon and sulfur found in the reactor effluent

stream might have been higher, because of a decreasing gasification efficiency and the saturation of the catalyst`s storage capacity.

A conclusion that we can definitely draw from these results is a poor mineralization of organically bound sulfur. This follows from the high amount of sulfur that was found in the organic extract phases. A complete liquefaction of the biomass with a mineralization of all hetero atoms in the preheater as required for PSI`s catalytic process was not achieved. A depletion of salts from the biomass could be achieved for phosphate and chloride but not for sulfate. Sulfate is probably formed from thiols also downstream of the salt separator.

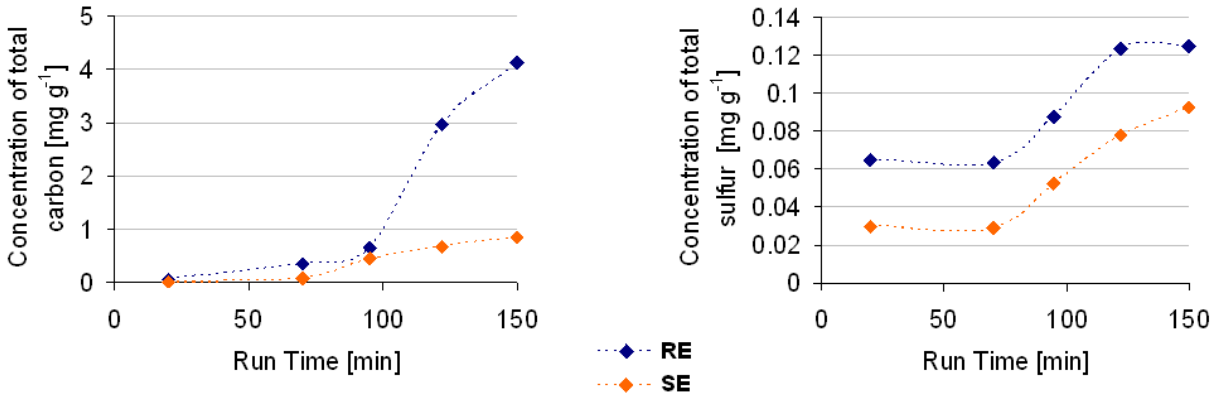

Figure 5-20: Total carbon and sulfur concentrations in the reactor effluent (RE) and salt separator effluent (SE) over the run time.

5.4.5 Catalytic reactor

The catalytic gasification in the reactor was performed at a setpoint temperature of 400°C over 40 g of 2% Ru/C. The space velocity of biomass entering the catalytic reactor could not be determined accurately because of the above mentioned difficulties. It was roughly estimated to be around 0.3-0.5 h^{-1} at the maximum, assuming that only 50-80 wt% of the biomass actually entered the rig because of the above described phase separation (see section 5.4.2). The mass flow of the salt separator effluent was subtracted from the feed. Not considered is the biomass depositing on the walls of the preheater, salt separator and above the catalyst bed. Compared to the results of the batch experiments and the parameter $\dot{\zeta}$ that has been introduced as an equivalent for the WHSV for a batch system in section 5.3.7, a WHSV of 0.3-0.5 h^{-1} is on the order of $\dot{\zeta}$ = 0.45 h^{-1} that has been found to yield full conversion.

The hourly amount of sulfur that was fed into the reactor was also roughly estimated to be 4 to 7 mmol h^{-1}. Segregation in the salt separator is not considered here. The amount of ruthenium in the reactor is 8 mmol and the amount of ruthenium exposed on the surface as determined by hydrogen chemisorption is 1 mmol. Following Equations 4-2 and 4-3, see section 4.4.4), the exposure time t_1 after which a full coverage of the catalyst surface by sulfur is expected, is 8-15 min and t_2 is 1-2 h. Since the steam reforming and methanation reactions are structure sensitive and occur preferentially at low coordinated ruthenium atoms (see section 3.6.1), the number of catalytically active ruthenium atoms is presumably much lower than the number of exposed ruthenium atoms as used to determine t_1. Thus, an even lower equivalent of sulfur is possibly sufficient to deactivate the catalyst.

Regarding the gas production, we can see that a relatively stable gas production rate and gas composition were reached after the biomass feeding had been stopped (Figure 5-21). Just as the carbon in the reactor effluent, the presence of higher hydrocarbons (C_2–C_4) in the gas phase indicates a capacity overload of the catalyst. With the extraordinarily high production rate of H_2 in comparison to CH_4, it is obvious that the thermodynamic equilibrium of the methanation reaction has not been reached at any time of the experiment. A rapid deactivation of the catalyst is therefore likely. We have to assume that either the entire amount of sulfur in the biomass has been transferred to the catalytic reactor, poisoning the catalyst within the minimum amount of time, or the residence time was not sufficient, leading to the formation of insoluble deposits that further decrease the number of active sites.

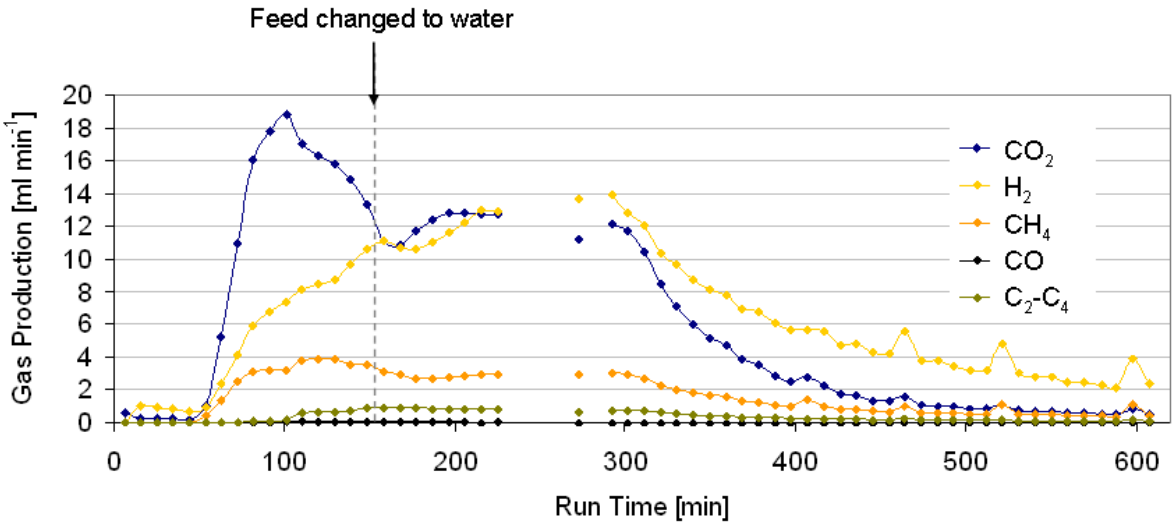

Figure 5-21: Gas production over the run time.

On the other hand, nearly no CO was formed during the whole run pointing to an un-inhibited water-gas shift reaction. Also the amount of methane points to some catalytic activity of the catalyst even after deactivation. The formation of methane in the absence of a catalyst is unlikely because the reaction of 3 and 4 equivalents of hydrogen is necessary (see section 3.4.3.3). The absence of methane in the product gas of an uncatalyzed glycerol degradation is shown in chapter 5.7. However, in uncatalyzed liquefaction experiments of fermentation residue methane is produced (see Figure 5-22). Methane can be the primary product of degradation reactions such as decarboxylation or decarbonylation of small organic molecules, e.g. acetic acid (see 3.4.3.2). Furthermore, metals traces (e.g. Fe) in the fermentation residue or the reactor walls can catalyze the methanation reaction (see sections 3.6.2 and 5.1). However, the latter is unlikely because the high CO concentration in the product gas of the batch experiments point to no catalytic activity, since the water-gas shift reaction is fast in a catalyzed system [68].

The comparison of the uncatalyzed batch experiment and the continuous experiment suggests a residual water-gas shift activity of the catalyst. A residual reforming and methanation activity is also likely. This would be in agreement with other researchers [71], and has been confirmed by continuous experiments with glycerol (see chapter 5.6).

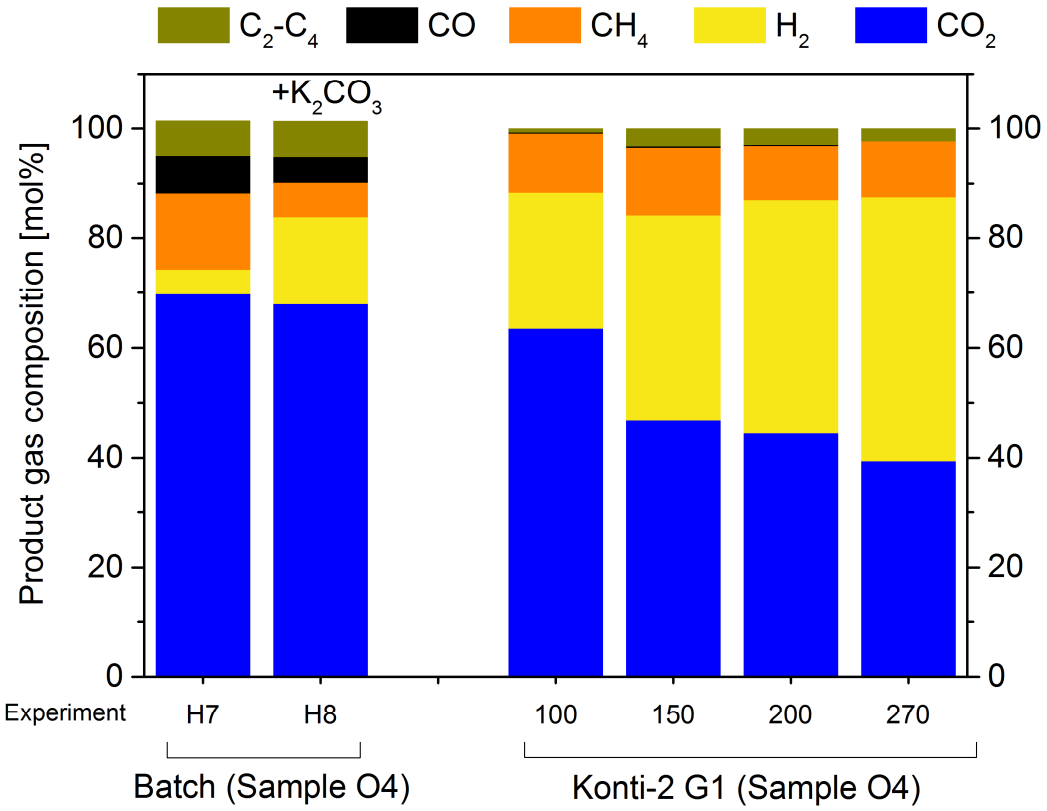

Figure 5-22: Comparison of gas composition in batch experiments without catalyst (compare section 5.3.2) and the continuous experiment at different times.

5.4.6 Conclusions

The gasification run with fermentation residue showed that the pumping and the liquefaction of a 3-4 wt% slurry could be generally realized for 150 min. No large coke particles were found in the filters or particle traps that would have indicated particle growth. A phase separation of the feed before entering the preheater caused difficulties in determining elemental balances.

The mineralization of sulfur was not successful. A substantial portion of the non-mineralized sulfur was transferred to the reactor. A depletion of some ions from the biomass stream could be achieved in the salt separator. An enrichment in the salt separator effluent was missing for certain ions. This was caused by the formation of a solid phase in the salt separator.

The catalytic reactions (gasification and methanation) were incomplete from the beginning, indicating a rapid deactivation of the catalyst or a too high WHSV. Despite of this, methane was produced at a constant concentration and nearly no CO was found. This indicates a residual activity of the deactivated catalyst which is in agreement with the results of other experiments (see chapter 5.6). The methane may

also originate from biomass degradation reactions or from catalytic activity of metal traces in the fermentation residue, e.g. Fe.

Massive amounts of tar were produced in the experiment. During cool-down they caused plugging of the line downstream of the reactor. It is unclear in which part of the rig the tars have been produced. In the salt separator effluent the amount of methanol soluble compounds was higher than in the reactor effluent. This indicates that the tars have been produced either in the preheater or in the salt separator. During flushing at experimental conditions the tars were not removed. It was therefore assumed that they deposited on hot surfaces during the experiment and were not redissolved by the supercritical water.
Since a plugging was only observed during cool-down of the salt separator, it is possible that they redissolved in the subcritical water. This observation also points to an accumulation of the tars in the salt separator. The reactor was still at 400°C during cool-down of the salt separator. The fact that the redissolved tars passing the catalytic reactor were not degraded indicates that the catalyst was overloaded despite of its residual activity after deactivation.
Tar formation of lignin-rich biomass was also reported by other groups. Also in the presence of a catalyst, Osada reported the formation of THF-soluble and water insoluble compounds (see section 3.5.3). In the catalytic batch experiments reported in chapter 5.3, no tars were formed at high catalyst loadings. In the presence of a catalyst intermediates are rapidly degraded. If intermediates polymerize faster than they can be degraded, e.g. at low catalyst loadings, tars are produced. Once produced, they will hardly be degraded.
Furthermore, the results of this experiment indicate that the miscibility of tars with supercritical water is limited. At ambient conditions, tars are soluble in polar organic solvents. The solvent properties of supercritical water are comparable to unpolar solvents, whereas subcritical water behaves like polar solvents (see section 3.4.1.3). It is possible that also at elevated temperatures tars are better miscible with polar solvents. The solvent properties of water would thus explain the poor miscibility with supercritical water and the higher miscibility with subcritical water.

5.5 Liquefaction of fermentation residues in a continuous reactor setup (Konti-2)

5.5.1 Introduction

As the continuous gasification test run has demonstrated, the steps preceeding the conversion in the catalytic reactor, that is the mineralization of sulfur and the desalination of the stream, require further development. A viable option would be the dosing of an oxidizing agent into the preheater or salt separator to oxidize all sulfur to sulfuric acid similar to supercritical water oxidation processes [13]. Müller proposed the addition of $NaNO_3$ to the feed [19]. From the energetical point of view, however, this is pointless. The requirement of an oxidizing agent would have to be considered a further energetic input, because the production of the additive is energy intense. Furthermore, an oxidizing agent would also attack the carbonaceous backbone, bringing about a decrease of the methane yield and thus of the energetic efficiency of the entire process. The observation discussed in section 5.6.2 of sulfate becoming reduced in the presence of biomass supports this assumption.
For this reason, varying the process parameters was the only feasible approach to optimize both, the removal of biomass bound hetero-atoms and the salt separation.

These two tasks are generally different and therefore individual optimum conditions are expected. For the salt separation, the optimum process parameters had been investigated earlier. From these studies it is known that high temperatures and low pressures promote the separation efficiency (see section 3.4.2.2). Furthermore, low flow rates in the salt separator and thus long residence times could be beneficial for a proper separation of the phases. Peterson showed that very high flow rates reduce the salt precipitation [170]. Both, heat transfer and flow patterns are influenced by the flow rate and can change the formation of phases.
For biomass degradation reactions the choice of optimum process parameters is more difficult. The reaction regime changes with the fluid density (see section 3.4.3). In (pseudo)-supercritical water, i.e. at pressures below the (pseudo)-critical pressures, free radical reactions are favored that lead to a fast degradation of biomass to gaseous products [64]. On the other hand, the solubility of organic molecules is an important parameter influencing the reactions, which is closely connected with the fluid density (see section 3.4.1.3). The optimum solvent properties of supercritical

water depend on the nature of the different solute molecules. As shown in the previous chapter (5.4), tars are poorly miscible with (pseudo-) supercritical water. At long residence times tars can further polymerize and form coke [19].

Since the total flow rate and the salt separator dimensions are given, the residence time does not have to be considered as variable. Thus, the independent process parameters are temperature, pressure and the salt separator effluent flow rate. The following questions were addressed in the following chapter:

- Does an increase of the salt separator temperature increase the mineralization rate of sulfur?
- How do higher temperatures influence the tar formation?
- Does an increase of the salt separator effluent flow rate significantly increase the salt separation?
- How does this affect the carbon mass balance?

For this purpose, liquefaction experiments have been performed at two different salt separator temperatures (430°C and 470°C) and two different effluent flow rates (2 and 3 ml min^{-1}). The pressure was constantly at 28 MPa. The reactor had been removed from the test rig to reduce the dead volume and to optain an insight into the composition of the desalinated biomass stream, avoiding further changes by gasification and adsorption phenomena. An empty tube replaced the reactor. The "reactor replacement" effluent will be termed "back" effluent.
Fermentation residue O5 was used for the liquefaction experiments. To avoid phase separation, 1 mg g_{wet}^{-1} of xanthan was added to the feed. Additionally, 68 mg g_{DM}^{-1} of K_2CO_3 was added to avoid coke formation in the preheater. The fermentation residue was milled in a food mill. The wet sieving was omitted in order to approximate more realistic conditions, since the liquefaction was apparently successful in the gasification experiment. For the feed composition see Table 5-1. From both effluent streams a collective sample was taken, starting from the moment when biomass feeding was initiated and ending 1 h after the feed was changed back to water. These samples should enable the determination of an integral elemental balance. A quantification of the product gases was not possible for all experiments because the concentrations were beyond the GC's detection limit. Note that the product gases

were diluted with nitrogen before measurement to provide a gas flow sufficient for GC measurements

5.5.2 General observations

The duration of the experiments was limited to 120 min when pressure changes started to become problematic. In experiment L2 severe pressure fluctuations over the preheater and soon also over the filters at the back effluent occurred. After 70 min the experiment had to be stopped because of a complete blockage of the back effluent line. The sample collection was stopped, too. The pressure fluctuations over the preheater occurred again in experiment L3, but to a lesser extent; this could not be explained by the higher salt separator temperature in experiment L2, because it did not affect the preheater temperatures.

The gas production was too low for a quantification of the components in all runs. CO_2 and C_4H_x could be detected occasionally. Higher hydrocarbons ($>C_4$) could be identified in the FID signals, however they were not calibrated. Methane was only detected in traces.

After flushing over at least 8 hours, the system was cooled down and finally depressurized. For experiment L2, the system was cooled down as soon as the plugging occurred. In all experiments, large quantities of sediment and tars were flushed out of the particle traps (Figure 5-23). Generally, a viscous, bitumen-like material was found in filter 2, which caused pressure drops on the order of several MPa. The material was soluble in methanol. In filter 1, a paste-like matter had accumulated, which was insoluble in water, hexane and methanol (Figure 5-24).

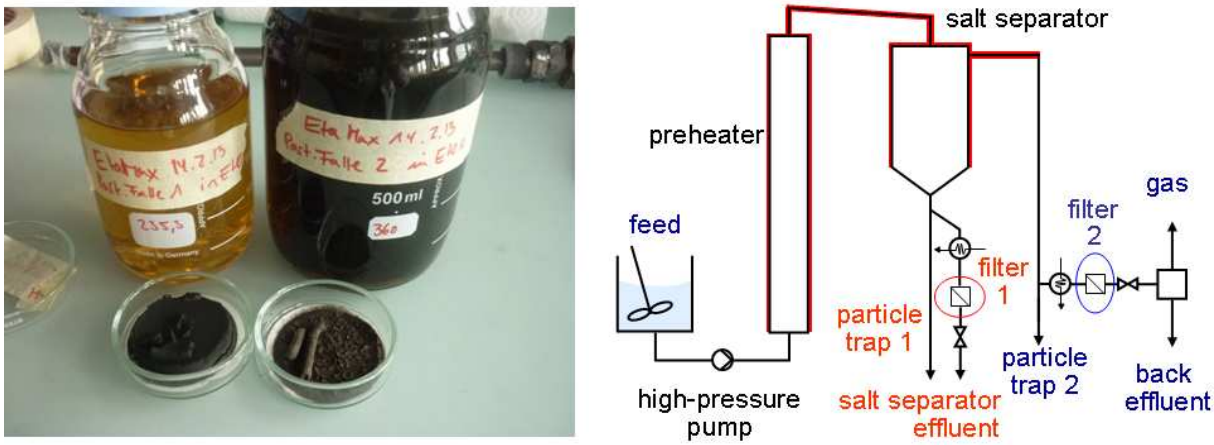

Figure 5-23: Left picture: Solid deposits and tars dissolved in ethanol withdrawn from the particle traps after experiment L1 (left: salt separator effluent, right: at back effluent). Right: Simplified scheme of the Konti-2 indicating the positions of the filters and points of withdrawal.

Figure 5-24: Tar deposits in filters after experiment L1; left: filters at back effluent (2), right: filter at salt separator effluent (1).

Electron micrographs of the fermentation residue solids show typical organic fiber structures (Figure 5-25). Electron back scattering detection reveals that the fibers are organic and no metal attrition or any kind of other inorganic impurity. This has also been confirmed by EDX measurements.

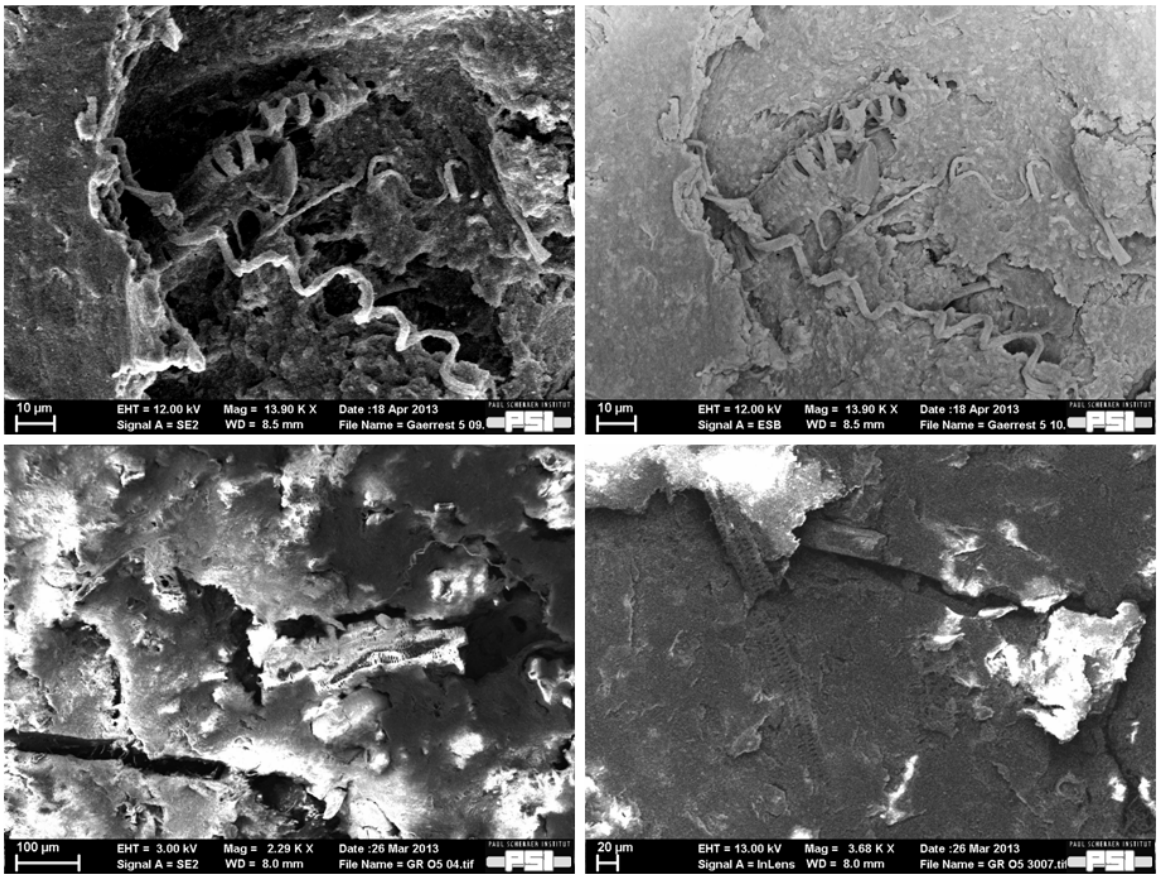

Figure 5-25: SEM images of the fermentation residue O5 solids. Top right: Electron backscattering detection.

The solids recovered from both particle traps have been examined by electron microscopy as well (Figure 5-26). They generally appear as an amorphous mass. The mass consists of merged structure elements. Müller described the shape typical secondary coke formed from pure glycerol as clearly defined hollow spheres merging together [19]. However, a spherical structure was not visible in particle trap contents. It has to be mentioned that coke samples resulting from crude glycerol were reported to show a less distinct shape [19]. Therefore, the amorphous mass was interpreted as secondary coke or unconverted solids.

Furthermore, structure elements of the feed material can be found in both particle traps, particularly in particle trap 1. Electron backscattering detection and EDX signals indicate that also these structure elements are organic. The similarity with the fibers found in the fermentation residue was obvious. It can be concluded that solids were not completely liquefied in the preheater at a temperature of 350°C and salt separator at 430°C. This can be due to a passivation by carbonization of the outer layer of the particle or to the mechanism of primary coke formation described by Antonietti et al. [67] (see section 3.4.3.2).

Table 5-2: Elemental composition of fermentation residue O5 and the content of the particle traps after experiment L1.

Element	Feed O5 [mg g^{-1}] (dry)	Particle trap 1 [mg g^{-1}] (dry)	Particle trap 2 [mg g^{-1}] (dry)
C	396	230	450
S	16	18	19
N	42	10	20

The solids in particle trap 1 have a carbon content of 230 mg g^{-1} whereas the carbon content is 450 mg g^{-1} for the solids found in particle trap 2. This indicates an increased carbonization level of the solids found in particle trap 2. Müller et al. reported an increased carbon content in coke at higher residence times at subcritical conditions (300-350°C) and no coke formation for pure glycerol and glucose in supercritical water [19]. However, the higher carbonization level of the particles found in trap 2 can be interpreted in a way that coke formation proceeded in the supercritical water conditions of the salt separator. If the particles found in particle trap 1 settle relatively fast, they reach the cool zone rapidly. The particles found in particle trap 2 have to circulate within all temperature zones of the salt separator for at least one time before they leave it at the top exit (see Figure 4-8). Since the salt separator is not isothermal, pseudo-subcritical conditions may prevail in some zones of the salt separator. Note that the pseudo-critical temperature of pure water at 28 MPa is 395°C. At lower temperatures, pseudo-subcritical conditions prevail. The presence of biomass and gases may furthermore influence the properties of water.
Another possible explanation for the higher carbonization level of the particles found in trap 2 could be that those particles are more prone to be transported to the top outlet of the salt separator by buoyant forces, e.g. because of a lower density. Minerals, e.g. sands settle relatively fast and are thus recovered in the particle trap 1.

Sulfur was further enriched in the solid residues in both particle traps. This points to an insufficient removal from the carbonaceous backbone and is thus in accordance with the results from the gasification experiment G1.

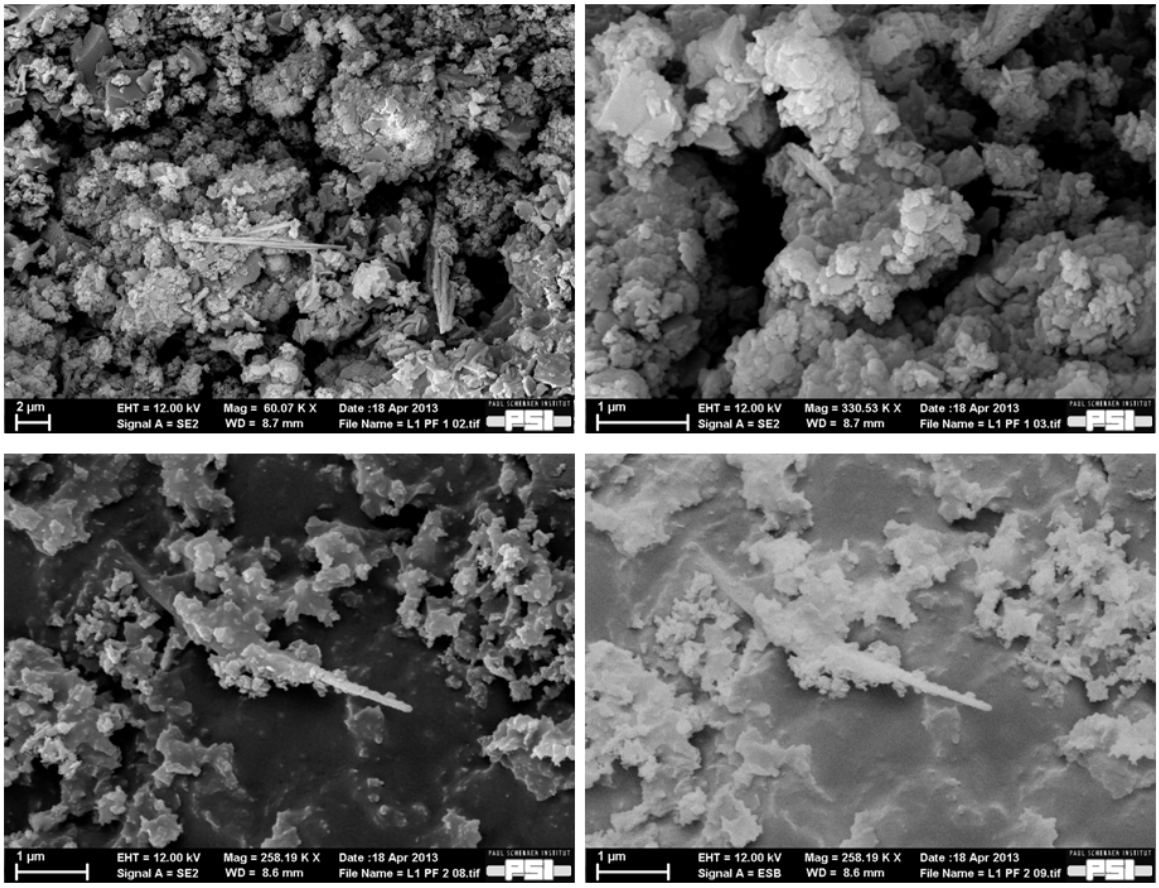

Figure 5-26: SEM images of the solids found in particle trap 1 (top) and in particle trap 2 (bottom) in experiment L1. Bottom right: Electron backscattering detection.

In experiment L3, crystals were observed in the salt separator effluent and the particle trap 1 content. The crystals show a trapezoid shape (Figure 5-27). EDX analysis revealed a high content of magnesium and phosphorus. The shape has a strong similarity with struvite ($MgNH_4PO_4 \cdot H_2O$). The EDX pattern is similar to the one of a pure struvite sample [171]. Struvite is formed in the presence of ammonia and is stable under alkaline conditions. All effluents had a pH between 7 and 9. The formation of ammonia by deamination of organic amines under hydrothermal conditions has been described in literature [62, 63]. Elliott et al. [84] reported an outside crust on the Ru/C catalyst in which magnesium is associated with phosphorus after gasification of distillers' dried grains and solubles at subcritical conditions. In their experiments, salt precipitates had led to a plugging of the reactor. Withdrawal of struvite from the salt separator is therefore advantageous to avoid depoision on the catalyst and furthermore to recover the minerals of the biomass. The recovery of phosphorus of biomass is particularly important for the use as fertilizers.

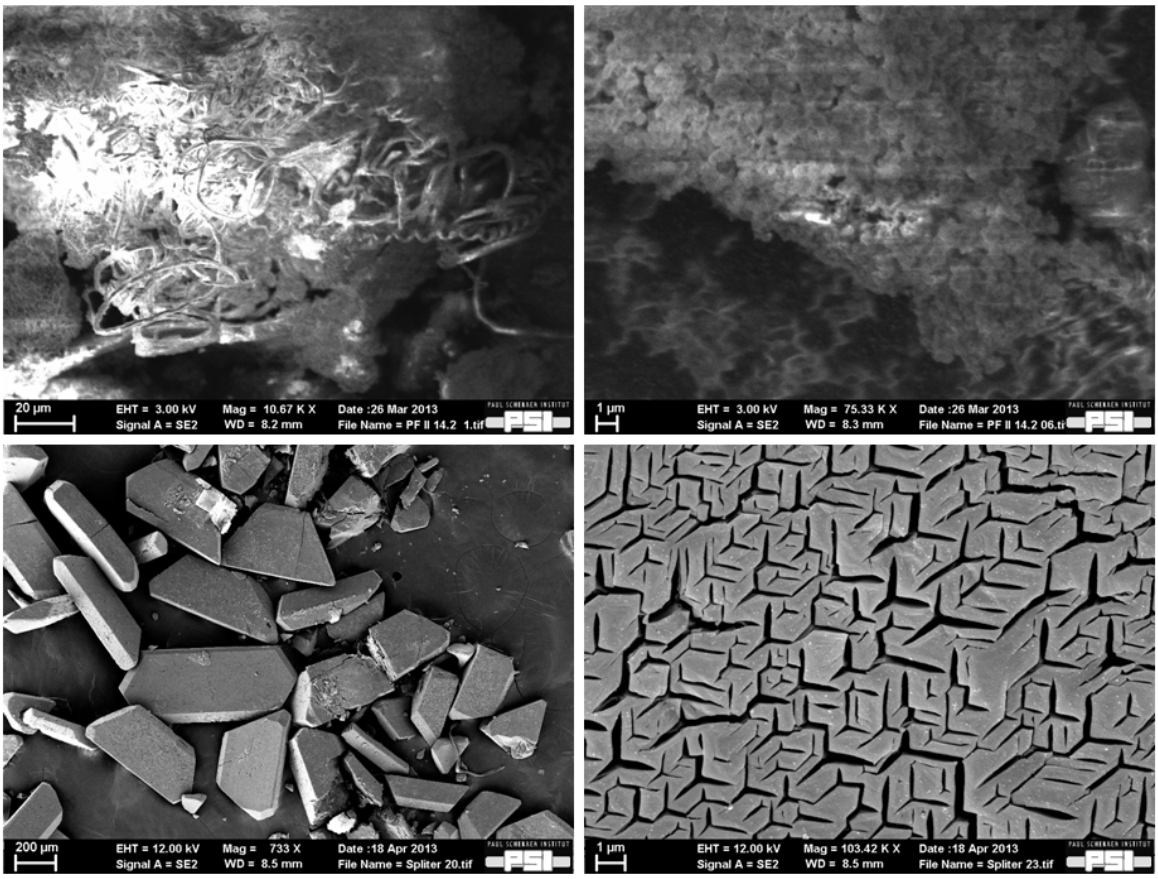

Figure 5-27: SEM images of the solids found in particle trap 2 of experiment L1 (top). Crystals containing magnesium and phosphorous (EDX) found in the salt separator effluent of experiment L3, right: close-up view.

The recovery of carbon during the experiment was fairly poor. Exemplarily the overall recovery of carbon has been quantified for experiment L1, including the carbon that was not recovered in the effluent samples. All flushing residues were collected for carbon quantification. In Figure 5-28 the carbon distribution over the extract phases of both effluent streams is shown. Additionally the carbon recovered by flushing the test rig with ethanol after cool-down can be seen. From this figure it becomes clear that almost half of the carbon did not leave the system under process conditions. The respective compounds are soluble in ethanol and have the typical smell of tars, similar to the material found on the filter (Figure 5-24). These tars is very likely responsible for the observed pressure fluctuations over the filters, since they become viscous after cool-down. It is unclear, whether they play a role in the pressure fluctuations observed in the hot zone (L3). The formation of sticky tars during hydrothermal conversion of lignin-rich biomass has already been reported for subcritical conversion processes by Elliott et al. where it led to plugging of transfer lines (see chapter 3.8). It was not mentioned if the respective sections were hot or cold [85]. Osada et al reported the formation of THF soluble residues by the

gasification of lignin and lignin-rich natural biomass at 400°C [82] (see section 3.5.3). Since the fermentation residue is a lignin-rich feedstock, these findings are in agreement with other groups.

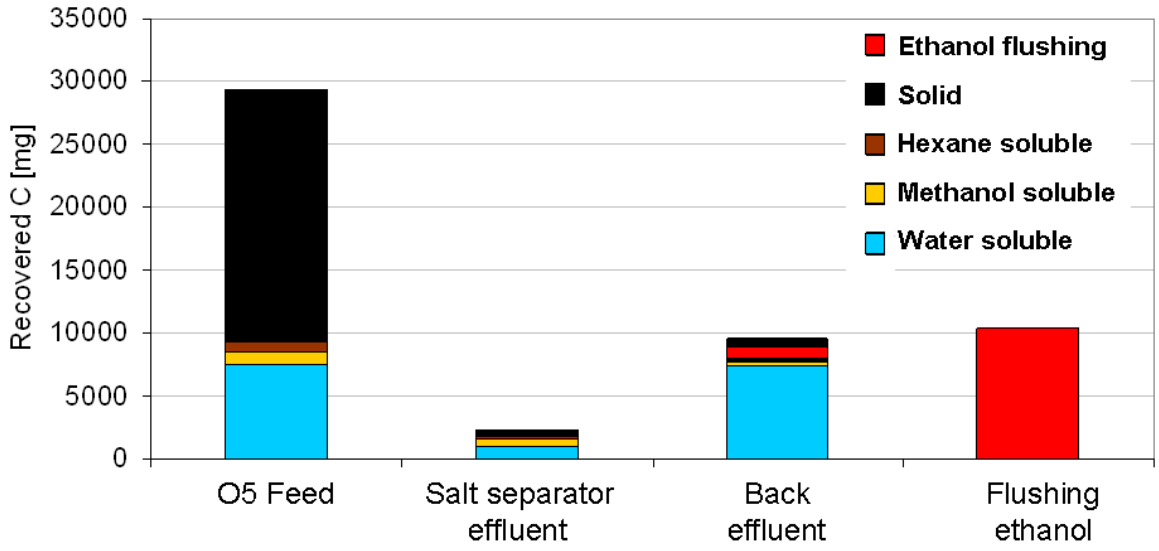

Figure 5-28: Carbon recovery for liquefaction experiment L1. The solid residue of the liquefied biomass was found in the respective particle traps and filters. "Ethanol flushing" refers to the amount of carbon that was dissolved by ethanol flushing of the whole system after cool-down.

The recovery of carbon after extraction of the effluent samples with hexane and methanol is shown in Figure 5-29. Even though the overall recovery is not satisfying, general trends are visible. Water soluble carbon compounds generally have a higher concentration in the back effluent. This can be explained by the fact that molecules that leave the salt separator at the top exit are more likely to dwell in the hottest zone of the salt separator. A rapid degradation occurs at supercritical conditions (see section 3.4.3).

The recovery of methanol soluble compounds is rather inconsistent between the experiments. Since experiment L1 and L3 were done at identical set point temperatures, a comparable sum of methanol soluble compounds from both streams would be expected. The inconsistency is very likely caused by the adhesive properties of tars that lead to a poor recovery from the plant.

Hexane soluble carbon is found in small amount in both effluent streams. In comparison, around 4 mg g^{-1} hexane soluble carbon was found in the reactor effluent stream of the gasification experiment towards the end of the run (see section 5.4.3). Note that in the liquefaction experiments the concentration is averaged over the run time due to the collective sampling. Also the amount of hexane soluble carbon of the feed was also higher for the sample used in the gasification experiment O4 (~10-20

mg g^{-1} including dilution). From the decrease between feed and effluents it can therefore be concluded that aliphatic compounds are at least to some extent degraded by un-catalytic conversion. A potential influence of alkali supplement leading to alkaline hydrolysis also has to be considered here (compare section 3.6.5).

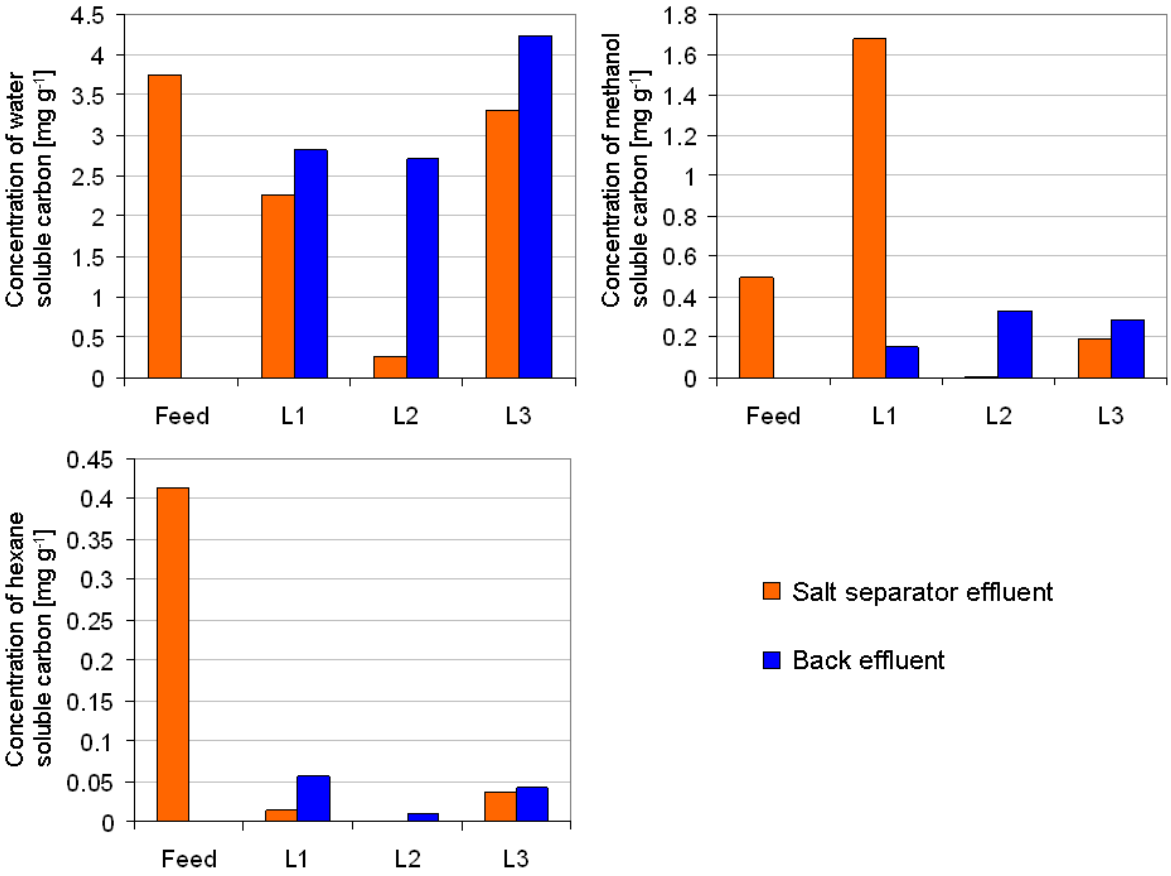

Figure 5-29: Carbon concentrations in the back effluent and salt separator effluent (collective sample), itemized by the extract phases.

5.5.3 Influence of the salt separator temperature

In experiments L2, the salt separator temperature was varied. The temperature profiles for water and fermentation residue under liquefaction conditions barely show any differences for the experiment L1 at 430°C (Figure 5-30). For L2 (470°C) the temperature profile appears slightly more balanced in the presence of biomass whereas the profile for pure water shows a distinct summit. This can be explained by mixing effects caused by the higher temperature difference between the incoming fluid jet and the salt separator. Peterson reported a deeper penetration and dispersion of the jet entering the salt separator in the case of high temperature difference [170]. Also the gas production which was slightly higher for experiment L2 could contribute to a mixing. The shape of the temperature profile could also

result from isolating deposits on the salt separator wall, which has been reported by Müller [19]. Generally, the temperature is some 10-15 K below the set point temperature at the maximum.

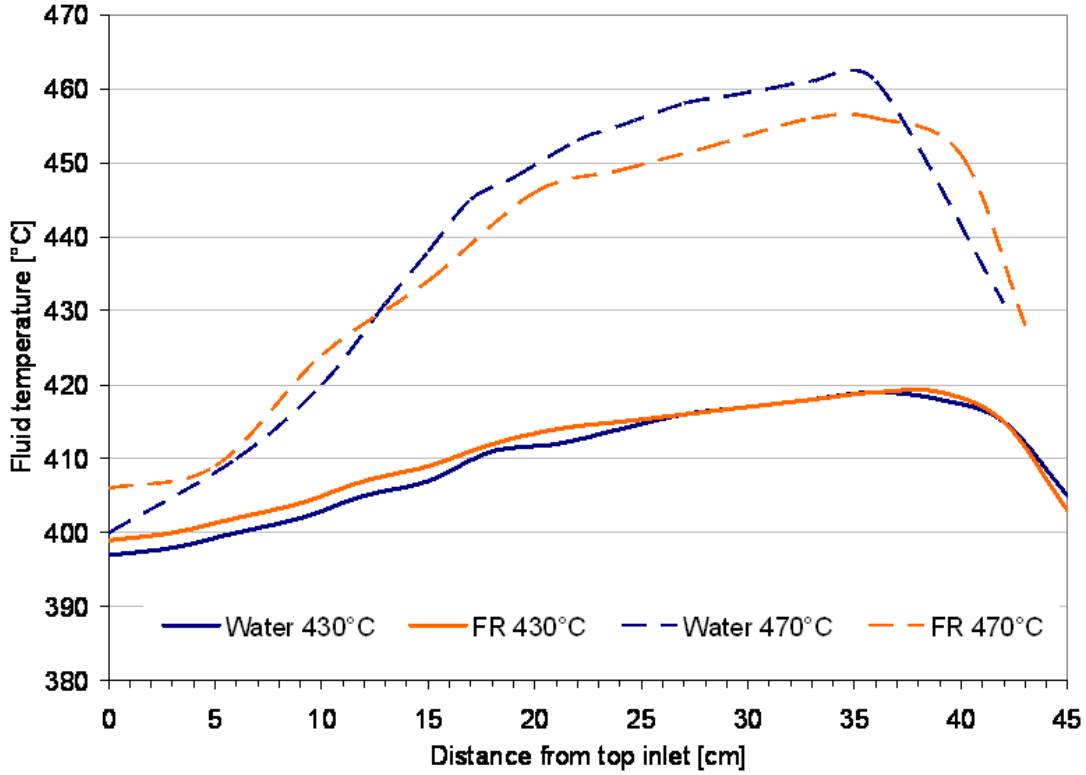

Figure 5-30: Axial temperature profiles in the salt separator starting at the top inlet of the dip tube; FR = Fermentation residue.

Even though experiment L2 had to be stopped prematurely, the slopes of the conductivities provide interesting results (Figure 5-31). While the conductivity of the back effluent rose faster for the high salt separator temperature, the increase was delayed for the salt separator effluent. However, no conclusions on the salt separation efficiency could be made, because no steady-state had been reached. Generally that salt separation is more effective at higher temperatures because of the lower fluid density. With the same salt separator this has been shown for pure salt solutions [19]. The initial trend of the conductivities could be explained by the mixing effects at higher temperatures mentioned earlier, however little is known about the fluid dynamics in the salt separator in the presence of biomass.

This experiment showed that a temperature of 460°C inside the salt separator at its hottest spot leads to massive tar formation and is therefore not recommended.

Since experiment L2 had to be interrupted prematurely, a comparison of the recovered effluent solution was obsolete. It was therefore not considered.

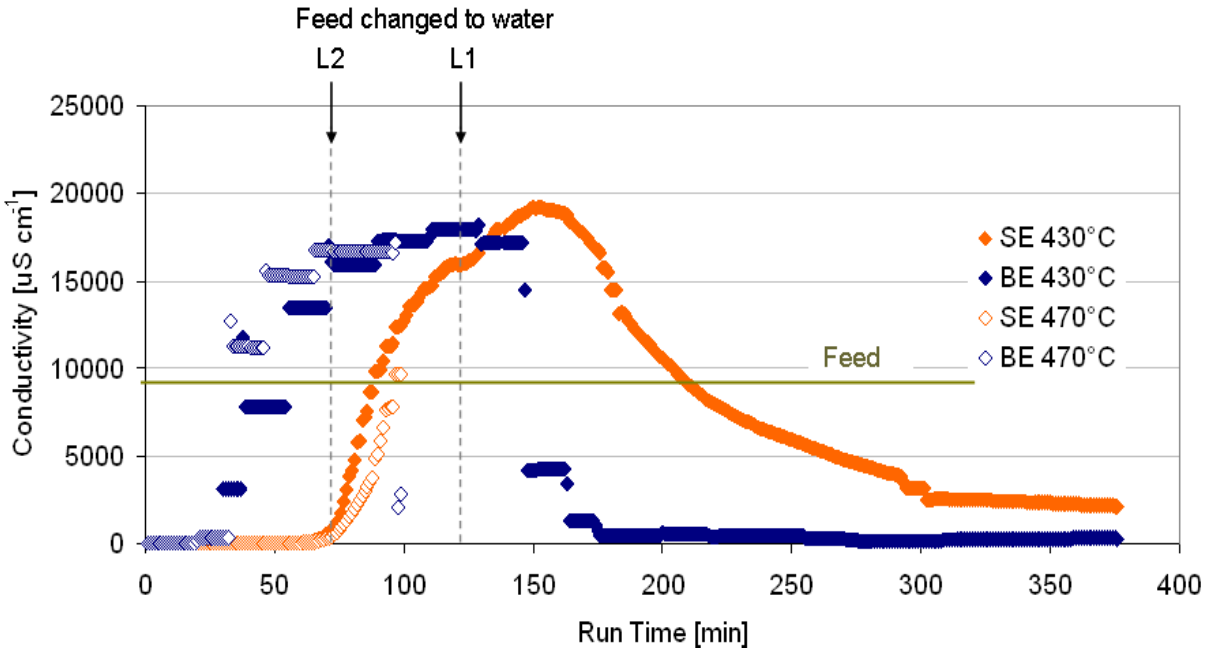

Figure 5-31: Conductivity of the salt separator effluent (SE) and of the back effluent (BE) over the run time for experiment L1 (430℃) and L2 (470° C).

5.5.4 Influence of the salt separator effluent flow rate

Experiments L1 and L3 were performed at different salt separator effluent flow rates. In Figure 5-32 it can be clearly seen that the conductivity of the salt separator effluent starts increasing earlier for the higher flow rate. This is most likely due to the shorter residence time in the salt separator outlet. The conductivity of the back effluent increases with a delay in comparison to the lower rate, but reaches the same level towards the end of the experiment. The final conductivities of salt separator effluent and back effluent are similar, indicating a poor salt separation. The fact that the conductivities of both effluent streams are higher than the conductivity of the feed can be explained by the formation of organic acids.

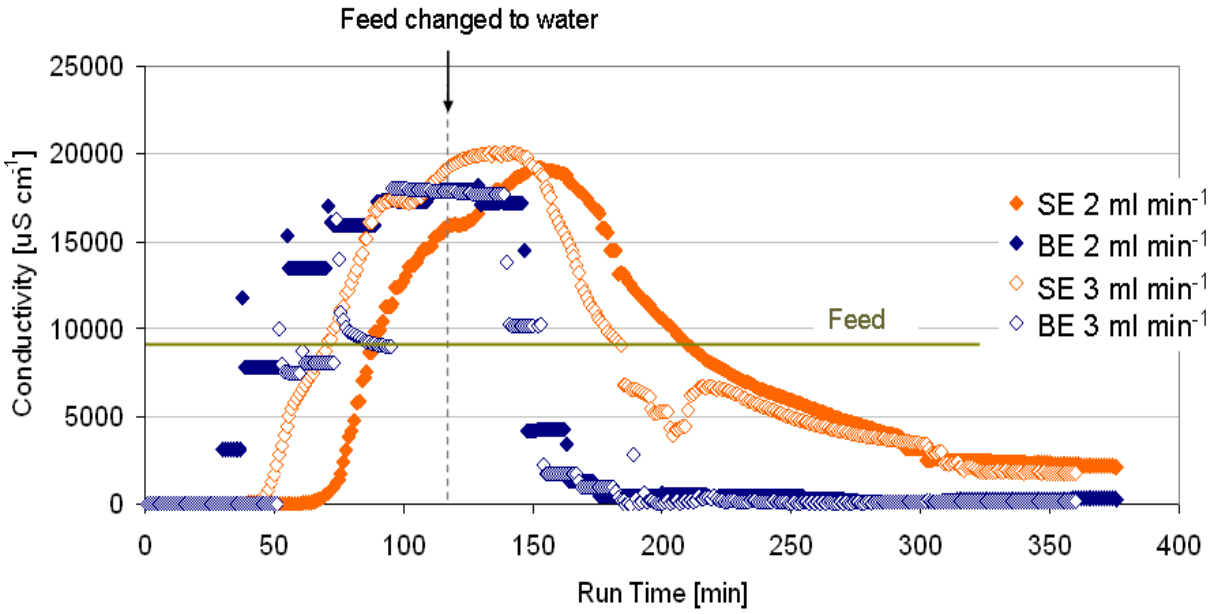

Figure 5-32: Conductivity of the salt separator effluent (SE) and the back effluent (BE) over the run time for experiment L1 (2 ml min^{-1}) and L3 (3 ml min^{-1}).

The separation efficiency of selected salts can be seen in the plot of concentrations in the collective samples (Figure 5-33). Potassium has a similar concentration in both effluent streams and is neither enriched nor depleted in comparison to the feed concentration. Magnesium is clearly depleted from the back effluent. A corresponding enrichment in the salt separator effluent could not be observed. All other minerals are depleted in both effluent streams. Interestingly they can also not be found in the salt separator effluent during cool-down. The only explanation for this is that the corresponding salts have formed solid phases that were still partially soluble at the given temperature. Note that the temperature at the lower part of the salt separator is sharply decreasing. During flushing at experimental conditions the deposits may therefore have slowly dissolved before the salt separator was cooled down after several hours. Compared to the results of the gasification experiment, where large amounts of salts were detected during cool-down we can conclude that a salt separator set point temperature of 430°C is not sufficient to remove potassium. Except for K_2SO_4 which is a type 2 salt, the most common potassium salts are type 1 salts (see section 3.4.2.2). Müller showed the beginning of a separation of K_2SO_4 at a set point temperature of 410°C. For binary and ternary type 1 salt solutions a considerable separation effect was visible at 440°C [19]. Schubert reported that at a temperature of 430°C the extent of separation was rather low and depended on the salt mixture [27]. The missing salt separation in the liquefaction experiments L1 and

L3 is therefore not in contradiction with these observation. A shift of the temperature necessary for a proper separation in the presence of biomass is also supposable. Organic molecules strongly influence the phase behavior of water and water-salt mixtures (see section 3.4.1.6). For a multi-component aqueous system the network of interactions is very complex and can hardly be predicted.

In this experiment a change in the effluent flow rate had no effect. From previous experiments by Schubert it is known that reduced flow rates typically increase the salt concentration in the salt separator effluent without influencing the separation efficiency [28]. For a process optimization a small effluent rate is advantageous because this would lead to a reduced loss of biomass. Noteworthy is that Schubert conducted the experiment at a salt separator set point temperature of 500°C and in the absence of biomass. The temperature of 430°C was obviously not high enough to cause any salt separation; therefore, different effluent rates would hardly make a difference.

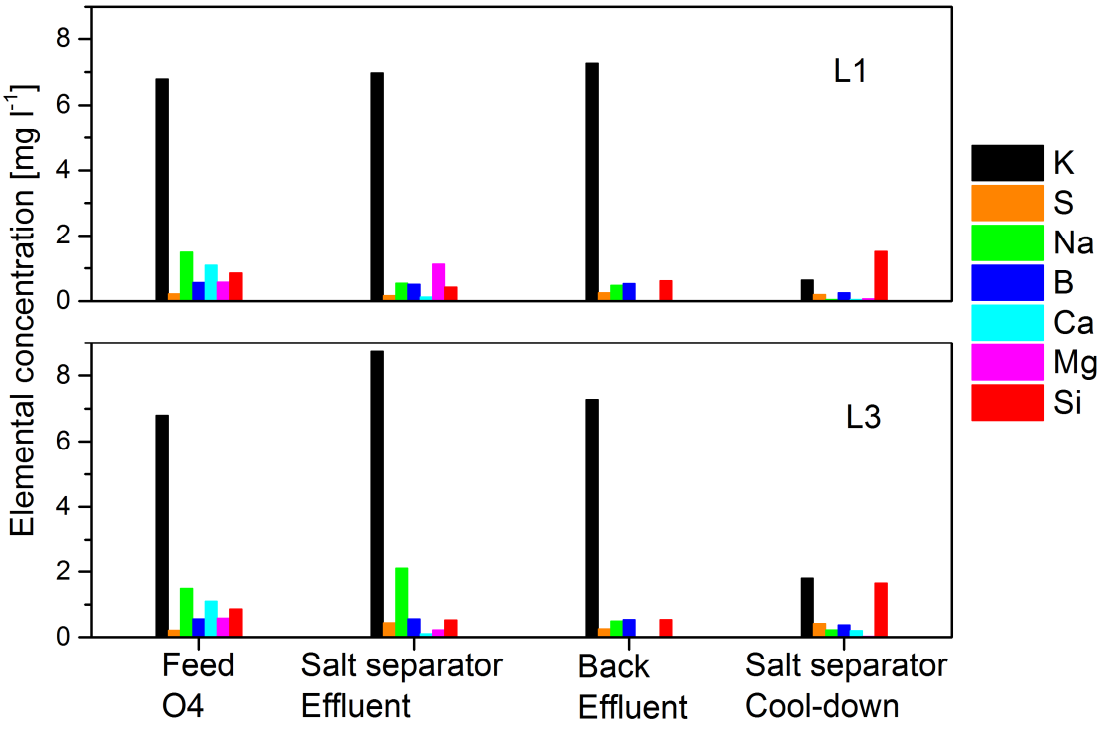

Figure 5-33: Distribution of minerals over the effluent streams of experiments L1 and L3 (Determined by ICP measurement).

5.5.5 Conclusion

These experiments showed that the liquefaction was partially successful. Some particles were not fully liquefied and passed the salt separator. Particles that left the salt separator from the top exit showed a higher carbonization level than the feed and the particles that were found in the salt separator effluent particle trap. They can therefore be considered as coke or coke precursors. If a catalytic reactor was present, these particles would be directed into the catalyst bed. This could lead to blocking of active sites and may be another reason for the rapid deactivation that was observed in the gasification experiment (discussed in section 5.4.5).

Sticky tars were produced in a high amount. Around half of the feed carbon did not leave the system. It could be removed by flushing with ethanol after cool-down. This observation suggests a poor miscibility of tars with water at 400-430°C and 28 MPa. The tars were probably formed in the preheater. Subcritical conditions were reported to promote tar formation [19]. A phase separation between highly condensed compounds (tars) and supercritical water could have occurred in the salt separator. This may have led to further condensation of the "tar-phase", resulting in the observed coke formation. A similar phenomenon of coke formation was reported for hydrothermal upgrading of heavy oils [151] (see section 3.8).

At a salt separator set point temperature of 430°C the salt separation was low. No difference was observed at different effluent rates. A temperature of 470°C instantly led to short-term blockings at different sections of the system. The experiment had to be stopped prematurely. The influence of a high temperture on the salt separation efficiency could thus not be determined. For the same reason no evidence could be given for influence of the temperature on the mineralization rate of sulfur.

It is concluded that high temperatures at comparably low pressures that are advantageous for salt separation promote the formation of tars and lead to a blocking of the system. A temperature of 430°C and a pressure of 28 MPa was not sufficient for salt separation, but still led to a considerable amount of tars and coke.

5.6 Investigations on the regeneration of catalysts deactivated by sulfur poisoning

(Parts of this chapter are based on experiments that were performed within the context of a bachelor thesis by T. Wölfl [172].)

5.6.1 Introduction

The previous sections have pointed out that a complete removal of sulfur from the biomass stream cannot be achieved solely by the existing process steps. The chemical environment inside the reactor is too complex to direct reactions by process parameters, only because requirements are conflictive for different reactions. But even if the mineralization of sulfur and the salt separation were successful, a small amount corresponding to the solubility of the respective salt in supercritical water would still enter the reactor. A sulfur absorbing material placed upstream of the catalyst bed could help avoiding catalyst poisoning, however, also such a material will become saturated over the time. Generally, a complete elimination of sulfur is nearly impossible to achieve with a reasonable effort. For this reason, a regeneration of the catalyst has to be considered.

An oxidative regeneration has already been tested by different members of our group. Waldner treated an in-situ sulfur poisoned 2% Ru/C catalyst in the test rig Konti-1 with 1wt% H_2O_2 solution at 30 MPa and 50-90°C and found the conversion to recovered first, but then steadily decreasing again over time [108]. Schubert et al. then tested three different regeneration methods with the same catalyst and setup: a method described by Osada et al. based on flushing with subcritical water [147], second a reductive regeneration with formic acid and third an oxidative regeneration, similar to the method tested by Waldner, but with the difference of using 2wt% H_2O_2 at a temperature of 125-200°C [60]. They solely found the oxidative regeneration to show a positive effect and interpreted this as a proof that the oxidation state of the poisoning sulfur is -2 or 0. A decreasing conversion of the regenerated catalyst over time was not reported as by Waldner, however, turbidities in the effluent occurring from time to time pointed to a limited conversion. Furthermore, the temperature profiles of the regenerated catalyst were between those of the fresh and the poisoned catalyst. Schubert et al. attributed this to an incomplete regeneration caused by a low contact frequency of the gaseous oxygen with the catalyst. Analytics of the catalyst revealed an enormous reduction of the BET surface

area and the MSA. Since the same catalyst was used for all three regeneration tests, it could not be stated which one was responsible for this change.

Taking up this issue, the in-situ poisoning and regeneration of the catalyst was repeated with the catalyst being characterized after every step. By this, the effect of the oxidative regeneration procedure on the structure of the catalyst system and on its performance was investigated. Here, the focus was on the technical feasibility of regenerating a catalyst bed of a considerable length (around 25 cm) rather than the processes at molecular level.

In parallel, Dreher et al. further elucidated the nature and mechanism of sulfur poisoning by in-situ XAS measurements of a 2% Ru/C catalyst. They found S^{2-} irreversibly adsorbed on the ruthenium surface with a coverage of 40% [71]. They also looked into the oxidative regeneration using a protocol similar to Waldner and Schubert and found the ruthenium to be fully oxidized to RuO_2 at a temperature of 100°C. The regenerated catalyst was fully reactivated. Dreher et al. used a catalyst bed of 0.2 g of 30 mm length [148], while the dimensions of the test rig Konti-1 allow experiments with around 10 g catalyst at a bed length of 20-30 cm. As a result of the capacity of Konti-1, the flow velocity velocities are by factor of around 2 lower than in the setup used by Dreher et al. Therefore, longer treatment times are necessary to reach comparable molar ratios of oxidizing agent and ruthenium.

Hence, oxidative regeneration leads to the oxidation of both, ruthenium (+II to +IV) and of the poisoning sulfide to sulfate, which is assumed to be flushed off the catalyst bed as H_2SO_4 because of its fairly good solubility in water. But why did the same method lead to an incomplete regeneration in the experiments performed by Waldner et al. and Schubert et al.?

In the following section, basically two approaches for answering this question were investigated. Both are founded on the fact that the catalyst bed`s mass used in the experiments of Waldner and Schubert et al. was about 50 times larger compared to Dreher et al. The first approach is the possibility of sulfate being adsorbed in the catalyst bed. A long catalyst bed would in this case increase the residence time of sulfate in the catalyst bed. Secondly, the oxidative treatment may lead to an attack of the support material in the top layer. This may lead to a loss of ruthenium in this section, while the oxygen is consumed and thus layers further downstream in the catalyst bed will not be regenerated.

The following questions should be answered by the tests described in this section.

- Is sulfate adsorbed on the catalyst bed under supercritical and near critical conditions?
- Is sulfate reduced in the presence of biomass or even solely by the carbon support?
- Which characteristics of the poisoned and regenerated catalyst may be responsible for the limited performance after regeneration?

A list of all continuous experiments can be found in Table Appendix C.

5.6.2 Preliminary tests on sulfate reduction

The role of sulfate in ruthenium poisoning is discussed controversially in literature. Osada et al. stated various types of sulfur including sulfuric acid acting as catalyst poison [147], while Schubert et al. and Dreher et al. affirm reduced sulfur species being the ones involved in deactivation phenomena [60, 148]. It has to be mentioned that using a batch apparatus in Osaka's experiments, the catalyst was exposed to the respective sulfur species in the presence of biomass. A reduction is therefore possible. Besides that, the presence of sulfate on the spent catalyst as detected by XPS in Osada's study may be due to oxidation of the sample after opening the reactor.

A simple test in a batch reactor was supposed to clarify whether sulfate is reduced by biomass. Furthermore it was tested whether the carbon support of a 2% Ru/C catalyst is able to reduce sulfate. This may occur by steam reforming of the support, formation of H_2 or methane via the WGS and methanation reactions and a subsequent reduction of sulfate by those.
In test SO4-1, the reactor was filled with 0.01 M K_2SO_4 solution and 6 g of 2% Ru/C. In test SO4-2, the 0.01 M K_2SO_4 solution was prepared with a 20 wt% glycerol solution. No catalyst was used in test SO4-2. The reaction time was 60 min for both experiments; both were performed at a sandbath temperature of 400°C and at 30 MPa. The product gas diluted in argon was analyzed for its H_2S content. For experiment SO4-1, the test was negative (<10 ppm). The product gas of experiment SO4-2 contained measurable amounts of H_2S.
GC-SCD measurements showed no signals for the liquid sample of experiment SO4-1, while a plethora of peaks was detected for experiment SO4-2. No

predominant compound was identified for SO4-2. At the retention times of the standard substances thiophene benzothiophene and dibenzothiophene no major peak was visible.

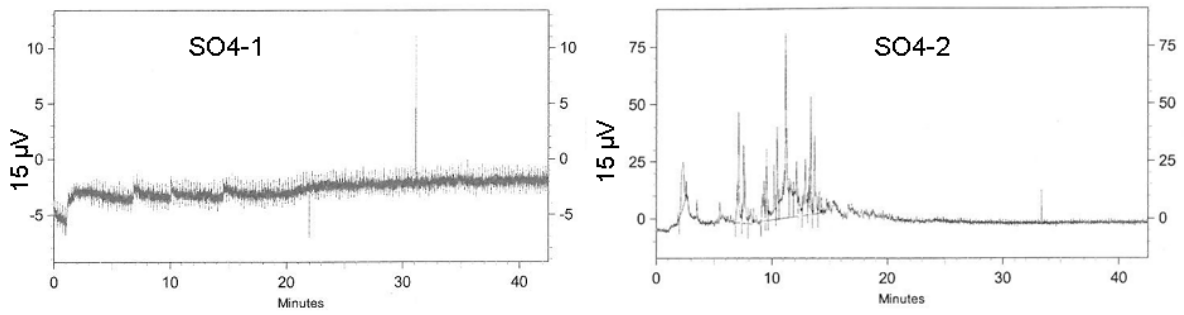

Figure 5-34: GC-SCD measurements of the liquid reaction products of experiments SO4-1 and SO4-2.

We conclude from this experiment that sulfate is reduced by biomass. It is therefore not surprising that sulfate can cause catalyst deactivation if biomass is present as it was the case in the experiment of Osada et al. However, a reduction of sulfate by the carbon support was not observed in this experiment.

5.6.3 In-situ treatment of a 2% Ru/C catalyst with K_2SO_4 in the absence of biomass

Based on the findings of the previous section and the aforementioned state of knowledge that reduced sulfur species present the actual catalyst poison, we would expect no poisoning effect of sulfate in the absence of biomass. To verify this, in the continuous test rig Konti-1 a thoroughly flushed 2% Ru/C catalyst (10 g) was treated with an aqueous 0.002 M K_2SO_4 solution at a flow rate of 5 ml min^{-1} under typical reaction conditions (400°C, 30 MPa, 4 h, experiment SC1). Afterwards it was again flushed with pure subcritical water (350°C, 16 h). In a control experiment gasification of a 10 wt% glycerol solution yielded only around 60 instead of the 100% carbon gasification efficiency obtained before the sulfate treatment (Figure 5-36). Also the gas composition pointed to non-equilibrium conditions (Figure 5-35). The experimental conditions were 400°C setpoint temperature and 30 MPa at a flow rate of 5 ml min^{-1}. Note that the temperature inside the reactor dropped to around 380°C during gasification.

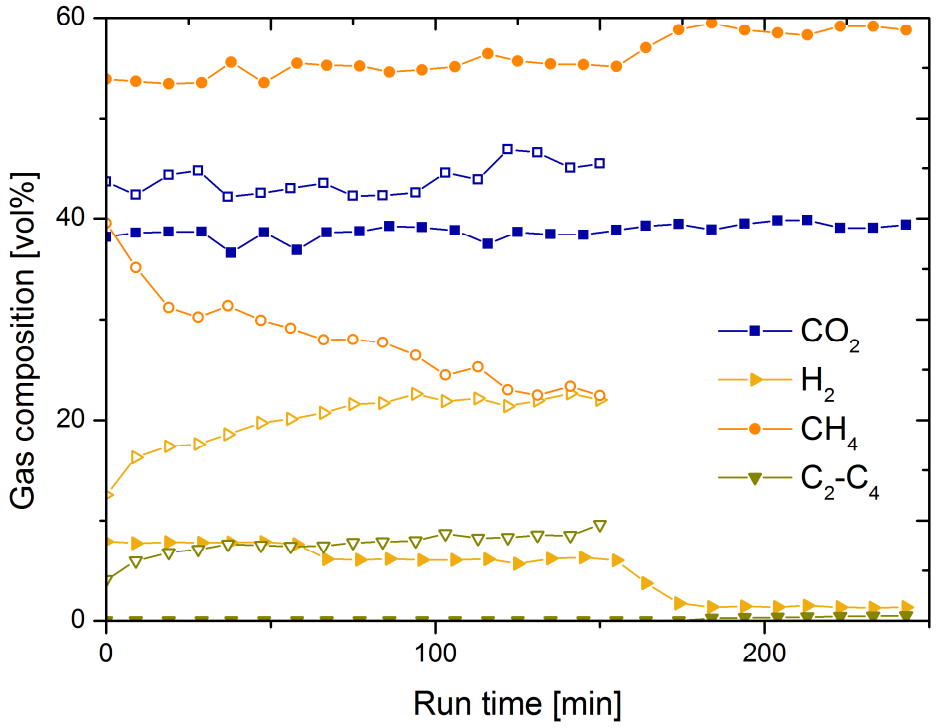

Figure 5-35: Gas composition for the gasification of a 10 wt% glycerol solution over a 2% Ru/C catalyst before (full symbols, SC1a) and after (open symbols, SC1c) treatment with a 0.002 M aqueous K_2SO_4 solution. The reaction conditions were 400℃ and 3 0 MPa (full symbols: 440℃ before t=150 min because of a temperature regulation error).

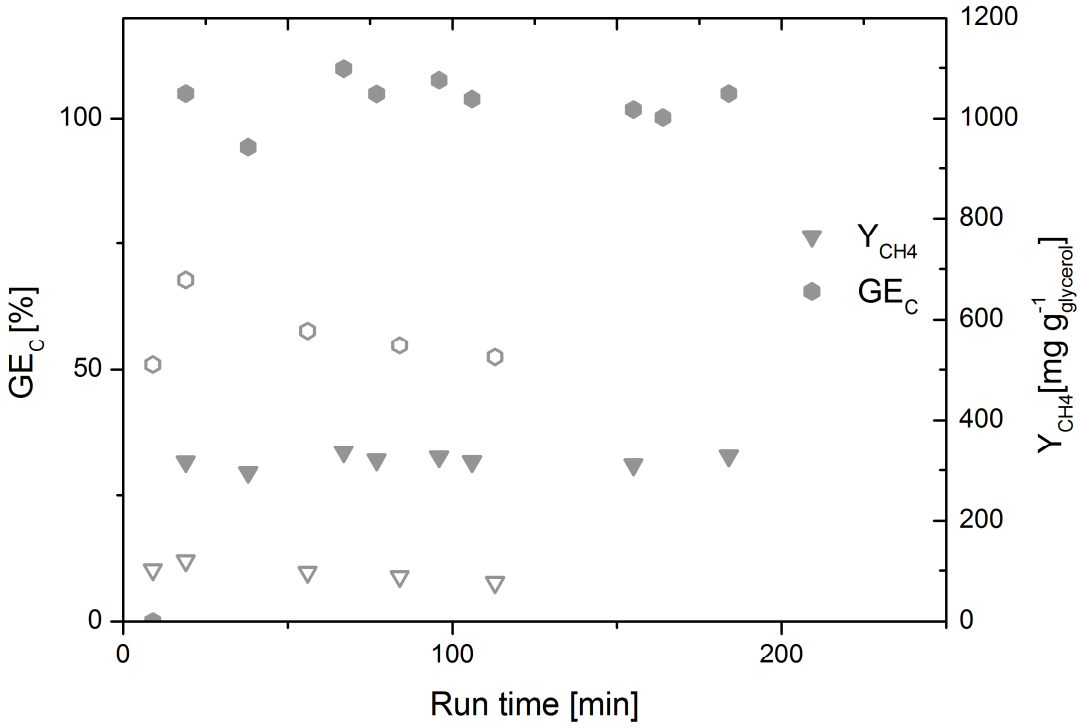

Figure 5-36: Gasification efficiency and methane yield for the gasification of a 10 wt% glycerol solution over a 2% Ru/C catalyst before (full symbols, SC1a) and after (open symbols, SC1c)

treatment with a 0.002 M aqueous K_2SO_4 solution. The reaction conditions were 400℃ and 30 MPa (full symbols: 430℃ before t=150 min because of a temperature regulation error).

Two possible explanations can be considered for this: first an adsorption effect of sulfate on the catalyst (metal or support). The adsorbed sulfate may or may not poison the catalyst as such. However, if the adsorption is strong enough, it will remain on the catalyst surface until organic molecules appear, reducing it. Then it will poison the catalyst. The identification of S^{VI} on a poisoned catalyst by ex-situ measurement of the sulfur K-edge XANES [71], even though it has been stated as negligible in amount, would be in agreement with this assumption. Secondly, some reforming of the catalyst may have occurred despite of the results from the batch experiment. During the treatment with K_2SO_4, traces of CO_2 with a decreasing tendency were detected in the effluent, supporting the reforming hypothesis (see Figure 5-37). Furthermore, a direct attack of sulfate, which is present as sulfuric acid in supercritical conditions [60], can be assumed, leading to the degradation of the support and thereby to the emergence of reduced sulfur species.

A sample of the catalyst was used for further analysis (sample 1).

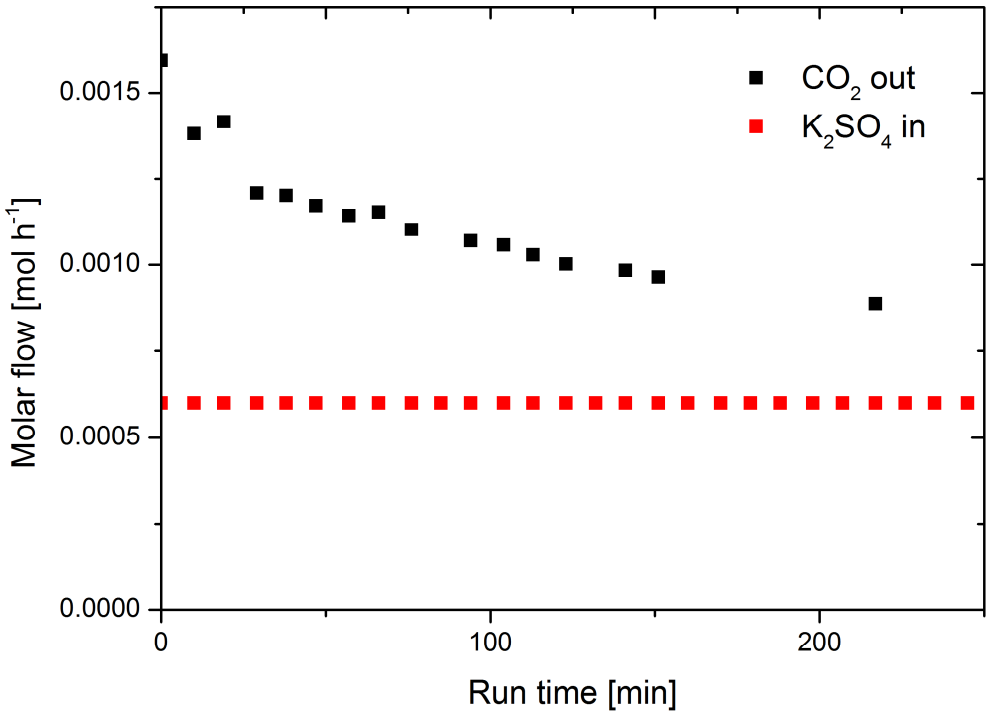

Figure 5-37: Molar flow rates of K_2SO_4 fed into the reactor at 400℃ and 30 MPa and CO_2 detected in the effluent (gaseous), experiment SC1b.

5.6.4 In-situ poisoning of a 2% Ru/C catalyst with K_2SO_4 in the presence of glycerol and oxidative regeneration

A 2% Ru/C catalyst (10g) was poisoned in-situ during gasification of a 20 wt% glycerol solution supplemented with K_2SO_4 at a concentration of 0.002 M (400°C/380°C, 29 MPa, 5 ml min^{-1}, experiment SC4). With a molar sulfur flow rate of 0.6 mmol h^{-1} and a ruthenium loading of 2 mmol in the reactor, t_2 = 198 min and with an exposed ruthenium amount of 0.25 mmol t_1 = 25 min were calculated following Equations 4-2 and 4-3 (section 4.4.4). The deactivation set in after around t_3 = 75 min as can be seen by a drop of the carbon gasification efficiency and a simultaneous shift of the gas composition away from the equilibrium (Figure 5-38). The required time t_3 is unexpectedly high, considering that a maximum surface coverage corresponding to $RuS_{0.33}$ and no bulk sulfidization was found by Dreher et al. [71]. We can therefore assume that either sulfate was not fully converted to sulfide or that not the total amount was adsorbed on the ruthenium surface. This is supported by an observed increase in the conductivity of the effluent before a full deactivation was reached. Possibly some sulfate was additionally adsorbed on the support and could therefore not act as catalyst poison.

The carbon gasification efficiency reached a rather constant level of 20% with a constant methane content of around 10%, which is higher than an uncatalyzed conversion (see section 5.7.3.2), pointing to some residual activity of the catalyst. This result is in accordance with Dreher et al. [71]. In the gasification experiment with fermentation residue, a constant level of methane was observed (see section 5.4.5).

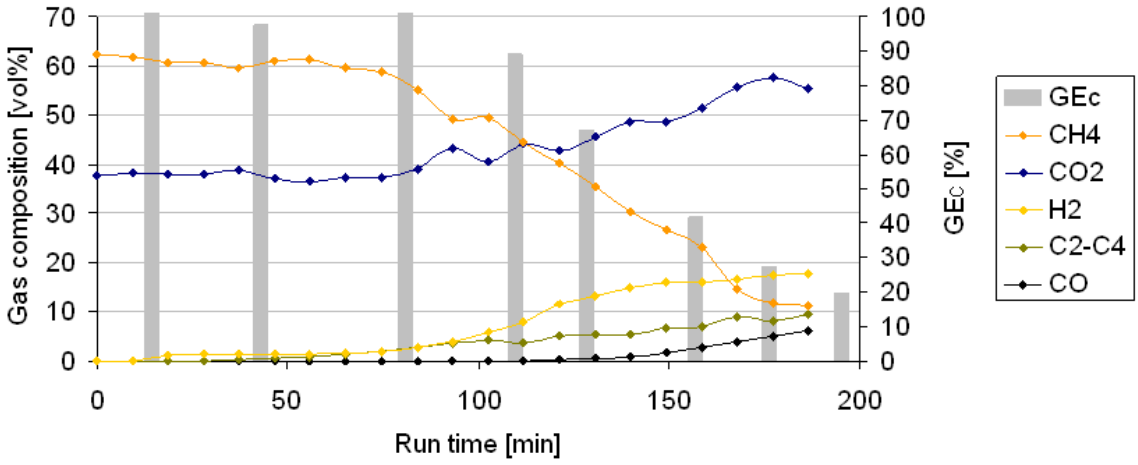

Figure 5-38: Gas composition and carbon gasification efficiency for in-situ poisoning of a 2% Ru/C catalyst with 0.002 M K_2SO_4 during gasification of a 10 wt% glycerol solution (400°C, 29 MPa, SC4).

The catalyst was removed from the reactor for further analysis (sample 2). The same procedure was repeated with a fresh catalyst loading (experiment SC5). After flushing for several hours, the temperatures were set to 125°C. Regeneration was done with a 2% H_2O_2 solution for 150 min. The temperature inside the reactor rose to 130°C, presumably because of the exothermic decomposition of H_2O_2. After regeneration, the catalyst was again thoroughly flushed. A control gasification experiment of a 10 wt% glycerol solution showed the same behavior as reported by Waldner [108]: first, the carbon gasification efficiency and gas composition were similar to experiments with a fresh catalyst; then a gradual decrease and shift away from the equilibrium was observed over the time (Figure 5-39). The regenerated catalyst was removed for further analysis after the experiment (sample 5).

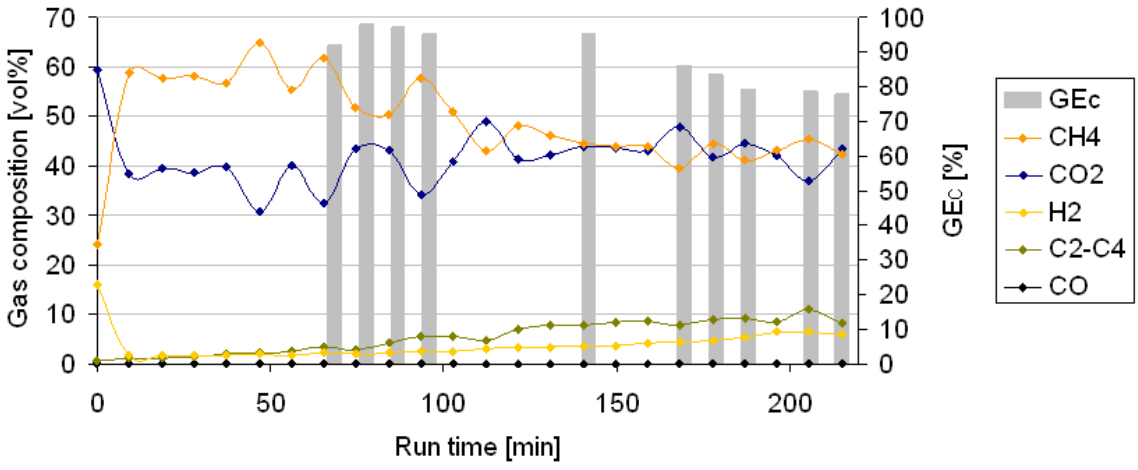

Figure 5-39: Gas composition and carbon gasification efficiency during gasification of a 10 wt% glycerol solution over a 2% Ru/C catalyst after in-situ sulfur poisoning and oxidative regeneration by a 2% H_2O_2 solution at 125℃ for 150 min (400℃, 28 MPa, expe riment SC5).

In a further experiment, regeneration with a 3% H_2O_2 solution, also at 125°C, was tested (experiment SC3). The duration of the treatment was reduced to 70 min because of a measurable CO_2 evolution. This method led to an improved regeneration effect, even though the molar ratio $n(H_2O_2)/n(Ru)$ was lower compared to the experiment SC5 (see Table Appendix C). As it can be seen in Figure 5-40 the carbon gasification efficiency decreased at a lower rate. Also the shift in the gas composition was less pronounced. The catalyst was again removed from the reactor for inspection (sample 3).

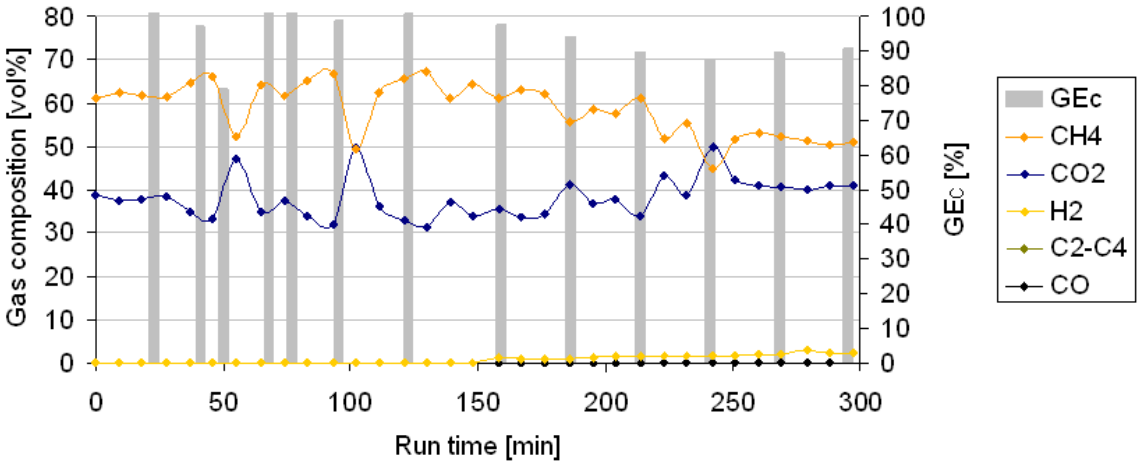

Figure 5-40: Gas composition and carbon gasification efficiency during gasification of a 10 wt% glycerol solution over a 2% Ru/C catalyst after in-situ sulfur poisoning and oxidative regeneration by a 3% H_2O_2 solution at 125℃ for 70 min (400℃, 30 MPa, exper iment SC3).

A further increase in the H_2O_2 concentration is expected to have a detrimental effect on the catalyst support. Since activated carbon is not stable against strongly oxidizing agents, its decomposition is likely. The evolution of CO_2 during regeneration with the 3% H_2O_2 solution points to such a degradation.

A test under more extreme conditions was done in order to gain a better assessment of the catalyst system's stability against the oxidizing environment. A fresh catalyst was treated with a 2% H_2O_2 solution at 125°C for 180 min (experiment SC4). The catalyst sample recovered after this test is referred to as sample 4.

A visual inspection of the regenerated catalyst samples revealed some change for the catalyst layer directly below the top inlet of the reactor (Figure 5-41). The metallic luster of the fresh catalyst had vanished and the surface appeared dull and showed some cracks (Figure 5-41). In sample 4 the surface was heavily cracked and the catalyst bed had even visibly shrunk by few centimeters in height. Samples 1 and 2 that were poisoned but not regenerated, exhibited different characteristics. The surface was apparently intact, yet less lustrous than the fresh one. White spots, supposedly stemming from attrition of the ZrO_2 pellets placed upstream or even from precipitated salts, were visible.

Figure 5-41: Photographs of spent catalyst samples 1-5 (see Table 5-3). Samples were taken from the top layer of the catalyst bed.

Table 5-3: List of 2% Ru/C samples with the respective poisoning and regeneration conditions and the corresponding BET surface area (BET SA) and metal surface area (MSA) as determined with gas sorption methods (see section 4.7.8). Sample 6 represents the fresh catalyst. (1) Actual measured temperature inside the reactor 130°C; (2) poor linear fitting.

Sample No.	Poisoning conditions (+0.002 M K_2SO_4)	Regeneration conditions	BET SA [m^2 g^{-1}]	MSA [m^2 g^{-1}]
1	400℃, no biomass, 4 h	-	1098	0.1 (2)
2	400℃, 10% glycerol, 3.5 h	-	869	0
3	460℃, 10% glycerol, 5 h	125℃ (1), 3% H_2O_2, 70 min	886	0.4 (2)
4	-	125℃ (1), 2% H_2O_2, 180 min	1123	0.9
5	400℃, 10% glycerol, 3.5 h	125℃ (1), 2% H_2O_2, 150 min	1208	0.3 (2)
6	Fresh catalyst, not poisoned	-	1194	1.2

Nitrogen physisorption measurements point to a minor decrease of the surface area of the sample poisoned in the presence of organics (2) and the sample regenerated by a 3% H_2O_2 solution (3). For sample 2, the decrease can possibly be explained by a blocking of pores by carbon deposits, which arose from incomplete reforming.

Carbon deposits could not be measured by TPO because they could not be distinguished from the carbon support. For ruthenium on ceramic supports such deposits were found (see 5.7.3.4). For sample 3, the reason for the decreased surface area is most likely the harsh regeneration procedure burning off the outer layer of the grain (compare Figure 5-41). A change in the BET surface area as a result of carbon degradation can, however, not easily be correlated to the amount of degradation. Degradation may either lead to a decrease or to an increase of the surface area. The latter can be explained by a better accessibility of some pores or the creation of additional pores.

The metal surface area of all samples that had been poisoned was significantly smaller than the one of the fresh catalyst. For samples 1 and 2, which had not been regenerated, it was even close to zero. The decreased metal surface area after regeneration can be explained by a decrease of the ruthenium loading (leaching) or by an incomplete regeneration.

Sample 4 which had only been treated with 2% H_2O_2 without a preceding poisoning showed a lesser decrease of the metal surface area. From this we can conclude that the decrease in the metal surface area of poisoned and regenerated catalysts resulted from an incomplete regeneration rather than from ruthenium leaching caused by the burn-off of the support. However, some contribution by ruthenium leaching cannot be excluded. This could only be clarified by a quantification of ruthenium. A partial regeneration of the catalyst by oxidative treatment was found.

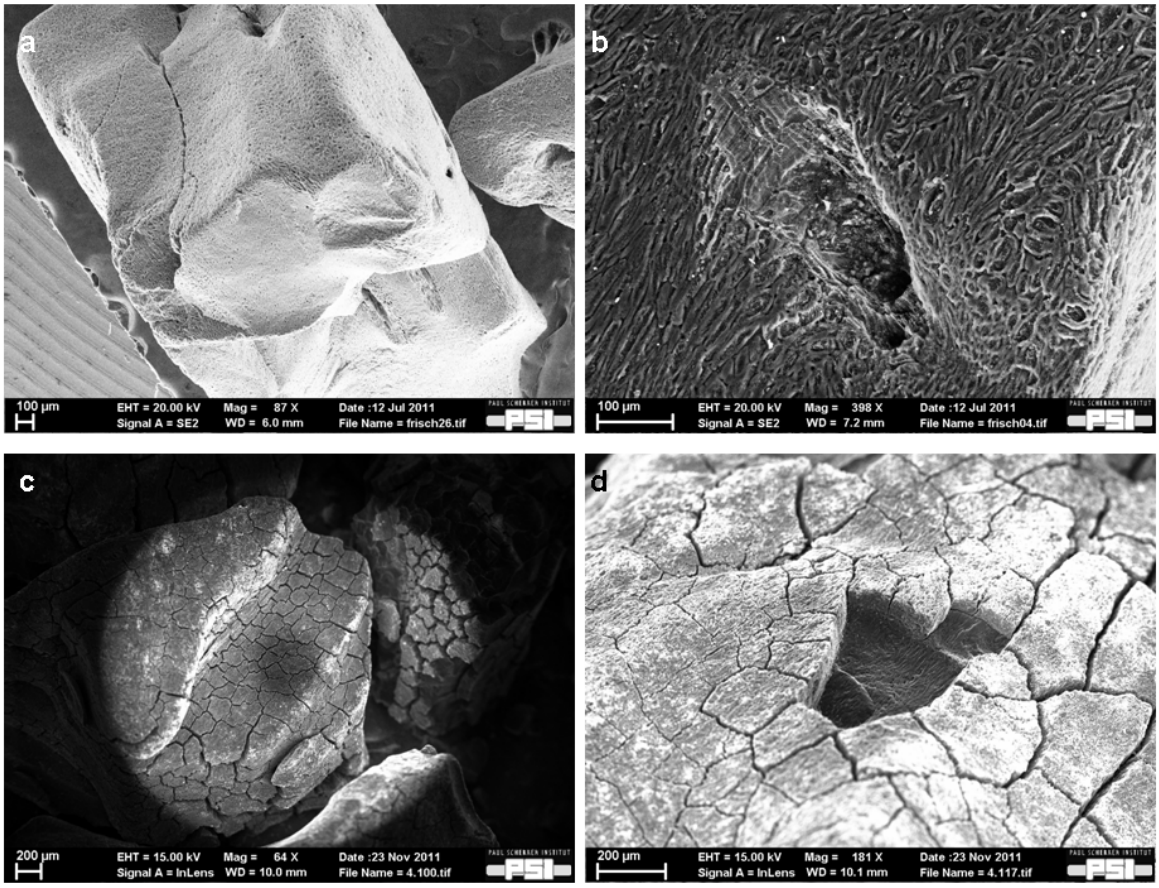

Figure 5-42: SEM images of a fresh (top) and spent (bottom) 2% Ru/C catalyst after treatment with a 2% H_2O_2 solution at 125℃ over 3h in a continuous reactor (sample 4). Left: entire catalyst grain; right: closeup view of the surface structure. The hole in (b) is given by the organic structure of the precursor material (coconut shell). In (d) the surface is flaked off.

The visual appearance of the magnified surface of the fresh and spent catalyst (sample 4) by SEM differed significantly (Figure 5-42). Whereas the surface of the fresh catalyst exhibited a tissue-like structure documenting the organic origin of the material (pyrolyzed coconut shell), the spent sample appeared as if the top layer had been abraded. The whole surface was covered with fine and coarse cracks. Crystals were visible, scattered on the surface of the grain (Figure 5-44). These crystals appeared bright by back scattered electron imaging. At some spots underneath the cracked top layer of the grain, needle-like structures were found. These structures also appeared bright by back scattered electron imaging. Via EDX measurement they were identified as ruthenium. It appears that these ruthenium needles present a cast of the pores in a carbon framework that had been burned off (Figure 5-43). However it is unclear, why they are present in a coherent structure.

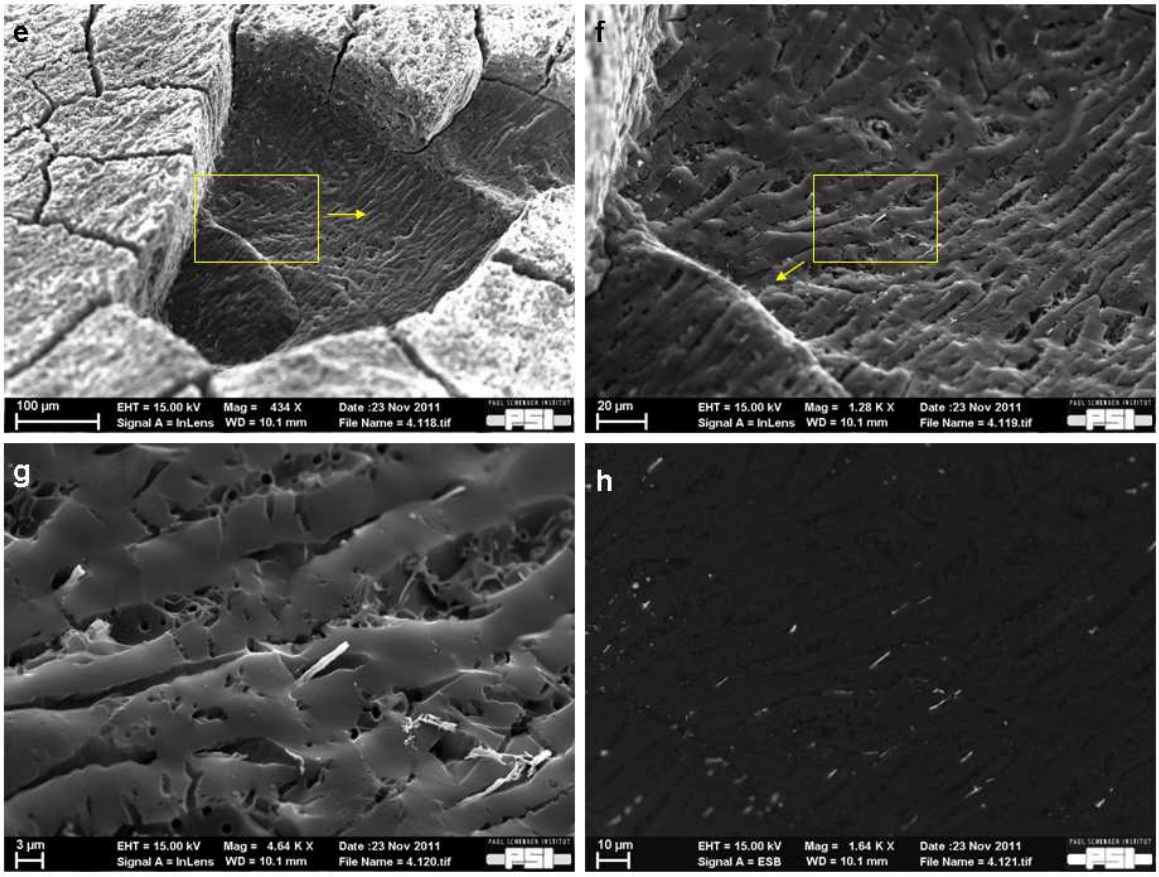

Figure 5-43: SEM images of a 2% Ru/C catalyst after treatment with a 2% H_2O_2 solution at 125℃ over 3 h in a continuous reactor (sample 4). e-g: zooming into a spot underneath the spent top layer. h: section g with backscattered electron detection.

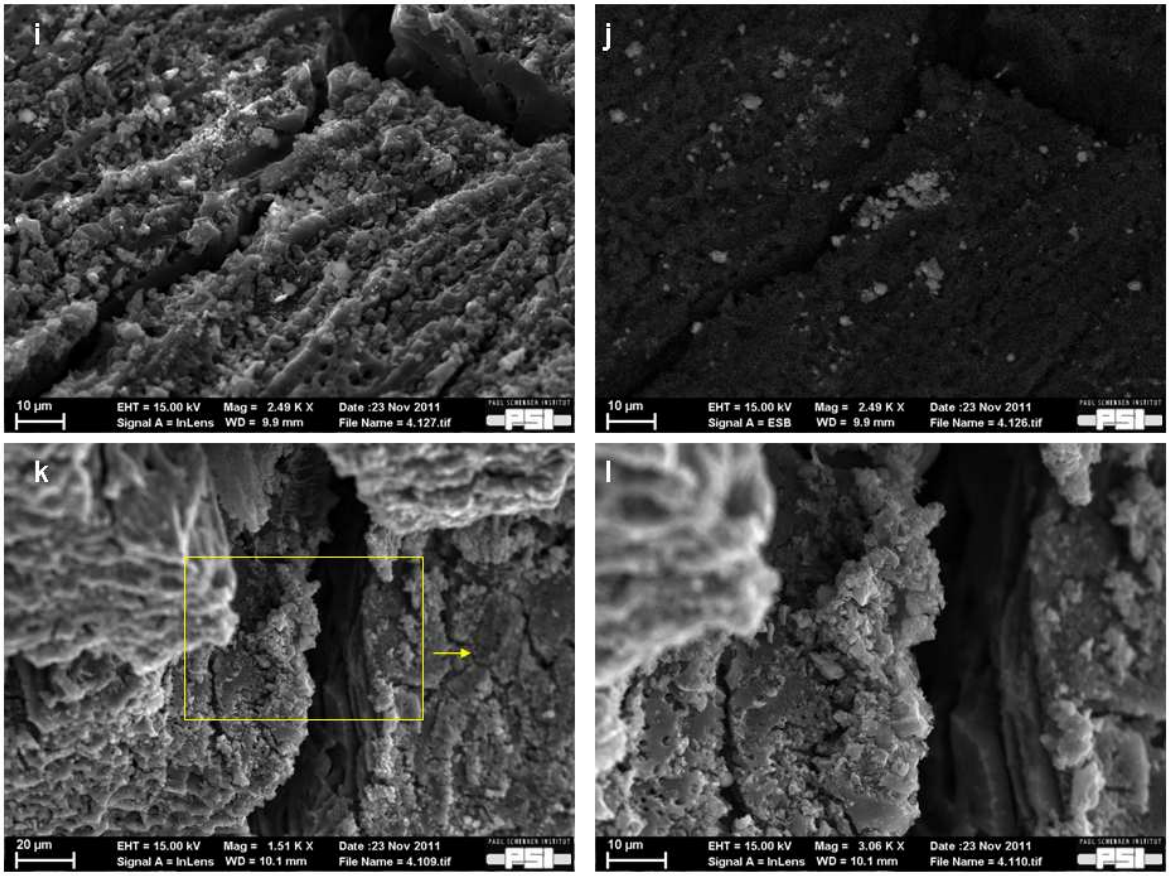

Figure 5-44: SEM images of a 2% Ru/C catalyst after treatment with a 2% H_2O_2 solution at 125°C for 3 h in a continuous reactor (sample 4). i: crystals (Ru and Zr by EDX) on the surface. j: section i with backscattered electron detection. k: crack with crystals. l: close-up view of k.

Also sulfur poisoned catalysts were damaged by the oxidative treatment. The oxidative regeneration with a 3% H_2O_2 solution for 70 min (Figure 5-45, m+n), however, had a lower impact than with a 2% H_2O_2 solution for 150 min (Figure 5-45, o+p).

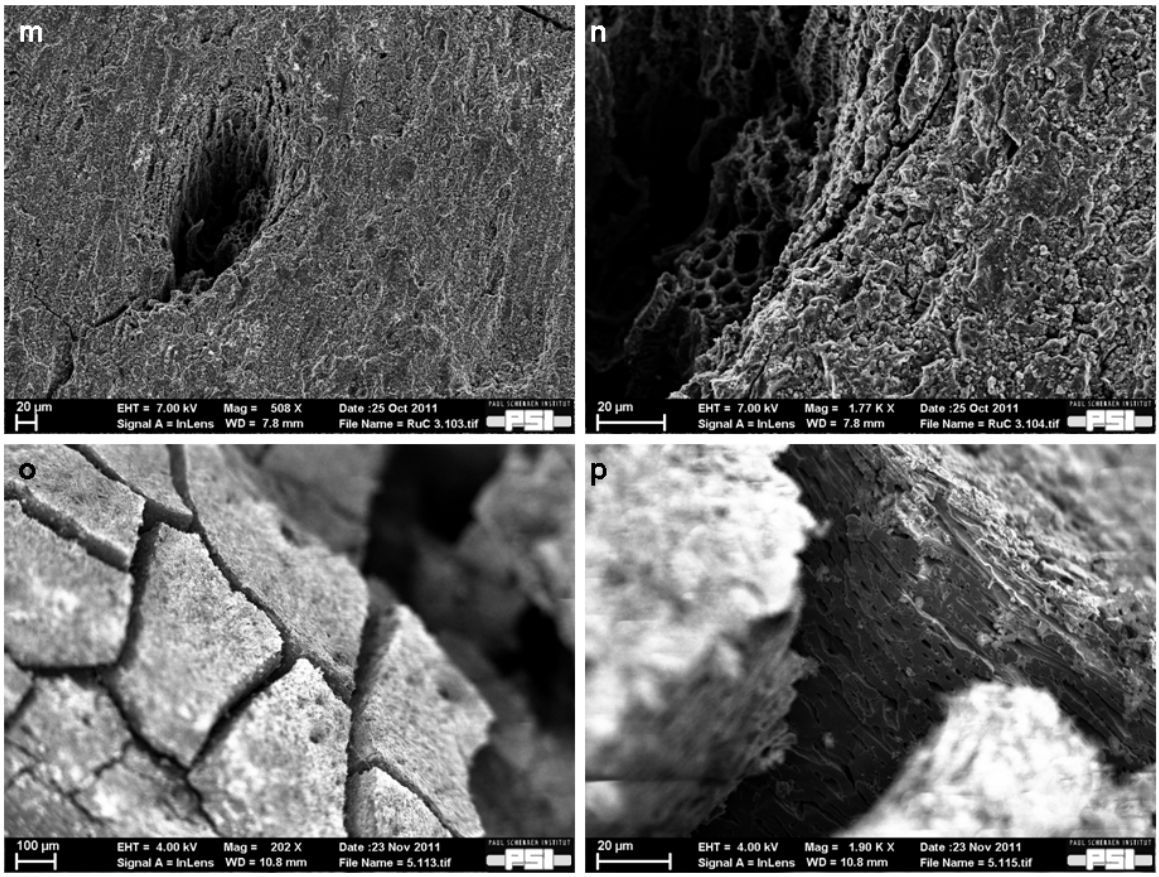

Figure 5-45: SEM images of a 2% Ru/C catalyst after treatment with a 3% H_2O_2 solution for 70 min (sample 3, top row) and with a 2% H_2O_2 solution for 150 min (sample 5, bottom row) at 125°C in a continuous reactor. m: pore from organic precursor material with cracks. n: close-up view of m. o: cracks. p: close-up view of o (with organic capillaries in sectional view).

5.6.5 In-situ poisoning of a 2% Ru/TiO_2 catalyst with K_2SO_4 in the presence of glycerol and regeneration methods

As the results of the previous section revealed, the carbon support is obviously not suitable for oxidative regeneration methods. Other hydrothermally stable materials and catalyst systems based on refractory oxides will be discussed in section 5.7. Those materials are more stable towards an oxidizing environment. Thus, a 2% Ru/TiO_2 (rutile) catalyst was tested for its behavior during poisoning and

regeneration, similar to the procedure described for the 2% Ru/C catalyst (experiment ST1). It has to be mentioned that the 2% Ru/TiO_2 catalyst's performance in terms of highest WHSV leading to full conversion was lower compared to the commercial 2% Ru/C catalyst. A glycerol concentration of 5% could be converted at nearly 100% carbon gasification efficiency over 24 hours. Therefore, the poisoning experiments and control experiments after regeneration were done at a glycerol concentration of 5% for this catalyst.

Because of the higher bulk density of the TiO_2 support, a mass of 31 g of the catalyst was used for a catalyst bed length comparable to the experiments done with 2% Ru/C. With the same molar sulfur flow rate of 0.6 mmol h^{-1} and a ruthenium loading of 6.2 mmol in the reactor, t_2 = 10.3 h and with an exposed ruthenium amount of 0.074 mmol t_1 = 7.4 min were calculated following Equations 4-2 and 4-3 (section 4.4.4). The deactivation set in after around t_3 = 60 min. This is surprisingly in the same order of magnitude compared to the 2% Ru/C catalyst, even though the total amount of ruthenium was considerably higher and the amount of exposed ruthenium likewise lower. The only parameter that was in the same order of magnitude for both experiments was the catalyst bed length.

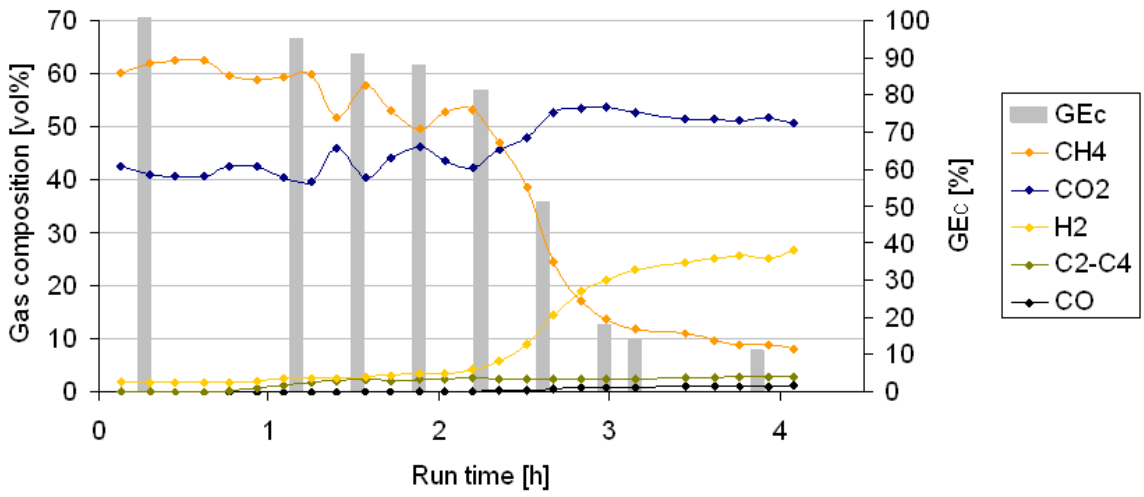

Figure 5-46: Gas composition and carbon gasification efficiency during in-situ poisoning of a 2% Ru/TiO_2 catalyst with 0.002 M K_2SO_4 during gasification of a 5 wt% glycerol solution (400°C, 30 MPa, experiment ST1a).

The results from Osada's method [147], based on flushing with subcritical water, are questionable, because the catalyst had been poisoned ex-situ (see section 3.7.4). It is therefore unclear, whether the sulfur was already washed off the catalyst during wettening with water or effectively by the supercritical flushing. Osada et al. used a

Ru/TiO_2 catalyst. Since Schubert et al. were not successful regenerating a Ru/C catalyst poisoned in-situ by this method, it is unclear whether this had to do with Osada`s experimental setup or with the type of catalyst they used. Hence, we repeated the regeneration method with the 2% Ru/TiO_2 catalyst. During flushing at 300°C over four hours, a very slight increase in the effluent's conductivity was registered.

The result of the control gasification experiment (400°C/360°C, 28 MPa, 5 g min^{-1}, 5wt% glycerol) was indeed surprising (Figure 5-47): even though a complete regeneration could not be achieved, the carbon gasification efficiency had increased from around 10 to 70% and the gas composition was near the thermodynamic equilibrium. The reversibility of the Ru-S binding in the case of a TiO_2 support in contrary to the carbon support points to a difference in the chemical environment of the Ru-S binding in both systems. Ammonia desorption measurements give a higher ammonia uptake for TiO_2 compared to 2% Ru/C if normalized to the BET surface area of meso- and makroporous structures and to the sample weight (Table 5-4). 92% of the surface area of the carbon support are mikropores [28]. Meso- and makropores are accessible for ammonia (>2 nm). The neat support of the Ru/C catalyst was not available for measurement. However, only a minor fraction of the support is covered with ruthenium. From the striking difference of the ammonia uptake per accessible surface area it can be concluded that the acidity of the TiO_2 support is higher than of the carbon support. The acidity of the support may influence the electronic environment of ruthenium on the respective support materials and may thus lead to the observed difference in binding strength. Further clarification of this phenomenon can only be given by more sophisticated analytical tools (e.g. XAS).

Anyhow, the recovered conversion was not stable. After three hours, the carbon gasification efficiency had already dropped to 40% and the gas composition shifted away from the equilibrium.

Table 5-4: Ammonia uptake determined by ammonia desorption measurements. (mes): excluding BET surface area of microporous structures.

Sample	Ammonia uptake [µmol]	Sample weight [mg]	BET SA [$m^2 g^{-1}$]	BET $SA_{(mes)}$ [$m^2 g^{-1}$]	Ammonia uptake [µmol $m^{-2}_{(mes)}$]
2% Ru/C	0.4	42.5	1194	96	0.1
TiO_2	0.5	51.7	3.9	3.9	2.5

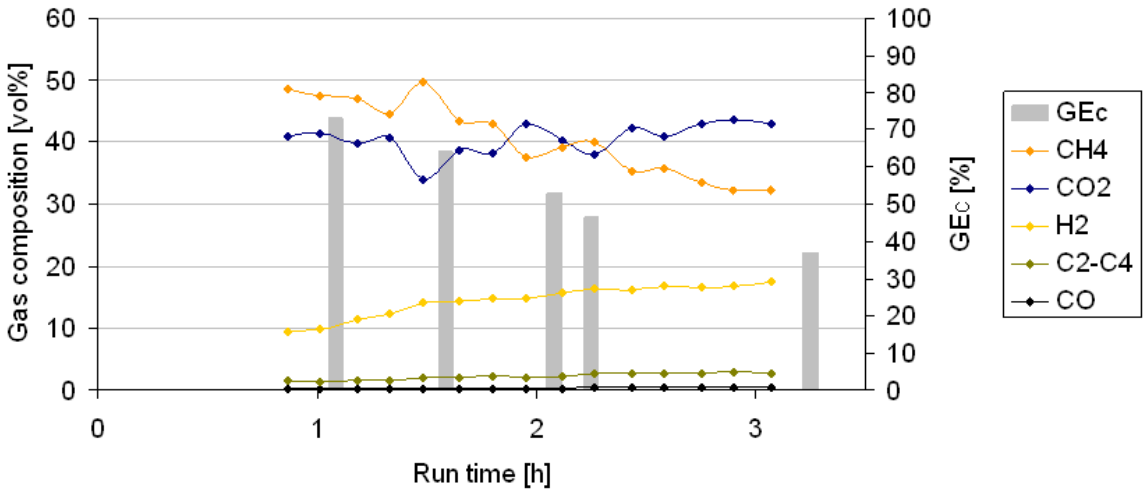

Figure 5-47: Gas composition and carbon gasification efficiency during gasification of a 5 wt% glycerol solution over a 2% Ru/TiO_2 catalyst after in-situ sulfur poisoning and regeneration by subcritical flushing at 300℃ for 4 h (400℃, 30 MP a, experiment ST1c).

The oxidizing regeneration with a 2% H_2O_2 solution at 125°C/130°C for 120 min led to a full recovery of the conversion at equilibrium product gas composition (Figure 5-48). But again it was not stable on the long term. The decrease was less dramatic compared to the Ru/C catalyst, but still after 18 h only 40% of the original carbon gasification efficiency was observed. It has to be mentioned that the molar ratio n(H_2O_2)/n(Ru) was around 3 times lower than for the regeneration experiments with Ru/C. The regeneration was thus more effective. A decrease of the metal surface area of the regenerated catalyst could not be determined because the accuracy of the chemisorption measurement was low for the low MSA of 2% Ru/TiO_2 samples (see Table 5-5). Harsher regeneration conditions (e.g. higher H_2O_2 concentration) have not been tested but may lead to better regeneration results. A reason for the decreasing metal surface area can also be a leaching of ruthenium. Since the ruthenium content of the catalyst grain has not yet been determined with good accuracy, the question remains unresolved. The constant BET surface area points to the stability of the support material in the oxidative environment (Table 5-5). The visual appearance of fresh, used and regenerated catalyst pellets differed only marginally (Figure 5-49). The grey color had become slightly paler and traces of attrition are visible for both, the catalyst pellets that were used for gasification only, and the ones that were poisoned and regenerated. The similarity of the used and the regenerated catalyst points to some minor alteration of the surface structure at the first contact to the hydrothermal medium, but no further changes even by oxidative regeneration

conditions. SEM images of the fresh and regenerated catalyst look similar (Figure 5-50). A structural change of the support material could not be observed.

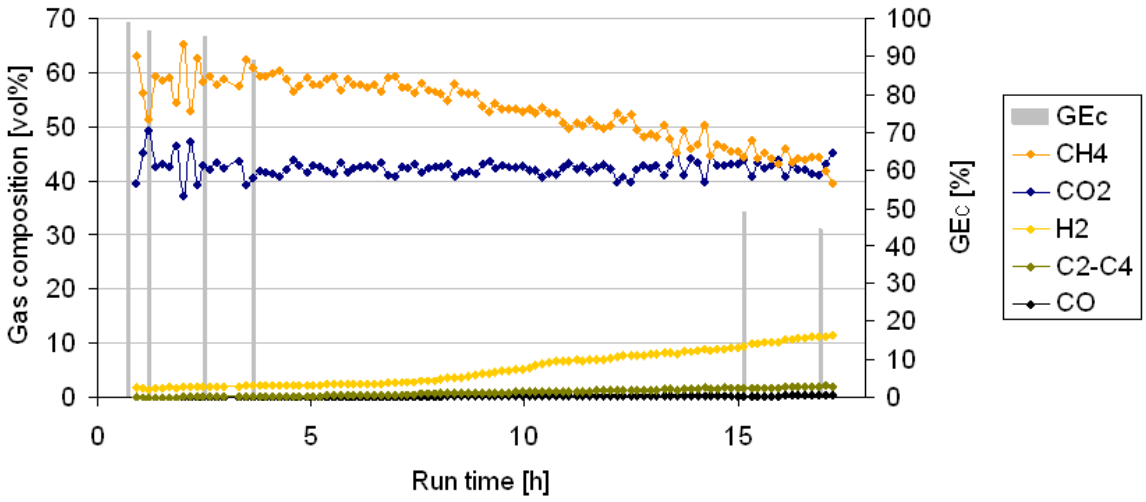

Figure 5-48: Gas composition and carbon gasification efficiency during gasification of a 5 wt% glycerol solution over a 2% Ru/TiO_2 catalyst after in-situ sulfur poisoning and oxidative regeneration by 2% H_2O_2 solution at 125℃ for 120 min (400℃, 30 MPa, expe riment ST1e).

Figure 5-49: Photographies of fresh (a) , used for gasification (b) and poisoned/regenerated (c) 2% Ru/TiO_2 (8) catalyst. Samples were taken from the top layer of the catalyst bed.

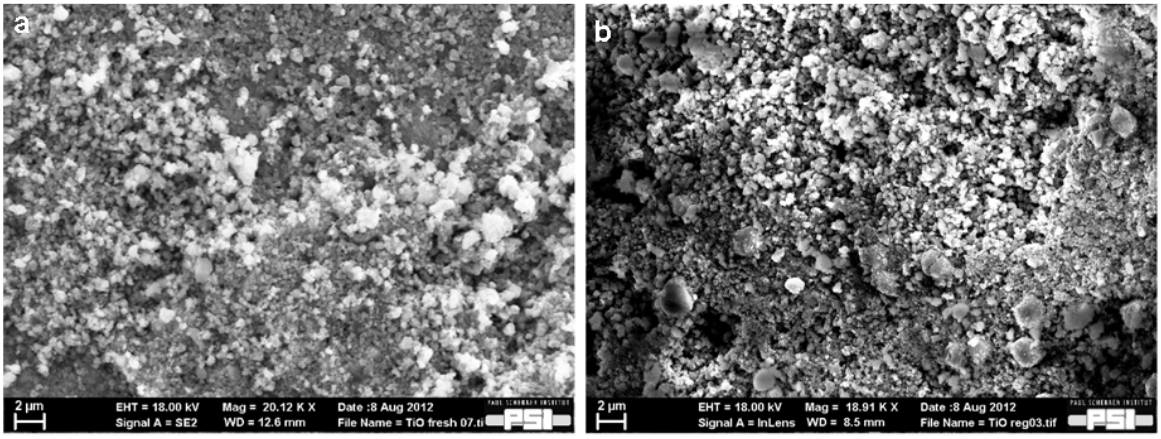

Figure 5-50: SEM images of a fresh 2% Ru/TiO_2 catalyst (a) and after treatment with a 2% H_2O_2 solution over 150 min (b) at 125℃ in a continuous reactor.

Table 5-5: List of 2% Ru/TiO_2 samples with the respective poisoning and regeneration conditions and the corresponding BET surface area (BET SA) and metal surface area (MSA) as determined with gas sorption methods (see section 4.7.8). Sample 3 represents the fresh catalyst. (1) Actual measured temperature inside the reactor 130℃; (2) poor linear fitting.

Sample No.	Poisoning conditions	Regeneration conditions	BET SA [m^2 g^{-1}]	MSA [m^2 g^{-1}]
c	400℃, 5% glycerol, 4 h	125℃ (1), 2% H_2O_2, 150 min	4.0	0.1 (2)
b	Used for gasification	-	4.0	0.2 (2)
a	Fresh catalyst	-	4.4	0.1 (2)

5.6.6 Conclusion

From the poisoning experiments in the absence of organic matter it is concluded that reduction of sulfate by the carbon support occured only to a marginal extent. In the presence of organic matter, sulfate was reduced by a considerable amount to various organic sulfur species as well as sulfide.

Sulfate deactivated the 2% Ru/C catalyst in the absence of organic matter. It is unclear whether this effect was due to this undetectably small amount of reduced sulfur species that may result from reduction by the carbon support or to an adsorption of sulfate on the catalyst or support which was reduced when being contacted with organic molecules.

An oxidative regeneration of sulfur poisoned ruthenium catalysts leads to a recovery of the initial conversion. In case of the 2% Ru/C catalyst, the instability of the recovered conversion could be explained by oxidative degradation of the support material. This probably led to a consumption of oxygen within the first fraction of the catalyst bed just behind the top inlet. The amount of oxygen reaching the following fractions of the catalyst bed was thus reduced; therefore the catalyst in the rear fractions was not completely regenerated. At a low flow velocity as it was used for these experiments (~4.6 cm min^{-1}) in comparison to the catalyst bed length (20-25 cm) such effects might be particularly pronounced. Some leaching of ruthenium as a result from the support material burn-off is likely. A smaller decrease of the metal surface area by H_2O_2 treatment of a fresh catalyst sample, however, pointed to a minor contribution of ruthenium leaching to the decreased conversion. A shorter regeneration period with a 3% H_2O_2 solution led to better regeneration results than a

longer period with a 2% H_2O_2 solution. If the oxygen consumption was dependent on the catalyst surface and not on the concentration of H_2O_2, more oxygen would be available for the regeneration in the case of a higher H_2O_2 concentration, particularly for the catalyst bed fraction with a longer distance to the top inlet.

A 2% Ru/TiO_2 catalyst showed a partial regeneration effect by flushing with subcritical water, which was not the case for the 2% Ru/C catalyst. This points to a difference in the chemical environment of the Ru-S binding. Ammonia desorption measurements suggested a higher acidity of the TiO_2 support compared to the carbon support, which may influence the electronic environment of ruthenium and thus the binding strength of Ru-S. More detailed studies on this effect via XAS will be interesting, especially with respect to the development of more sulfur resistant catalysts.

Oxidative regeneration of the poisoned Ru/TiO_2 catalyst led to a recovered conversion that showed a higher durability than the regenerated Ru/C catalyst. Structural changes of the support could not be observed. Higher concentrations of H_2O_2 may therefore further improve the regeneration efficiency of the Ru/TiO_2.

5.7 Selection of hydrothermally stable refractory oxide catalyst supports

(Parts of this chapter are based on experiments that were performed within the context of a Diplom thesis by F. Mayr [173].
Furthermore, parts of this chapter are published in [174].)

5.7.1 Introduction

The poor stability of the carbon support under an oxidizing environment asks for alternatives. The microporous structure of the carbon support of the 2% Ru/C catalyst that has been used for the majority of experiments described in the previous sections is not optimal, too. A large amount of the surface area is not or poorly accessible for most substances, including ruthenium. Ruthenium covers only the outer surface of the grain (egg-shell catalyst). Therefore, the extremely large surface area of the activated carbon support and thus the volume of the grain is hardly utilized.

Reforming of large molecules as they occur in natural feedstocks, is more delicate than of small molecules. This has already been shown by gasification experiments in section 5.4. Besides the mass transport limitations that can be an issue for long transport distances in the pores of the support material, it is likely that also a more complex set of active sites is required for the reforming of large molecules. An ideal catalyst should therefore provide a highly dispersed metal surface which is well-accessible for large molecules. Mesoporous support materials may therefore be more suitable than the microporous ones, to provide this increased accessibility of the inner surface area.

A screening of mesoporous support samples based on refractory oxides was done with respect to the formulation of a new catalyst system that provides

- a better accessibility for large molecules to the active sites on the one hand, and
- a higher resistance towards an oxidizing environment on the other hand.

Eleven commercial support samples were provided by *Norpro Saint Gobain* (Stow, USA). The composition of the samples can be found in Table Appendix D. This screening was performed in two stages: first, assessing the stability of the material towards supercritical water using a batch system, and secondly, testing the performance and the stability of selected catalyst systems in the continuous reactor setup Konti-1.

In this context, the term performance was understood as the highest feed concentration that could be completely converted to a gas mixture with the thermodynamic equilibrium composition by a given catalyst bed volume and flow rate, or in other words, the highest WHSV leading to full conversion and equilibrium product gas composition. It was reported that intermediates tend to polymerize at the surface of the catalyst [114] which may cause fouling and hence promote catalyst deactivation at incomplete conversion levels. The common method of determining catalytic activity by running the experiment at high space velocities and thus at incomplete conversion was not used here, because deactivation caused by this effect may distort the results of the stability test. Then again, the performance was tested by a stepwise increase of the feed concentration until the gas yield significantly differed from the equilibrium state.

The aim of this study was to assess the general performance of a set of ruthenium catalysts at technically relevant operating conditions. In particular, it was not attempted to operate in a regime controlled by kinetics, and thus the performance data must not be used to calculate rates or catalyst activities.

5.7.2 Stability tests of the neat support materials in a batch reactor

The eleven support samples were aged in a supercritical water environment (430°C, ρ>0.3 g ml^{-1}) for 20 hours in order to characterize them regarding their physical stability as well as the stability of their crystalline structure towards a hydrothermal environment. This was done in mini-batch reactors. The reactor was loaded with 2.5 g of support material and 1.5 ml of water.

The BET surface area of the support samples was determined before and after the aging procedure. Additional information on the crystal structure before and after aging was obtained from XRD measurements. The samples showing the best stability in this test were treated for a second time following the same procedure.

Table Appendix D gives the BET surface area measured for all samples before aging, after the first aging procedure, and after the second aging procedure for selected samples.

The selection of the samples subjected to a second aging procedure was based on the physical stability of the extrudates after the first aging step and the stability of the crystal structure as determined with XRD. The support materials based on tetragonal ZrO_2 (samples 1-4) showed a partial structural conversion to the more stable monoclinic form (see Figure 5-51). For sample 2 the reflexes corresponding to the monoclinic form were minuscule, though. Therefore, the composition of sample 2 was considered to be a relatively stable form of tetragonal ZrO_2 at supercritical conditions. A shift of the crystal structure to rutile for the support material sample based on anatase (sample 6) as it has been observed by Elliott et al. [107] in subcritical water, was not observed (see Figure 5-52). The residence time in our experiments was shorter, though. Besides that, for pressures below 70 MPa the conversion from anatase to rutile is reported to take place at temperatures above 600-700°C under hydrothermal conditions [175]. A growth of crystals, however, could be deduced from the increasing sharpness and intensities of the reflexes. Physical stability of the extrudates was not given after treatment in hydrothermal environment.

No apparent difference can be found in the diffractograms of fresh and aged samples based on monoclinic ZrO_2 (see Figure 5-53).

For the second aging step we chose samples 2, 5, 7, 8, 10 and 11. The BET surface area measured after the second aging procedure was supposed to indicate whether the structure had reached a stable state during the first aging or if this process was still ongoing.

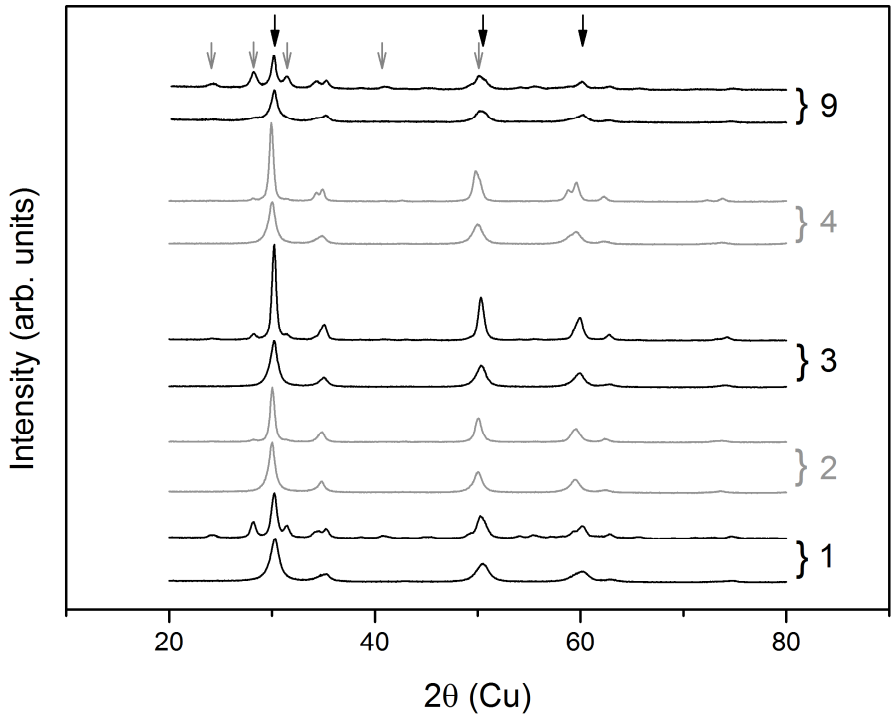

Figure 5-51: X-ray diffractograms of fresh (lower diffractogram) and aged (upper diffractogram) support samples based on tetragonal ZrO_2; black arrows: characteristic reflexes for tetragonal ZrO_2, grey arrows: characteristic reflexes for monoclinic ZrO_2.

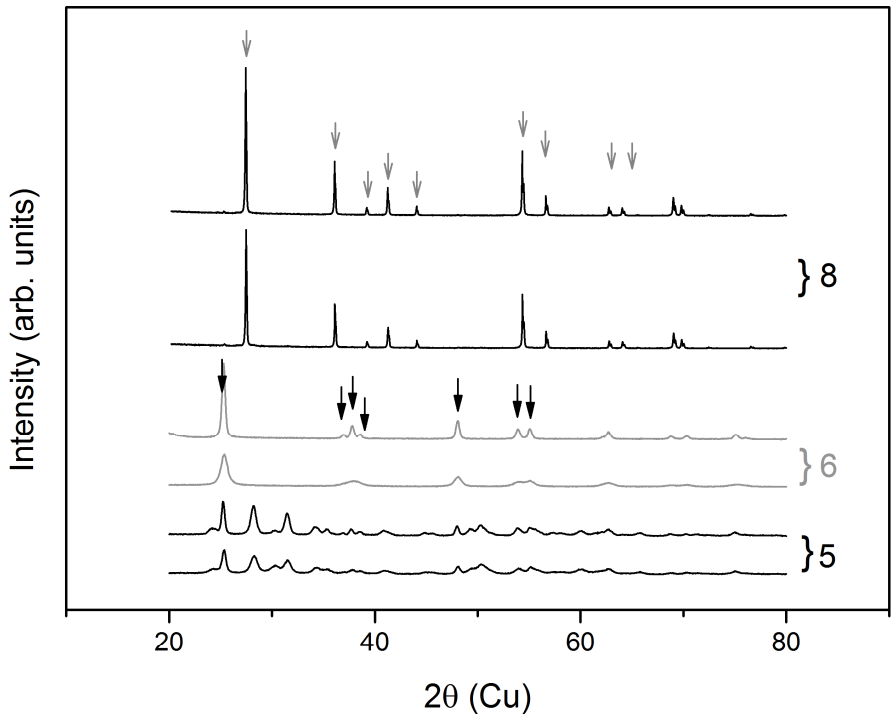

Figure 5-52: X-ray diffractograms of fresh (lower diffractogram) and aged (upper diffractogram) support samples based on TiO_2; black arrows: characteristic reflexes for anatase, grey arrows: characteristic reflexes for rutile.

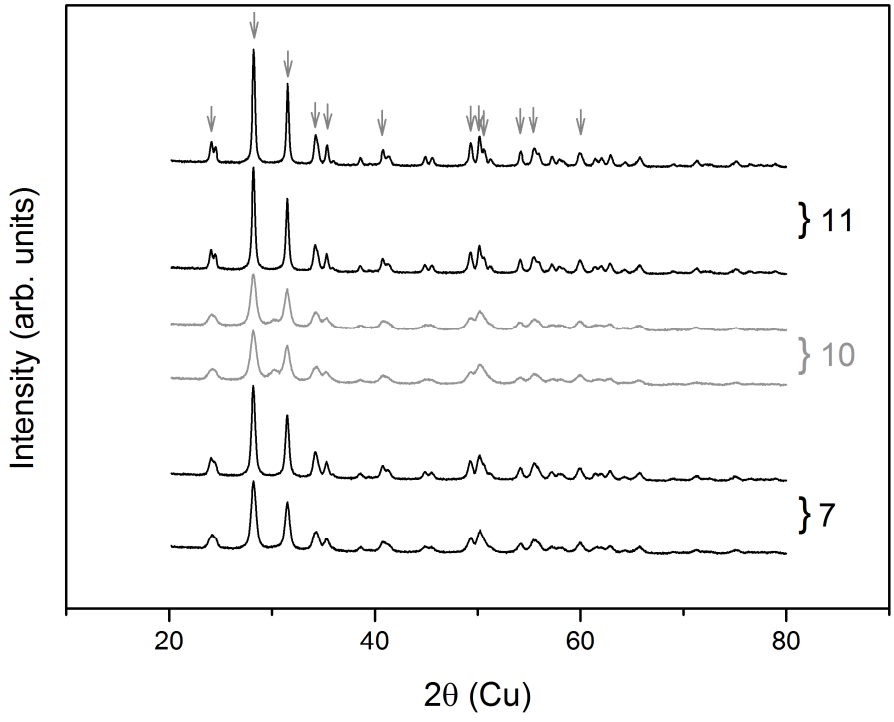

Figure 5-53: X-ray diffractograms of fresh (lower diffractogram) and aged (upper diffractogram) support samples based on monoclinic ZrO_2; grey arrows: characteristic reflexes for monoclinic ZrO_2.

Based on the behavior in the second aging run, we selected sample 2 as representative for tetragonal ZrO_2, sample 5 for a mixed structure, samples 7 and 11 for monoclinic ZrO_2 and sample 8 for rutile for further investigations by impregnating with active metal and performance tests in a continuous reactor setup. Sample 10 was not further considered because it showed the highest change in surface area within the group of monoclinic ZrO_2. A list of experiment can be found in Table Appendix E.

5.7.3 Performance and stability tests in the continuous reactor setup Konti-1

In the performance and stability tests that were done in the continuous test rig Konti-1, the conversion of glycerol at different concentrations and the stability of the conversion were tested for different catalyst systems. The aim of this test was to determine the highest WHSV at which full gasification could be maintained over 24 h without a significant change in the product gas composition.

The first performance and stability test comprised the gasification of a 6 wt% glycerol solution. In the case it was successful a second run was performed with an 11 wt% glycerol solution at a respectively higher WHSV. The next concentration level was 16 wt% and the last one 19 wt%. A concentration higher than 85 wt% glycerol for the pure organic stream (19 wt% for the mixture) could not be pumped because of the high viscosity.
Since the flow rates were kept constant for all experiments, the WHSV changed only in dependence on the feed concentration. The corresponding WHSV`s were: 0.6 h^{-1}, 1.1 h^{-1}, 1.6 h^{-1} and 2 h^{-1}.

5.7.3.1 Thermodynamic equilibrium gas composition for gasification of glycerol solutions

The equilibrium gas composition for the glycerol solutions was calculated with the software *Aspen plus* as the composition corresponding to a minimum in the Gibbs free energy at 28.5 MPa and 400°C, 380°C, and 360°C (Figure 5-54). Since the temperature was not constant over the reactor bed due to exothermic and

endothermic reactions (Figure 5-57), the temperature for the estimation of the corresponding equilibrium gas composition had to be chosen deliberately. The influence of the temperature on the thermodynamic equilibria is more pronounced for low feed concentrations.

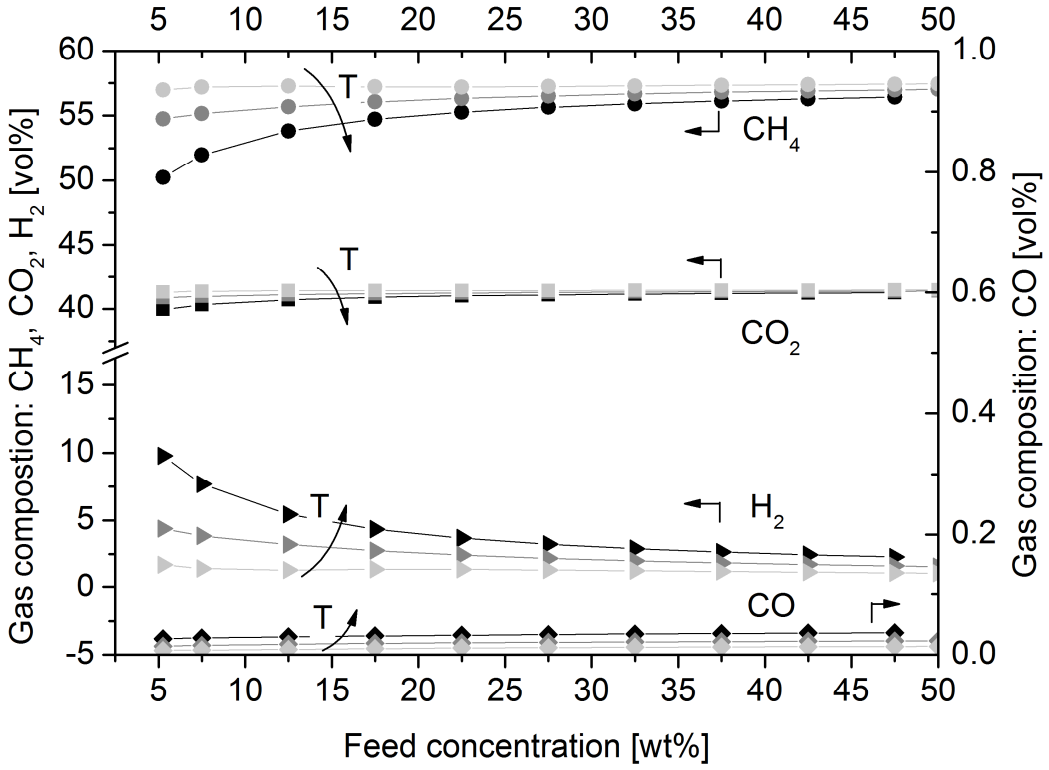

Figure 5-54: Equilibrium gas composition (dry) for glycerol and water at different feed concentrations and 28.5 MPa and 400℃ (black symbol s), 380℃ (dark grey symbols) and 360℃ (light grey symbols) as calculated by Aspen plus.

5.7.3.2 Continuous experiment with the neat support material (sample 2)

The necessity of a catalyst for methane production at 400°C is shown by a blank experiment, where the reactor was filled with neat support material (sample 2) only. In the absence of ruthenium, the gas composition showed a high concentration of CO_2 and H_2 and a significant concentration of CO and higher hydrocarbons (C_2-C_4). The H_2 yield increased with decreasing feed concentration. The other gasses showed opposite trends. Methane was only produced in traces (Figure 5-55). The carbon gasification efficiency was between 10 and 20% for all concentrations (Figure 5-56).

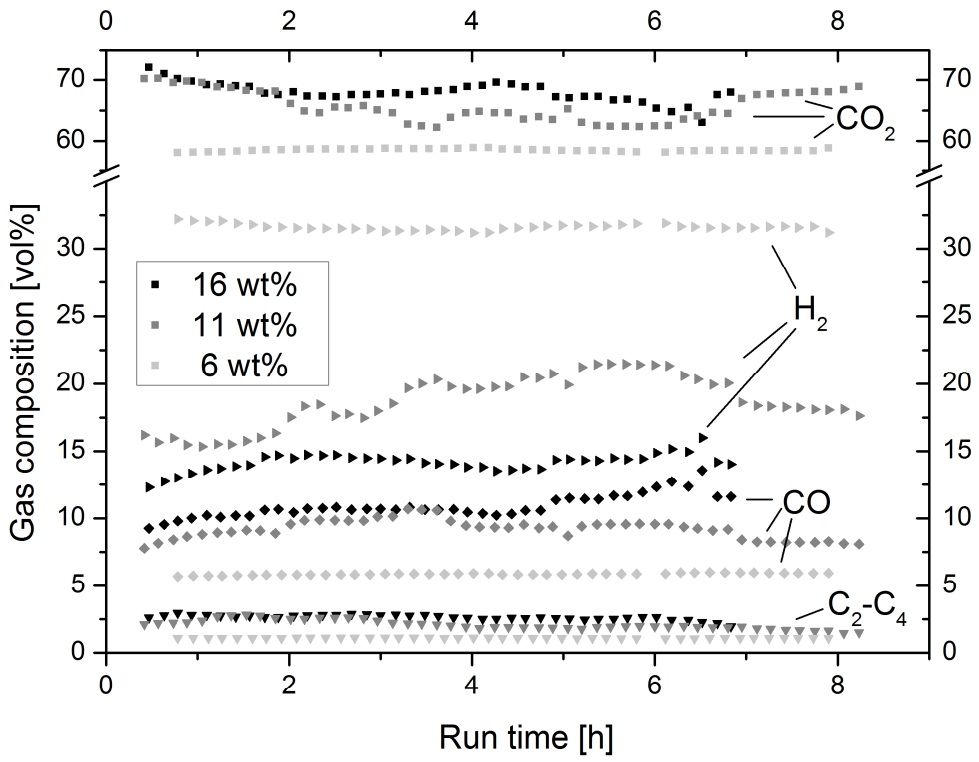

Figure 5-55: Gas composition over time on stream for the gasification of a glycerol solution at different feed concentrations (in wt%) over the neat support sample 2 at 400℃ setpoint temperature and 28.5 MPa (experiments Ba-Bc).

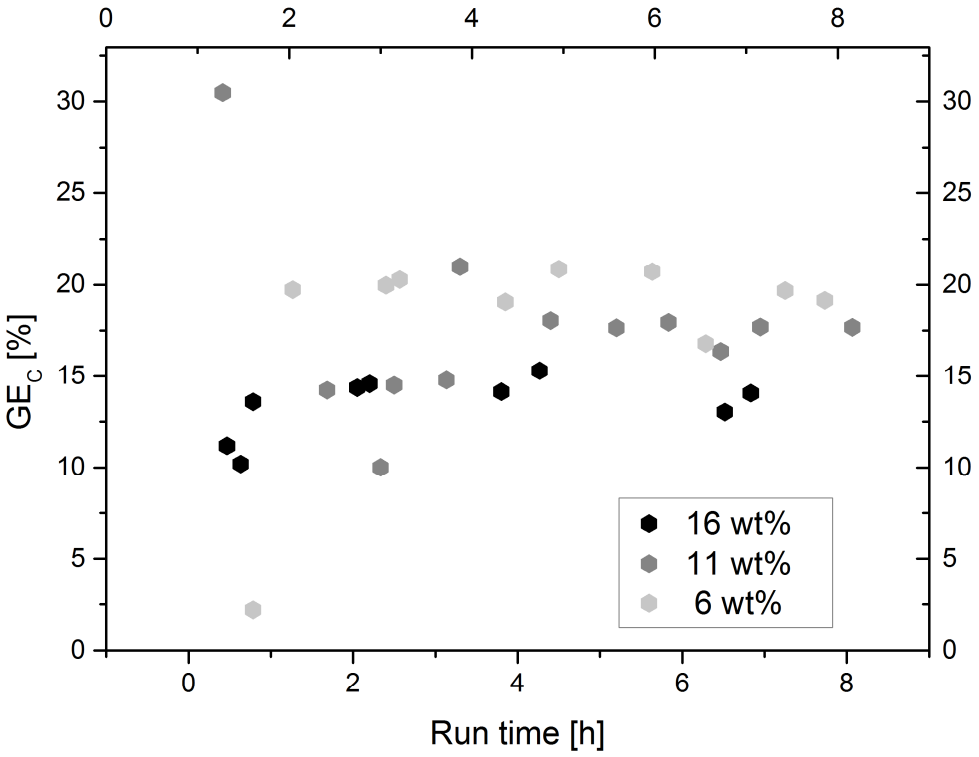

Figure 5-56: Carbon gasification efficiency over time on stream for the gasification of a glycerol solution at different feed concentrations (in wt%) over the neat support sample 2 at 400℃ setpoint temperature and 28.5 MPa (experiments Ba-Bc).

The temperature profile shown in Figure 5-57 for a 6 wt% glycerol solution and water exhibited the typical decrease of the temperature at the entrance of the reactor as compared to pure water, which had been attributed to the endothermic steam reforming reaction by Schubert [28] and later to the negative enthalpy of mixing of the product gases with supercritical water by Kraft, which is assumed to have an even stronger impact [176]. However, this decrease is weak compared to the one measured during the gasification of 6 wt% glycerol solution with a 2 wt% Ru/ZrO_2 catalyst (sample 2). The fact that the temperature is not increasing towards the end of the reactor indicates that some reaction and thus gas production takes place over the entire catalytic bed.

A temperature drop in the catalytic experiment is detected already before the catalyst bed. In this zone only the neat support material is present; therefore, the temperature profile in this zone should be identical to the uncatalyzed experiment. This mismatch can be explained by different possible effects:

- Backmixing of the fluid from the cooler zone caused by local pressure fluctuations resulting from gas production in the catalyzed experiment
- Backmixing of the fluid from the cooler zone by dispersion . We estimated the axial Peclet number to be ca. 2, which would point to a fair amount of axial dispersion
- Heat conduction along the thermowell for the movable thermocouple
- Altered heat capacity and/or diffusivity of the fluid due to gas production in the catalyzed experiment

A different reactivity between the two experiments in the early zone of the reactor can be excluded, because it is filled with the same material.

The temperature in the catalytic bed ranges from 390°C to 360°C. Concerning the thermodynamic modeling, we assume the exit temperature of the catalytic bed to be the determining one.

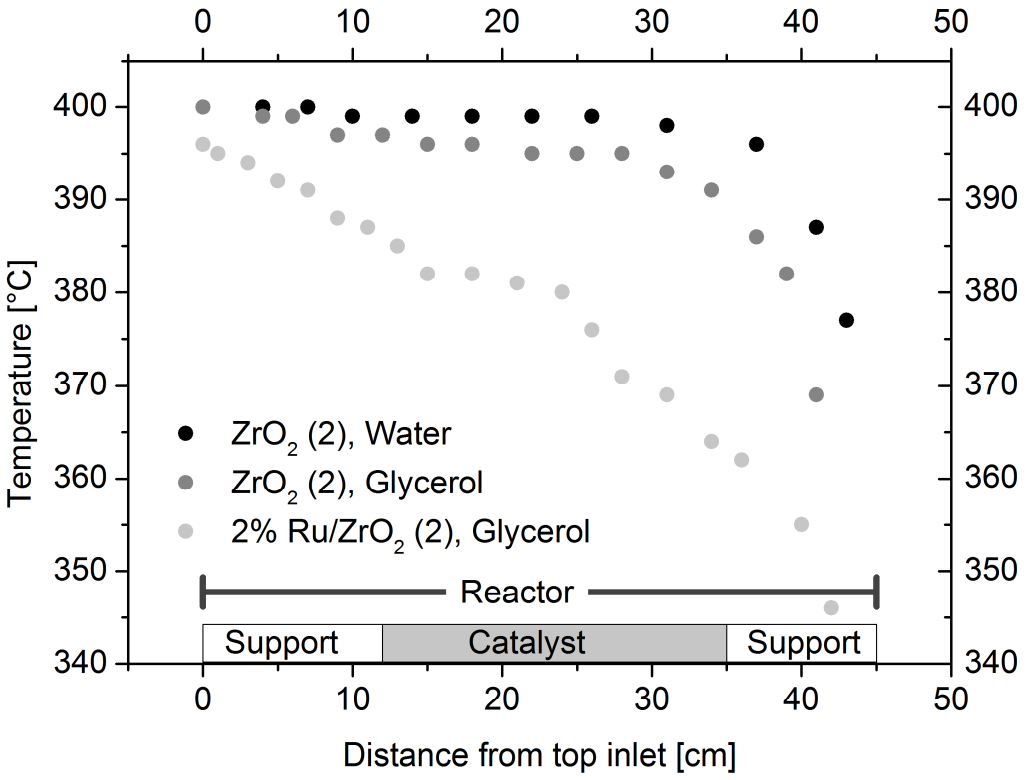

Figure 5-57: Axial temperature profiles over the reactor length for pure water and for the gasification of a 6 wt% glycerol solution with a catalyst (experiment 2N2a) and without catalyst (experiment Ba). The position of the catalyst bed is marked.

5.7.3.3 Continuous gasification experiments with 2% ruthenium catalyst systems

Support samples 2, 5, 7, 8 and 11 were subjected to the performance test with a 6 wt% glycerol solution at an average WHSV of 0.6 h^{-1}. At the beginning of the experimental run, the carbon gasification efficiency was close to 100% for all samples except for sample 5 with a carbon gasification efficiency of below 20% (Figure 5-58, sample 5 is not considered because of a reactor blocking after 2 h). There was no decrease observed over 24 h. Also the methane yield was high throughout the experiment.

For samples 2, 7 and 8 the gas composition was very close to the thermodynamic equilibrium values calculated for the temperature range of 365-375°C, which was measured at the end of the catalytic bed for those three samples (Figure 5-59 and Figure 5-54). Sample 2 showed the highest methane yield and the lowest hydrogen yield of all samples. Sample 11 showed an elevated H_2 yield right from the beginning, which can be explained with the higher temperature of 380°C at the end of the catalytic bed. Sample 5 showed a gas composition far from equilibrium and was therefore not considered further.

After 10 hours of time on stream, a slight increase in the amount of higher hydrocarbons (ethane, propane, butane) and H_2 in the product gas was observed for samples 8 and 11, indicating incomplete steam reforming and methanation reactions. CO was not detected at any time during the experiment, allowing the assumption that the water-gas shift reaction was not kinetically limited. Sample 7 showed only a very slight increase in H_2 production. Sample 2 showed no change in gas composition over the whole experimental run.

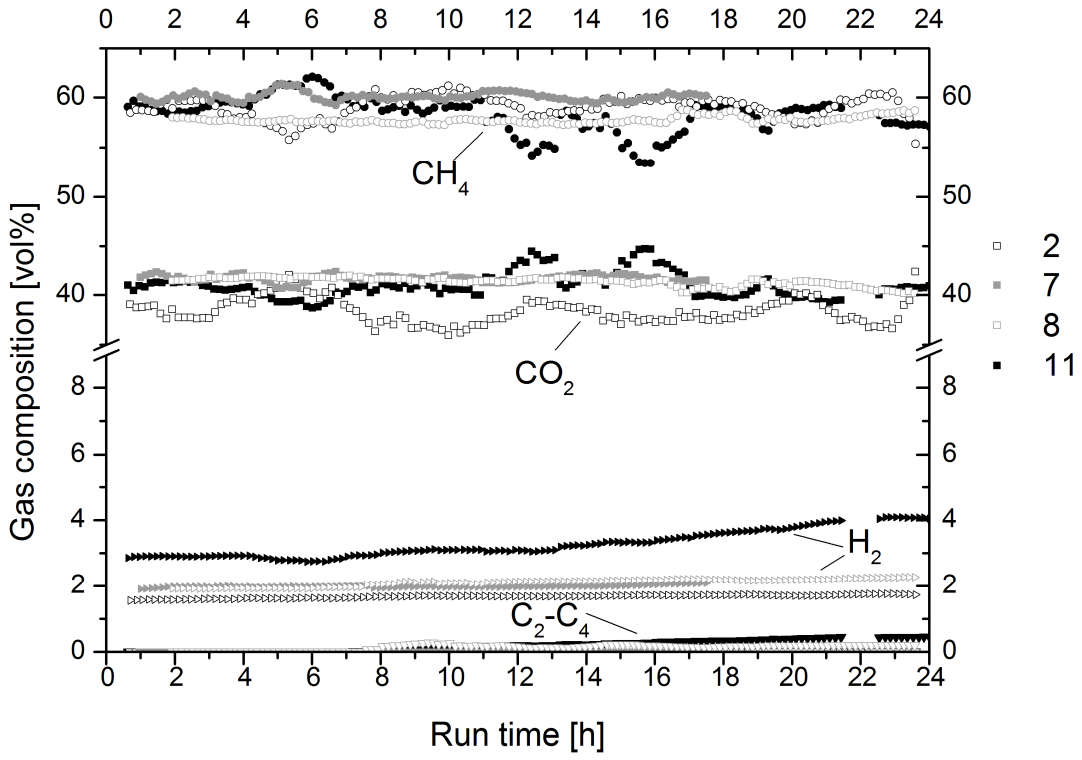

Figure 5-58: Gas composition over time on stream for the gasification of a 6 wt% glycerol solution over 2 wt% supported ruthenium catalysts (experiments 2N2a, 2N7a, 2N8a, and 2N11a) at 400℃ setpoint temperature and 28.5 MPa; the ave rage WHSV was 0.6 h^{-1}.

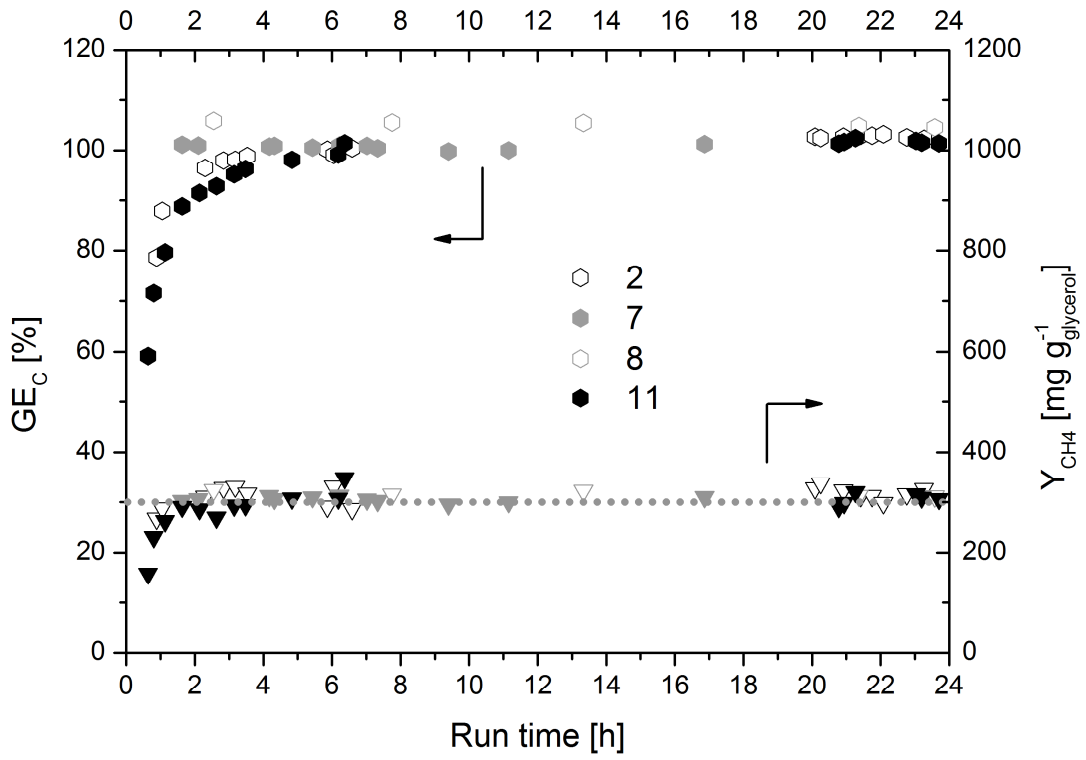

Figure 5-59: Carbon gasification efficiency (hexagons) and methane yield (triangles) over time on stream for the gasification of a 6 wt% glycerol solution over 2 wt% supported ruthenium catalysts (experiments 2N2a, 2N7a, 2N8a, and 2N11a) at 400℃ setpoint temperature and 28.5 MPa; the average WHSV was 0.6 h^{-1}. The dotted line indicates the maximum theoretical methane yield for the calculated equilibrium composition at the end of the catalyst bed.

The temperature profiles measured at the beginning and at the end of the experimental runs did not differ for samples 2, 7, 8 and 11.

Because of the drift in gas composition for samples 8 and 11, the WHSV was considered too high for a high methane yield. Those samples were therefore not subjected to a run with a higher feed concentration.

Samples 2 and 7 were then subjected to an experimental run with an 11 wt% glycerol solution.

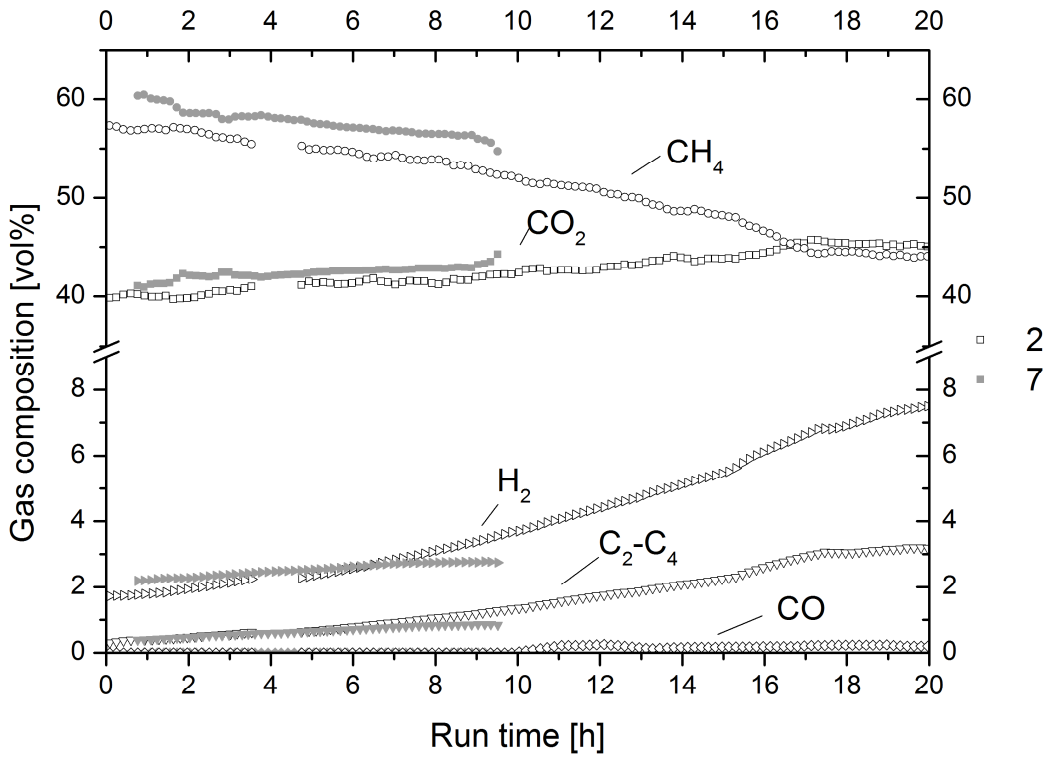

Figure 5-60: Gas composition over time on stream for the gasification of an 11 wt% glycerol solution over 2 wt% supported ruthenium catalysts (experiments 2N2b and 2N7b) at 400℃ setpoint temperature and 28.5 MPa; the average WHSV was 1.1 h^{-1}.

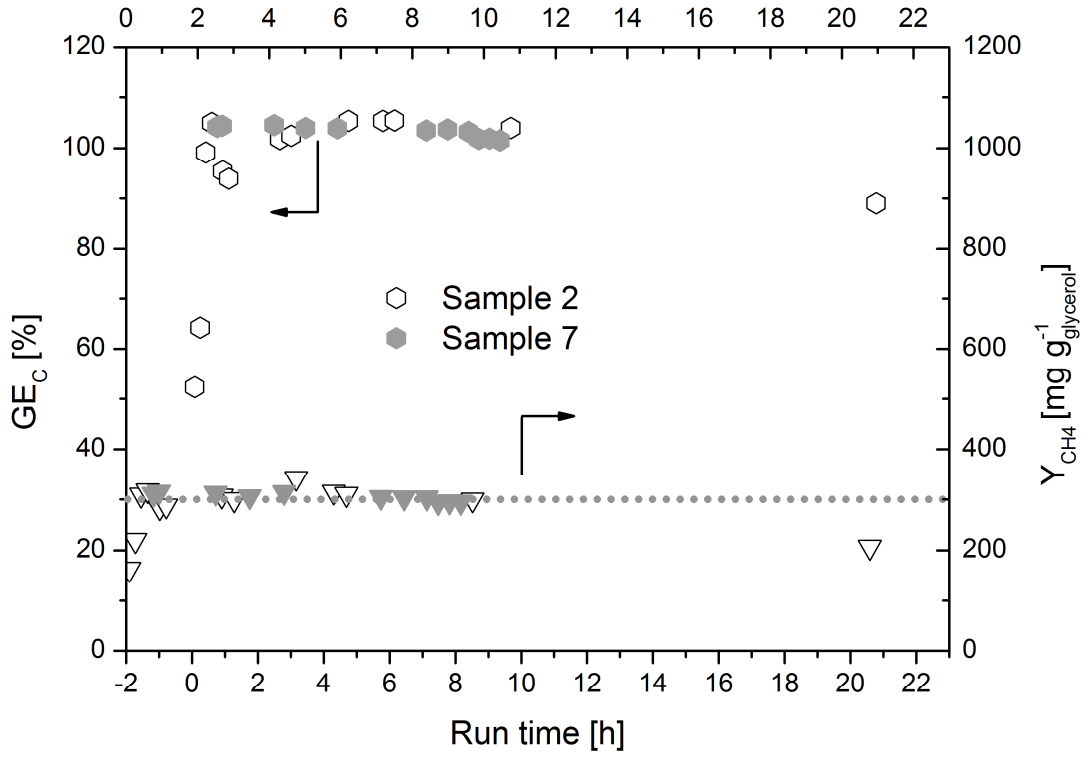

Figure 5-61: Carbon gasification efficiency (hexagons) and methane yield (triangles) over time on stream for the gasification of an 11 wt% glycerol solution over 2 wt% supported ruthenium catalysts (experiments 2N2b and 2N7b) at 400℃ setp oint temperature and 28.5 MPa; the average WHSV was 1.1 h^{-1}. The dotted line indicates the maximum theoretical methane yield.

For both samples, gasification of the 11 wt% glycerol solution occurred at 100% carbon conversion at the beginning of the run (Figure 5-61). In the gas composition, however, a drift away from the equilibrium values was observed early on (Figure 5-60). The methane yield dropped continuously over time, while the yields of hydrogen and higher hydrocarbons increased. This change in gas composition points towards an incomplete steam reforming and methanation reaction. The occurrence of CO after 10 hours of time on stream for sample 2 indicates that the water-gas shift reaction became kinetically limited as well. The experiment with sample 7 was not conducted any longer than 10 hours because of a technical defect; however, the same trend became visible already after a few hours. After 20 h of time on stream, a decrease in the gasification efficiency by around 20% was observed for sample 2, see Figure 5-61.

To assess whether the change in gas composition as well as the decrease in gasification efficiency during gasification of the 11 wt% glycerol solution was due to too high a space velocity or to aging of the catalyst, a control experiment with a 6 wt% glycerol solution was performed.

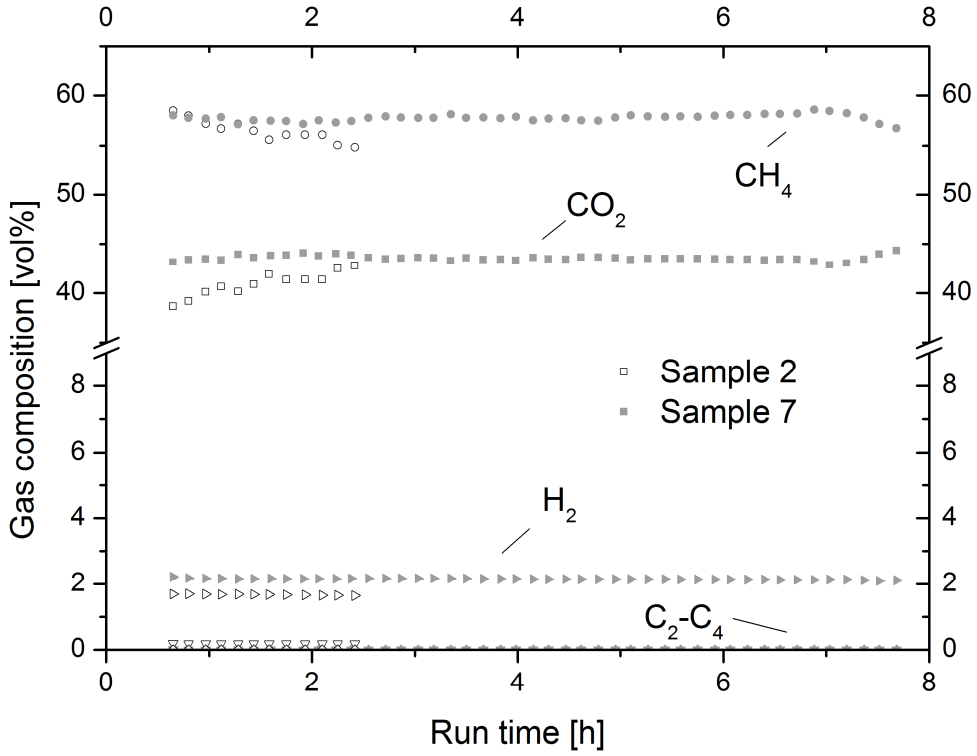

Figure 5-62: Gas composition over time on stream for the gasification of a 6 wt% glycerol solution after the gasification of an 11 wt% glycerol solution over 2 wt% supported ruthenium catalysts (experiments 2N2c and 2N7c) at 400℃ setp oint temperature and 28.5 MPa; the average WHSV was 0.6 h^{-1}.

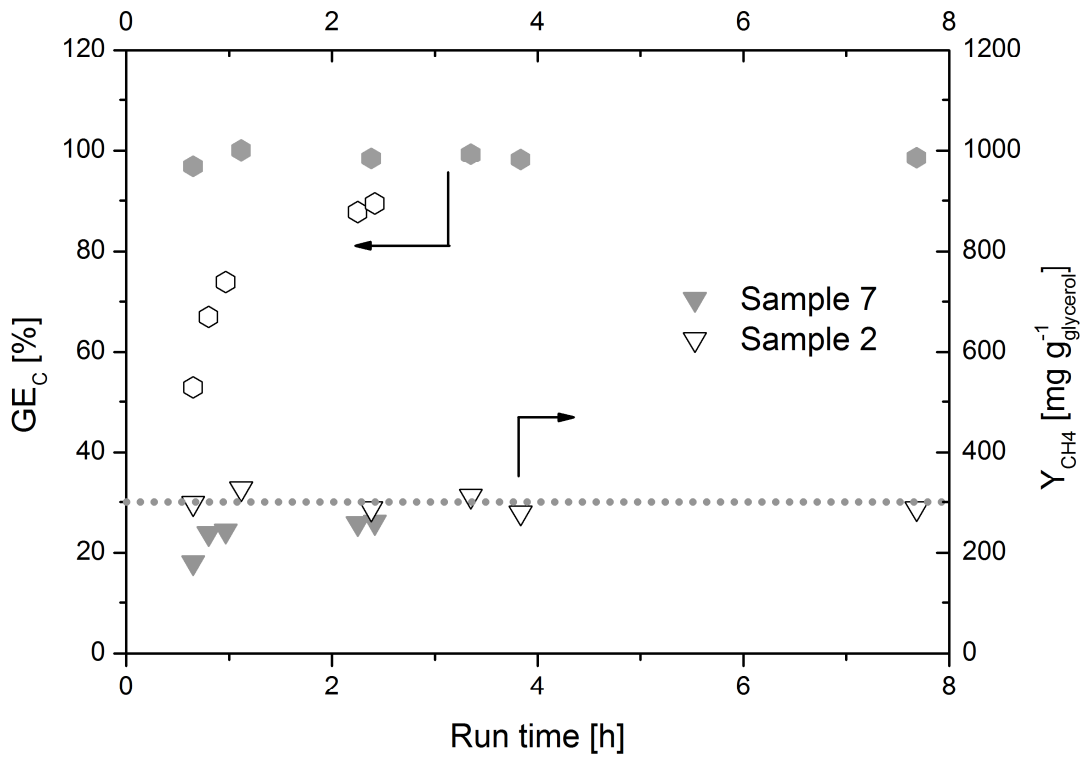

Figure 5-63: Carbon gasification efficiency (hexagons) and methane yield (triangles) over time on stream for gasification of a 6 wt% glycerol solution after gasification of 11 wt% glycerol solution over 2 wt% supported ruthenium catalysts (experiments 2N2c and 2N7c) at 400℃ setpoint temperature and 28.5 MPa; the average WHSV was 0.6 h^{-1}. The dotted line indicates the maximum theoretical methane yield.

In this experiment, the carbon gasification efficiency was 100% and the methane yield at the maximum for sample 7 (Figure 5-63). For sample 2, after a run-in period the initial conversion was reached as well. No CO and only a very small amount of higher hydrocarbons were detected (Figure 5-62). H_2 was produced at a level similar to the end of the first run with the 6 wt% glycerol solution. We can assume that the higher amount of hydrogen in comparison to the beginning of the first run is either due to a kinetic limitation of the methanation reaction or to a very slight increase of the temperature that could not be detected, shifting the equilibrium towards H_2. The miniscule amount of higher hydrocarbons and CO in the product gas indicates that the steam reforming reaction as well as the water-gas shift reaction were not affected by overload of the catalyst. No further change in the gas composition was observed over 8 hours.

5.7.3.4 Structural analyses of 2% ruthenium catalyst systems

Withdrawal of the catalyst from the reactor revealed that samples 2, 8, and 11 maintained their shape. Samples 7 and 5 were found to partially disaggregate to a fine powder.

The BET surface area of the impregnated catalysts was identical to the one of the neat support material; only for sample 11 it was smaller. The BET surface area of the used samples was lower compared to the fresh ones, except for sample 11, for which it was higher (see Table 5-6). The decrease was not more than 12% of the initial surface area (sample 2). The minor extent of the surface area loss is very likely due to the pretreatment of the catalyst in supercritical water before impregnation.

The metal surface area of all samples was found to have decreased during gasification. However, a direct correlation between metal surface area and performance could not be established. The metal surface area of samples 7 and 11, for instance, were larger than that of sample 2, while the latter showed the best performance. For sample 8, an increase of the MSA after gasification was observed, however the accuracy of the measurement was low in this case. If there was an increase, it may be due to the deposition of corrosion products of the reactor.

The decrease of the metal surface area may result from the formation of carbon deposits on top of the active sites. This assumption is supported by temperature programmed oxidation (TPO) measurements with IR analysis of the evolved gas, where small amounts of CO_2 were found for all used catalyst samples. Other potential causes are: particle growth due to migration of ruthenium clusters on the surface or a leaching of ruthenium during gasification. However, no data supporting either of these alternative explanations could be obtained.

Table 5-6: BET surface area (BET SA), metal surface area (MSA) and metal dispersion (D) of fresh and used 2% Ru catalyst samples a. (1) poor linear fitting, (2) sample not analyzed.

Sample	BET SA (fresh) [m^2/g_{cat}]	BET SA (used) [m^2/g_{cat}]	MSA (fresh) [m^2/g_{cat}]	MSA (used) [m^2/g_{cat}]	D (fresh) [%]	D (used) [%]
2	38.5	33.9	1.1	0.3	11.6	3.2

5	n.a. [2]	n.a. [2]	< 0.1 [1]	n.a. [2]	0.7 [1]	n.a. [2]
7	41.4	37.2	1.9	1.2	19.8	12.8
8	4.4	4.0	0.1 [1]	0.2 [1]	1.2 [1]	2.6 [1]
11	19.8	25.6	1.3	0.3	13.4	3.3

5.7.3.5 Continuous gasification experiments with 5% ruthenium loading

In the previous sections, catalysts based on ceramic support were tested. Sample 2 (ZrO_2, stabilized tetragonal structure) as a catalyst system with 2% Ru loading showed a promising performance and stability. Yet, the WHSV at which full conversion took place was by one order of magnitude lower compared to the commercial 2% Ru/C catalyst, i.e. 0.6 h^{-1} vs. 11 h^{-1}. A simple explanation for this could be the lower BET surface area that was determined for the ceramic support materials. However, the measured metal surface area of the 2% Ru/C catalyst points to a relatively small share of the total surface area that is effectively utilized (egg shell catalyst). Theoretically, the ceramic ZrO_2 (2) sample and even the physically most stable rutile sample (8) provide more than sufficient surface area to reach a metal dispersion comparable to the 2% Ru/C catalyst. The measured metal surface area of some of the ceramic catalyst systems is lower in comparison, though. Reasons for the lower ruthenium dispersion on the ceramic surface could be:

- a lower utilizable surface area
- an unsatisfactory impregnation method leading to the formation of large crystals
- catalyst-support interactions leading to the formation of larger crystals

If the first reason was true, a higher catalyst loading should not markedly increase the performance of the catalyst. An increase of the performance would on the other hand support the assumption of a poor distribution of ruthenium over the utilizable surface.

We therefore did experiments with a 5% ruthenium loading of the support samples 2 and 8, in order to clarify whether the utilizable surface of the respective support sample was already covered by ruthenium or could be utilized more efficiently. The mass of the catalyst used for the performance tests of the 5% ruthenium catalysts and

hence the catalyst bed length was identical to the experiments at 2% ruthenium loading. Thus, at identical feed concentrations the WHSV was also identical to the experiments with 2% ruthenium loading. So a possible effect of the increasing ruthenium amount could be identified.

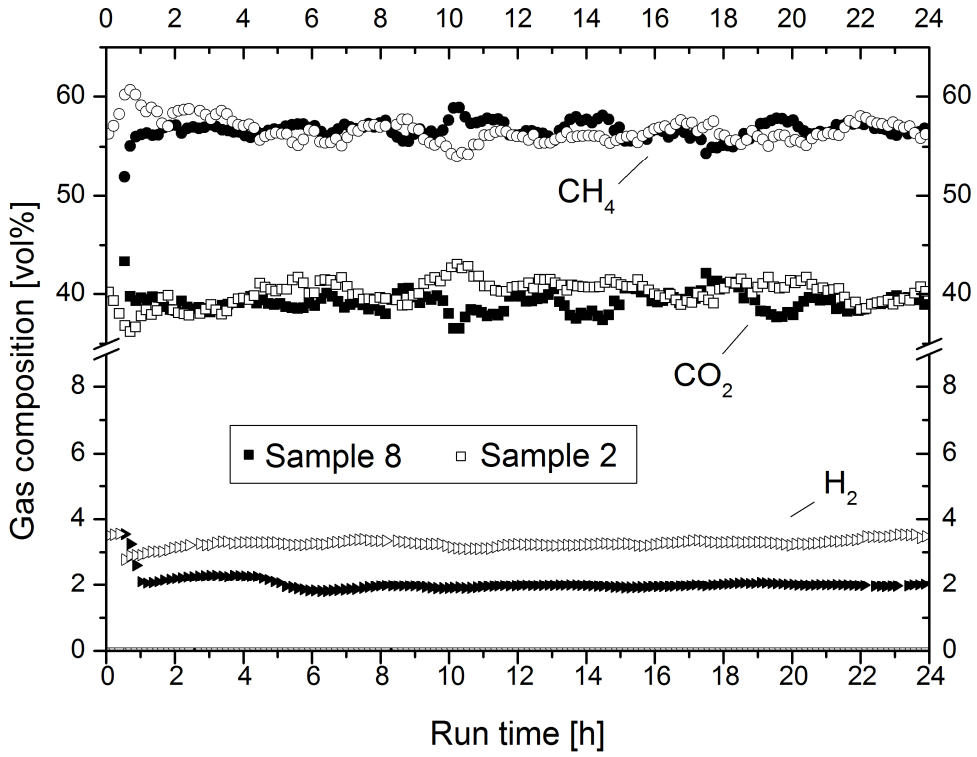

Figure 5-64: Gas composition over time on stream for the gasification of a 6 wt% glycerol solution over a 5 wt% supported ruthenium catalyst (experiments 5N2a and 5N8a) at 400℃ setpoint temperature and 28.5 MPa; the average WHSV was 0.6 h^{-1}.

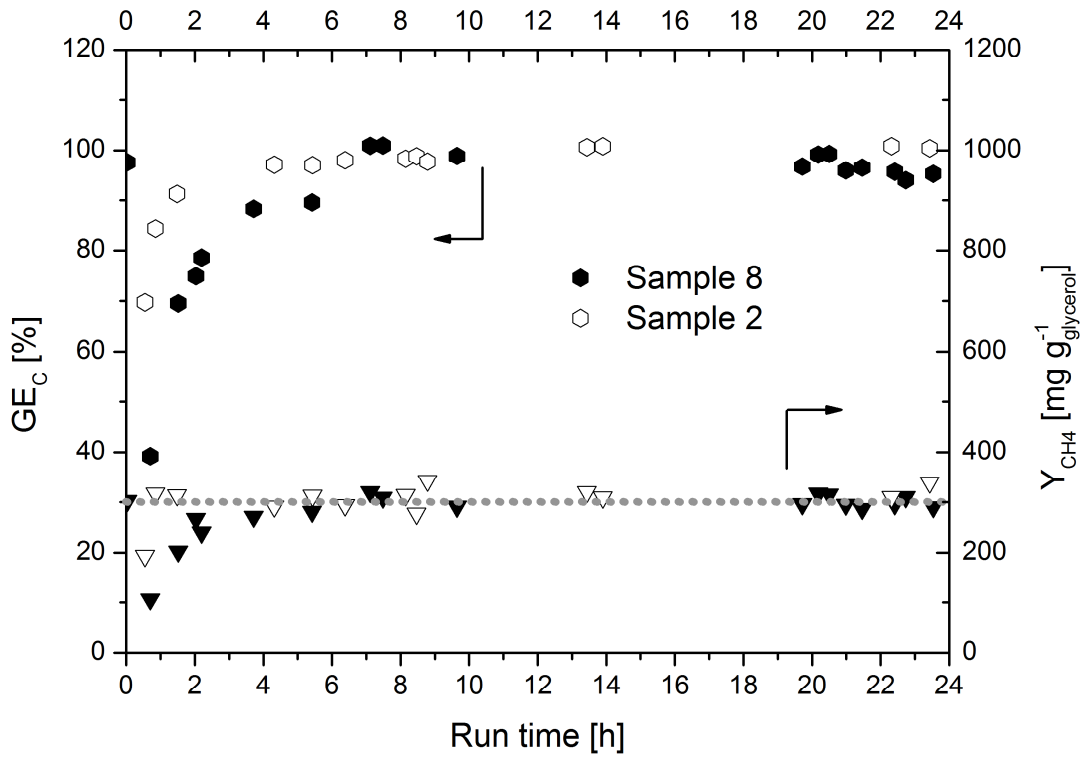

Figure 5-65: Carbon gasification efficiency (hexagons) and methane yield (triangles) over time on stream for gasification of a 6 wt% glycerol solution over a 5 wt% supported ruthenium catalyst (experiments 5N2a and 5N8a) at 400℃ setp oint temperature and 28.5 MPa; the average WHSV was 0.6 h^{-1}. The dotted line indicates the maximum theoretical methane yield

Gasification of a 6 wt% glycerol solution over 5% Ru/ZrO_2 (2) and 5% Ru/TiO_2 (8) led to full conversion during 24 h with a maximum methane yield (Figure 5-65). The gas composition did not change over the run time (Figure 5-64). For sample 8 this result implicates an improvement of the performance. Since sample 2 showed a stable conversion of a 6% glycerol solution already at 2% Ru loading, this result is not surprising. However, the hydrogen yield of sample 2 has increased compared to the experiment with 2% Ru loading, while sample 8 showed hardly any difference in the hydrogen yield. Here, the temperature profiles provide supporting information (Figure 5-66). While the temperature profiles during gasification of a 6% glycerol solution over a 2% and 5% Ru/TiO_2 (8) catalyst are fairly similar, they diverge for the respective Ru/ZrO_2 (2) catalysts. The higher temperature at the outlet of the 5% Ru/ZrO_2 (2) catalyst bed results in a higher hydrogen yield for thermodynamic reasons. But how can this difference in temperature profiles be explained? The same amount of feed is fully converted to gas and the same amount of gas has to be dissolved in supercritical water, which should result in the same amount of heat consumption, independent on the catalyst loading. A possible explanation is a very

sudden conversion, leading to a sharp drop in the temperature within the first centimeters of the catalyst bed. The temperature gradient is then larger than in the case of a more distributed reaction, resulting in an increased heat transfer from the oven, which is regulated to a constant temperature of 400°C. At a distance of 40 cm, when the heated zone ends, more heat has been transferred to the fluid compared to the situation, where the temperature gradient is low at the entrance of the catalyst bed. This observation would then point to an increased performance of the Ru/ZrO_2 (2) catalyst at the higher ruthenium loading.

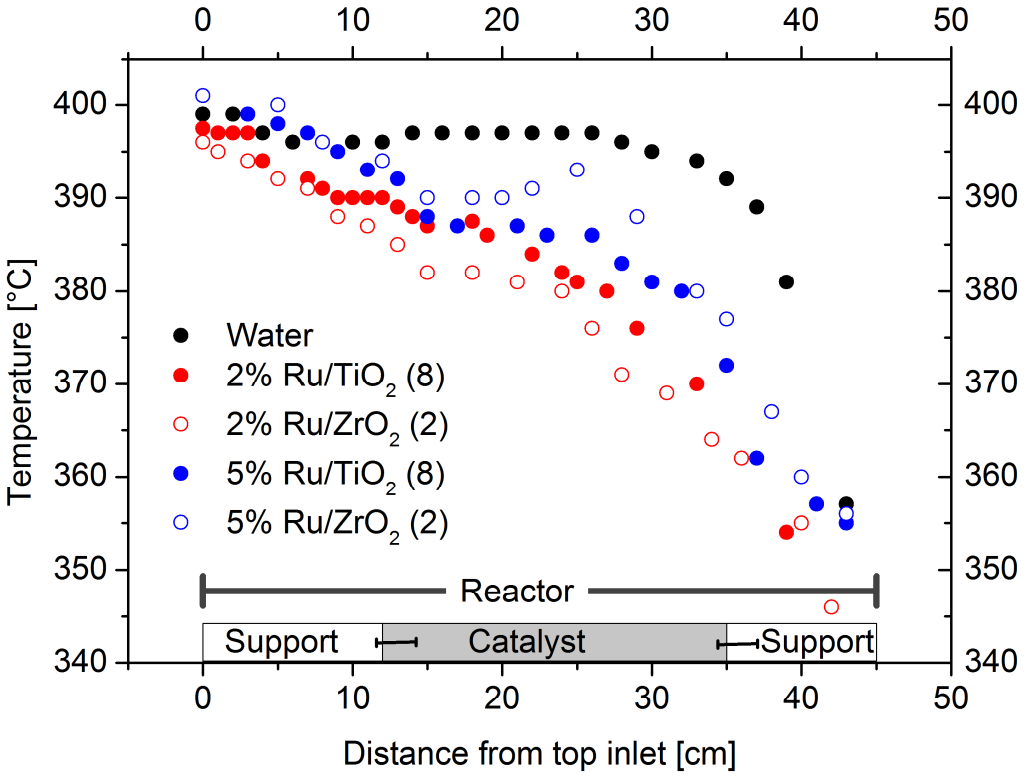

Figure 5-66: Axial temperature profiles over the reactor length for pure water and for the gasification of a 6 wt% glycerol solution. The position of the catalyst bed is marked (experiments 2N2a, 5N2a, 2N8a, and 5N8a).

Gasification of an 11% glycerol solution led to a full conversion for the 5% Ru/TiO_2 (8) catalyst (Figure 5-68); however, a clear trend in the gas composition away from the thermodynamic equilibrium, especially by the appearance of higher hydrocarbons, points to an incomplete reforming (Figure 5-67). For the 5% Ru/ZrO_2 (2) catalyst, full conversion at the equilibrium gas composition could be maintained over 24 h. This shows clearly, that the higher ruthenium loading increases the performance of the Ru/ZrO_2 (2) catalyst.

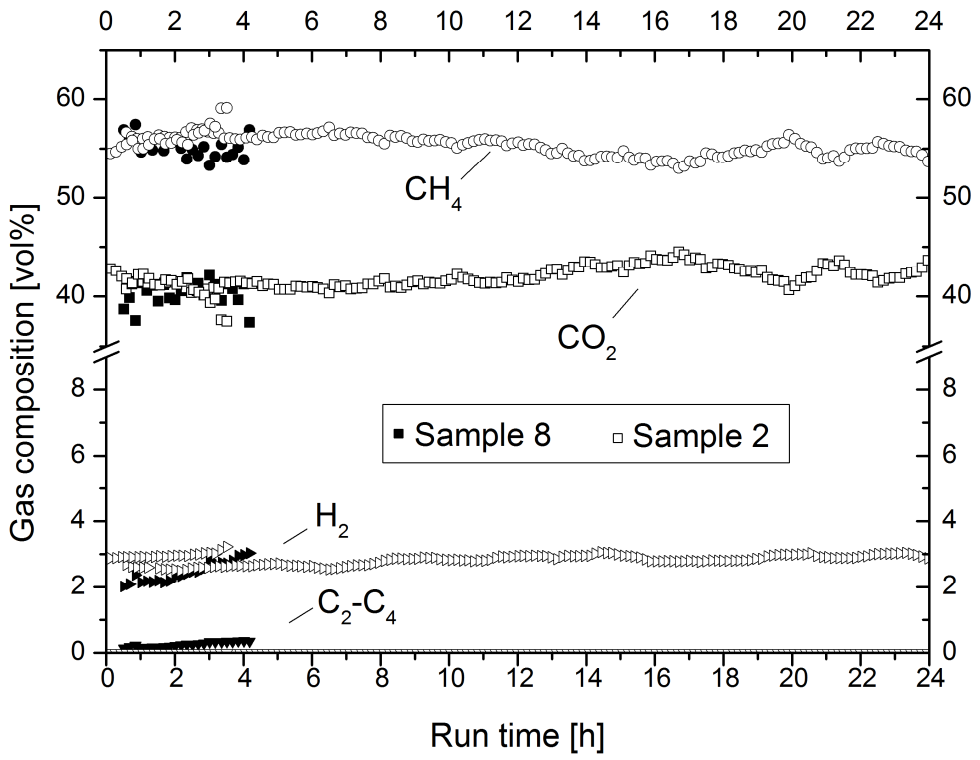

Figure 5-67: Gas composition over time on stream for the gasification of an 11 wt% glycerol solution over a 5 wt% supported ruthenium catalyst (experiments 5N2b and 5N8b) at 400℃ setpoint temperature and 28.5 MPa; the average WHSV was 1.1 h^{-1}.

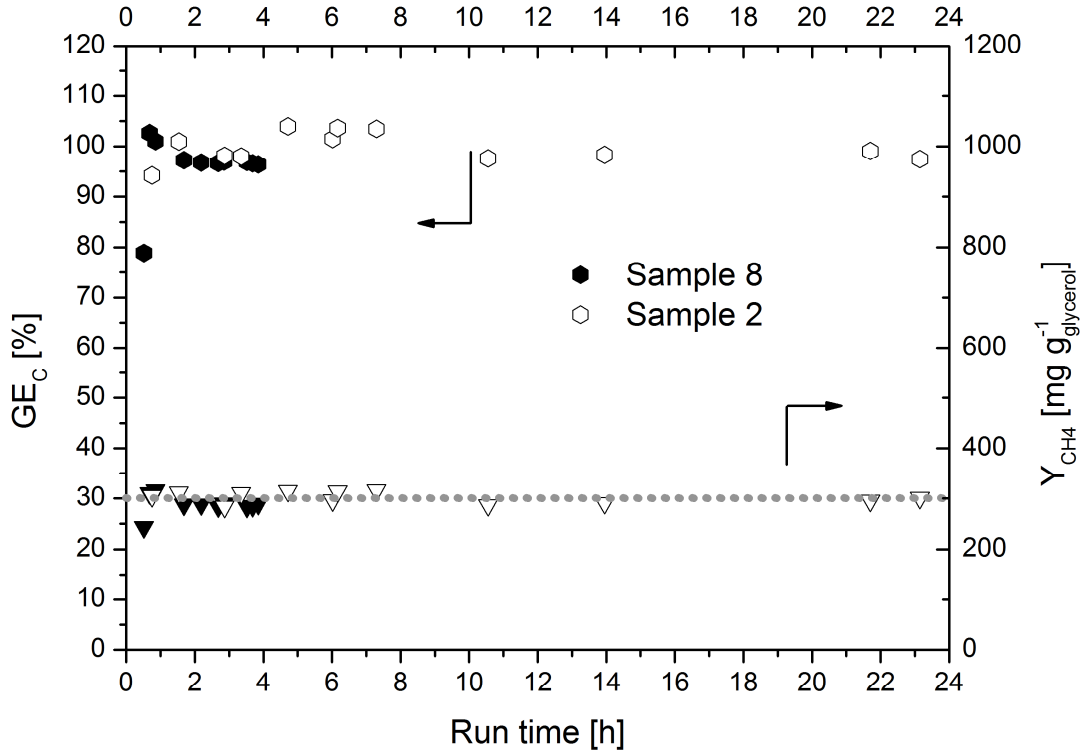

Figure 5-68: Carbon gasification efficiency (hexagons) and methane yield (triangles) over time on stream for gasification of a 11 wt% glycerol solution over a 5 wt% supported ruthenium

catalyst (experiments 5N2b and 5N8b) at 400℃ setpo int temperature and 28.5 MPa; the average WHSV was 1.1 h^{-1}. The dotted line indicates the maximum theoretical methane yield.

Gasification of 16 and 19 wt% glycerol solution was tested for the 5% Ru/ZrO_2 (2) catalyst only. At 16 wt% (WHSV 1.6 h^{-1}), still full conversion could be achieved for 24 h with a small but constant amount of higher hydrocarbons in the product gas (Figure 5-69 and Figure 5-70). Finally for the 19 wt% glycerol solution (WHSV 2 h^{-1}), a limit was reached. Deterioration of the performance over time on stream could be observed here. Therefore, 16 wt% glycerol at a WHSV of 1.6 h^{-1} is the highest concentration leading to full conversion at equilibrium gas composition for the 5% Ru/ZrO_2 (2) catalyst. In comparison, the Ru/C catalyst showed full conversion for a 10 wt% glycerol solution in previous tests by Schubert et al. [60]. In the experiments performed by Schubert et al. a comparable length of the catalyst bed was used, which resulted in a higher WHSV because of the difference in the bulk densities of the support materials. For the 10 wt% glycerol solution, the WHSV was 5 h^{-1}. Therefore, the performance of the 5% Ru/ZrO_2 (2) catalyst relative to the amount of ruthenium is lower than the one of the 2% Ru/C catalyst.

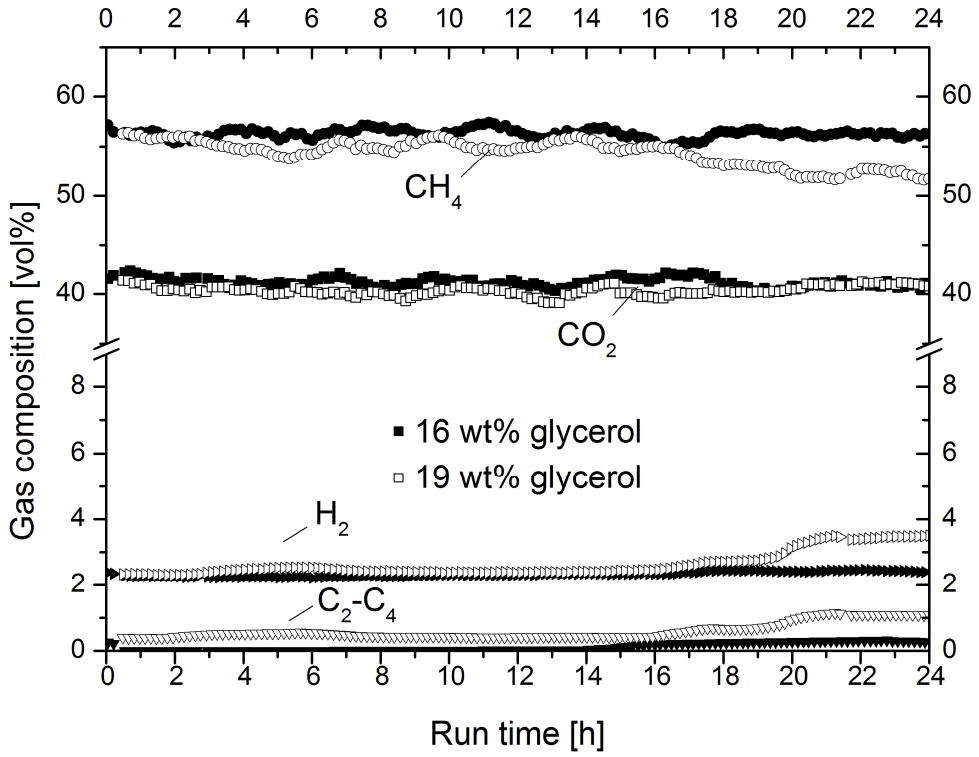

Figure 5-69: Gas composition over time on stream for the gasification of a 16 and 19 wt% glycerol solution over a 5 wt% supported ruthenium catalyst (experiments 5N2c and 5N2d) at 400℃ setpoint temperature and 28.5 MPa; the averag e WHSV was 1.6 and 2 h^{-1}, respectively.

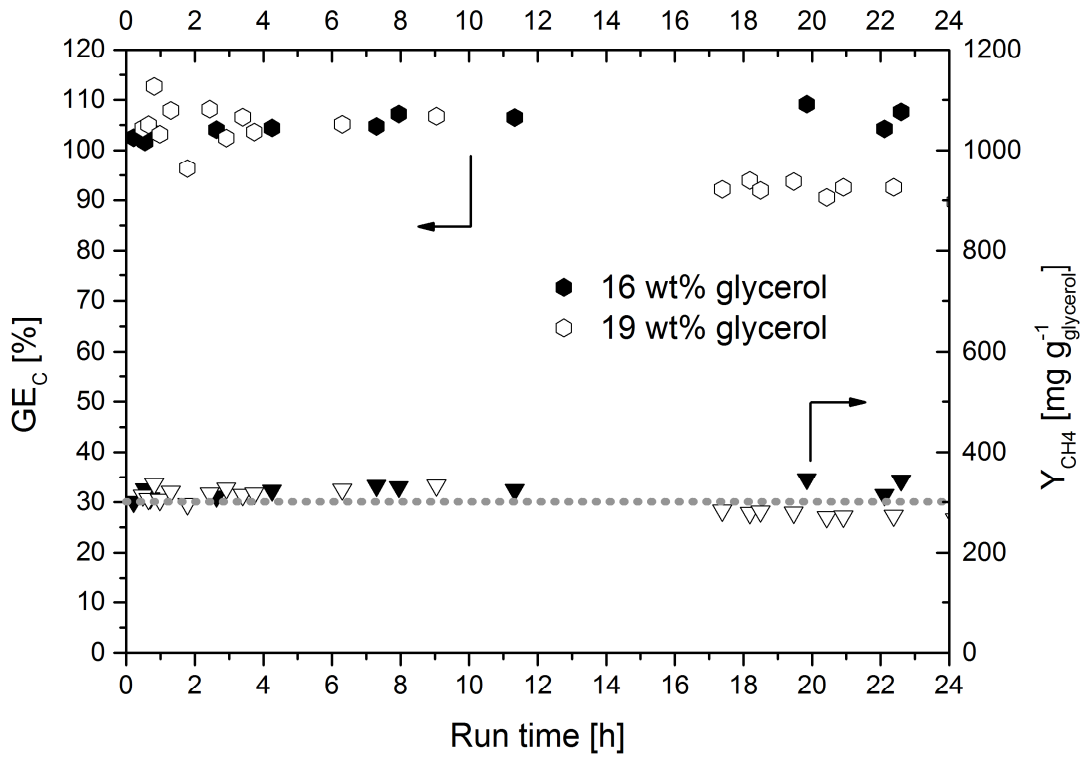

Figure 5-70: Carbon gasification efficiency (hexagons) and methane yield (triangles) over time on stream for gasification of a 16 and 19 wt% glycerol solution over a 5 wt% supported ruthenium catalyst (experiments 5N2c and 5N2d) at 400℃ setpoint temperature and 28.5 MPa; the average WHSV was 1.6 and 2 h^{-1}, respectively. The dotted line indicates the maximum theoretical methane yield.

After gasification of a 19 wt% glycerol solution, a 16 wt% glycerol solution was gasified to test if the incomplete conversion of the 19 wt% glycerol solution was due to aging or due to a catalyst overload. A full gasification with equilibrium product gas composition pointed to the latter, supporting the assumption that a 16 wt% glycerol at a WHSV of 1.6 h^{-1} is the highest concentration leading to full conversion at equilibrium gas composition for the 5% Ru/ZrO_2 (2) catalyst

5.7.3.6 Structural analyses of the 5% ruthenium catalyst systems

With a 5% ruthenium loading, the metal surface area is increasing compared to a 2% loading: from 1.1 to 3.4 m^2 g^{-1} for sample 2 and from 0.1 to 0.4 m^2 g^{-1} for sample 8 (Table 5-6 and Table 5-7).

Similar to the respective support samples with 2% ruthenium loading, the metal surface area decreased significantly after use for gasification. The level to which it had decreased was higher for the 5% loading, though it is not clear if a stable level had already been reached.

Coverage by carbon deposits due to the incomplete conversion of the 19 wt% glycerol solution is unlikely, since full gasification of a 15% glycerol solution could be observed again after this test.

The metal surface area of sample 8 did not alter during gasification. The fairly poor dispersion of the fresh catalyst can therefore be assumed stable.

Table 5-7: BET surface area (BET SA), metal surface area (MSA) and metal dispersion (D) of fresh and used 5% Ru catalyst samples. (1) poor linear fitting, (2) sample not analyzed.

Sample	BET SA (fresh) [m^2/g_{cat}]	BET SA (used) [m^2/g_{cat}]	MSA (fresh) [m^2/g_{cat}]	MSA (used) [m^2/g_{cat}]	D (fresh) [%]	D (used) [%]
2	37	28	3.4	0.7	14	3
8	4.5	4.5	0.4 (1)	0.4	1.7 (1)	1.8

5.7.3.7 Performance test of a bimetallic Ru-Re catalyst

In various studies, the activity of catalysts could be increased by the presence of a second metal (see section 3.6.4). Furthermore, a bimetallic Ru-Re catalyst has been reported to show increased sulfur tolerance compared to a pure Ru catalyst for the reduction of levulinic acid to γ-valerolactone [120]. Since sulfur tolerance of a catalyst is of particular importance for the gasification process of natural biomass in supercritical water, a bimetallic Ru-Re catalyst was tested to assess its catalytic performance and stability in glycerol gasification, and furthermore, for its catalytic performance in the presence of sulfur.

The ZrO_2 sample 2 was impregnated stepwise with Ru and Re at an equimolar ratio. The total metal loading was chosen to result in the same molar loading as the 5% Ru catalyst, being 2.5 wt% Ru and 5 wt% Re. With this loading, a slightly increased performance compared to the 2% Ru/ZrO_2 (2) system was expected. In case of a significant improvement of the performance by the presence of Re, the conversion could be compared with the 5% Ru/ZrO_2 (2) system.

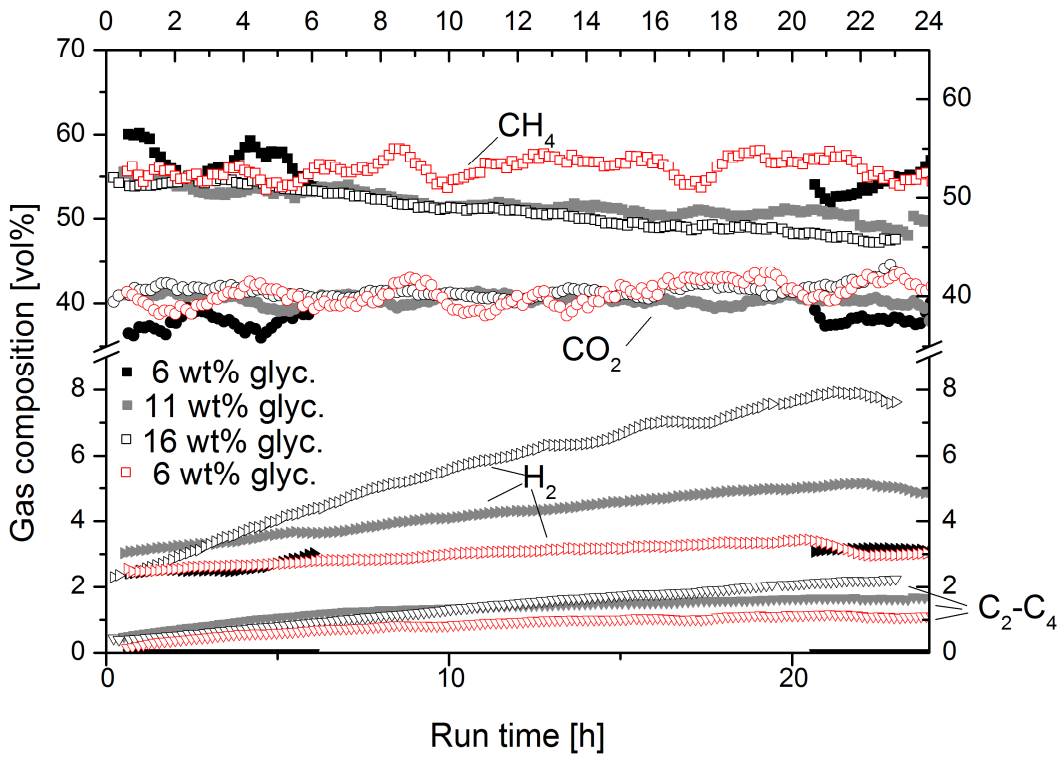

Figure 5-71: Gas composition over time on stream for the gasification of a 6, 11 and 16 wt% glycerol solution over a 7.5 wt% supported bimetallic Ru-Re catalyst (experiments 7.5N2a-7.5N2d) at 400℃ setpoint temperature and 28.5 MPa; the average WHSV was 0.6, 1.1 and 1.6 h^{-1}, respectively.

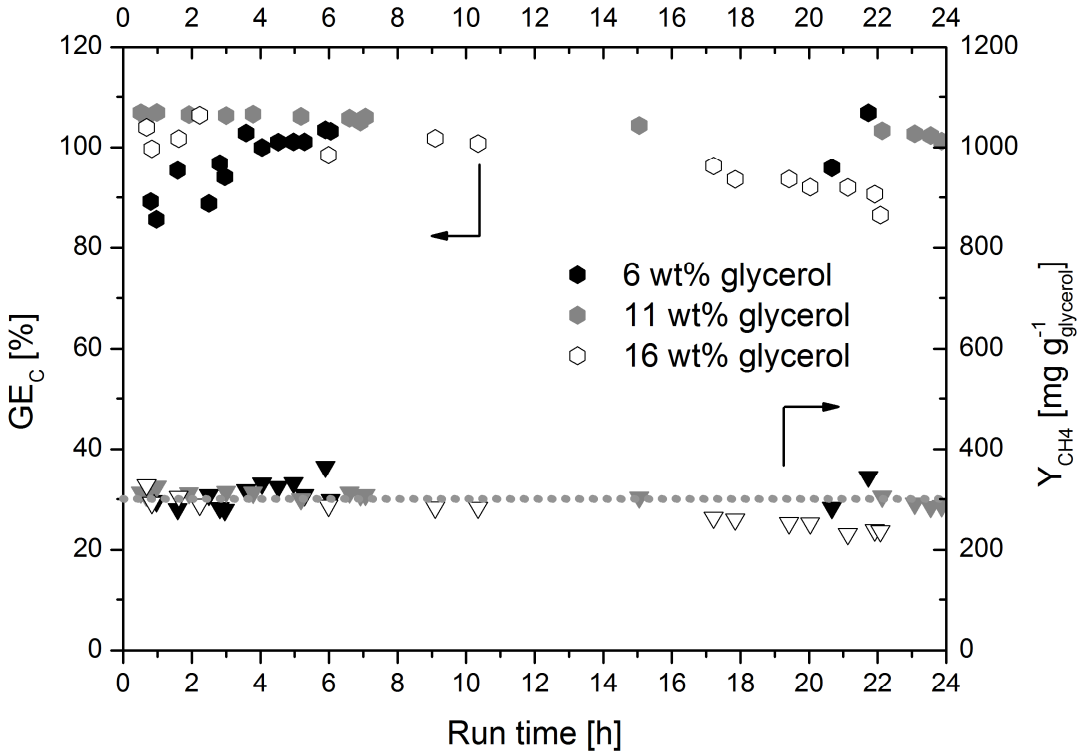

Figure 5-72: Carbon gasification efficiency (hexagons) and methane yield (triangles) over time on stream for gasification of a 6, 11 and 16 wt% glycerol solution over a 7.5 wt% supported bimetallic Ru-Re catalyst (experiments 7.5N2a-7.5N2d) at 400℃ setpoint temperature and 28.5

MPa; the average WHSV was 0.6, 1.1 and 1.6 h^{-1}, respectively. The dotted line indicates the maximum theoretical methane yield.

The results of the gasification experiments with a 6, 11, and 16 wt% glycerol solution are shown in Figure 5-71 and Figure 5-72. During gasification of a 6 wt% glycerol solution a slight increase of the H_2 concentration was observed. This can be interpreted as a hint for a small, yet undetected change in the reactor outlet temperature and thus in the position of the reaction zone. The reforming was still complete. From the temperature profile which is between the one of the 2% Ru/ZrO_2 and the 5% Ru/ZrO_2 (2) system we can conclude that the reforming reaction occurs faster than at 2% Ru loading and is thus completed within a shorter fraction of the catalyst bed (Figure 5-73).

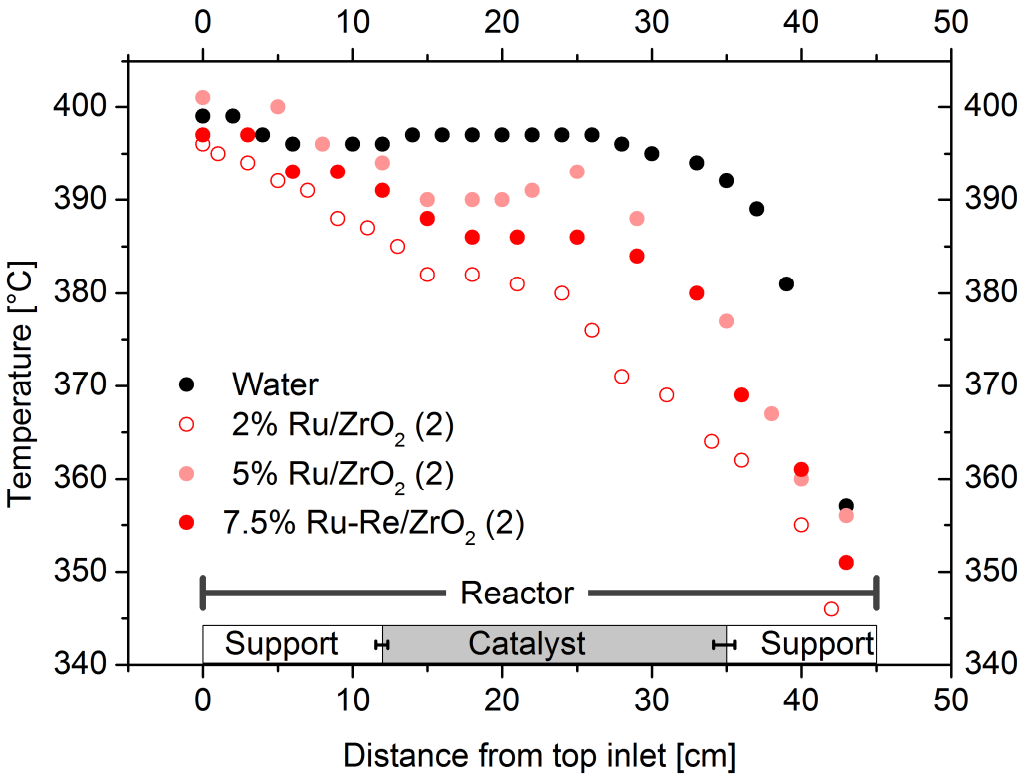

Figure 5-73: Axial temperature profiles over the reactor length for pure water and for the gasification of a 6 wt% glycerol solution. The position of the catalyst bed is marked. (experiments 2N2a, 5N2a, and 7.5N2a).

For the gasification of an 11% glycerol solution over the 7.5 wt% Ru-Re/ZrO_2 (2) system, higher hydrocarbons were produced from the beginning, continuously increasing over the run time. In this respect, it did not differ from the 5% Ru/ZrO_2 system, though the temperature profiles still indicate a slightly faster steam reforming (Figure 5-74). This was, however, already expected from the 0.5% higher

Ru loading. Still the temperature profile of the 5% Ru/ZrO_2 (2) system points to a higher reforming rate. Gasification of a 16 wt% glycerol solution led to a decreasing carbon gasification efficiency after around 15 h. A second gasification run of 6 wt% glycerol led to a considerable amount of higher hydrocarbons detected from the beginning of the experiment, which was not the case during the first gasification of a 6 wt% glycerol solution. This can be interpreted as an aging phenomenon of the catalyst, either by irreversible carbon deposits due to an earlier incomplete conversion or by changes in the Ru dispersion. A distinct improvement of the catalytic performance by the presence of Re can therefore not be confirmed.

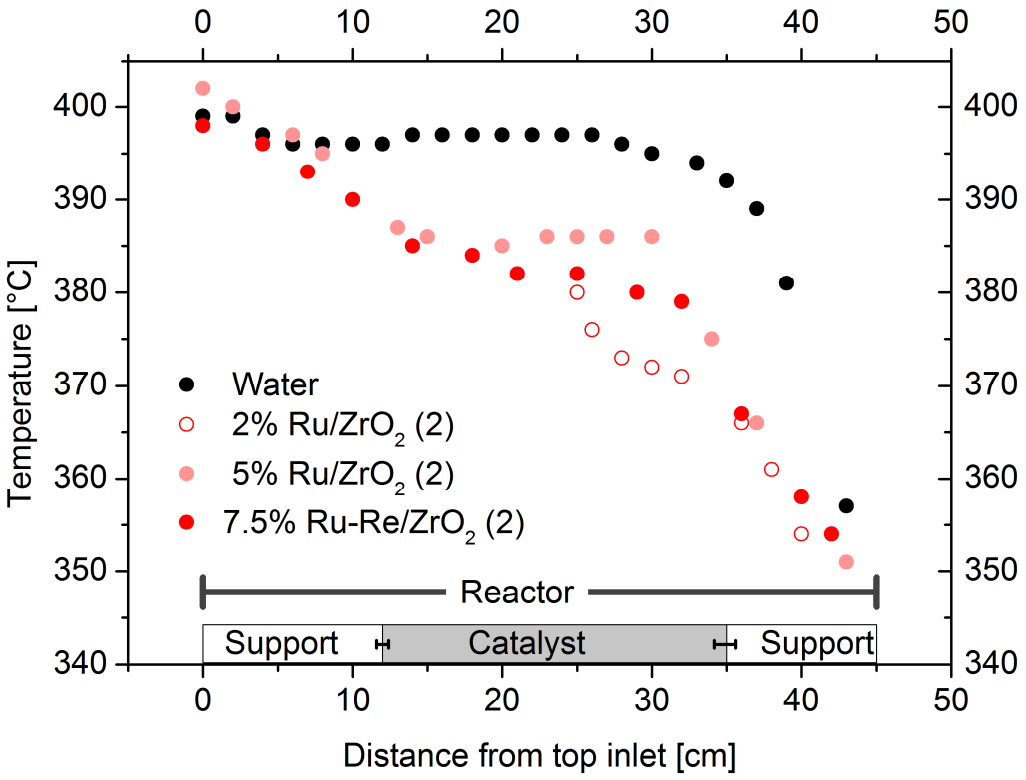

Figure 5-74: Axial temperature profiles over the reactor length for pure water and for the gasification of a 11 wt% glycerol solution. The position of the catalyst bed is marked. (experiments 2N2b, 5N2b, and 7.5N2b).

Finally, the sulfur resistance of the 7.5 wt% $Ru-Re/ZrO_2$ (2) catalyst was tested in a gasification experiment with a 6% glycerol solution in the presence of 0.002 M K_2SO_4. With a molar sulfur flow rate of 0.6 mmol h^{-1} and a metal loading of 6.2 mmol in the reactor, a t_2 = 24.8 h and with an exposed metal amount of 3.39 mmol t_1 = 5.7 h were calculated. It has to be mentioned that the amount of exposed metal determined by H_2 chemisorption measurements is strongly underestimated for Re, because adsorption of H_2 on Re is very low at temperatures below 100°C =[177]=[177]. We can therefore assume that the amount of exposed Ru is relatively close to the measured

total amount of metal. Since Re is expected to show little conversion by itself, the missing information on the number of Re surface atoms is acceptable for this first qualitiative assessment of the influence of Re on the catalytic performance on Ru. Therefore, an optimization of the chemisorption method was not done.

Gas composition and carbon gasification efficiency during the in-situ poisoning experiment are shown in Figure 5-75. A significant response to the poisoning was observed after around 100 min. The carbon gasification efficiency reached a stable level at around 20% of the initial value. An in-situ poisoning experiment with a Ru/ZrO_2 (2) system was not done for comparison, because the results of this experiment were not considered promising.

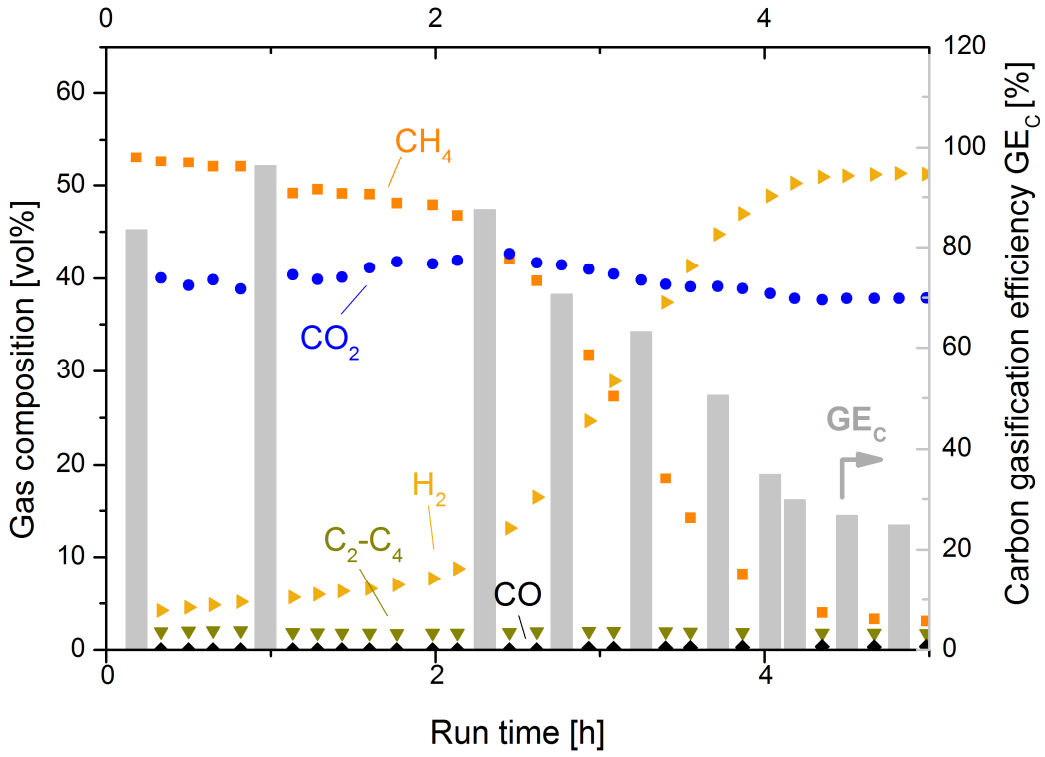

Figure 5-75: Gas composition and carbon gasification efficiency during gasification of a 6 wt% glycerol solution with 0.002 M K_2SO_4 over a 7.5 wt% Ru-Re/ZrO_2 (2) catalyst at 400℃ setpoint temperature and 28.5 MPa (experiment 7.5N2e).

Similar to the regeneration test applied for the 2% Ru/TiO_2 system (5.6.5), the poisoned catalyst was flushed with subcritical water for 18 h. A gasification test with a 6 wt% glycerol solution led to a poor recovery of the initial conversion (Figure 5-76). Starting with around 50% of the initial carbon gasification efficiency, the conversion decreased rapidly. The gas composition, which had slightly shifted in the direction of the thermodynamic equilibrium, was not stable, too.

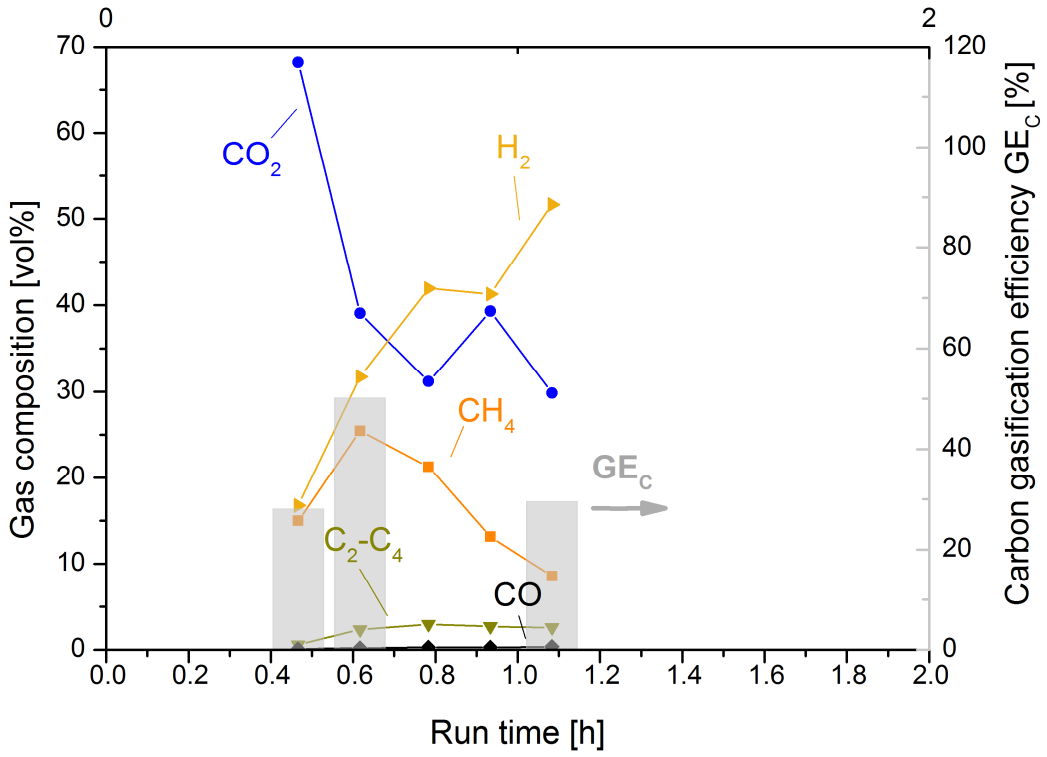

Figure 5-76: Gas composition and carbon gasification efficiency during gasification of a 6 wt% glycerol solution over a 7.5 wt% Ru-Re/ZrO_2 (2) catalyst after poisoning with 0.002 M K_2SO_4 and a flushing period at subcritical conditions (400℃ setpoint temperature, 28.5 MPa, experiment 7.5N2g).

5.7.3.8 Conclusions

Supercritical water is an extraordinarily aggressive medium. Therefore, only few materials can be considered as support materials for catalysts in catalytic supercritical water gasification. Out of 11 commercial support material samples that have been subjected to a screening, we could find five materials showing physical stability after 20 hours of treatment in supercritical water (Samples 2, 5, 7, 8 and 11). Most of the samples, except for sample 8 (rutile) showed a significant decrease of BET surface area. In a second aging step nearly no more decrease of the surface area could be detected.

For the performance test the samples were thus aged before impregnation with active metal. After impregnation with 2% ruthenium, sample 2, 7 and 8 showed a promising performance in terms of the highest WHSV that led to a complete gasification for 24 h. Sample 2 is a ZrO_2 stabilized in the tetragonal structure by HfO_2 and La_2O_3. In the literature, tetragonal ZrO_2 had not been considered as support material for supercritical water applications because of its lacking stability. Sample 7

appeared to be physically unstable when coated with ruthenium, while samples 2 and 8 proved excellent stability over the total experimental run. The BET surface area decreased only to a minor extent, which we attribute to the aging step before impregnation. The ASA showed a minor decrease for all samples.

Samples 2 and 8 were impregnated with 5% ruthenium. For both samples an improvement of the performance could be achieved. For sample 2 the highest WHSV leading to full and stable conversion was 1.7 h^{-1}, which is, however, lower than the performance of the commercial 2% Ru/C catalyst.

A bimetallic 7.5% Ru-Re/ZrO_2 (2) catalyst showed a performance that was similar to the one of the 2%Ru/ZrO_2 (2) catalyst. An improved sulfur tolerance as it was reported by Braden et al. [120] was not confirmed. In contrary to the 2% Ru/TiO_2, which showed partial regeneration, the initial performance could not be recovered by flushing with subcritical water.

6 Summary, Conclusions and Prospects

Fermentation residues of biogas plants represent a feedstock that is considered promising for SNG production via hydrothermal gasification. They are waste products still containing a considerable amount of organic matter, providing an energy source. Due to their high water content and minerals, they cannot be used for combustion.

For this work, the fermentation residue that is collected from the overflow of a two-stage fermentation plant was used for SNG production in a continuous gasification experiment on a test rig resembling PSI's catalytic gasification process (Konti-2). It was the first time a feedstock containing solids was converted in the Konti-2.

In batch experiments the fermentation residues were widely liquefied in the absence of a catalyst. In the presence of a catalyst they could be completely gasified to a methane-rich gas. However, at low catalyst loadings, the conversion was incomplete. This was attributed to the relatively high sulfur content (around 1 wt% of the DM).

In PSI's catalytic gasification process the biomass bound heteroatoms S, N, and P are assumed to be mineralized during the heat-up. The minerals can be removed by a salt separator, avoiding the transportation to the catalytic reactor. In the case of efficient sulfur mineralization and salt separation, no catalyst deactivation by sulfur poisoning would occur. The results of batch experiments without a catalyst suggested that the sulfur is still largely organically bound after liquefaction; however, in a batch system back-reactions of possibly released sulfur during cool-down cannot be excluded, therefore the results may not be representative for a continuous process.

In the continuous experiment the pumping and the liquefaction of the fermentation residue could be realized, except for sedimentation of particles in the pump. Also the salt separation was efficient at a salt separator temperature of 450°C. However, the catalytic gasification was incomplete, probably because of both, catalyst overload and sulfur-poisoning. Sulfur was not efficiently mineralized during heat-up and could thus not be removed in the salt separator.

Furthermore, a high amount of tars was produced during the process, which stuck in the salt separator and could not be dissolved in supercritical water. During cool-down of the salt separator, the tars were redissolved. They passed the catalytic reactor and accumulated in the line plugging the filter downstream of the reactor.
Interestingly, they were not converted by the catalyst. In the batch experiments, tars were only found in marginal amounts. A reason for the high amount of tars formed in the continuous process could be the fact that heat-up, i.e. the liquefaction, was performed in the absence of a catalyst, while in the batch experiments the catalyst was present from the beginning. This points to a first tar production in the preheater. If the tars are not miscible with supercritical water as suggested by the results of this experiment, they form a second phase in the salt separator where supercritical water conditions prevail. An extraction of smaller molecules by the supercritical water phase may promote a condensation of the tar phase. This is in agreement with observations from bitumen upgrading experiments in supercritical water [151]. It is assumed that once produced, the tars are hardly converted by the catalyst. They strongly contribute to catalyst deactivation by fouling, and therefore it is necessary to prevent already the first condensation of tar precursors.

Further continuous experiments performed with Konti-2 without a catalytic reactor were done to investigate the first process steps more deeply, i.e. the liquefaction in the preheater and the salt separator as well as the salt separation. By stabilizing the suspension of the fermentation residue with xanthan, sedimentation in the pump could be avoided and thus a more constant feeding was achieved. A carbon mass balance revealed that around 50% of the total feed carbon did neither leave the rig during the experiment at 430°C salt separator temperature nor during flushing with water at experimental conditions and during cool-down. It was only soluble in ethanol at ambient conditions. Pressure fluctuations on the order of several MPa were observed for all experiments. No salt separation was observed at 430°C salt separator temperature. At 470°C, the rig was blocked after 70 min.
Solid particles were found in the particle traps of the salt separator and the back effluent. The level of carbonization was higher for the particles that left the salt separator from the top outlet. In both particle traps, organic structures of the fermentation residue and amorphous structures were visible by SEM imaging, indicating both, primary and secondary coke formation.

All experiments were done at a pressure of 28 MPa. At these conditions the density of the supercritical water is very low (< 200 kg m^{-3}). The solvent properties of water are closely connected to the density. The dielectric constant of supercritical water is comparable to those of unpolar organic solvents such as hexane. Therefore the solvent properties are assumed to be similar to unpolar organic solvents as well. It is therefore possible that supercritical water at low densities is poorly miscible with heavy tars even at elevated temperatures. A better misciblility might be achieved at higher pressures of supercritical water, because the dielectric constant increases with the temperature. On the other hand, this would be disadvantageous for the salt separation, since low water densities are beneficial in this case.

Further investigations on the phase behavior of water and tars at elevated temperatures and pressures are necessary to understand the condensation of tars. The first condensation of tar precursors in the preheater may be reduced in the presence of a catalyst; however, this would also require a long-term sulfur-tolerant catalyst in this case.

The mineralization and separation of sulfur during heat-up is another remaining problem. Sulfur was detected in the methanol-soluble (tars), the water-soluble (salts and hydrophilic organic molecules), as well as the hexane-soluble (aliphatic organic molecules) fractions of the effluent streams.

In the environment of reducing biomass, sulfur was mainly released as H_2S, which is in accordance with the literature (see section 3.7). Although it was also reported that the addition of alkali hydroxides captures H_2S in the water phase, no improvement of the sulfur mineralization could be achieved via this step in this work. These findings clearly show that beside tar formation the key step of the process is the sulfur handling. For sulfur handling, one might think of a heterogeneous catalyst in the preheater or sulfur traps leading to a semi-continuous switching between two redundant system legs for regeneration and maintenance of the traps. Both pathways might be options to overcome the process boundaries due to sulfur, which need more detailed investigations.

From the experiments with fermentation residue it is concluded that primary coke formation occurs, indicating an incomplete liquefaction of the biomass. Tars are

hardly degraded and lead to the formation of coke, which is assumed to contribute to the catalyst deactivation besides sulfur-poisoning. As already mentioned, control and prevention of tar formation is the second key step of the applied process. The influencing factors are by far not understood completely, especially in the presence of solid compounds.

In a second part of this work, catalyst regeneration methods were investigated. From previous studies it was known that a sulfur-poisoned Ru/C catalyst cannot be regenerated by flushing with subcritical water or by reductive treatment with formic acid. Only an oxidative treatment resulted in a reactivation of the catalyst. However, the performance of the reactivated catalyst was reduced compared to the fresh one. Therefore, the influence of both, sulfur and oxidizing agent (H_2O_2) on the catalyst system were investigated with respect to structural changes. It was found that the catalyst deactivated by treatment with sulfate in the absence of a reducing agent, which is in contradiction to other findings claiming sulfide to be the poisoning species. It is therefore assumed that the catalyst support acts as reducing agent if no biomass is present. The oxidative treatment led to a degradation of the catalyst support. The metal surface area of the regenerated catalyst was lower than the initial one, pointing to an incomplete regeneration. Ruthenium leaching as a consequence of the degradation of the support was assumed to play a negligible role, since an oxidative treatment of the fresh catalyst led to a minor decrease of the metal surface area.

New catalyst systems based on commercial refractory oxide supports were synthesized and screened in a further part of this work. These support materials were expected to show an increased stability towards an oxidizing environment. Furthermore, it was assumed that an improved utilization of the catalyst pellet could be achieved by the mesoporous structure of the support. The commercial Ru/C catalyst that was used for the other experiments was a microporous egg-shell catalyst. A 5% Ru/ZrO_2 catalyst showed the best performance within the tested systems. The support material was a tetragonal ZrO_2 stabilized with HfO_2 and La_2O_3. A rutile support was also stable under hydrothermal conditions; however, the

performance was lower compared to the Ru/ZrO_2 system at equal ruthenium loading.

The 2% Ru/TiO_2 (rutile) system showed a higher stability towards an oxidizing environment. Furthermore, flushing with subcritical water led to a partial reactivation after sulfur-poisoning. This indicated a reversibility of the Ru-S binding in the case of the TiO_2 support. The different acidities of the support materials, carbon and rutile, were assumed to influence the electronic environment of the Ru-S interaction. Further investigations are necessary to elucidate this phenomenon. The characteristic of the Ru/TiO_2 system could be interesting with respect to more sulfur tolerant catalysts. However, the catalytic performance of this system needs to be optimized.

6.1 References

[1] C. P. Timmer. Reflections on food crises past. *Food Policy*, 35(1):1–11, February 2010.

[2] T. Yoshida and Y. Matsumura. Gasification of cellulose, xylan, and lignin mixtures in supercritical water. *Ind. Eng. Chem. Res.*, 40(23):5469–5474, 2001.

[3] T. Yoshida, Y. Oshima, and Y. Matsumura. Gasification of biomass model compounds and real biomass in supercritical water. *Biomass Bioenerg*, 26(1):71–78, 2004.

[4] T. Minowa and T. Ogi. Hydrogen production from cellulose using a reduced nickel catalyst. *Catal. Today*, 45:411–416, October 1998.

[5] M. Osada, O. Sato, M. Watanabe, K. Arai, and M. Shirai. Water Density Effect on Lignin Gasification over Supported Noble Metal Catalysts in Supercritical Water. *Energy Fuels*, 20(3):930–935, 2006.

[6] F. Vogel, M. Waldner, T.-B. Truong, E. De Boni, and S. Stucki, inventors; Paul Scherrer Institut, assignee. Verfahren zur Erzeugung von Methan und Methanhydrat aus Biomasse (Process for the production of methane and methane hydrate from biomass), Patent PCT 05021601.9/EP 0502210. 2005.

[7] EBA. Biogas in Europe 2011. European Biogas Association, Brussels, Belgium; available online: http://www.european-biogas.eu, 15.05.2012.

[8] D. Wilken, Fachverband Biogas e.V., Freising, Germany. personal communications, 17.04.2013.

[9] Branchenzahlen 2011 und Prognose der Branchenentwicklung 2012/2013. Fachverband Biogas e.V., Freising, 2012.

[10] Einsatz von Gärresten aus der Biogasproduktion als Düngemittel, 4. Auflage. Bayrische Landesantstalt für Landwirtschaft, Freising, Germany, 2013.

[11] Schweizerische Qualitätsrichtlinie 2010 der Branche für Kompost und Gärgut. Inspektoratskommission der Kompostier- und Vergärbranche der Schweiz, Schönbühl-Urtenen, Switzerland, 2010.

[12] Verordnung 1069/2009 des Europäischen Parlaments und des Rates, 2009.

[13] A. Kruse and E. Dinjus. Hot Compressed Water as Reaction Medium and Reactant - 2. Degradation Reactions. *J. Supercrit. Fluids.*, 41(3):361–379, 2007.

[14] A. Peterson, F. Vogel, R. Lachance, M. Froeling, M. Antal, Jr., and J. Tester. Thermochemical Biofuel Production in Hydrothermal Media: A Review of Sub- and Supercritical Water Technologies. *Energy Environ. Sci.*, 1(1):32–65, 2008.

[15] http://webbook.nist.gov/chemistry.

[16] D. Fernandez, A. Goodwin, E. Lemmon, J. Sengers, and R. Williams. A Formulation for the Static Permittivity of Water and Steam at Temperatures from 238 K To 873 K at Pressures up to 1200 MPa, Including Derivatives and Debye-Huckel Coefficients. *J. Phys. Chem. Ref. Data,* 26(4):1125–1166, 1997.

[17] D. Lide. *CRC Handbook of Chemistry and Physics*. Internet Version 2005, <http://www.hbcpnetbase.com>, CRC Press, Boca Raton, FL, 2005, 2005.

[18] M. Modell. *Gasification and liquefaction of forest products in supercritical water*, chapter 6, pages 95–119. Elsevier, London, 1985.

[19] J. Müller. Hydrothermal Gasificatioin of Biomass - Investigations on coke formation and continuous salt separation with pure and real substrates. PhD thesis, ETH Zürich, 2012.

[20] H. Weingärtner and E. Franck. Überkritisches Wasser als Lösungsmittel. *Angew. Chem.*, 117:2730–2752, 2005.

[21] P. Savage, S. Gopalan, T. Mizan, C. Martino, and E. Brock. Reactions at supercritical conditions: Applications and fundamentals. *AIChE Journal*, 41:1723–1778, 1995.

[22] A. Kruse and E. Dinjus. Hot Compressed Water as Reaction Medium and Reactant: Properties and Synthesis Reactions. *J. Supercrit. Fluid.*, 39(3):362 – 380, 2007.

[23] F Armellini. Phase Equilibria and Precipitation Phenomena of Sodium Chloride and Sodium Sulfate in Sub- and Supercritical Water. PhD thesis, Massachusetts Institut of Technology, 1993.

[24] J. Tester, P. Marrone, M. DiPippo, K. Sako, M. Reagan, T. Arias, and W Peters. Chemical reactions and phase equilibria of model halocarbons and salts in sub- and supercritical water (200-300 bar, 100-600°C). *J. Supercrit. Fluids*, 13(1-3):225–240, 1998.

[25] M. Schubert, J. Regler, and F. Vogel. Continuous salt precipitation and separation from supercritical water. part 1: Type 1 salts. *J. Supercrit. Fluids*, 52(1):99–112, 2010.

[26] M. Schubert, J. Regler, and F. Vogel. Continuous salt precipitation and separation from supercritical water. part 2. type 2 salts and mixtures of two salts. *J. Supercrit. Fluids*, 52(1):113–124, 2010.

[27] M. Schubert, J. Aubert, J. Müller, and F. Vogel. Continuous salt precipitation and separation from supercritical water. part 3: Interesting effects in processing type 2 salt mixtures. *J. Supercrit. Fluids*, 61(0):44–45, 2012.

[28] Martin Schubert. Catalytic hydrothermal gasification of biomass - salt recovery and continuous gasification of glycerol solutions. PhD thesis, ETH Zürich, 2010.

[29] W. Lamb, G. Hoffman, and J. Jonas. Self-diffusion in compressed supercritical water. *J. Chem. Phys.*, 74(12):6875–6880, 1981.

[30] M. Holz, S. Heil, and A. Sacco. Temperature-dependent self-diffusion coefficients of water and six selected molecular liquids for calibration in accurate ^{1}H NMR PFG measurements. *Phys. Chem. Chem. Phys.*, 2:4740–4742, 2000.

[31] W. Flarsheim, Y. Tsou, I. Trachtenberg, K. Johnston, and A. Bard. Electrochemistry in near-critical and supercritical fluids. 3. studies of bromide, iodide, and hydroquinone in aqueous solutions. *J. Phys. Chem.*, 90(16):3857–3862, 1986.

[32] M. Goemans, E. Gloyna, and S. Buelow. Mass transfer of SCWO processes: Molecular diffusion and mass transfer coefficients of inorganic nitrate species in sub-

and supercritical water. *Proceedings of the Second International Symposium on Adcanved Oxidation Technologies, San Francisco, USA*, 1996.

[33] R. Schloegl. H. Tyrell, K. Harris: Diffusion in liquids, a theoretical and experimental study, Butterworth, London 1984. 448 Seiten. *Ber. Bunsen. phys. Chem.*, 89(2):209–210, 1985.

[34] T. Butenhoff, M. Goemans, and S. Buelow. Mass diffusion coefficients and thermal diffusivity in concentrated hydrothermal $NaNO_3$ solutions. *J. Phys. Chem.*, 100(14):5982–5992, 1996.

[35] A. Bandura and S. Lvov. The Ionization Constant of Water over Wide Ranges of Temperature and Density. *J. Phys. Chem. Ref. Data*, 35(1):15–30, 2006.

[36] Y. Guo, S. Wang, D. Xu, Y. Gong, H. Ma, and X. Tang. Review of Catalytic Supercritical Water Gasification for Hydrogen Production from Biomass. *Renew. Sust. Energ. Rev.*, 14(1):334–343, 2010.

[37] W. Marshall and E. Jone. Liquid-Vapor Critical Temperatures of Aqueous Electrolyte Solutions. *J. Inorg. Nucl. Chem.*, 36:2313–2318, 1974.

[38] V. Valyashko. *Aqueous Systems at Elevated Temperatures and Pressures. Physical Chemistry in Water, Steam and Hydrothermal Solutions*, chapter Phase equilibria of water-salt systems at high temperatures and pressures, pages 597–641. Elsevier Ltd., 2004.

[39] G. Morey. The solubility of solids in gases. *Econ. Geol.*, 52:225–251, 1957.

[40] V. Rumyantsev. Selection Mineralizers in the Hydrothermal Synthesis and Growth of Crystals. *Soviet Physics-Crystallography*, 22(5), 1977.

[41] V. Valyashko. Phase Equilibria in Water-Salt Systems: Some Problems of Solubility at Elevated Temperature and Pressure. In *High Temperature High Pressure Electrochemistry in Aqueous Solutions*, volume 4, pages 153–157. National Association of Corrosion Engineers, 1976.

[42] W. Bühler, E. Dinjus, H. Ederer, A. Kruse, and C. Mas. Ionic reactions and pyrolysis of glycerol as competing reaction pathways in near- and supercritical water. *J. Supercrit. Fluids*, 22(1):37–53, 2002.

[43] M. Antal, A. Brittain, C. DeAlmeida, S. Ramayya, and J. Roy. Heterolysis and homolysis in supercritical water. In *ACS Symposium Series*, 329:77–86. *J. Am. Ceram. Soc.*, 1987.

[44] O. Bobleter. Hydrothermal degradation of polymers derived from plants. *Prog. Polym. Sci.*, 19(5):797–841, 1994.

[45] M. Sasaki, B. Kabyemela, R. Malaluan, S. Hirose, N. Takeda, T. Adschiri, and K. Arai. Cellulose hydrolysis in subcritical and supercritical water. *J. Supercrit. Fluids*, 13:261 – 268, 1998.

[46] M. Sasaki, T. Adschiri, and K. Arai. Kinetics of cellulose conversion at 25 MPa in sub- and supercritical water. *AIChE Journal*, 50(1):192–202, 2004.

[47] E. Harris, J. D'Ianni, and H. Adkins. Reaction of hardwood lignin with hydrogen. *J. Am. Chem. Soc.*, 60(6):1467–1470, 1938.

[48] H. Nimz. Das Lignin der Buche - Entwurf eines Konstitutionsschemas. *Angew. Chem.*, 86(9):336–344, 1974.

[49] K. Lundquist. On the separation of lignin degradation products. *Acta Chem.. Scand.*, 18:1316–1317, 1964.

[50] S. Masselter, A. Zemann, and O. Bobleter. Analysis of lignin degradation products by capillary electrophoresis. *Chromatographia*, 40(1-2):51–57, 1995.

[51] B. Kabyemela, T. Adschiri, R. Malaluan, and K Arai. Glucose and fructose decomposition in subcritical and supercritical water: detailed reaction pathway, mechanisms, and kinetics. *Ind. Eng. Chem. Res.*, 38(8):2888–2895, 1999.

[52] Z. Srokol, A.-G. Bouche, A. van Estrik, R. Strik, T. Maschmeyer, and J. Peters. Hydrothermal upgrading of biomass to biofuel; studies on some monosaccharide model compounds. *Carbohyd. Res.*, 339(10):1717–1726, 2004.

[53] M. Antal Jr., W. Mok, and G. Richards. Mechanism of formation of 5-(hydroxymethyl)-2-furaldehyde from D-fructose and sucrose. *Carbohyd. Res.*, 199(1):91–109, 1990.

[54] A. Kruse and A. Gawlik. Biomass conversion in water at 330-410 °C and 30-50 MPa. Identification of key compounds for indicating different chemical reaction pathways. *Ind. Eng. Chem. Res.*, 42(2):267–279, 2003.

[55] A. Chuntanapum and Y. Matsumura. Char formation mechanism in supercritical water gasification process: A study of model compounds. *Ind. Eng. Chem. Res.*, 49(9):4055–4062, 2010.

[56] G. Luijkx, F. Rantwijk, and H. van Bekkum. Hydrothermal formation of 1,2,4-benzenetriol from 5-hydroxymethyl-2-furaldehyde and D-fructose. *Carbohyd. Res.*, 242(0):131–139, 1993.

[57] H.L. Barnebey and A.C. Brown. Continuous fat splitting plants using the colgate-emery process. 25(3):95–99–, 1948.

[58] M. Watanabe, T. Iida, and H. Inomata. Decomposition of a Long Chain Saturated Fatty Acid with some Additives in Hot Compressed Water. *Energ. Convers. Manage.*, 47(1819):3344–3350, 2006.

[59] R. Holliday, J.. King, and G. List. Hydrolysis of vegetable oils in sub- and supercritical water. *Ind. Eng. Chem. Res.*, 36(3):932–935, 1997.

[60] M. Schubert and F. Vogel. Axpo Naturstrom Fonds Report: Regenerierung von Katalysatoren für die Hydrothermale Vergasung nasser Biomasse. Technical report, Paul Scherrer Institut, 2011.

[61] S. Ramayya, A. Brittain, C. Dealmeida, W. Mok, and M. Antal. Acid-catalyzed cehydration of alcohols in supercritical water. *Fuel*, 66(10):1364–1371, 1987.

[62] N. Sato, A. Quitain, K. Kang, H. Daimon, and K. Fujie. Reaction kinetics of amino acid decomposition in high-temperature and high-pressure water. *Ind. Eng. Chem. Res.*, 43(13):3217–3222, 2004.

[63] D. Klingler, J. Berg, and H. Vogel. Hydrothermal reactions of alanine and glycine in sub- and supercritical water. *J. Supercrit. Fluids*, 43(1):112–119, 2007.

[64] A. Kruse. Supercritical Water Gasification. *Biofuels, Bioprod. Biorefin.*, 2(5):415–437, 2008.

[65] M. Arakane, T. Imai, S. Murakami, M. Takeuchi, M. Ukita, M. Sekine, and T. Higuchi. Resource recovery from excess sludge by subcritical water combined with magnesium ammonium phosphate process. *Water Sci. Technol.*, 54(9):81–86, 2006.

[66] S.Yildiz Bircan, H. Kamoshita, R. Kanamori, Y. Ishida, K. Matsumoto, Y. Hasegawa, and K. Kitagawa. Behavior of heteroatom compounds in hydrothermal gasification of biowaste for hydrogen production. *Appl. Energ.*, 88(12):4874–4878, 2011.

[67] M. Antonietti and M.-M. Titirici. Coal from carbohydrates: The "chimie douce" of carbon. *Comptes Rendus Chimie*, 13(1-2):167–173, 2010.

[68] F. Vogel. *Handbook of Green Chemistry, Volume 2: Heterogenous Catalysis*, chapter Catalytic Conversion of high-moisture biomass to synthetic natural gas in supercritical water, pages 281–324. WILEY-VCH Verlag GmbH & Co. KGaA Weinheim, 2009.

[69] N. Boukis, V. Diem, W. Habicht, and E. Dinjus. Methanol Reforming in Supercritical Water. *Ind. Eng. Chem. Res.*, 42(4):728–735, 2003.

[70] S. Kersten, B. Potic, W. Prins, and W. Van Swaaij. Gasification of Model Compounds and Wood in Hot Compressed Water. *Ind. Eng. Chem. Res*, 45(12):4169–4177, 2006.

[71] M. Dreher, B. Johnson, A. Peterson, M. Nachtegaal, J. Wambach, and F. Vogel. Catalysis in supercritical water: Pathway of the methanation reaction and sulfur poisoning over a Ru/C catalyst during the reforming of biomolecules. *J. Catal.*, 301(0):38–45, 2013.

[72] X. Xu, Y. Matsumura, J. Stenberg, and M. Antal. Carbon-Catalyzed Gasification of Organic Feedstocks in Supercritical Water. *Ind. Eng. Chem. Res.*, 35:2522–2530, 1996.

[73] Y. Matsumura, X. Xu, and M. J. Antal. Gasification Characteristics of an Activated Carbon in Supercritical Water. *Carbon*, 35(6):819 – 824, 1997.

[74] M. Antal, S.Allen, D. Schulman, X. Xu, and R. Divilio. Biomass gasification in supercritical water. *Ind. Eng. Chem. Res.*, 39(11):4040–4053, 2000.

[75] H. Munetsuna, M. Tamai, Y. Noda, and Y. Matsumura. Supercritical water gasification staged at intervals for hydrogen fermentation residue of food waste. *J. Jpn. I.Energ.*, 89(12):1173–1178, 2010.

[76] A. Kruse, D. Meier, P. Rimbrecht, and M. Schacht. Gasification of Pyrocatechol in Supercritical Water in the Presence of Potassium Hydroxide. *Ind. Eng. Chem. Res.*, 39(12):4842–4848, 2000.

[77] G. Sdü-Yekarum and A. Kruse. Influence of salts on the subcritical water-gas shift reaction. *J. Supercrit. Fluids*, 66:207-214, 2011.

[78] N. Boukis, U. Galla, H. Müller, and E. Dinjus. Hydrothermal Gasification of Glycerol on the Pilot Scale. In *16th European Biomass Conference & Exhibition*, Valencia, Spain, 2008.

[79] D. Elliott and L. Sealock. *Low Temperature Gasification of Biomass Under Pressure*, pages 937–950. Elsevier, London, 1985.

[80] A. Kruse, A. Krupka, V. Schwarzkopf, C.Gamard, and T. Henningsen. Influence of proteins on the hydrothermal gasification and liquefaction of biomass. 1. Comparison of different feedstocks. *Ind. Eng. Chem. Res.*, 44(9):3013–3020, 2005.

[81] A. Kruse, P. Maniam, and F. Spieler. Influence of proteins on the hydrothermal gasification and liquefaction of biomass. 2. Model compounds. *Ind. Eng. Chem. Res.*, 46(1):87–96, 2006.

[82] M. Osada, A. Yamaguchi, N. Hiyoshi, O. Sato, and M. Shirai. Gasification of sugarcane bagasse over supported ruthenium catalysts in supercritical water. *Energy Fuels*, 26 (6):3179-3186, 2012.

[83] D. Elliott, G. Neuenschwander, M. Phelps, T. Hart, A. Zacher, and L. Silva. Chemical Processing in High-Pressure Aqueous Environments. 6. Demonstration of Catalytic Gasification for Chemical Manufacturing Wastewater Cleanup in Industrial Plants. *Ind. Eng. Chem. Res.*, 38(3):879–883, 1999.

[84] D. Elliott, G. Neuenschwander, T. Hart, R. Butner, A. Zacher, M. Engelhard, J. Young, and D. McCready. Chemical Processing in High-Pressure Aqueous Environments. 7. Process Development for Catalytic Gasification of Wet Biomass Feedstocks. *Ind. Eng. Chem. Res.*, 43(9):1999–2004, 2004.

[85] D. Elliott, G. Neuenschwander, T. Hart, L. Rotness, A. Zacher, D. Santosa, C. Valkenburg, S. Jones, and S. Tjokro Rahardjo. *Catalytic Hydrothermal Gasification of Lignin-Rich Biorefinery Residues and Algae - Final Report*. Pacific Norhwest National Laboratory: Richland, WA, 2009.

[86] B. Yan, J. Wu, C. Xie, F. He, and C. Wei. Supercritical Water Gasification with Ni/ZrO_2 Catalyst for Hydrogen Production from Model Wastewater of Polyethylene Glycol. *J. Supercrit. Fluids*, 50(2):155–161, 2009.

[87] D. Elliott, L. Sealock, and E. Baker. Chemical-processing in High-pressure Aqueous Environments .2. Development of Catalysts for Gasification. *Ind. Eng. Chem. Res.*, 32(8):1542–1548, 1993.

[88] D. Elliott, L. Sealock, and E. Baker. Chemical Processing in High-Pressure Aqueous Environments. 3. Batch Reactor Process-Development Experiments for Organics Destruction. *Ind. Eng. Chem. Res.*, 33(3):558–565, 1994.

[89] D. Elliott, M. Phelps, L. Sealock, and E. Baker. Chemical Processing in High-Pressure Aqueous Environments. 4. Continuous-flow reactor process-development experiments for organics destruction. *Ind. Eng. Chem. Res.*, 33(3):566–574, 1994.

[90] J. Wambach, M. Schubert, M. Dobeli, and F. Vogel. Characterization of a spent Ru/C catalyst after gasification of biomass in supercritical water. *Chimia*, 66(9):706–711, 2012.

[91] K. Park and H. Tomiyasu. Gasification Reaction of Organic Compounds Catalyzed by RuO2 in Supercritical Water. *Chem. Commun.*, (6):694–695, 2003.

[92] W. Ketchie, E. Maris, and R. Davis. In-situ X-ray Absorption Spectroscopy of Supported Ru Catalysts in the Aqueous Phase. *Chemistry of Materials*, 19(14):3406–3411, 2007.

[93] A. Yamaguchi, N. Hiyoshi, O. Sato, M. Osada, and M. Shirai. Lignin Gasification over Supported Ruthenium Trivalent Salts in Supercritical Water. *Energy Fuels*, 22(3):1485–1492, 2008.

[94] A. Yamaguchi, N. Hiyoshi, O. Sato, M. Osada, and M. Shirai. EXAFS Study on Structural Change of Charcoal-Supported Ruthenium Catalysts during Lignin Gasification in Supercritical Water. *Catal. lett.*, 122(1-2):188–195, 2008.

[95] S. Rabe, M. Nachtegaal, T. Ulrich, and Frédéric Vogel. Towards Understanding the Catalytic Reforming of Biomass in Supercritical Water. *Angw. Chem. Int. Ed.*, 49:1–5, 2010.

[96] M. Dreher, E. De Boni, M. Nachtegaal, J. Wambach, and F. Vogel. Design of a continuous-flow reactor for in situ x-ray absorption spectroscopy of solids in supercritical fluids. *Review of Scientific Instruments*, 83(5):054101, 2012.

[97] G. Jones, J. Jakobsen, S. Shim, J. Kleis, M.Andersson, J. Rossmeisl, F. Abild-Pedersen, T. Bligaard, S. Helveg, B. Hinnemann, J. Rostrup-Nielsen, I. Chorkendorff, J. Sehested, and J. . Nørskov. First principles calculations and experimental insight into methane steam reforming over transition metal catalysts. *J.Catal.*, 259(1):147–160, 2008.

[98] S. Vendelbo, M. Johansson, J. Nielsen, and I. Chorkendorff. Is the methanation reaction over Ru single crystals structure dependent? *Phys. Chem. Chem. Phys.*, 13(10):4486–4493, 2011.

[99] J. Rostrup-Nielsen, K. Pedersen, and J. Sehested. High temperature methanation: Sintering and structure sensitivity. *Appl. Catal. A: General*, 330(0):134–138, 2007.

[100] I. Czekaj and J. Wambach. DFT modelling of Ru nanoparticles supported on graphene and graphite surface: A study of the B_5 active sites localisation. *submitted manuscript*, 2013.

[101] R. van Hardeveld and A. van Montfoort. The influence of crystallite size on the adsorption of molecular nitrogen on nickel, palladium and platinum: An infrared and electron-microscopic study. *Surf. Sci.*, 4(4):396–430, 1966.

[102] M. Vannice. The catalytic synthesis of hydrocarbons from H_2/CO mixtures over the group VIII metals: V. the catalytic behavior of silica-supported metals. *J. Catal.*, 50(2):228–236, 1977.

[103] J. Rostrup-Nielsen. *Steam Reforming Catalysts*. Teknisk Forlag, Copenhagen, 1975.

[104] C. Satterfield. *Heterogeneius catalysis in industrial practice, 2nd edn*. McGraw-Hill, New York, 1991.

[105] T. Sato, M. Osada, M. Watanabe, M. Shirai, and K. Arai. Gasification of alkylphenols with supported noble metal catalysts in supercritical water. *Ind. Eng. Chem. Res.*, 42(19):4277–4282, 2003.

[106] M. Waldner, F. Krumeich, and F. Vogel. Synthetic Natural Gas by Hydrothermal Gasification of Biomass Selection Procedure towards a Stable Catalyst and Its Sodium Sulfate Tolerance. *J. Supercrit. Fluids*, 43(1):91–105, 2007.

[107] D. Elliott, T. Hart, and G. Neuenschwander. Chemical Processing in High-Pressure Aqueous Environments. 8. Improved Catalysts for Hydrothermal Gasification. *Ind. Eng. Chem. Res.*, 45(11):3776–3781, 2006.

[108] M. Waldner. Catalytic Hydrothermal Gasification of Biomass for the Production of Synthetic Natural Gas. PhD thesis, ETH Zurich, 2007.

[109] M. Osada, O. Sato, K. Arai, and M. Shirai. Stability of supported ruthenium catalysts for lignin gasification in supercritical water. *Energy Fuels*, 20(6):2337–2343, 2006.

[110] X. Hao, L. Guo, X. Zhang, and Y. Guan. Hydrogen production from catalytic gasification of cellulose in supercritical water. *Chem. Eng. J.*, 110(1-3):57–65, 2005.

[111] N. Boukis, N. Claussen, K. Ebert, R. Janssen, and M. Schacht. Corrosion screening tests of high-performance ceramics in supercritical water containing oxygen and hydrochloric acid. *J. Eur. Ceram. Soc.*, 17(1):71–76, 1997.

[112] A. Byrd, S. Kumar, L. Kong, H. Ramsurn, and R. Gupta. Hydrogen production from catalytic gasification of switchgrass biocrude in supercritical water. *Int. J. Hydrogen Energ.*, 36(5):3426–3433, 2011.

[113] A. Yamaguchi, N. Hiyoshi, O. Sato, K. Bando, M. Osada, and M. Shirai. Hydrogen Production from Woody Biomass over Supported Metal Catalysts in Supercritical Water. *Catal. Today*, 146(1-2):192 – 195, 2009.

[114] A. May, J. Salvado, C. Torras, and D. Montane. Catalytic gasification of glycerol in supercritical water. *Chem. Eng. J.*, 160(2):751–759, 2010.

[115] A. Chakinala, D. Brilman, W. van Swaaij, and S. Kersten. Catalytic and non-catalytic supercritical water gasification of microalgae and glycerol. *Ind. Eng. Chem. Res.*, 49(3):1113–1122, 2010.

[116] J. Sinfelt. *Bimetallic Catalysts-Heterogeneous*. John Wiley & Sons, Inc., 2002.

[117] J. Rodriguez and D. Goodman. High-pressure catalytic reactions over single-crystal metal surfaces. *Surf. Sci. Rep.*, 14:1–107, 1991.

[118] W. Sachtler. The second rideal lecture. what makes a catalyst selective? *Faraday Discuss. Chem. Soc.*, 72:7–31, 1981.

[119] J. Rodriguez and J. Hrbek. Interaction of sulfur with well-defined metal and oxide surfaces: unraveling the mysteries behind catalyst poisoning and desulfurization. *Acc. Chem. Res.*, 32(9):719–728, 1999.

[120] D. Braden, C. Henao, J. Heltzel, C. Maravelias, and J. Dumesic. Production of liquid hydrocarbon fuels by catalytic conversion of biomass-derived levulinic acid. *Green Chem.*, 13(7):1755–1765, 2011.

[121] Abdul-Majeed Azad and Martin J. Duran. Development of ceria-supported sulfur tolerant nanocatalysts: Rh-based formulations. *Appl. Catal. A: General*, 330(0):77–88, 2007.

[122] A. Azad and D. Sundararajan. A phenomenological study on the synergistic role of precious metals in the steam reforming of logistic fuels on trimetal-supported catalysts. *Advances in Materials Science and Engineering*, page 12, 2010.

[123] M. Garcia Jarana, J. Sánchez-Oneto, J. Portela, E. Nebot Sanz, and E. Martínez de la Ossa. Supercritical water gasification of industrial organic wastes. *J. Supercrit. Fluids*, 46(3):329–334, 2008.

[124] D. Elliott, R. Hallen, and L. Sealock. Aqueous catalyst systems for the water-gas shift reaction. 2. mechanism of basic catalysis. *Ind. Eng. Chem. Prod. Res. Dev.*, 22(3):431–435, 1983.

[125] A. Sinag, A. Kruse, and V. Schwarzkopf. Key compounds of the hydropyrolysis of glucose in supercritical water in the presence of K_2CO_3. *Ind. Eng. Chem. Res.*, 42(15):3516–3521, 2003.

[126] J. Gadhe and R. Gupta. Hydrogen Production by Methanol Reforming in Supercritical Water: Suppression of Methane Formation. *Ind. Eng. Chem. Res*, 44(13):4577–4585, 2005.

[127] X. Hao, L. Guo, X. Mao, X. Zhang, and X. Chen. Hydrogen production from glucose used as a model compound of biomass gasified in supercritical water. *Int. J. Hydrogen Energ.*, 28(1):55–64, 2003.

[128] M. Osada, T. Sato, M. Watanabe, M. Shirai, and K. Arai. Catalytic Gasification of Wood Biomass in Subcritical and Supercritical Water. *Combust. Sci. Technol.*, 178(1-3):537–552, 2006.

[129] B. Kuster and H. Temmink. The influence of ph and weak-acid anions on the dehydration of d-fructose. *Carbohyd. Res.*, 54(2):185–191, 1977.

[130] M. Watanabe, Y. Aizawa, T. Iida, T. Aida, C. Levy, K. Sue, and H. Inomata. Glucose reactions with acid and base catalysts in hot compressed water at 473 K. *Carbohyd. Res.*, 340(12):1925–1930, 2005.

[131] M. Alif, K. Matsumoto, and K. Kitagawa. On-line mass spectrometric analysis of hydrothermal reactions for biomass model sample containing sulfur compounds. *Microchemical Journal*, 99(2):394–399, 2011.

[132] Q. Liu, H. Hu, S. Zhu, Q. Zhou, W. Li, X. Wei, and K. Xie. Desulfurization of coal by pyrolysis and hydropyrolysis with addition of KOH/NaOH. *Energy Fuels*, 19(4):1673–1678, 2005.

[133] A. Kishita, T. Moriya, C. Hong, H. Enomoto, H. Kamimura, S. Takahashi. Upgrading of bitumen with supercritical water for a system combined with sagd. *ACS Fuel Div.*, 43:741-745, 1998.

[134] Hans G. Schlegel. *Allgemeine Mikrobiologie*. Georg Thieme Verlag Stuttgart, 1984.

[135] M. Giordano, K. Saito, R. Hell, H. Takahashi, S. Kopriva S. Sulfur assimilation in photosynthetic organisms: molecular functions and regulations of transporters and assimilatory enzymes. *Annu Rev Plant Biol.*, 62:157–84, 2011.

[136] I. Iwasaki and T. Ozawa. Genesis of sulfate in acid hot spring. *Bull. Chem. Soc. Japan*, 33:1018–1019, 1960.

[137] S. Oana and H. Ishikawa. Sulfur isotopic fractionation between sulfur and sulfuric acid in the hydrothermal solution of sulfur dioxide. *Geochem. J.*, 1:45–50, 1966.

[138] A. Ellis and W. Giggenbach. Hydrogen sulphide ionization and sulphur hydrolysis in high temperature solution. *Geochim.Cosmochim. Ac.*, 35(3):247–260, 1971.

[139] A. Katritzky, D. Nichols, M. Siskin, R. Murugan, and M. Balasubramanian. Cheminform abstract: Reactions in high-temperature aqueous media. *Chem. Rev.*, 101(26):837–892, 2001.

[140] B. Yang, Songbai Tian, and Shanlin Zhao. A study of thermal decomposition of alkanethiols in pressure reactor. *Fuel Process. Technol.*, 87(8):673–678, 2006.

[141] A. Kishita, S. Takahashi, F. Jin, Y. Yamasaki, T. Moriya, and H. Enomoto. Decomposition of benzothiophene, dibenzothiophene, and their derivates in subcritical and supercritical water with alkali. *Journal of the Japan Petroleum Institute*, 85 (5):272–280, 2005.

[142] O. Ogunsola and N. Berkowitz. Removal of heterocyclic S and N from oil precursors by supercritical water. *Fuel*, 74(10):1485–1490, 1995.

[143] B. Vogelaar, M. Makkee, and J.Moulijn. Applicability of supercritical water as a reaction medium for desulfurisation and demetallisation of gasoil. *Fuel Process. Technol.*, 61(3):265–277, 1999.

[144] M. Osada, N. Hiyoshi, O. Sato, K. Arai, and M. Shirai. Reaction Pathway for Catalytic Gasification of Lignin in Presence of Sulfur in Supercritical Water. *Energy Fuels*, 21(4):1854–1858, 2007.

[145] M. Osada, N. Hiyoshi, O. Sato, K. Arai, and M. Shirai. Effect of Sulfur on Catalytic Gasification of Lignin in Supercritical Water. *Energy Fuels*, 21(3):1400–1405, 2007.

[146] A. Haiduc, M. Brandenberger, S. Suquet, F. Vogel, R. Bernier-Latmani, and C. Ludwig. SunCHem: An Integrated Process for the Hydrothermal Production of Methane from Microalgae and CO_2 Mitigation. *J. Appl.Phycol.*, 21(5):529–541, 2009.

[147] M. Osada, N. Hiyoshi, O. Sato, K. Arai, and M. Shirai. Subcritical Water Regeneration of Supported Ruthenium Catalyst Poisoned by Sulfur. *Energy Fuels*, 22(2):845–849, 2008.

[148] M. Dreher. paper in preparation. 2013.

[149] Y. Matsumura, T. Minowa, B. Potic, S. Kersten, W. Prins, W. van Swaaij, B. van de Beld, D. Elliott, G. Neuenschwander, A. Kruse, and M. Jerry Antal Jr. Biomass gasification in near- and super-critical water: Status and prospects. *Biomass Bioenerg.*, 29(4):269–292, 2005.

[150] T. Sato, T. Adschiri, K. Arai, G. Rempel, and F. Ng. Upgrading of asphalt with and without partial oxidation in supercritical water. *Fuel*, 82(10):1231–1239, 2003.

[151] M. Watanabe, S. Kato, S. Ishizeki, H. Inomata, and R.Smith Jr. Heavy oil upgrading in the presence of high density water: Basic study. *J. Supercrit. Fluids*, 53:48–52, 2010.

[152] M. Morimoto, Y. Sugimoto, Y. Saotome, S. Sato, and T. Takanohashi. Effect of supercritical water on upgrading reaction of oil sand bitumen. *J. Supercrit. Fluids*, 55(1):223–231, 2010.

[153] M. Brandenberger. Catalyst dissolution and biomass gasification studies under hydrothermal conditions. Master's thesis, EPFL, Switzerland, 2007.

[154] Martin Schubert, Martin Brandenberger, Christian Ludwig, and Frederic Vogel. Methangewinnung durch heterogen katalysierte, hydrothermale Vergasung nasser Biomasse. In *41. Jahrestreffen deutscher Katalytiker, Feb 27-29*, Weimar, Germany, 2008.

[155] Characterization of sludges, Determination of the loss on ignition of dry mass. DIN EN 2879:2001-02, Beuth, 2001.

[156] Characterization of sludges, Determination of dry residue and water content. DIN EN 12880:2001-02, Beuth, 2001.

[157] P. Van Soest H. Goering. Forage fiber analyses (apparatus, reagents, procedures and some applications). *USDA Handbook No. 379*, Superintendent of Documents, US Government Printing Office, Washington, D.C. 20402, 1970.

[158] Neutral Detergent Fiber in Feeds, Filter Bag Technique, Ankom Technology Method 6. http://www.ankom.com/analytical-procedures.aspx.

[159] Acid Detergent Fiber in Feeds, Filter Bag Technique, Ankom Technology Method 5. http://www.ankom.com/analytical-procedures.aspx.

[160] Method for Determining Acid Detergent Lignin in the DaisyI Incubator, Ankom Technology - 08/05. http://www.ankom.com/analytical-procedures.aspx.

[161] M. Hodes, P. Griffith, K. Smith, W. Hurst, W. Bowers, and K. Sako. Salt Solubility and Deposition in High Temperature and Pressure Aqueous Solutions. *AIChE Journal*, 50(9):2038–2049, 2004.

[162] I. Leusbrock, S. Metz, G. Rexwinkel, and G. Versteeg. Quantitative approaches for the description of solubilities of inorganic compounds in near-critical and supercritical water. *J. Supercrit. Fluids*, 47(2):117–127, 2008.

[163] H. Baierlein. Zur Löslichkeit von Salzen in überkritischem Wasserdampf. PhD thesis, Universität Erlangen-Nürnberg, 1983.

[164] S Brunauer, PH Emmett, and E Teller. Adsorption of Gases in Multimolecular Layers. *J. Am.Chem.Soc.*, 60:309–319, 1938.

[165] R. Dalla Betta. Measurement of Ruthenium Metal Surface Area by Chemisorption. *Journal of Catalysis*, 34(1):57 – 60, 1974.

[166] DIN 66136-1:2004-03 Determination of the dispersion degree of metals using gas chemisorption -Part 1: Principles. Beuth Verlag GmbH, 10772 Berlin, 2004,

[167] M. Mehring, M. Elsener, and O. Kröcher. Development of a TG-FTIR system for investigations with condensable and corrosive gases. *Journal of Thermal Analysis and Calorimetry,* 105(2):545–552, 2011.

[168] H. Zöhrer and F. Vogel. Hydrothermal catalytic gasification of fermentation residues from a biogas plant. *Biomass and Bioenergy* 53:138–148, 2013.

[169] M. Waldner and F. Vogel. Renewable production of methane from woody biomass by catalytic hydrothermal gasification. *Ind. Eng. Chem. Res.*, 44(13):4543–4551, 2005.

[170] A. Peterson. Biomass Reforming Processes in Hydrothermal Media. PhD thesis, Massachusetts Institute ofTechnology, Cambridge, USA, 2009.

[171] Y.-K. Jeong and J.-S. Kim. A new method for conservation of nitrogen in aerobic composting processes. *Bioresource Technol.*, 79(2):129–133, 2001.

[172] T. Wölfl. Untersuchungen zur Desaktivierung von Katalysatoren bei der hydrothermalen Vergasung von Modellsubstanzen eines Gärrestes aus einer Biogasanlage. Bachelor's thesis, FH Bingen, Germany, 2012.

[173] F. Mayr. Eignungstest von Trägermaterialien für die hydrothermale Vergasung von nasser Biomasse in der kontinuierlichen Laboranlage Konti-1. Diplom thesis, TU Dresden, Germany, 2013.

[174] H. Zöhrer, F. Mayr, and F. Vogel. Stability and performance of ruthenium catalysts based on refractory oxide supports in supercritical water conditions. *Energy Fuels* 27:4739–4747, 2013.

[175] E. Osborn. Subsolidus reactions in oxide systems in the presence of water at high pressures. *J. Am. Ceram. Soc.*, 36(5):147–151, 1953.

[176] S. Kraft. Modellierung und Simulation eines Festbettreaktors zur hydrothermalen Vergasung von nasser Biomasse. Master's thesis, Paul Scherrer Institut /TU Wien, 2011.

[177] L. Okal and J. Kepinsky. *Focus on Catalysis Research*. Nova Science Publishers Inc., 2006.

7 Appendix

Appendix A: List of all catalysts used. n.a.: not analyzed. (1) see Table 4-1. *poor linear fitting.

Designation	Loading	Support	BET SA [$m^3\ g^{-1}$]	MSA [$m^3\ g^{-1}$]	Pellet size [mm]	Bulk density [$kg\ m^{-3}$]
2% Ru/ZrO_2 (2)	2 wt% Ru	2[(1)]	38.5	1.1	3	1360
5% Ru/ZrO_2 (2)	5 wt% Ru	2[(1)]	37	3.4	3	1390
7.5% Ru-Re/ZrO_2	2.5 wt% Ru, 5 wt% Re	2[(1)]	n.a.	5.6	3	1400
2% Ru/TiO_2 (8)	2 wt% Ru	8[(1)]	4.4	0.1*	3	1410
5% Ru/TiO_2 (8)	5 wt% Ru	8[(1)]	4.5	0.4*	3	1430
2%Ru/ZrO_2 (11)	2 wt% Ru	11[(1)]	19.8	1.3	1.5	1390
2% Ru/ZrO_2-TiO_2 (5)	2 wt% Ru	5[(1)]	-	<0.1*	3	990
2% Ru/ZrO_2 (7)	2 wt% Ru	7[(1)]	41.4	1.9	3	1210
2% Ru/ZrO_2 (DKKK)	2 wt% Ru	ZrO_2 (DKKK)	47.2	1.6	1.25-2	1230
2% Ru/C	2 wt% Ru	Pyrolyzed coconut shell	1194	1.2	ca 2-4	570

Appendix B: List of all batch experiments.

Code	Sample	Feed conc. [mg g^{-1}]	Catalyst system	[S/Ru] molar ratio [mol mol^{-1}]	Heating rate [K min^{-1}]	Tempera-ture [℃]	Final pressure [mPa]	Reaction time [min]	Residence time >300℃ [min]	Comments
A1V	O3	39	2% Ru/ZrO_2 (DKKK)	5.0	>50	376	-	7.5	5	Mini-batch
A1H	O3	39	2% Ru/ZrO_2 (DKKK)	4.9	>50	378	-	6.5	5	Mini-batch
A2V	O3	39	2% Ru/ZrO_2 (DKKK)	4.7	>50	376	-	7.5	5	Mini-batch
A2H	O3	39	2% Ru/ZrO_2 (DKKK)	4.8	>50	378	-	6.5	5	Mini-batch
A3V	O3	39	2% Ru/ZrO_2 (DKKK)	4.9	>50	383	-	12.5	10	Mini-batch
A3H	O3	39	2% Ru/ZrO_2 (DKKK)	4.8	>50	386	-	11.5	10	Mini-batch
A4V	O3	39	2% Ru/ZrO_2 (DKKK)	4.9	>50	383	-	12.5	10	Mini-batch
A4H	O3	39	2% Ru/ZrO_2 (DKKK)	4.9	>50	383	-	11.5	10	Mini-batch
A5V	O1	120	2% Ru/C	3.4	>50	378	-	10	7.5	Mini-batch
A5H	O1	120	2% Ru/C	3.5	>50	380	-	10	8.5	Mini-batch
A6V	O1	120	2% Ru/C	3.5	>50	383	-	15	12.2	Mini-batch
A6H	O1	120	2% Ru/C	3.4	>50	385	-	15	13.5	Mini-batch
A7V	O1	120	2% Ru/C	3.4	>50	385	-	15	12.2	Mini-batch

A7H	O1	120	2% Ru/C	3.3	>50	388	-	15	13.5	Mini-batch
A8V	O1	120	2% Ru/C	2.8	>50	376	-	10	7.5	Mini-batch
A8H	O1	120	2% Ru/C	2.8	>50	377	-	10	8.5	Mini-batch
G0	Untreated gas mix, composition: 28% CO, 19% CO_2,10% CH_4, 4% C_2H_8, 1% N_2, 38% H_2									
G1	Gas mix	1 g water	2% Ru/C	0	>50	n/a	19.7	15	n/a	T-couple broke
G2	Gas mix	8 g water	2% Ru/C	0	>50	n/a	25.7	30	n/a	T-couple broke
G3	Gas mix	8 g water	2% Ru/C	0	>50	n/a	30.4	90	n/a	T-couple broke
G4	Gas mix	8 g water	2% Ru/C	0	>50	401	28.7	30	27	Catalyst elevated in cage
G5	Gas mix	8 g water	2% Ru/C	0	>50	398	28.4	60	53	Catalyst elevated in cage
G6	Calculated equilibrium for gas mix G0 at 400℃, 30 MPa									
SO4-1	0.01 M K_2SO_4		2% Ru/C	10	>50	400	28	60	55	
SO4-2	20wt% glycerol + 0.01 M K_2SO_4		-		>50	400	30	60	55	
R1	O3	39	2% Ru/C	0.27	>50	416	33	60	56	$\dot{\zeta}$ = 0.17 [kg (kg h)
R2	O3	39	2% Ru/C	0.30	>50	413	34	30	25	$\dot{\zeta}$ = 0.45 [kg (kg h)
R3	O3	39	2% Ru/C	0.19	>50	417	34	15	11	$\dot{\zeta}$ = 0.66 [kg (kg h)
R4	O3	39	2% Ru/C	0.28	>50	380	26	10	5	$\dot{\zeta}$ = 2.10 [kg (kg h)
C1	O3	39	-	-	>50	413	31	60	55	
C2	O3	39	2% Ru/ZrO_2 (DKKK)	0.21	>50	414	35	60	55	
C3	O3	39	2% Ru/C	0.21	>50	414	35	60	54	
C3	O3	39	2% Ru/C	0.21	>50	414	35	60	54	

Code	Sample	Feed conc. [mg g^{-1}]	Catalyst system	[S/Ru] molar ratio [mol mol^{-1}]	Heating rate [K min^{-1}]	Tempera-ture [℃]	Final pressure [mPa]	Reaction time [min]	Residence time >300℃ [min]	Comments
S1	O3	39	2% Ru/C	0.29	>50	419	31	60	54	pH after reaction: 8.5
S2	O3	39	2% Ru/C	0.58	>50	415	30	60	54	pH after reaction: 8.5
S3	O3	39	2% Ru/C	0.68	>50	409	30	60	54	pH after reaction: 8.5
S4	O3	39	2% Ru/C	1.01	>50	415	30	60	54	pH after reaction: 8.5
S5	O3	39	-	∞	>50	413	31	60	55	pH after reaction: 8.5
S6	S1	49	2% Ru/C	0.14	>50	413	35	60	55	pH after reaction: 4
S7	S1	51	2% Ru/C	0.13	>50	420	36	60	55	pH after reaction: 5
T1	O3	39	2% Ru/C	0.42	>50	365	23	30	24	
T2	calculated equilibrium for fermentation residue O3 at 400℃, 30 MPa									
T3	O3	39	2% Ru/C	0.40	>50	402	32	30	25	
T4	O3	39	2% Ru/C	0.48	>50	419	33	33	26	
T5	O3	39	2% Ru/C	0.44	>50	430	35	30	27	
H1	O3	78	-	-	<5	406	31	103	70	No Additive pH after reaction: 8.5
H2	O3	78	-	-	<5	397	29	106	65	1 mg g^{-1} (DM) KOH pH after reaction: 8.5
H3	O3	78	-	-	<5	408	31	97	56	0.5 mg g^{-1} (DM) Na_2CO_3 pH after reaction: 8.5
H4	O3	78	-	-	<5	408	32	100	63	1 mg g^{-1} (DM) $CaCO_3$ pH after reaction: 8.5
H5	O3	78	-	-	<5	406	32	93	57	1 mg g^{-1} (DM) K_2CO_3 pH after reaction: 8.5

H6	O3	78	-	-	-	-	-	-	-	Untreated, pH: 7.5
H7	O4	63	-	-	<5	412	35	100	67	No Additive pH after reaction: 8.5
H8	O4	63	-	-	<5	414	33	102	32	1 mg g^{-1} (DM) K_2CO_3 pH after reaction: 8.5
H9	O4	63	-	-	-	-	-	-	-	untreated
H10	S1	82	-	-	<5	413	33	107	67	No Additive pH after reaction: 4
H11	S1	82	-	-	<5	415	33	108	66	6 mg g^{-1} (DM) K_2CO_3 pH after reaction: 6
H12	S1	82	-	-	-	-	-	-	-	untreated

Appendix C: List of Konti-1 experiments with sulfur poisoning and regeneration.

Code		Catalyst	Catalyst mass	Setpoint temperature	Temperature (end of catalyst bed)	Pressure	Organic feed	Duration	Molar ratio $n(H_2O_2):n(Ru)$
			[g]	[℃]	[℃]	[MPa]	-	[h]	-
SC1	a	2%Ru/C	10.25	400	440*/380℃	30	10 wt% Glycerol	4.7	
	b			350	350	30	H_2O	16	
	c			400	380	30	0.002 wt% K_2SO_4	4	
	d			400		30	10 wt% Glycerol	3.1	
SC2	a	2%Ru/C	10.86	400	380	31	10 wt% Glycerol/ 0.002 M K_2SO_4	3.5	
SC3	a	2%Ru/C	8.9	460	420	30	10 wt% Glycerol/ 0.002 M K_2SO_4	5	
	b			125	130	29	3% H_2O_2	70 min	175
	c			400	380	29	10 wt% Glycerol	3.4	
SC4			9.1	125	125	29	2% H_2O_2	3	294
SC5	a	2%Ru/C	8.9	400	380	28	10 wt% Glycerol/ 0.002 M K_2SO_4	3.5	
	b			125	130	28	2% H_2O_2	2.5	250
	c			400	380	28	10 wt% Glycerol	4	
ST1	a	2% Ru/TiO_2	31	400	360	30	5 wt% Glycerol/ 0.002 M K_2SO_4	4	
	b			300	300	30	H_2O	4	
	c			400	360	30	5 wt% Glycerol	3	
	d			125	130	30	2% H_2O_2	2.5	72
	e			400	360	30	5 wt% Glycerol/ 0.002 M K_2SO_4	4	

Appendix D: Composition of samples 1-11 (t: tetragonal); diameter of pellets; BET surface area of fresh sample; BET surface area of samples aged (1) once and (2) twice for 20 h at 430°C; Deviation of BET surface area (a) between fresh sample and sample aged once and (b) between sample aged once and twice; Physical stability ((yes) = stable but traces of attrition); Crystallographic stability ((yes) = minuscule changes); * crystal particle growth but no phase change

Sample No.	Composition (given by manufacturer)	Diameter of pellets [mm]	BET Surface area [m^2/g] fresh sample	BET Surface area [m^2/g] aged (1)	Change (a) %	BET Surface area [m^2/g] aged (2)	Change (b) %	Physical stability	Crystallo-graphic stability
1	t-ZrO_2 94%, HfO_2 2.4%, SiO_2 3%	1.5	156	57	-64			yes	no
2	t- ZrO_2 88.2%, HfO_2 1.77%, La_2O_3 9.7%	3	114	42	-64	39	-6	(yes)	(yes)
3	t- ZrO_2 90.44%, HfO_2 1.85%, SiO_2 0.11, Y_2O_3 7.34%, Al_2O_3 0.17%	3	114	35	-69			no	no
4	t- ZrO_2 78.75%, HfO_2 1.56%, SiO_2 0.6, CeO_2 18.83%, Al_2O_3 0.72%	3	101	28	-72			(yes)	no
5	ZrO_2 56.7%, TiO_2 41.3%, $HfO_2$1.1%, SiO_2 0.4%	3	78	48	-38	47	-3	(yes)	(yes)
6	TiO_2 anatase	3	151	49	-67			no	(yes)*
7	ZrO_2 monoclinic	3	54	43	-21	42	-3	(yes)	yes
8	TiO_2 rutile	3	3.9	3.9	-0.8	4.2	8.8	yes	yes
9	t- ZrO_2 82.4%, HfO_2 1.49%, Al_2O_3 0.17%, WO_3 15.94%	3	115	74	-35			(yes)	no
10	ZrO_2 monoclinic	3	90	74	-18	69	-7	(yes)	yes
11	ZrO_2 monoclinic	1.5	26	24	-8	24	0	yes	yes

Appendix E: List of Konti-1 experiments for catalyst screening.

Code		Catalyst	Catalyst mass	Setpoint temperature	Temperature (end of catalyst bed)	Pressure	Organic feed	Duration	WHSV
			[g]	[℃]	[℃]	[MPa]		[h]	[h^{-1}]
Blank	a	-	-	400	395	28.5	6 wt% Glycerol	8	-
Blank	b			400	392	28.5	11 wt% Glycerol	8	-
Blank	c			400	390	28.5	16 wt% Glycerol	7	-
2N2	a	2%Ru/ZrO_2 (2)	30	400	365	28.5	6 wt% Glycerol	24	0.6
	b			400	358	28.5	11 wt% Glycerol	24	1.1
	c			400	365	28.5	6 wt% Glycerol	2.5	0.6
2N5	a	2%Ru/ZrO_2–TiO_2(5)	32	400	n.d.	28.5	6 wt% Glycerol	2	0.6
2N7	a	2%Ru/ZrO_2 (7)	27	400	367	28.5	6 wt% Glycerol	24	0.6
	b			400	367	28.5	11 wt% Glycerol	24	1.1
	c			400	367	28.5	6 wt% Glycerol	8	0.6
2N8	a	2%Ru/TiO_2 (8)	31	400	360	28.5	6 wt% Glycerol	24	0.6
2N11	a	2%Ru/ZrO_2 (11)	30	400	377	28.5	6 wt% Glycerol	24	0.6
5N2	a	5%Ru/ZrO_2 (2)	30	400	375	28.5	6 wt% Glycerol	24	0.6
	b			400	373	28.5	11 wt% Glycerol	24	1.1

	c			400	373	28.5	16 wt% Glycerol	24	1.6
	d			400	375	28.5	19 wt% Glycerol	24	2
	e			400	n.d.	28.5	16 wt% Glycerol	4	1.6
5N8	a	5%Ru/TiO_2 (8)	30	400	370	28.5	6 wt% Glycerol	24	0.6
	b			400	365	28.5	11 wt% Glyc	24	1.1
	c			400	370	28.5	6 wt% Glycerol	2	0.6
7.5N2	a	7.5%Ru-Re/ZrO_2 (2)	30	400	380	28.5	6 wt% Glycerol	24	0.6
	b			400	378	28.5	11 wt% Glyc	24	1.1
	c			400	370	28.5	16 wt% Glycerol	24	1.6
	d			400	n.d.	28.5	6 wt% Glycerol		0.6
	e			400	387	28.5	6 wt% Glycerol + 0.002 M K_2SO_4	5	0.6
	f			300	n.d.	28.5	water	12	-
	g			400	n.d.	28.5	6 wt% Glycerol	1	0.6

Appendix F: Scheme of the test rig Konti-2:

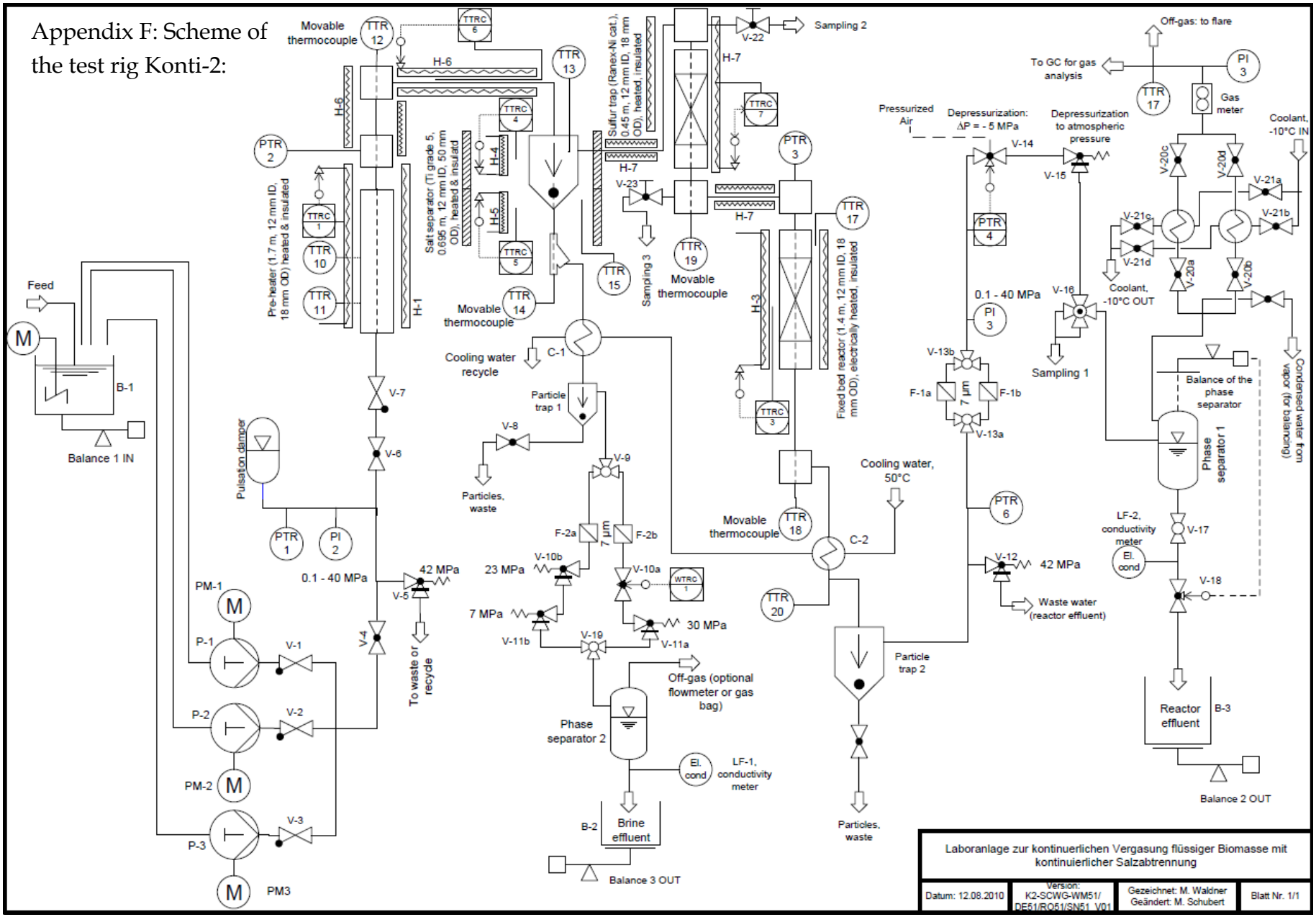

Appendix G: Scheme of the test rig Konti-1:

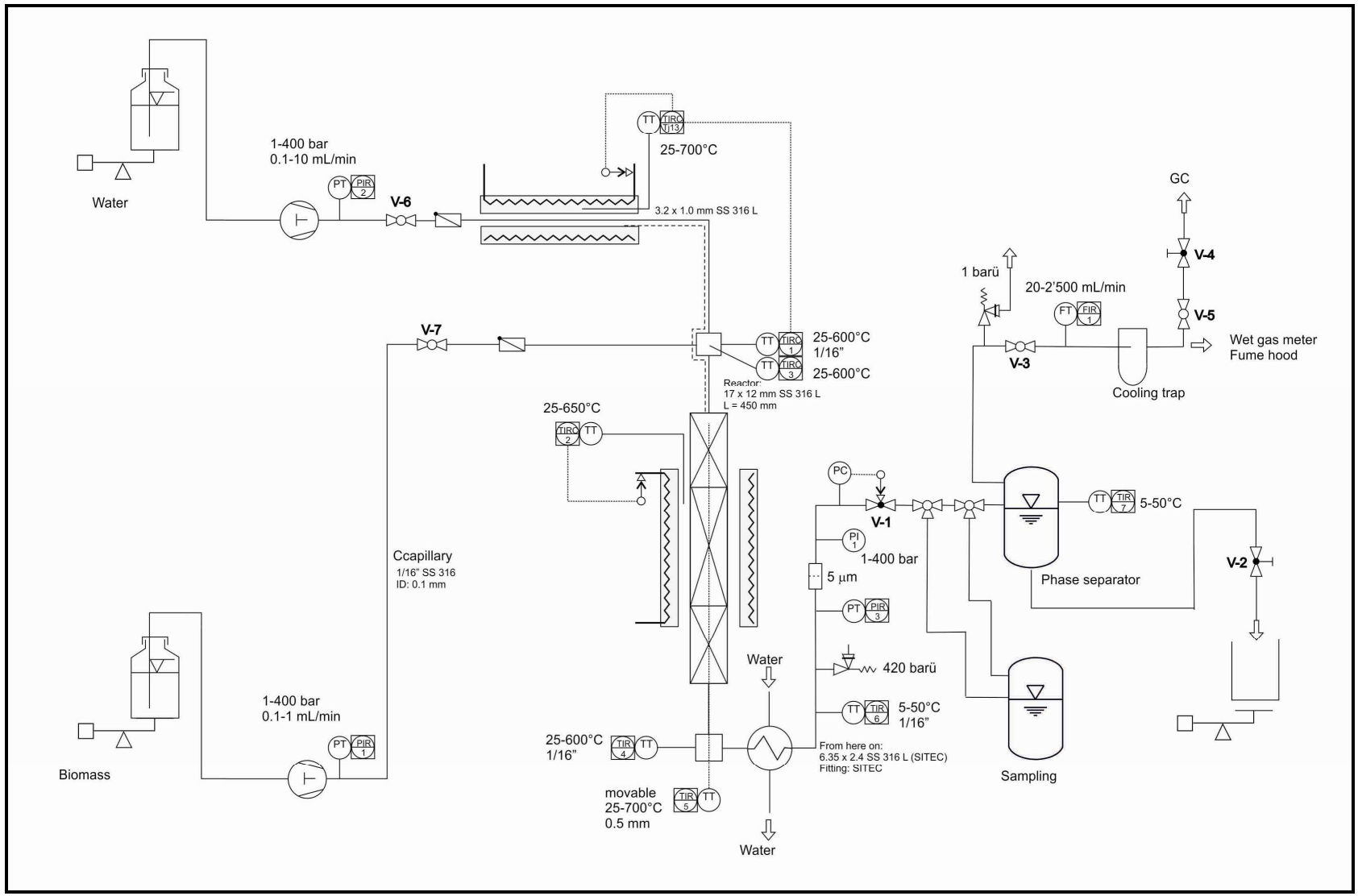

List of publications

Peer reviewed articles:

H. Zöhrer, F. Vogel. Hydrothermal catalytic gasification of fermentation residues from a biogas plant. Biomass Bioenergy 53:138-148, 2013.

H. Zöhrer, F. Mayr, and F. Vogel. Stability and performance of ruthenium catalysts based on refractory oxide supports in supercritical water conditions. Energy Fuels, 27:4739-4747, 2013.

Conference posters:

H. Zöhrer, M. Schubert, F. Vogel. Regeneration methods for sulfur-poisoned catalysts in supercritical water gasification. ProcessNet-Jahrestagung 2012, Karlsruhe, Germany, September 11-13, 2012.

Conference talks

H. Zöhrer, F. Vogel. Hydrothermal gasification of fermentation residue. 20th European Biomass Conference and Exhibition 2012, Milan, Italy, June 18-22.

H. Zöhrer, E. De Boni, F. Vogel. Hydrothermal catalytic gasification of fermentation residue in a continuous reactor. ProcessNet-Jahrestagung 2012, Karlsruhe, Germany, September 11-13.

H. Zöhrer, E. De Boni, F. Vogel. Hydrothermal gasification of fermentation residue in a continuous plant with continuous salt separation. 2st European Biomass Conference and Exhibition 2013, Copenhagen, Denmark, June 3-7.